UNIVERSIDADE FEDERAL DO PARANÁ

RHEINLAND-PFÄLZISCHE TECHNISCHE UNIVERSITÄT
KAISERSLAUTERN-LANDAU (RPTU)

LEDIANE MARCON

INVESTIGATION OF SPATIAL AND TEMPORAL DYNAMICS OF EBULLITION IN IMPOUNDMENTS

CURITIBA (BRAZIL)
LANDAU (GERMANY)
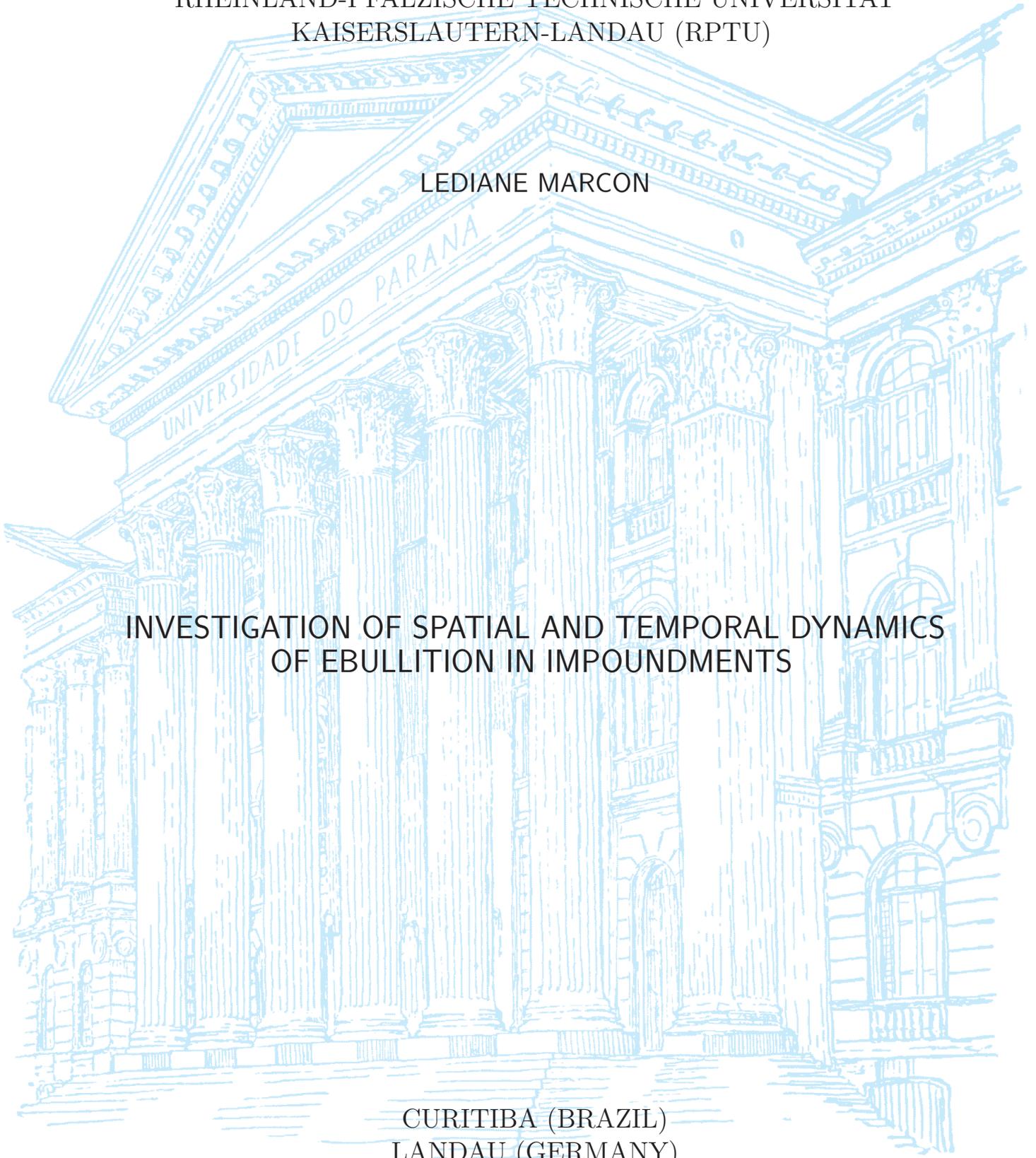
2023

LEDIANE MARCON

INVESTIGATION OF SPATIAL AND TEMPORAL DYNAMICS OF EBULLITION IN IMPOUNDMENTS

Tese apresentada ao curso de Pós-Graduação em Engenharia de Recursos Hídricos e Ambiental, setor de tecnologia, Universidade Federal do Paraná, e ao Departamento de Ciências Naturais e Ambientais da Universidade RPTU Kaiserslautern-Landau (Alemanha), como requisito parcial à obtenção do título de Doutora em Engenharia de Recursos Hídricos e Ambiental e Doutora em Ciências Naturais.

Orientador: Dr.-Ing Tobias Bleninger
Federal University of Paraná

Co-orientador: D.Sc. Michael Männich
Federal University of Paraná

Orientador: Dr. Andreas Lorke
RPTU Kaiserslautern-Landau

CURITIBA (BRAZIL)
LANDAU (GERMANY)

2023

MINISTÉRIO DA EDUCAÇÃO
SETOR DE TECNOLOGIA
UNIVERSIDADE FEDERAL DO PARANÁ
PRÓ-REITORIA DE PESQUISA E PÓS-GRADUAÇÃO
PROGRAMA DE PÓS-GRADUAÇÃO ENGENHARIA DE
RECURSOS HÍDRICOS E AMBIENTAL - 40001016021P0

APPROVAL MINUTE

The Examining Board is designated by the Faculty of the Graduate Program of the Federal University of Paraná in ENGENHARIA DE RECURSOS HÍDRICOS E AMBIENTAL where invited to argue the DISSERTATION of PHILOSOPHY DOCTOR by **LEDIANE MARCON** , entitled: **Investigation of spatial and temporal dynamics of ebullition in impoundments**, under the supervision of Dr. TOBIAS BERNWARD BLENINGER, which and after assessment of the candidate and the work, the Examining Board decided for the APPROVAL in the present rite.

The granting of the title of philosophy doctor is contingent upon the fulfillment of all the requirements indicated by the Examining Board and terms determined in the regulation of the Graduate Program.

CURITIBA, July 18th, 2023.

Eletronic Signature
20/07/2023 16:23:37.0
TOBIAS BERNWARD BLENINGER
President of the Examining Board

Eletronic Signature
21/07/2023 19:32:50.0
MARCELO GOMES DA SILVA
External Member (OUTRAS)

Eletronic Signature
21/07/2023 12:41:26.0
DANIEL HENRIQUE MARCO DETZEL
Internal Member(UNIVERSIDADE FEDERAL DO PARANÁ)

Eletronic Signature
22/07/2023 03:14:39.0
SARIAN KOSTEN
External Member (WAGENINGEN UNIVERSITY)

Eletronic Signature
25/07/2023 12:40:37.0
ANDREAS LORKE
Co-Advisor

Eletronic Signature
25/07/2023 14:05:10.0
MICHAEL MANNICH
Co-Advisor

Centro Politécnico, Bloco V - CURITIBA - Paraná - Brasil
CEP 81531-990 - Tel: (41) 3361-3210 - E-mail: ppgerha@ufpr.br
Documento assinado eletronicamente de acordo com o disposto na legislação federal Decreto 8539 de 08 de outubro de 2015.
Gerado e autenticado pelo SIGA-UFPR, com a seguinte identificação única: 298827
**Para autenticar este documento/assinatura, acesse https://siga.ufpr.br/siga/visitante/autenticacaoassinaturas.jsp
e insira o codigo 298827**

To my beloved parents Lídia Marcon and Léo Marcon, who have spared no effort in supporting and motivating me at every stage of my life. They are my example of kindness, perseverance, and faith.

Acknowledgements

"Ando devagar porque já tive pressa e levo esse sorriso porque já chorei demais
Hoje me sinto mais forte mais feliz, quem sabe. Só levo a certeza de que muito pouco sei ou nada sei
Conhecer as manhas e as manhãs, o sabor das massas e das maçãs
É preciso amor pra poder pulsar. É preciso paz pra poder sorrir. É preciso a chuva para florir ...
... Cada um de nós compõe a sua história, e cada ser em si carrega o dom de ser capaz e ser feliz."
(Almir Sater e Renato Teixeira)

This dissertation thesis is based on three scientific articles submitted to peer-reviewed journals, in which one article (i) is published, one (ii) is accepted for publication , and the third one (iii) is under review. The articles are listed below (ordered by date):

i. Marcon, Lediane; Sotiri, Klajdi; Bleninger, Tobias; Lorke, Andreas; Männich, Michael; Hilgert, Stephan. (2022). **Acoustic mapping of gas stored in sediments of shallow aquatic systems linked to methane production and ebullition patterns** . Frontiers in Environmental Science. doi: 10.3389/fenvs.2022.876540. (Full text is presented in Appendix A).

ii. Marcon, Lediane; Schwarz, Michael; Backes, Laura; Offermann, Mara; Schreiber, Felix; Hilgert, Stephan; Sotiri, Klajdi; Jokiel, Christian, Lorke, Andreas. (2022). **Linking sediment gas storage to the methane dynamics in a shallow freshwater reservoir**. Accepted in JGR-Biogeosciences. doi: 10.1029/2022JG007365. (Full text is presented in Appendix B).

iii. Marcon, Lediane; Bleninger, Tobias; Männich, Michael; Ishikawa, Mayra; Hilgert, Stephan; Lorke, Andreas. (2023). **Exploring the temporal dynamics of methane ebullition in a subtropical freshwater reservoir**. Submitted to Plos One. (Full text is presented in Appendix C).

RESUMO

As águas interiores, como os reservatórios de água doce, são fontes significativas e variáveis do gás de efeito estufa metano para a atmosfera. Em corpos d'água, o metano é principalmente produzido no sedimento de fundo rico em matéria orgânica, onde o metano pode se acumular, formar vazios de gás e ser transportado para a atmosfera por bolhas que escapam do sedimento. O transporte de metano mediado por bolhas, também conhecido como ebulição de metano, é uma via comumente dominante de emissões de metano em reservatórios de água doce. A ebulição resulta de uma interação complexa de vários processos físicos e biogeoquímicos simultâneos que atuam em diferentes escalas de tempo, resultando em fluxos variáveis no espaço e no tempo. Embora a maior parte da produção e do acúmulo de gás acontece no sedimento, há uma falta de dados in situ sobre o armazenamento de gás em reservatórios e sobre a interação entre o armazenamento de gás em sedimentos com o balanço e com a ebulição de metano. Diversas variáveis ambientais são determinantes na ebulição; no entanto, ainda é um desafio simular a dinâmica temporal da ebulição e identificar os fatores determinantes em diferentes sistemas. Portanto, o principal objetivo desta tese foi investigar o efeito de diferentes fatores na regulação da variabilidade espacial e da dinâmica temporal da ebulição do metano em reservatórios. Foram investigados dois reservatórios contrastantes, um subtropical e outro temperado. Medições de alta frequência de fluxos de ebulição, variáveis ambientais e mapeamento do gás no sedimento baseado em acústica foram realizadas em ambos os reservatórios e compõem o conjunto de dados para este estudo. Os principais resultados foram apresentados em três manuscritos científicos. A distribuição espacial de gás no sedimento foi controlada principalmente pela deposição de sedimentos e pela profundidade da água, em que as regiões rasas com alta deposição de sedimentos tiveram elevado acúmulo de gás. As mudanças temporais na quantidade de gás no sedimento foram influenciada pelos componentes do balanço de metano no reservatório e pela dinâmica temporal da ebulição. Embora o sedimento possa armazenar dias de produção potencial acumulada de metano, o que poderia manter meses de fluxo médio de ebulição, os períodos de ebulição intensificada levam a um esgotamento do gás armazenado no sedimento. Os fatores que agem em grande escala espacial e que controlam a ebulição, como mudanças na pressão, resultaram na sincronização de eventos de ebulição em diferentes locais de monitoramento. No entanto, o grau de correlação da ebulição com as variáveis ambientais variou de um sistema para outro e com o tempo. A estratificação térmica foi considerada um modulador importante na relação entre a ebulição e outras variáveis ambientais, como as correntes de fundo e a turbulência. A dinâmica temporal da ebulição pode ser capturada e reproduzida por modelos empíricos em função de variáveis ambientais conhecidas; no entanto, os modelos não conseguiram reproduzir as variabilidades subdiárias da ebulição e apresentaram baixo desempenho quando transferidos de um sistema para outro. Por fim, embora ainda haja questões em aberto, os resultados deste trabalho contribuiem para o avanço do conhecimento da complexa dinâmica da ebulição do metano e seus controles em reservatórios de água doce.

Palavras-chaves: Emissões de metano. Séries temporais de ebulição. Armazenamento de gás no sedimento.

ABSTRACT

Inland waters, such as freshwater impoundments, are significant and variable sources of the greenhouse gas methane to the atmosphere. In water bodies, methane is mainly produced in the organic-matter rich bottom sediment, where it can accumulate, form gas voids, and be transported to the atmosphere by gas bubbles escaping the sediment. The bubble mediated transport of methane, known as methane ebullition, is a commonly dominant pathway of methane emissions in freshwater reservoirs. Ebullition results from a complex interplay of several simultaneous physical and bio-geochemical processes acting at different timescales, leading to highly variable fluxes in both space and time. Although the sediment matrix is a hot spot for gas production and accumulation, there is a lack of in-situ data on free gas storage in reservoirs and the interaction among sediment gas storage, methane budget, and methane ebullition. Several environmental variables are known to be ebullition drivers; however, simulating the temporal dynamics of ebullition and identifying the governing factors across different systems remains challenging. Therefore, the main goal of this thesis was to investigate the effect of different drivers on the spatial variability and temporal dynamics of methane ebullition in impoundments. Two contrasting reservoirs, one subtropical and one temperate, were investigated. High-frequency measurements of ebullition fluxes and environmental variables, and acoustic-based mapping of gas content in the sediment were performed in both reservoirs, constituting the dataset for this study. The main findings were presented in three main scientific manuscripts. The spatial distribution of gas content in the sediment was primarily controlled by sediment deposition and water depth, with shallow regions of high sediment deposition were hot spots of free gas accumulation in the sediment. Temporal changes in gas content in the sediment were linked to the methane budget components in the reservoir and further influenced by the temporal dynamics of ebullition. While the sediment could store days of accumulated potential methane production, which could sustain months of mean ebullition flux, periods of intensified ebullition led to a depletion of gas stored in the sediment. Large spatial scale ebullition drivers, such as pressure changes, resulted in the synchronization of ebullition events across different monitoring sites. Nevertheless, the degree of correlation between ebullition and environmental variables varied from one system to another and over time. Thermal stratification was an important modulator in the relationship between ebullition and other environmental variables, such as bottom currents and turbulence. The temporal dynamics of ebullition could be captured and reproduced by empirical models based on known environmental variables. However, these models failed to reproduce the sub-daily variabilities of ebullition and demonstrated poor performance when transferred from one system to another. Lastly, although some questions remain unanswered, the findings from this study contribute to advancing the understanding of the complex dynamics of methane ebullition and its controls in freshwater reservoirs.

Key words: Methane emissions. Ebullition time-series. Sediment gas storage.

ZUSAMMENFASSUNG

Binnengewässer, wie z. B. Talsperren, sind wichtige sich stetig verändernde Quellen des Treibhausgases Methan. In Gewässern wird Methan hauptsächlich in Bodensedimenten, welche reich an organischen Substanzen sind, produziert. Dort sammelt sich Methan an, bildet gasgefüllte Hohlräume und wird durch aus dem Sediment entweichende Gasblasen in die Atmosphäre transportiert. Der Transport von Methan in aufsteigenden Gasblasen, auch als Methan-Ebullition bezeichnet, ist ein häufig vorherrschender Mechanismus in Süßwasserreservoirs. Die Ebullition resultiert aus einem komplexen Zusammenspiel mehrerer physikalischer und biogeochemischer Prozesse, die auf unterschiedlichen Zeitskalen ablaufen. Das führt zu räumlich und zeitlich sehr variabeln Gasflüssen. Obwohl die Sedimentmatrix ein Hotspot der Gasproduktion und -akkumulation ist, mangelt es für Talsperren an In-situ-Daten über die freie Gasspeicherung in Sedimenten und die Wechselwirkung zwischen Gasspeicherung, Methanbudget und Methan-Ebullition. Man weiß, dass mehrere Umweltvariablen die Ebullition beeinflussen. Es ist jedoch nach wie vor schwierig, die zeitliche Dynamik der Ebullition zu simulieren und die bestimmenden Faktoren in verschiedenen Systemen zu ermitteln. Das Hauptziel dieser Arbeit bestand somit darin, die Auswirkungen verschiedener Einflussfaktoren auf die räumliche Variabilität und die zeitliche Dynamik der Methanemissionen aus Stauseen zu untersuchen. Es wurden zwei verschiedene Stauseen, einer in der subtropischen und einer in der gemäßigten Klimazone, untersucht. In beiden Stauseen wurden Hochfrequenz-Messungen der Methanflüsse und der Umweltvariablen, sowie eine akustische Kartierung des Gasgehalts im Sediment durchgeführt, welche gemeinsam den Datensatz für diese Studie bilden. Die wichtigsten Ergebnisse wurden in drei wissenschaftlichen Manuskripten veröffentlicht. Die räumliche Verteilung des Gasgehalts im Sediment wurde hauptsächlich durch die Sedimentablagerung und die Wassertiefe beeinflusst, wobei flache Regionen mit großen Mengen an Sediment Hotspots der Ansammlung von freiem Gas im Sediment waren. Es wurde aufgezeigt, dass zeitliche Veränderungen des Gasgehalts im Sediment mit den verschiedenen Komponenten des Methan-Budgets der Talsperre zusammenhängen und durch die Dynamik der Ebullition beeinflusst werden. Obwohl das Sediment die potenzielle Methanproduktion von mehreren Tagen speichern könnte, was wiederum die Aufrechterhaltung eines durchschnittlichen Ebullitionsflusses über Monate ermöglicht, führen Perioden verstärkter Ebullition zu einer Erschöpfung des im Sediment gespeicherten Gases. Einflussfaktoren mit großer räumlicher Ausdehnung, wie z. B. Druckveränderungen, führten zu einer Synchronisierung von Ebullitionsereignissen an verschiedenen Messstellen. Das Ausmaß, in dem die Ebullition mit Umweltvariablen korreliert, variierte jedoch von einem System zum anderen und zeitlich. Die thermische Schichtung erwies sich als wichtiger Parameter in der Beziehung zwischen Ebullition und anderen Umweltvariablen, wie z. B. Bodenströmungen und Turbulenzen. Die zeitliche Dynamik der Ebbullition konnte durch empirische Modelle in Abhängigkeit von bekannten Umweltvariablen erfasst und reproduziert werden. Jedoch konnten die Modelle auf Schwankungen für Zeiträume, welche kürzer als ein Tag waren, nicht angewandt werden und lieferten bei der Übertragung zwischen unterschiedlichen Systemen schlechte Resultate. Obwohl einige Fragen unbeantwortet blieben, tragen die Ergebnisse dieser Studie zum Verständnis der komplexen Dynamik der Methan-Ebullition und ihrer Einflussfaktoren in Talsperren bei.

Schlüsselwörter:: Methan-Emissionen. Ebullitions-Zeitserien. Gasspeicherung im Sediment.

Contents

1 Introduction

1.1 Freshwater reservoirs and contributions to methane emissions

Reservoirs of different sizes have been constructed worldwide with various purposes as for water supply, energy generation, flood control, agriculture use, and recreation. Like any construction projects, there are associated drawbacks. The construction of a reservoir by damming a river alters the riverine characteristics of the impounded water body, transforming it to a lentic system. These alterations are manifold and include reduced flow velocity, increased sediment retention (VÖRÖSMARTY et al., 2003), reduced vertical mixing, modification of the vertical distributions of substances and their concentration in the water column and sediment (FRIEDL; WÜEST, 2002), as well as changes in the transfer of nutrients along the entire river system (MAAVARA et al., 2020).

The impact of reservoirs on the carbon cycle has been extensively discussed in the literature, particularly after the publication of Rudd et al. (1993), which raised questions about reservoirs as source of greenhouse gas, such as methane (CH_4) and carbon dioxide (CO_2). Studies have highlighted the potential of aquatic systems to both store carbon (BERNARDO et al., 2017) and release carbon into the atmosphere (COLE et al., 2007). More recently, Vachon et al. (2020) showed a positive net of carbon emissions to the atmosphere when CH_4 is considered . However, Saunois et al. (2016) emphasized that CH_4 emissions from inland waters and wetlands remain the main source of uncertainty in the global methane budget.

Concerns about CH_4 concentration in the atmosphere have grown, especially following reports from the Intergovernmental Panel on Climate Change (IPCC). These reports draw attention to the significant radiative forcing of CH_4 in the atmosphere compared to CO_2 (80 times greater than CO_2 for a 20-years lifespan) and the 150% rise in CH_4 concentration compared to pre-industrial levels (IPCC, 2021). In this context, investigations have been conducted on the contributions of freshwater reservoirs and other inland waters to the CH_4 emissions. Greenhouse gas emissions (GHGs) from aquatic systems are of particular concern given the increasing number of impoundments. A global database has identified over 38000 dams worldwide (with dam lengths exceeding $150\,\mathrm{m}$ and reservoir lengths exceeding $500\,\mathrm{m}$) along with their corresponding reservoirs (MULLIGAN; SOESBERGEN; SÁENZ, 2020). When smaller reservoirs are considered, Lehner et al. (2011) pointed that there are more than 16 million impoundments with a surface area larger than $100\,\mathrm{m}^2$, which can act as sources of CH_4 to the atmosphere. In a recent review of literature data, Lauerwald et al. (2023) reported CH_4 emissions from reservoirs ranging from 9.8 to $52\,\mathrm{Tg}$ per year. However, considering the combined impact of global warming on more impacted and eutrophic ecosystems, the contribution of reservoirs to CH_4 emissions is expected to increase (ROSENTRETER et al., 2021).

1.2 Carbon cycle in the water and methane pathways

Carbon is an important nutrient widely present in aquatic environments, existing in both organic fractions (Dissolved Organic Carbon – DOC and Particulate Organic Carbon – POC) and inorganic fraction (Dissolved Inorganic Carbon – DIC), with both fractions combined to form the Total Carbon (TC) (ESTEVES, 2011). Inland waters are known to play an important role in the global carbon cycle. The reported emissions ($1.4\,\mathrm{PgC}\,\mathrm{yr}^{-1}$) are comparable to the net production of terrestrial ecosystems

$(2\,\mathrm{PgC\,yr^{-1}})$, while the amount of organic carbon buried in the sediment is greater in inland waters $(0.6\,\mathrm{PgC\,yr^{-1}})$ than in the ocean floor $(0.1\,\mathrm{PgC\,yr^{-1}})$ (TRANVIK et al., 2009).

Carbon can enter water bodies through various pathways, such as groundwater water and runoff from the catchment and surrounding areas, as well as atmospheric exchange. Internally, the interaction among different trophic levels contributes to the transformation of carbon from one fraction to another (ESTEVES, 2011), and flooded areas serve as sources of organic matter and carbon (TEODORU et al., 2012). The allochthonous and the autochthonous loading of organic carbon can be distributed throughout the water column or settle in the bottom sediment, where carbon may become buried and removed from the active carbon cycle (MENDONÇA et al., 2017); or can be mineralized into simpler organic compounds or inorganic fractions and be transported back to the water column, incorporated into biota biomass, or even transferred to the atmosphere. The primary inflows and outflows of carbon in water bodies are presented in Figure 1.
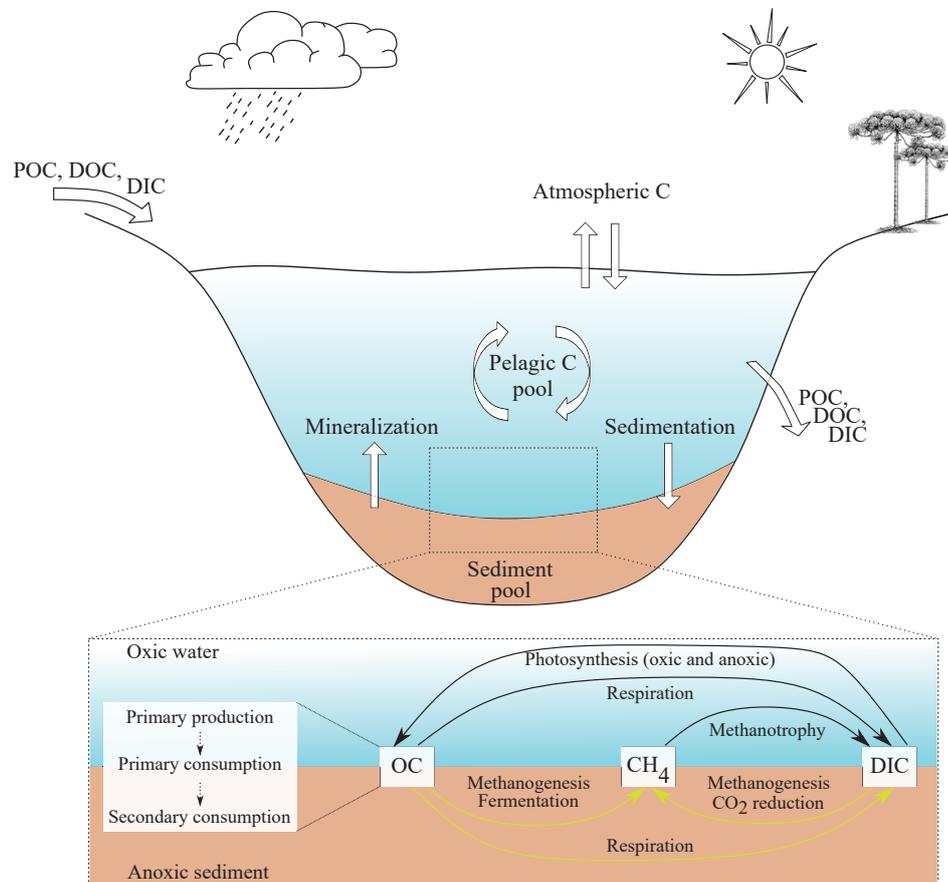
Figure 1 – Overview of the carbon cycle in water indicating the inflow and outflow of particulate organic carbon (POC), dissolved organic carbon (DOC), and dissolved inorganic carbon (DIC); the exchange of carbon with the atmosphere; water column and sediment carbon pools. It is detailed the carbon transformation under oxic conditions (bottom chart and black arrows) and anoxic conditions (bottom chart and yellow arrows). It is important to mention that the oxic or anoxic conditions are not restricted to water or sediment compartments, it is rather dependent on the availability of oxygen. The organic carbon (OC) transits among the different trophic levels and can be transformed into methane (CH_4) or to an inorganic form (DIC) as CO_2. Based on Tranvik et al. (2009) and adapted from Esteves (2011).

The transformations of carbon in water depend on temperature, pH, and oxygen conditions. The availability of oxygen indicates the prevailing processes. Respiration and photosynthesis can occur under either oxic or anoxic conditions, as shown in Figure 1. During photosynthesis, dissolved inorganic carbon

is converted to organic compounds using light. In respiration, dissolved organic carbon is oxidized to carbon dioxide under oxic conditions (consuming oxygen), and under anoxic conditions, it is oxidized to carbon dioxide plus a radical, with nitrate and sulfate acting as final electron acceptors (ESTEVES, 2011). Methane formation and oxidation through microbial microbial activity are also important processes.

The primary path of CH_4 formation in natural systems is through microbial metabolism, known as methanogenesis, which accounts for more than 85% of CH_4 production (VALENTINE et al., 2004). Two major processes of CH_4 formation are mentioned in the literature: acetoclastic reactions and CO_2 reduction (WETZEL, 1983; ESTEVES, 2011), as indicated in the lower portion of Figure 1. The relative contribution of these processes to total CH_4 production may vary across different environments (VALENTINE et al., 2004), however Praetzel et al. (2019) summarized that environments with a higher proportion of readily decomposable organic matter (such as autochthonous organic matter) tend to be dominated by the acetoclastic pathway, while environments with recalcitrant allochthonous compounds the CO_2 reduction is more important.

The production of CH_4 is known to occur under very low redox conditions following the reduction of O_2, NO_3^-, Fe^{3+}, Mn^{4+} and SO_4^{2-} (SMITH et al., 2003). This is because the production of CH_4 as a terminal electron acceptor step is less thermodynamically favourable in terms of energy yields compared to other electron acceptors (PRAETZEL et al., 2019). Wetzel (1983) suggests that the presence of nitrate, nitrite, and sulfate in the sediment or water column can reduce methanogenesis activity either through metabolic inhibition or by serving as preferable electron acceptors. Nevertheless, CH_4 production under oxic conditions has also been reported. Tang et al. (2014) suggest that the oversaturation of CH_4 found in oxic waters is a result of local CH_4 production combined with reduced CH_4 oxidation due to excessive light in the top oxic water layer.

In contrast to production, CH_4 consumption or sinks in sediment and water column occur through CH_4 oxidation and fluxes responsible for gas transport and transfer (i.e diffusion, plant-mediated and aquatic organisms transport, degassing, and ebullition). Methane is oxidized by bacterial activity known as methanotrophy, which converts it to carbon dioxide in the presence of oxygen. These bacteria are found in regions where both CH_4 and oxygen are available, such as at water-sediment interface (ESTEVES, 2011). Thottathil et al. (2018), studying lakes in Quebec, Canada, estimated that 30% of epilimnion CH_4 is oxidized during summertime. However, methanotrophic bacteria can be inhibited by an excess of oxygen and light, and factors controlling their availability, such as DOC, may enhance methanotrophs (THOTTATHIL et al., 2018). Anaerobic CH_4 oxidation is also reported as a result of bacteria activity, and this process can oxidize up to 35% of the total CH_4 produced, varying from one ambient to another (MARTINEZ-CRUZ et al., 2018).

The contribution of different fluxes to CH_4 emissions from the sediment-water to the atmosphere varies among water bodies. Diffusion is a molecular process that results from the random motion of molecules and leads to mass transport from regions of high concentrations to regions of low concentrations, tending towards an equilibrium state (CHAPRA, 2008). It can be enhanced by turbulence (e.g. in the water or in the air) and diminished in porous media (e.g. in the sediment matrix) (CHAPRA, 2008). The transport of CH_4 mediated by plants may be important in systems dominated by aquatic plants, although the literature lacks sufficient studies on CH_4 flux from reservoirs in this context (ROSENTRETER et al., 2021). Regarding CH_4 transport by aquatic organisms, McGinnis et al. (2017) studied the migration patterns of *Chaoborus* spp larvae and pointed that these organisms contribute to gas transport in two ways: by using dissolved CH_4 to inflate their tracheal sacs and rise in the water column, and by disturbing the sediment and releasing trapped gas bubbles. However, Carey et al. (2018) concluded from monitoring campaigns and laboratory analysis that CH_4 transport by *Chaoborus* represents less than 1% of the diffusive flux during stratified periods. According to the authors' findings, the contribution

of these organisms to gas transport depends on species, organisms density, and water column mixing. The degassing flux of CH_4 from water occurs as a result of drastic pressure changes, such as when water passes through turbines, spillways, and reservoir outlets (GOLDENFUM, 2012). Lastly, CH_4 ebullition refers to the transport of CH_4 through bubbles, mainly formed and released from the bottom sediment. Difusive, ebullitive, and degassing fluxes are the main CH_4 fluxes reported for freshwater reservoirs. In a study conducted by Deemer et al. (2016), who analysed CH_4 fluxes from freshwater reservoirs worldwide, the median ebullition flux was reported to be one order of magnitude higher than diffusive and degassing fluxes. However, for some systems, degassing was reported to be the dominant pathway of CH_4 emissions (MAECK et al., 2013; DELWICHE et al., 2022).

Although ebullition is an important pathway for CH_4 emissions, it is highly variable in space and time, making its measurement and quantification challenging. As a result, it is considered one of the main sources of uncertainties in estimating CH_4 emissions from freshwater reservoirs (ROSENTRETER et al., 2021). The variability of ebullition flux is caused by a combination of factors that influence CH_4 production, accumulation, and release from the sediment. Since ebullition is the main focus of this study, the governing processes are further addressed below.

1.3 Methane ebullition: governing processes and spatio-temporal dynamics

During the process of organic matter degradation, a portion of the produced CH_4 in sediment remains dissolved in the pore water. When the saturation level is reached, the molecules merge, forming free gas in a process referred as gas exsolution (SCANDELLA, 2010). Due to its low CH_4 solubility in water and its net production under anoxic conditions, CH_4 constitutes a significant proportion of the gas bubbles content in bubbles. Maeck, Hofmann and Lorke (2014) reported an average CH_4 concentration of 80% within bubbles collected from an impoundment in Germany. Similarly, Santos et al. (2006) found that up to 97% of bubble concentration in a Brazilian reservoir was methane.

The growth, shape, and movement of gas voids in the sediment are directly affected by sediment properties. In a laboratory experiment, Liu et al. (2018) observed that initial bubble growth in the sediment occurred through capillary invasion, and over time, bubbles expanded by displacing sediment while maintaining a preferred horizontal orientation. Liu et al. (2016) proposed a three-stage process for bubble formation and release. In stage 1, gas would accumulate, forming small bubbles that would move through capillary invasion. In stage 2, bubbles would expand and displace the sediment. And in stage 3, vertical conduits would form, and bubbles would be released from the sediment. The duration of each stage and the dominant mechanism of bubble growth depended on the grain size distribution. The fractures or conduits created by bubbles form pathways in the sediment toward the sediment-water interface, which can be reused by other bubbles for upward movement with less resistance (ALGAR; BOUDREAU; BARRY, 2011; SCANDELLA et al., 2011; BOUDREAU, 2012). Laboratory experiments have shown that bubble outlets can be reused over timescales of days and even months in some cases (SCANDELLA et al., 2017). However, under in-situ conditions, Scandella et al. (2016) observed that no spatial pattern of bubble outlets could be detected on timescales of hours and days.

As gas bubbles are buoyant in water, they rapidly ascend towards the surface after leaving the sediment matrix, with estimated rising velocities in the range of 0.1 to $0.6\,\mathrm{m\,s^{-1}}$ (OSTROVSKY et al., 2008; HILGERT; SOTIRI; FUCHS, 2019). Nevertheless, during their ascent, the bubbles interact with the surrounding water, and not all the gas content will reach the surface. McGinnis et al. (2006) proposed

a model for bubble dissolution in the water column where the amount of CH_4 reaching the atmosphere depends on the size of the bubble and the water depth. In deeper the water columns, a lower the amount of CH_4 can reach the atmosphere for a given initial bubble diameter. This is because a longer travel distance results in greater bubble dissolution, reducing the amount of CH_4 released into the atmosphere. For a lake with an average depth of $15\,\text{m}$, (DELWICHE; HEMOND, 2017) found that bubble dissolution can account up to 10% of the dissolved CH_4 in the hypolimnion.

It is important to mention that in addition to CH_4 transport, bubbles are also being studied for their effects on other processes. As bubbles ascend to the surface, they induce additional water mixing through circulation structures (STEPANENKO et al., 2010). In the sediment, the presence of gas is known for alter sediment structure, and bubble release events have been reported to have a significant potential for sediment resuspension (KLEIN, 2006). In a summary of literature studies and their own data, Schwarz, Marcon and Lorke (2023) highlighted that bubbles can transport a variety of substances to the water surface, such as heavy metals and pollutants. However, further studies are still needed for understanding and quantifying bubble-mediated transport.

As methane-rich bubbles primarily originate at the bottom sediments, the physical and geochemical conditions of the reservoir have an impact on the spatial distribution and temporal dynamics of CH_4 ebullition. Although these processes in nature do not occur within well-defined bounds or stages, but rather happen simultaneously with synergistic and overlapping effects, a sequence with five main steps was created to illustrate the different stages of ebullition and the main controlling variables (see Figure 2):

1. Organic matter (OM) entering reservoirs or from autochthonous production serves as the fuel for gas production;

2. Anoxic and low redox potential conditions favour the production of CH_4 by methanogenic bacteria;

3. CH_4, being a less soluble gas, can accumulate in the sediment until a supersaturation condition is reached, and molecules merge to form free gas spaces within the sediment;

4. The higher the gas production and the lower the gas loss in the sediment (through diffusion and oxidation), the larger the amount of gas available to form bubbles. These bubbles move and expand within the sediment through different modes. They remain in the sediment until they have enough buoyancy to overcome the total ambient pressure (hydrodynamic plus atmospheric) and sediment resistance;

5. During the ascent to the surface, the bubbles transport gas and substances from the sediment while interacting within the medium.

Spatially, ebullition is intensified in locations with elevated sediment accumulation, as a larger amount of organic matter would be deposited, thereby fuelling CH_4 production (SOBEK et al., 2012; DELSONTRO et al., 2011; MAECK et al., 2013). Nevertheless, the quality of organic matter also influences CH_4 production by bacterial activity. The presence of easily degradable organic matter enhances CH_4 production, as both allochthonous and autochthonous organic matter can be utilized by methanogenic bacteria for CH_4 production (GRASSET et al., 2018; PRAETZEL et al., 2019). Inflow rivers that bring fresh organic carbon to reservoirs can contribute to increased CH_4 production and ebullition, particularly in areas where organic matter is deposited (GRINHAM; DUNBABIN; ALBERT, 2018; DELSONTRO et al., 2011).

While it might be expected that water bodies with a large availability of nutrients would supply organic matter for decomposition and bubble formation, the response of ebullition to eutrophication
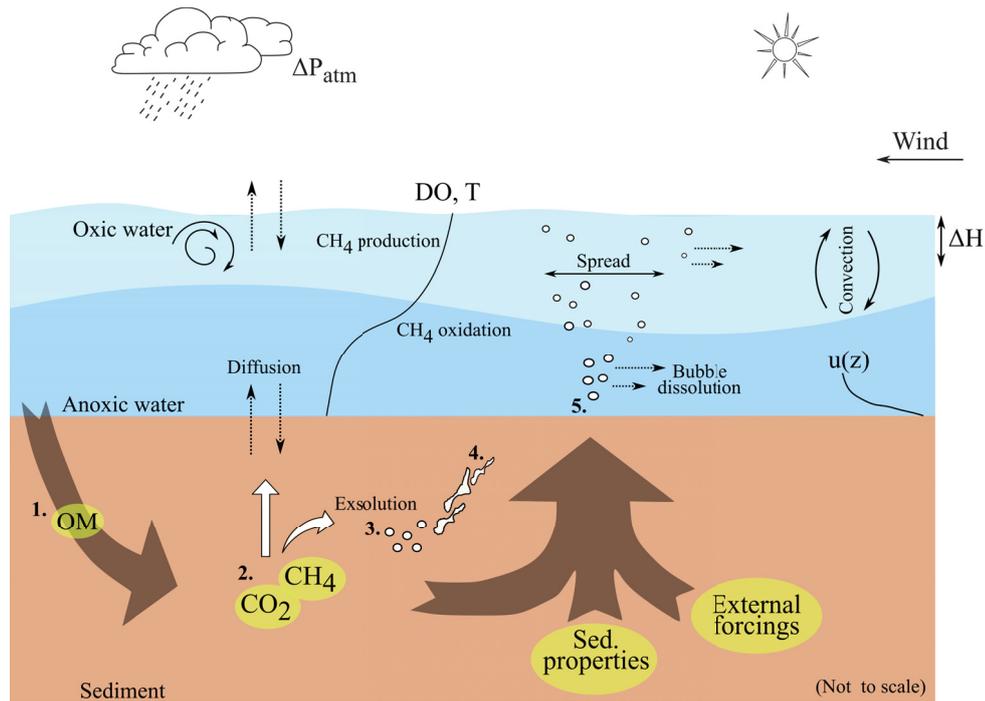
Figure 2 – Conceptual representation of methane production and gas voids formation in the sediment matrix and physical variables affecting the ebullition. The process from gas production to methane reaching the atmosphere was divided into five main stages, listed in the text.

is not straightforward. For instance, when examining chlorophyll-a concentrations, Grinham, Dunbabin and Albert (2018) concluded that there was a weak correlated with ebullition in a subtropical reservoir. Conversely, in a in nutrient-rich mesocosm in Denmark, Zhou et al. (2019) observed an increase in ebullition with higher chlorophyll-a levels. These findings suggest in this way other parameters may play a more significant role in influencing ebullition.

Temperature has manifold effects on gas fluxes, ranging from stratifications-related impacts to influences on biological activities and the solubility of dissolved gas. Yvon-Durocher et al. (2014) suggested that the dependency of CH_4 flux on temperature during seasonal variations is comparable to the dependency of microbial activities on temperature. Aben et al. (2017) proposed exponential relationships between ebullition and surface sediment temperature for various systems. According to their estimates, each degree increase in temperature can increase ebullition flux by 6 to 20%. The temperature dependence of biological reactions can be expressed in terms of Q_{10} values, which represent the increase in the considered reaction for a 10 °C rise in temperature (CHAPRA, 2008). DelSontro et al. (2016) calculated an ecosystem-level Q_{10} for ebullition and diffusion and observed that ebullition ($Q_{10} = 13$) was more affected by increase in temperature than diffusive flux ($Q_{10} = 10$). In the case of fluxes, the Q_{10} represents the combined effects of various factors and not only the temperature dependence of microbial processes. Nonetheless, Praetzel et al. (2019) suggested that the response of gas flux to temperature increase may not be uniformly distributed within a single lake, but could also depend on the quality of organic matter available in the sediment.

Pressure and pressure changes also have an impact on the gas void formation in the sediment and ebullition flux, as reductions in pressure at the sediment-water interface can trigger bubbling events. Previous studies have reported intensified ebullition events during periods of decreasing atmospheric pressure (CASPER et al., 2000; WIK et al., 2013; NATCHIMUTHU et al., 2016) and a decrease in hydrostatic pressure (SCANDELLA et al., 2011; MAECK; HOFMANN; LORKE, 2014). From incubation

experiments, Liu et al. (2016) suggested that changes in pressure can facilitate bubble escape from the sediment in two contrasting ways: an increase in pressure cause bubbles to narrow, making it easier for them to move upward, while a decrease in pressure allows bubbles to expand, providing enough buoyancy for them to leave the sediment. Thus, water depth also influences the spatial distribution of ebullition fluxes. Gas voids in the sediment begin to form when the sum of dissolved gas pressure exceeds the ambient pressure. Therefore, at greater water depths, higher pore water gas concentrations are required for bubble formation. Langenegger et al. (2019) demonstrated, using a modeling approach, the reduction of ebullition with increasing water depths, with the diffusive flux becoming the dominant CH_4 efflux from the sediment. Additionally, water depth also affects the actual amount of CH_4 transferred to the atmosphere by bubbles after their release, as gas bubbles in deeper water columns are exposed to longer periods of dissolution while rising toward the surface (MCGINNIS et al., 2006).

The top layer of the water is commonly regarded as the most dynamic portion due to the exchange of gas, heat, and momentum with the atmosphere occurs through this layer (FISCHER et al., 1979). Wind incidence over the water surface transports horizontal momentum from the atmosphere to the water column through vertically propagated turbulent motions (LORKE et al., 2003). In addition to surface stress, wind-generated waves contribute to momentum to the water column. Various motions, such as Stokes drift, Langmuir circulation, bottom currents, and thermal stratification conditions leading to seiches and internal waves, dissipate the input momentum (LORKE et al., 2003; SOCOLOFSKY; JIRKA, 2004).

Water turbulence, internal motions, and surface waves can impact ebullition flux into two main ways: first, by causing pressure fluctuations (BOUDREAU, 2003) and by disturbing the sediment, facilitating the release of bubbles (HOFMANN; FEDERWISCH; PEETERS, 2010; MAECK; HOFMANN; LORKE, 2014). Secondly, they regulate the loss of CH_4 from sediment matrix through direct diffusion or by supplying oxygen to the bottom layer, thereby enhancing CH_4 oxidation. Water turbulence is reported to erode the bottom layer at the sediment-water interface, increasing concentration gradients and consequently promoting CH_4 diffusion from the sediment. Lorke et al. (2003) noted that periodic motions occurring within the water column, such as seiching and internal waves, result in periodic oscillation of the diffusive boundary layer. Since this layer controls the diffusive exchange of substances, it can be expected that the availability of gas in the sediment to form free gas also oscillates. Joyce and Jewell (2003) compared ebullition fluxes with wind velocities and bottom currents at Gatun Lake and found that bottom currents correlate better with ebullition than wind velocities alone. According to the authors, this can be explained by the fact that currents causing shear at the bottom may be enhanced by other processes such as seiches and density currents, which are not considered when comparing fluxes with wind velocity.

While wind incidence over the water surface and convective motions enhance water column mixing, vertical temperature stratification causing a well-defined thermocline, dampens the vertical mixing (FISCHER et al., 1979). Wüest and Lorke (2003) pointed out that during stratified conditions, turbulence is weakened, and the magnitude of diffusivity is lower. During stratification periods, CH_4 diffusing from the sediment can accumulate in the bottom anoxic layer of water. When mixing occurs, the stored hypolimnetic CH_4 is mixed into the water column where it can be oxidized or released into the atmosphere (BASTVIKEN et al., 2004; GUÉRIN et al., 2016; VACHON et al., 2019). Conversely, the accumulation of CH_4 in the bottom water during stratification reduces the CH_4 concentration gradients across the sediment-water interface, leading to the accumulation of CH_4 in the sediment and an increase in ebullition flux (LANGENEGGER et al., 2019).

The role of sediment properties their interplay with other parameters in regulating CH_4 ebullition from the sediment is not yet clearly defined. However, it is already known that sediment properties

play an important role in gas dynamics within the sediment. Liu et al. (2016) have demonstrated the effect of sediment grain size for gas storage, while Smith et al. (2003) concluded that oxidation is more efficient in coarse-textured soils. Additionally, Hilgert, Sotiri and Fuchs (2019) highlighted the importance of hydrological regimes and drawdown periods in sediment reallocation within reservoirs. After drawdown, sediment tend to accumulate in a more central part of the reservoir, thereby altering the spatial distribution of emissions hotspots.

1.4 In-situ measurements of methane fluxes and sediment gas content

Different techniques have been employed for in-situ measurements of CH_4 fluxes in freshwater reservoirs. Eddy covariance is utilized to obtain spatially integrated CH_4 emissions (diffusion + ebullition) with high temporal resolution (VESALA et al., 2006; EUGSTER; DELSONTRO; SOBEK, 2011). Floating chambers placed at the water surface are also used to measure CH_4 emissions, capturing both diffusion and ebullition combined or solely diffusive flux. In the floating chambers, the CH_4 flux is calculated based on the increase of CH_4 concentration in the chamber's headspace over time. The gas can be manually sampled for subsequent laboratory analysis (MANNICH; FERNANDES; BLENINGER, 2017), or the CH_4 concentration in the headspace can be directly measured by a gas analyser connected to the chamber or CH_4 sensors (VACHON; PRAIRIE; COLE, 2010; BASTVIKEN et al., 2020).

In addition to floating chambers, the diffusive flux of CH_4 at the water surface can be estimated using the thin boundary layer method. This method calculates the flux based on the difference between the dissolved CH_4 concentration and the atmospheric equilibrium concentration, along with the gas transfer velocity (LISS; SLATER, 1974; WILKINSON; BODMER; LORKE, 2019). CH_4 emissions through degassing at a reservoir's dam or spillway are calculated by comparing the dissolved CH_4 concentrations upstream and downstream of the dam, along with the water discharge (GOLDENFUM, 2012).

Ebullition flux has been measured by various methods, including underwater imaging (WANG; SOCOLOFSKY, 2015), echo-sounder measurements (OSTROVSKY et al., 2008), and the deployment of bubble traps. Bubble traps, or inverted funnels, are conical structures used to collect rising bubbles in the water column. The gas volume can be estimated by manually sampling the captured bubbles (ROSA et al., 2006) or by using automatic sensors with logging capabilities. Automatic sensors enable estimation of the gas volume through calibrated partial pressure sensors (VARADHARAJAN; HERMOSILLO; HEMOND, 2010; MAECK; HOFMANN; LORKE, 2014) or optical-based sensors that measure the size of each individual bubble (DELWICHE; HEMOND, 2017). The main advantage of automatic bubble traps is their ability to provide long-term and high temporal resolution measurements.

In the sediment matrix, CH_4 is found dissolved in the pore water or as free gas. In-situ measurements of dissolved CH_4 concentration in the pore water can be obtained using dialysis pore water samplers (HILGERT et al., 2015). Alternatively, retrieved sediment cores can be taken to the laboratory, where the pore water is extracted using Rhizon tubes, and the CH_4 concentration is then measured (SEEBERG-ELVERFELDT et al., 2005). The estimation of free gas content in the sediment is currently performed by scanning extracted sediment cores with x-ray Computed Tomography (x-ray CT). However, it is important to note that disturbances caused during sampling can potentially affect the results (DÜCK et al., 2019a). Other methods, such as ground penetrating radar, are restricted to shallow freshwater systems (MUSTASAAR; COMAS, 2017), or the use of echo-sounders (ANDERSON; MARTINEZ, 2015; KATSNELSON et al., 2017). The latter method has the main advantages of providing in-situ mea-

surements without causing sediment disturbances and covering large areas. Nonetheless, its application in freshwater reservoirs is currently limited to a few locations.

1.5   Models for estimating methane ebullition

Mechanistic and empirical models have been used to simulate CH_4 ebullition from aquatic systems. Models serve as helpful tools for understanding processes and the interactions among variables in more detail. They also complement measurements, handle data gaps, and convert point data into spatially distributed information. The range of applications for mechanistic models spans from solving single bubble mechanics in the sediment (ALGAR; BOUDREAU, 2009; KATSMAN, 2015) to resolving the CH_4 mass balance (SCHMID; OSTROVSKY; MCGINNIS, 2017; LANGENEGGER et al., 2019; DELWICHE et al., 2022). The main limitations of applying mechanistic models lie in the availability of in-situ data on sediment properties and CH_4 fluxes to set up, calibrate, and validate the model.

Another approach is to simulate ebullition flux as a function of known environmental variables using empirical models, such as statistical and data-driven models. This group of models is relatively simpler to implement mathematically than mechanistic models and offers more flexibility in terms of mandatory input parameters. Empirical models have been applied to estimate the overall CH_4 emissions from freshwater reservoirs (PRAIRIE et al., 2021) and to investigate the dependence of ebullition on different environmental variables. For instance, in other systems, ebullition has been predicted as a function of one main variable, such as hydrostatic pressure (ZHAO; TEDFORD; LAWRENCE, 2022), chlorophyll-a (DELSONTRO; BEAULIEU; DOWNING, 2018), and temperature (WIK et al., 2014; ABEN et al., 2017), or as a combination of multiple variables, including organic matter content and sediment porosity (PRAETZEL et al., 2019), and wind speed (MCCLURE et al., 2020). Although empirical models have been successfully applied to simulate CH_4 ebullition in certain systems, their potential for application across various reservoirs requires further investigation.

1.6   Research gaps

Ebullition, a process with high variability in both time and space, occurs due to a combination of physical and biogeochemical factors that act on different scales. This makes accurately measuring and estimating gas emissions from water bodies a challenging task, especially considering the influence of changing environmental conditions caused by factors such as river damming and climate change (NATCHIMUTHU et al., 2016). The impact of atmospheric CH_4 on the global climate makes the quantification of ebullition fluxes from reservoirs and understanding the underlying controls of emissions highly important. Improving our understanding of the processes governing CH_4 in aquatic systems can lead to more reliable data on emissions from aquatic systems and better estimates of system-wide emissions. This information can also be useful for reservoir management and developing effective mitigation strategies aimed at reducing CH_4 emissions.

Bottom sediments rich in organic matter are hot spots of CH_4 production. In addition, the sediment matrix can store large amounts of CH_4 dissolved in pore water and as free gas. In a laboratory study, Liu et al. (2016) found that sediment can store gas up to 18% of its volume. Meanwhile, Peltola (2011) showed through modelling that setting a gas volume threshold in the sediment can enhance the prediction of CH_4 ebullition. Nevertheless, there is limited in-situ data available on gas storage in freshwater sediment in the form of free gas (bubbles). Furthermore, there is a need to establish better methods for measuring gas content in sediment in situ. Studies are being conducted on acoustic-based

methods to access gas content in sediment, which can cover a large area. In Lake Kinneret, located in Israel, researchers measured a gas fraction ranging from 0.2 to 3.8% using sound velocity (KATSNELSON et al., 2017; UZHANSKY et al., 2020). Anderson and Martinez (2015) measured gas content ranging from 0.01 to $12 \, \mathrm{L \, m^{-2}}$ based on acoustic backscatter in freshwater reservoirs in the United States,. However, these methods have not been applied to measure gas content distribution in sediment for other systems. Consequently, there is a lack of studies connecting in-situ measured sediment gas storage to the spatial and temporal dynamics of CH_4 budget components in reservoirs.

While some studies have looked at ebullition flux measurements, there is a need for more continuous and high-frequency measurements to reduce uncertainties and accurately estimate emissions (MAECK; HOFMANN; LORKE, 2014). In addition to improving CH_4 emissions estimates, long-term measurements of ebullition with high temporal resolution enable investigations of how ebullition responds to changes in environmental conditions. Ebullition is a stochastic process (DELSONTRO et al., 2015) that depends on various chemical, biological, and physical conditions, how they interact, and how the system reacts to these interactions. As a result, the extent to which ebullition is affected by different environmental factors may vary over time and across different systems. Further research is still required to better identify common patterns and drivers of ebullition.

Previous studies have tested the use of empirical models to estimate CH_4 ebullition, successfully predicting ebullition ($R^2 > 0.8$) based on environmental variables (WIK et al., 2014; MCCLURE et al., 2020; ZHAO et al., 2021). However, the applicability of these statistical and data-driven models across different systems and timescales, particularly in capturing and reproducing temporal dynamics of ebullition, requires further investigation. Moreover, previous studies have provided limited systematic comparisons of spatial and temporal variabilities of ebullition within individual systems. Linkhorst et al. (2020) found that in a freshwater reservoir in Brazil, temporal variability of CH_4 ebullition outweighed spatial variability. Nonetheless, it is crucial to explore and compare the temporal and spatial variabilities of ebullition in other systems.

A primary objective and a set of hypotheses were established for this study to address the highlighted research gaps. The forthcoming chapter will delineate the study objective and hypotheses in detail.

2 Research objective and hypotheses

Based on the literature overview, the main research gaps previously highlighted can be summarized as follows: There is a need for established methods to measure sediment gas content in situ, and there is a need to improve the existing data available on sediment gas content in freshwater reservoirs. Furthermore, it is necessary to identify the interactions between gas content in the sediment and CH_4 ebullition. Although continuous and high temporal resolution measurements of ebullition exist for a few reservoirs, further investigations are still required to understand the drivers of ebullition temporal dynamics across multiple freshwater reservoirs. Additionally, it is essential to evaluate the extent to which empirical models can be applied to simulate ebullition and to which timescales ebullition can be resolved. In light of these gaps, the main goal of this study was to investigate the effect of different spatial and temporal drivers on enhancing or dampening CH_4 ebullition in freshwater reservoirs. To achieve this goal, the following research questions and respective hypotheses were proposed:

Question 1: What is the spatial distribution of gas content in the sediment of different freshwater reservoirs? Which environmental variables control its distribution, and how does the sediment gas content influence CH_4 ebullition in reservoirs?

Hypothesis 1.1:   The interaction between sediment bulk properties (sediment thickness and organic matter content) and water depth, in conjunction with methane production, contributes to the spatial variability of gas content in the sediment. These parameters can be utilized to quantitatively explain the observed variability of gas content in the sediment.

Hypothesis 1.2:   As ebullition originates from the gas stored in the sediment matrix, the spatial variability of ebullition within a reservoir is modulated by the spatial variability of gas content in the sediment.

Hypothesis 1.3:   Within the methane budget, gas storage in the sediment significantly impacts the methane balance in freshwater reservoirs, particularly in modulating the temporal dynamics of methane ebullition.

Question 2: What are ebullition's primary temporal drivers and patterns across multiple reservoirs, and how does ebullition respond to the combination of these drivers? Can empirical models of ebullition be applied to predict ebullition in other systems, and for which timescales can ebullition be resolved?

Hypothesis 2.1:   The key factors that affect methane ebullition, such as temperature and pressure changes, are consistent across different reservoirs. However, the extent to which these factors impact the release of methane can vary from one reservoir to another and over time.

Hypothesis 2.2:   Empirical models incorporating multiple environmental variables can effectively capture and reproduce the temporal dynamics of methane ebullition in freshwater reservoirs over different timescales (minutes to seasonal variabilities).

3 Approach and thesis outline

3.1 Study sites and dataset

Two study sites were considered to address the main goal and the hypotheses proposed for this thesis (refer to Section 2). Together with other relevant variables, ebullition was monitored (see the reservoirs and monitoring sites in Figure 3). The studied reservoirs Passúna and pre-dam of Wupper, exhibit distinct characteristics in terms of location, climate region, and reservoir purpose. Passúna is a subtropical drinking-water reservoir situated in the southern region of Brazil, South America. In contrast, Wupper is a temperate flood control reservoir in western Germany, in Europe.
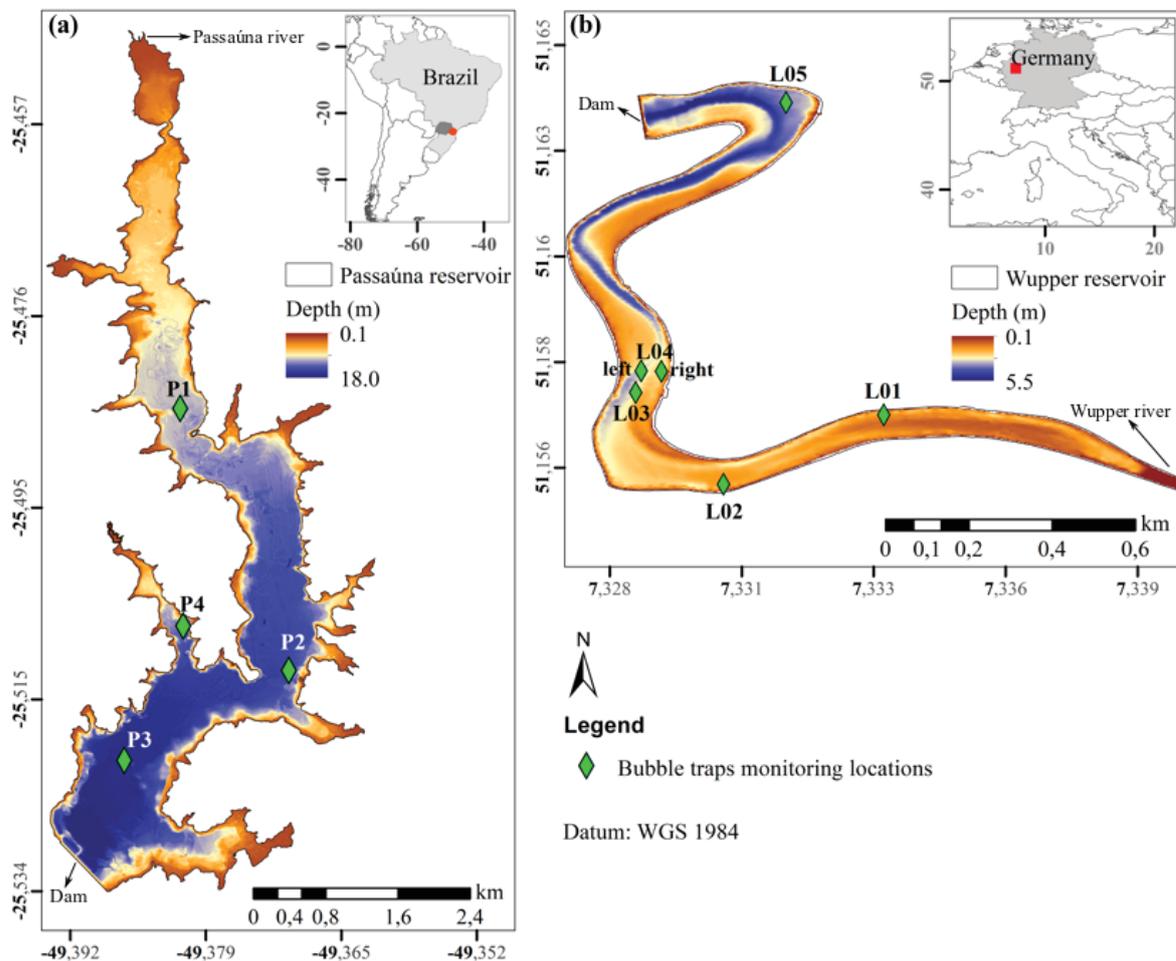
Figure 3 – (a) Bathymetric map of Passúna reservoir from Sotiri et al. (2021) with an inset map showing the location in southern Brazil. (b) Bathymetric map of Wupper reservoir with an inset map showing the location in western Germany. In both panels, the colour represents the depth ranges, and the symbols are the locations where the bubble traps were deployed for the monitoring of ebullition flux, see legends. On both maps, the dam's location and the main River's inflow are indicated by arrows. Not that the depth range and spatial scale are different between the Reservoirs.

Passúna reservoir was constructed in 1989 through the creation of a dam on the Passúna River. It is managed by the Water and Sanitation Company of Paraná State (Sanepar). The reservoir has a

surface area of 8.5 km² and an average depth of 8.3 m (SOTIRI et al., 2021). The main inflow river is the Passaúna River, which has an average discharge of $1.7\,\mathrm{m^3\,s^{-1}}$ (RAUEN; CASTRO; SILVA, 2017). The reservoir is situated in a subtropical region with an annual precipitation ranging from 1400 to 1600 mm (CAVIGLIONE et al., 2010) and an average annual air temperature of 22 °C. The mean sediment surface temperature during the monitoring period was 19.2 °C.

In contrast, the Wupper Reservoir was constructed 13 years earlier in 1976 by damming the River Wupper, primarily for flood control purposes. In 1987, a hydroelectric power plant with an installed capacity of 1.25 MW began operating, according to the reservoir operator Wupperverband [1]. The monitoring for this study was conducted at the pre-dam of the main reservoir, which here is also referred to as Wupper reservoir. The region where the reservoir is located experiences an average air temperature of 9.5 °C, with the possibility of snow occurring during winter months. The main tributary to the reservoir, Wupper River, has an average discharge of $3.3\,\mathrm{m^3\,s^{-1}}$. The reservoir has a surface area of 0.15 km², an average depth of 2.0 m, and recorded mean surface sediment temperature of 10.8 °C during the monitoring period. A summary of the main information regarding both study sites is presented in Table 1.

Table 1 – Summary of Passaúna and Wuppervorsperre reservoirs' main information. Data sources are provided in the table footnotes.

	Passaúna	Wupper
Impoundment year	1989	1976
Purpose	Public water supply	Flood control, hydro power generation
Catchment area (km²)	152.0	173.5
Volume (m³)	6 900 000 [a]	366 000 [d]
Surface area (km²)	8.5[a]	0.15 [d]
Mean depth (m)	8.3	2.0 [d]
Maximum depth (m)	18.1 [a]	5.6 [d]
Mean water inflow (m³ s⁻¹)	1.7 [b]	3.3
Water residence time (d)	325 [c]	0.8 [e]
Mean sediment temperature (°C)	19.2	10.8

[a] Sotiri et al. (2021)
[b] Rauen, Castro and Silva (2017)
[c] Ishikawa, Bleninger and Lorke (2021) estimated for February 2018 to February 2019
[d] Project Methane Gas Elimination's unpublished data
[e] Calculated as $\frac{\text{Volume}}{\text{mean inflow}}$

At Passaúna Reservoir, the monitoring and dataset cover the period from February 2017 to February 2020. The dataset comprises continuous measurements of environmental variables. Meteorological information, including atmospheric pressure, air temperature, and wind speed, was obtained from weather stations in the reservoir vicinity. Hydraulic data, such as discharge and water depth, were provided by the reservoir operator Sanepar. Water characteristics, including temperature, dissolved oxygen concentrations, chlorophyll-a, and water velocity fields, were obtained from Ishikawa, Bleninger and Lorke

---

[1] Hydroelectric power plant information can be found at `https://www.wupperverband.de/unsere-aufgaben/energiemanagement/erneuerbare-energien/wasserkraft/wasserkraft-wupper-talsperre`

(2021), Ishikawa et al. (2022b), Gurski (2022). Information regarding sediment distribution and sediment organic matter content was provided by Sotiri, Hilgert and Fuchs (2019), Sotiri et al. (2021).

Ebullition flux was monitored using four automated bubble traps (ABT, Senect GmbH - Germany) deployed at different locations in the Reservoir (see locations in Figure 3). The shallowest ebullition monitoring site, referred as P1, had a water depth of 8 m. The deepest location, site P3, had a water depth of 14 m. Site P4 was situated in a side arm of the reservoir with a water depth of 10 m, while site P2 had a water depth of 12 m and was located near the water treatment plant's intake facility. In addition, continuous monitoring of water temperature, dissolved oxygen concentrations, chlorophyll-a, and water velocity fields was conducted at site P2 from February 2018 to February 2019 (ISHIKAWA; BLENINGER; LORKE, 2021; ISHIKAWA et al., 2022b; GURSKI, 2022).

Furthermore, acoustic backscatter from two echo-sounder surveys was analysed to estimate gas content in the bottom sediment. The hydro-acoustic data was obtained from Sotiri, Hilgert and Fuchs (2019), Sotiri et al. (2021). The measurements were performed using a single-beam dual-frequency linear echosounder (EA400 Kongsberg Inc), and detailed device information is provided in Sotiri et al. (2021).

At the Wupper reservoir, the monitoring period extended from March 2020 to November 2021. Meteorological data of atmospheric pressure, wind speed, and air temperature were obtained from a weather station installed near the reservoir. Water inflow discharge from the Wupper River and additional atmospheric pressure data were provided by the reservoir operator (Wupperverband). Within the reservoir, continuous monitoring was conducted of sediment surface and water temperature, dissolved oxygen concentrations, and current velocity field. Ebullition flux was monitored at six monitoring sites distributed along the reservoir, with water depths ranging from 1.5 m at the upstream sites (L01 and L02) to 4 m at site L05. The locations of all monitoring sites are shown in Figure 3. Ebullition flux was monitored using automated bubble traps (ABT) and Optical bubble traps.

Hydro-acoustic surveys were also performed in the reservoir using the same echo-sounder (EA400 Kongsberg Inc) as in the Passaúna Reservoir measurements. Additionally, manual sampling of gas volume in the sediment was conducted to validate the echo-sounder measurements for estimating gas content in the sediment. At each monitoring site, monthly measurements were taken for dissolved methane concentration in the water, diffusive CH_4 fluxes at the water-air interface, oxidative CH_4 flux, and degassing at the dam. Sediment cores were retrieved from each monitoring site to estimate potential methane production, organic matter content, carbon and nitrogen content, and dissolved CH_4 concentration in the pore water.

Please refer to the scientific manuscripts in the Appendix for a thorough understanding of the in-situ measurements, including the devices used, time intervals for data recording, laboratory analysis, and calculations. The measurements conducted at the two study sites allowed for the examination of different aspects of CH_4 spatial variability and temporal dynamics. Moreover, the contrasting characteristics of the reservoirs, along with the extensive dataset, enabled to observe ebullition patterns across different systems.

3.2   Thesis outline

The acoustic backscatter from the echo-sounder surveys were utilized to estimated the gas content in the sediment of both Passaúna and Wupper reservoirs. At the Wupper Reservoir, manual sampling of gas volume from a defined sediment area was conducted to validate the gas content calculated based on the acoustic backscatter. The gas content in the sediment, estimated during two different years at the same season, was linked to the CH_4 budget in the reservoir. The CH_4 budget was derived from the

in-situ monitoring of ebullition flux, diffusive flux at water-air interface, degassing at the dam, oxidation flux, and laboratory analysis of incubated sediments to estimate potential methane production. These variables were analyzed to establish a connection between the spatial and temporal dynamics of sediment gas storage and the CH_4 budget. The investigation of spatial and temporal variations in gas content in the sediment was further conducted at the Passaúna Reservoir. This analysis involved the examination of sediment gas content in relation to sediment characteristics such as organic content, deposition patterns, potential methane production, and water depth, with the aim of elucidating observed spatial patterns. These aspects were explored to test hypotheses 1.1, 1.2, and 1.3 and are presented in the scientific manuscripts (i) and (ii) (Appendixes A and B, respectively).

To understand the primary temporal drivers of ebullition and test the hypothesis 2.1, the time-series of ebullition were analyzed in conjunction with time-series of environmental variables, including meteorological information, flow, hydrostatic pressure, dissolved oxygen concentration, and others. Subsequently, empirical models were employed using the identified main ebullition drivers to predict ebullition on short timescales (<1 day) as well as longer timescales (weekly to seasonal), testing in this way the hypothesis 2.2. Additionally, empirical models developed for other systems were tested for predicting ebullition at the Passaúna Reservoir with the goal to verify the applicability of empirical models for the prediction of ebullition across different systems. This analysis of ebullition temporal patterns was based on Passaúna Reservoir dataset. The results and discussions are presented in manuscript (iii) (Appendix C).

In this way, the main objective of this thesis, which involved the combination of two study sites, was addressed in to main parts: the spatial variability of gas content in the sediment and the temporal dynamics of ebullition. Although these two parts are represented separately, they are interconnected, as ebullition triggers might change with location and the controls of spatial variability are time-dependent. A graphical representation of the two groups along with the respective tested hypotheses is provided in Figure 4.

The main results of the three scientific manuscripts are summarized in Sections 4.1 and 4.2 of the Discussion (Chapter 4) and were applied to validate or refute the proposed hypotheses. In a further step, a comparative evaluation of CH_4 ebullition and sediment gas content variability between the two study sites was conducted. The results of this analysis are presented and discussed in Section 4.3, where ebullition flux at each monitoring site and sediment gas content were normalized by the respective maximum and minimum values from the combined dataset (e.g. maximum ebullition flux recorded at Passaúna and Wupper, and maximum gas content in the sediment at both reservoirs). The normalized data are then showed in a boxplot.

The overall findings regarding methane dynamics at each reservoir were further combined and discussed together in Section 4.4. Since temperature was an important parameter regulating ebullition, the relationship between reservoir-wide ebullition fluxes and sediment temperature was examined and discussed to obtain insights into the similarities and differences in ebullition patterns observed between the two study sites. Reservoir-wide ebullition for each reservoir was calculated as the average daily ebullition flux across all monitoring locations.

The overall conclusion for this thesis is presented in Chapter 5. This chapter highlights the results that support the proposed hypotheses and provides final remarks on this study.
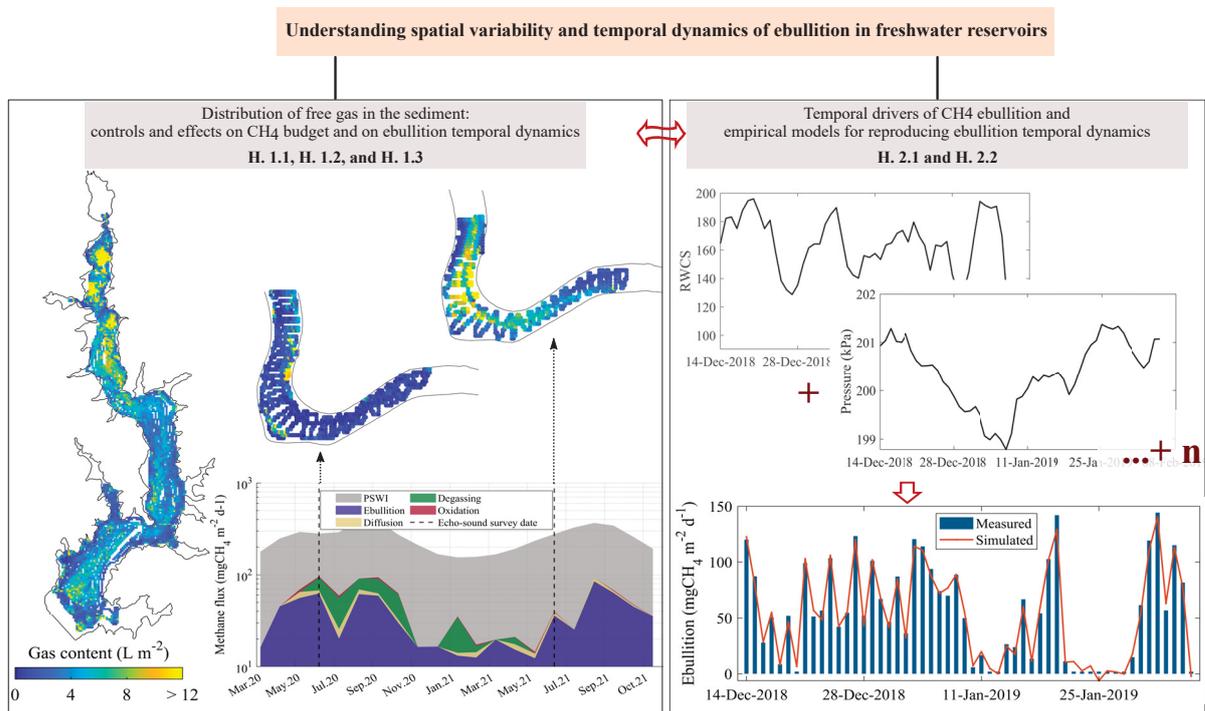
Figure 4 – Graphical representation illustrating the key contributions of this thesis in comprehending the spatio-temporal dynamics of ebullition in freshwater reservoirs. The thesis hypotheses (**H**) are grouped into two main categories: the spatial distribution of gas content in the sediment as a proxy for spatial variability of ebullition, and the temporal dynamics of ebullition. Nevertheless, interactions exist between the spatial variability and temporal dynamics of ebullition. The abbreviation PSWI refers to potential methane flux at the sediment water interface and RWCS to relative water column stability.

4 Discussion

This chapter highlights the main findings from three scientific manuscripts developed as part of this research, which together constitute this thesis. The complete manuscripts, along with their respective supplementary material, can be found in Appendix A, B, and C, as mentioned earlier. Here, the combined results are discussed to either support or challenge the hypotheses initially proposed in Chapter 2. Furthermore, a comparative discussion on the spatial and temporal variability of gas content in the sediment and ebullition is provided, and the insights gained from the two study sites investigated in this research are emphasized.

4.1 Gas content in the sediment: spatial variability and effect on ebullition

The in-situ quantification of gas content in the bottom sediment of reservoirs remains a challenge and has been limited to a small number of systems. Previous studies have utilized acoustic measurements to assess gas content in the sediment of Lake Kinneret in Israel (KATSNELSON et al., 2022; UZHANSKY et al., 2020) and reservoirs in the United States (ANDERSON; MARTINEZ, 2015). However, these methods have not been extensively tested in other systems. In this study, the method proposed by Anderson and Martinez (2015) was validated and applied to map the gas content in the bottom sediments of Passúna and Wupper reservoirs.

The average estimated gas content in the sediment of both reservoirs exhibited a similar order of magnitude ($1.5\,\mathrm{L\,m^{-2}}$ in 2020 and $5.1\,\mathrm{L\,m^{-2}}$ in 2021 for Wupper, as presented in Appendix B; $4.4\,\mathrm{L\,m^{-2}}$ in 2016 and $4.6\,\mathrm{L\,m^{-2}}$ in 2019 for Passaúna, as presented in Appendix A). These values corresponded to an average volumetric gas fraction ranging from 0.75% to 4.6%. The volumetric gas fractions were comparable to those found in lake Kinneret (up to 3.8% as reported by Katsnelson et al. (2017), Uzhansky et al. (2020)), but one order of magnitude lower than the 18.8% reported in laboratory experiments for clay sediments (LIU et al., 2016).

Both reservoirs exhibited longitudinal and transversal variations in sediment gas content, which were closely associated with spatial patterns of sediment deposition. Passaúna reservoir displayed a distribution of gas content similar to that of a typical reservoir, with higher gas accumulation observed in the upstream region where substantial sediment deposition occurred due to the inflow from the main river. In contrast, Wupper reservoir exhibited a more river-like pattern, with enhanced gas accumulation in the inner bends of the reservoir banks, where sediment also tends to accumulate. Discharge, flow speed, and reservoir morphology are key factors influencing sediment deposition and accumulation (SHOTBOLT; THOMAS; HUTCHINSON, 2005). At Passaúna reservoir, the combination of lower discharge ($1.7\,\mathrm{m^3\,s^{-1}}$) and lower average flow speed ($2.0\,\mathrm{cm\,s^{-1}}$, as reported by Ishikawa, Bleninger and Lorke (2021)), compared to Wupper reservoir, favoured sediment accumulation and elevated gas content near the inflow. In contrast, at Wupper reservoir, the higher mean discharge and flow speed ($3.3\,\mathrm{m^3\,s^{-1}}$ and $2.9\,\mathrm{cm\,s^{-1}}$, respectively) coupled with its narrower-elongated shape and bends led to greater sediment deposition in the inner parts of the bends, where gas accumulation was acoustically detected.

The spatial variability of gas content in the sediment was found to be influenced by several factors, including sediment deposition, organic matter content, temperature, potential methane production, and

water depth. Specifically, water depth played a significant role in modulating the magnitude of gas content, whereby deeper regions with comparable sediment deposition to shallow regions exhibited lower gas content in the sediment. To better understand this relationship, an artificial neural network was trained and demonstrated that organic matter content, sediment thickness, and water depth could explain 89% of the spatial variability in sediment gas content at Passaúna Reservoir. The remaining variability was attributed to other factors such as variations in potential methane production and the exposure of sediment to dissolved oxygen, which promotes CH_4 oxidation (for a more detailed discussion, refer to the complete discussion in Appendix A). Thus, sediment bulk properties, in conjunction with water depth and potential methane production, were identified as key factors controlling the spatial distribution of gas content in the sediment, thereby supporting the first hypothesis (H.1.1).

The interaction between gas stored in the sediment and components of the CH_4 budget, including ebullition, occurs as a dynamic two-way process. On one hand, fluxes such as ebullition, diffusion, oxidation, and degassing can remove CH_4 from the reservoir, depleting the amount of CH_4 stored in the sediment matrix when the outflow fluxes exceed methane production. On the other hand, an increase in gas content in the sediment enhances CH_4 efflux, particularly through ebullition (refer to Appendix B). The role of water depth has been identified as a significant modulating factor in these interactions. Previous studies conducted in Lake Kinneret have demonstrated a decrease in sediment gas content with increasing water depth (UZHANSKY et al., 2020), as higher hydrostatic pressure requires a higher CH_4 partial pressure for gas void formation (LANGENEGGER et al., 2019).

In the case of Passaúna Reservoir, characterized by greater water depths than Wupper (with an average of 8.3 m), the highest overall accumulated ebullition was observed at the shallowest monitoring site (P1), which also exhibited the highest gas content in the sediment (refer to Appendix A). However, when comparing the two deeper sites (P2 and P3), which had relatively lower gas content in the sediment compared to P1, prolonged periods of zero ebullition flux were recorded at these locations. Interestingly, ebullition was higher at the location with greater potential methane production but relatively lower sediment gas content (P2). Therefore, the second hypothesis (H.1.2) of this thesis was partially supported, as the availability of free gas in the sediment was found to contribute to the occurrence of ebullition. However, it is important to note that water depth, being a critical control on bubble release from the sediment, means that in deeper areas of the reservoir, the presence of free gas in the sediment does not necessarily correspond to higher ebullition. Thus, in hypothesis 1.2, the spatial variability of gas content in the sediment alone cannot fully explain the spatial variability of observed ebullition flux.

At both reservoirs, inter-annual variability of gas content in the sediment was observed. In the case of the Wupper reservoir, changes in sediment gas content from one year to another were attributed to variations within the components of the CH_4 budget, with ebullition being the primary pathway for CH_4 transport out of the reservoir. Consequently, periods of intensified CH_4 emissions resulted in lower sediment gas storage, leading to a temporary reduction in ebullition until the gas content in the sediment could be replenished through net CH_4 production (refer to Appendix B for details). Notably, an important aspect at the Wupper reservoir was the existence of a discrepancy in the CH_4 balance between production and measured fluxes (oxidation, diffusion, degassing, and ebullition). Several factors could contribute to this discrepancy, including potential overestimation of production rates and the occurrence of emission "hot moments" not captured within the available data (for a comprehensive discussion, see Appendix B). Nonetheless, the interaction between gas content in the sediment and components of the CH_4 budget suggested that sediment gas storage could partially account for the mismatch in the CH_4 balance, thereby supporting the hypothesis (H. 1.3) that sediment gas storage influences the temporal dynamics of ebullition. Therefore, when analyzing the CH_4 balance in freshwater reservoirs, it is crucial to consider sediment gas storage. This is further supported by the finding that the sediment in the Wupper

reservoir could store up to 9 days of accumulated potential methane production.

4.2   Temporal dynamics of ebullition and empirical models for flux prediction

Simple correlation analysis between ebullition and environmental variables provided insights into the controls on ebullition and the direction of their dependency. In both studied reservoirs, sediment surface temperature and reservoir stratification showed positive correlations with ebullition, while pressure (hydrostatic and atmospheric) and dissolved oxygen concentrations exhibited negative correlations with the fluxes (refer to Appendixes B and C). The dependency of ebullition on these variables has been previously reported in other lakes and reservoirs (NATCHIMUTHU et al., 2016; ABEN et al., 2017; BEAULIEU et al., 2018). However, correlation analysis (Spearman or Pearson correlation) can lead to spurious correlations, as exemplified by the significant negative correlation found between ebullition and chlorophyll-a at Passaúna Reservoir showed in Appendix C. The strength of correlation and the coherence between ebullition and individual forcings varied over the monitoring period and across the study sites, thus supporting the hypothesis 2.1.

Reservoir stratification played a significant role in modulating the dependency of ebullition on other drivers. In stratified systems, the vertical transport and exchange of gases and substances through the water column are reduced (VACHON et al., 2019; GUSEVA et al., 2020) resulting in accumulation of dissolved CH_4 in the bottom water layer. This, in turn, reduces the diffusion of CH_4 from the sediment to the overlaying water and favour ebullition flux (LANGENEGGER et al., 2019). In addition to its effect on methane transport, stratification conditions also influence other processes such as turbulence and internal motions within the reservoir, including dissipation rates near the sediment and bottom currents. These factors, in turn, affect the conditions at the sediment-water interface and the exchange of dissolved oxygen between water and sediment (WÜEST; LORKE, 2003). In the case of Passaúna Reservoir, during periods of higher dissipation rates at the bottom when the reservoir was partially stratified, the dissipation rate was found to trigger ebullition. Conversely, when the reservoir was fully stratified, the negative correlation between ebullition and dissipation rate suggested a weakening of ebullition, possibly due to enhanced diffusive transport of CH_4 to the water column (refer to Appendix C for a complete discussion). In Passaúna Reservoir, stratification in the deep areas was primarily influenced by the vertical temperature distribution (ISHIKAWA; BLENINGER; LORKE, 2021), while in the shallower Wupper system, higher discharge from the inflow river resulted in increased current speed, contributing to mixing of the water column. In Wupper, discharge showed a negative correlation with ebullition flux (Appendix B).

As thermal stratification of the reservoir influenced the dependency of ebullition on forcings, it also affected the synchronization of ebullition among the monitoring sites. Overall, the daily ebullition fluxes at the three main monitoring sites in Passaúna Reservoir exhibited synchronization (with a mean Kuramoto order parameter of 0.76±0.23, see Appendix C). However, the degree of flux synchronization showed a negative correlation with the stratification indicator (relative water column stability, RWCS). This observation, combined with the dependency of ebullition on various environmental parameters, suggests that during mixing periods, characterized by reduced CH_4 accumulation in the sediment, the temporal dynamics of ebullition are primarily influenced by external forcings acting over large spatial scales within the reservoir. Conversely, under thermal stratification, which promotes CH_4 production and accumulation while minimizing losses apart from ebullition, the modulation of ebullition temporal dynamics is influenced by site-specific characteristics, such as spatial heterogeneities of methane production. Consequently, the synchrony of ebullition events among locations is reduced.

Empirical models demonstrated good representation (R^2 from 0.7 to 0.96) of the daily and weekly variability of ebullition temporal dynamics at Passaúna Reservoir using environmental variables such as bottom current, velocity variance at the bottom, dissipation rate near the bottom, sediment temperature, dissolved oxygen concentrations near the bottom, atmospheric pressure, wind speed, relative water column stability, and total pressure. While these models improved the simulation of ebullition and its prediction at various timescales, they failed to reproduce ebullition at sub-daily scales (minutes or hours). Therefore, the hypothesis 2.2 proposed in this study was partially rejected. The inclusion of additional environmental variables enhanced the simulation of ebullition; however, the short-term variability of the fluxes at sub-daily timescales could not be resolved by the tested models.

While the main controls on ebullition reported in other systems were also identified as controlling factors in this study, the empirical models developed for those systems exhibited poor performance ($R^2 < 0.3$ and Nash-Sutcliffe efficiency < 0.23) when applied to simulate CH_4 ebullition at Passaúna Reservoir. This outcome was expected, given that the degree of dependency of ebullition on environmental forcings can vary between different systems. In a previous study, McClure et al. (2020) found that the environmental variables governing ebullition varied within monitoring locations in a single reservoir. However, in the case of Passaúna Reservoir, the higher synchronization of ebullition among the monitoring sites indicated similar ebullition controls across the reservoir on timescales greater than one day. Therefore, although empirical models have the potential to reproduce the temporal dynamics of ebullition in different areas within a reservoir, assuming synchronized fluxes, the coefficients of the models remain reservoir-specific. Consequently, the empirical relationships used to estimate ebullition should be tailored to each specific reservoir.

4.3 Spatio-temporal variability of sediment gas content and methane ebullition

The impact of the sampling design on the estimation and upscaling of CH_4 emissions from lakes and freshwater reservoirs has been extensively discussed in the scientific literature. Considering the temporal variability of ebullition, missing periods of intensified fluxes can lead to underestimation of emissions, whereas measuring ebullition only during peak moments can result in overestimation of emissions (WIK et al., 2013; MAECK; HOFMANN; LORKE, 2014). In a previous study on the Passaúna Reservoir, it was showed that shorter sampling periods (<2 d per season) have a higher probability of underestimating mean ebullition flux in winter compared to summer, as ebullition events are less frequent during colder months (MARCON et al., 2019). Temporal variability of ebullition has been reported to be generally higher than the spatial variability within the water body (WIK et al., 2013; LINKHORST et al., 2020). The daily fluxes observed in both studied reservoirs were not normally distributed (Kolmogorov-Smirnov test p-val<0.05), as indicated by the boxplots in Figure 5, with a dispersion of the fluxes.

Regarding thermal stratification, at Passaúna, the temporal variability of fluxes was greater when the reservoir was fully stratified. However, in the case of the Wupper Reservoir, such changes in variability could not be confirmed as the reservoir is mostly classified as partially stratified or mixed.

As previously discussed, the relationship between ebullition and gas content in the sediment is not linear, as it depends on depth, methane production in the sediment, and on ebullition drivers which are temporally variable. However, gas storage in the sediment is an important factor in the CH_4 balance in impoundments, and therefore, its variability may lead to changes in the spatial distribution of ebullition. When comparing both reservoirs, the overall spatial variability of gas content in the sediment is
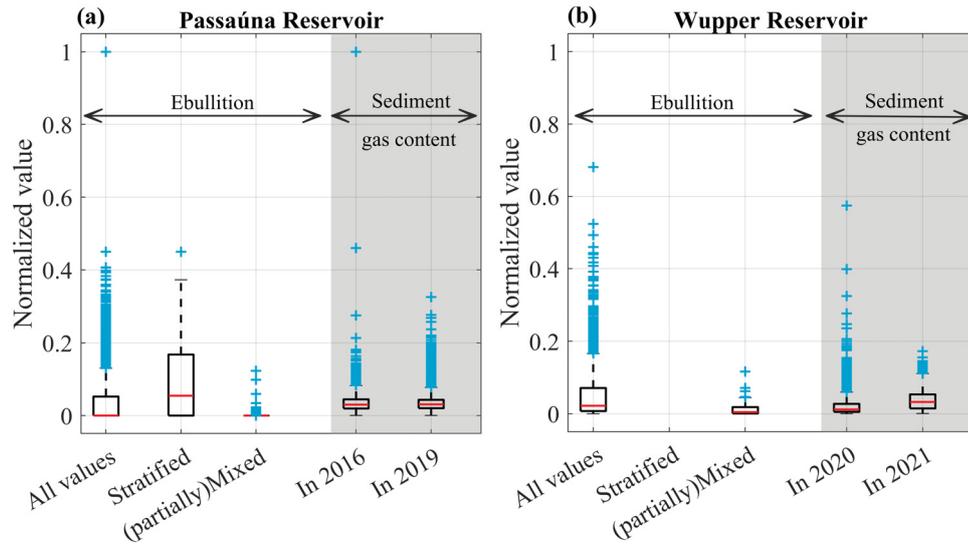
Figure 5 – (a) Boxplots of daily ebullition flux from all monitored sites (P1, P2, P3, and P4) and of sediment gas content acoustically estimated from two surveys conducted in 2016 and 2019. (b) Boxplots of daily ebullition flux from all monitored sites (from L01 to L05), and of sediment gas content acoustically estimated from two surveys conducted in 2020 and 2021. In both panels, the first boxplot shows all ebullition values, the second and third show ebullition grouped by reservoir's thermal stratification condition (using the RWCS), which was separated between stratified and mixed/partially stratified. The grey shaded area are the boxplots for the sediment gas content. Ebullition flux (in $mgCH_4\,m^{-2}\,d^{-1}$) and areal gas content (in $L\,m^{-2}$) were normalized by the maximum and minimum values combining both study sites (0—$587.1\,mgCH_4\,m^{-2}\,d^{-1}$ for ebullition and 0—$123.9\,L\,m^{-2}$ for sediment gas content) .The upper and lower limits of the boxes represent the 75th and 25th percentiles, respectively. The whiskers show the maximum and minimum values, the red line represents the median, and the blue crosses are outliers.

similar, with a comparable range of gas content. However, examining each reservoir separately, the range of gas content varied between surveys. In both cases, the largest range of gas content in the sediment was found in the survey with the relatively lower averaged sediment gas content (2016 for Passaúna and 2020 for Wupper). The main implication of the significant temporal variability of ebullition and the spatio-temporal variability of gas content in the sediment is the importance of conducting high-frequency measurements that cover different areas of the reservoirs (WIK et al., 2014; MAECK; HOFMANN; LORKE, 2014; MARCON et al., 2019).

4.4 Further comparison of the two studied sites

By investigating ebullition from two distinct reservoirs one important question arising was: how to generalize the main findings?

Overall, the mean ebullition flux during the warmest months measured at Passaúna ($81.2 \pm 35.1\,mgCH_4\,m^{-2}\,d^{-1}$) and at Wupper ($42.1 \pm 47.7\,mgCH_4\,m^{-2}\,d^{-1}$) reservoirs was lower than the mean CH_4 ebullition ($122.4\,mgCH_4\,m^{-2}\,d^{-1}$) reported for lakes and reservoirs worldwide (DEEMER et al., 2016). This discrepancy can be partly attributed to the different measurement techniques employed and variations in measurements' spatial and temporal coverage. Although a high temporal resolution and quasi-continuous ebullition time-series were utilized for flux calculation in both Passaúna and Wupper reservoirs, ebullition was not measured in the shallowest areas of the study sites and therefore, they were not included in the estimation of mean ebullition.

In the deeper subtropical reservoir (Passaúna), the sediment exhibited, on average, a higher organic matter content determined by Loss on Ignition (LOI), and was $10\,^\circ\mathrm{C}$ warmer compared to the temperate and shallower system of Wupper. The differences in temperature and water depth resulted in an anoxic bottom water layer in Passaúna, while Wupper showed higher dissolved oxygen concentrations near the bottom. The combination of mentioned conditions favoured a higher mean potential methane production in Passaúna compared to the average measured in Wupper, as bacterial activity is enhanced in warmer temperatures (YVON-DUROCHER et al., 2014), and CH_4 production is fuelled by organic matter content (GRASSET et al., 2018). These conditions were reflected in the amount of gas found in the bottom sediment, with Passaúna having approximately four times more CH_4 in the sediment matrix than Wupper reservoir. Consequently, the estimated gas turnover times in Passaúna reservoir were more than twice the values calculated for Wupper reservoir. Gas turnover times are connected to the replenishment of sediment with newly produced gas and were calculated as the ratio between the areal CH_4 content in the sediment and measured fluxes (see Table 2, and the discussion on Wupper reservoir in Appendix B).

Table 2 – Summary of overall results for both studied sites, Passaúna and Wupper Reservoirs. Mean values with their respective standard deviations are shown. Sediment temperature, dissolved oxygen concentrations (DO), and ebullition represent the mean values obtained from daily time-series. Loss on ignition (LOI), as a proxy for organic matter content, potential methane flux at the sediment water interface (PSWI), and ebullition are spatially averaged across all monitoring sites within each reservoir. The values shown correspond to the period when gas content was acoustically estimated in the sediment: Passaúna from January 1st to February 15th, of 2019 and Wupper for the entire months of June 2020 and June 2021, which, in both reservoirs, was during the summer season.

	Passaúna	**Wupper**
Mean depth (m)	8.3 [a]	2.0
Mean sediment temperature (°C)	22.1±0.6	12.0±0.6
Mean DO near bottom (mg L^{-1})	0.1±0.05	7.2±1.8
Mean LOI at $550\,^\circ\mathrm{C}$ (%)	17.0±8.5 [a]	11.9±1.3
Mean PSWI at top 15 cm (mgCH$_4$m^{-2}d^{-1})	351.3±251.2	260.1±86.8
Mean CH$_4$ ebullition (mgCH$_4$m^{-2}d^{-1})	81.2±35.1	42.1±47.7
Ecosystem-level Q$_{10}$ (−) [b]	7.2	9.9
Mean gas content in sediment (L m^{-2})	5.3	3.3
Mean CH$_4$ content in the sediment (mgCH$_4$ m^{-2})	7004.5	1648.6
Areal CH$_4$ free gas in the sediment / PSWI (d)	19.9	6.3
Areal CH$_4$ free gas in the sediment / Ebullition (d)	86.3	39.2

[a] Sotiri et al. (2021)
[b] The Q$_{10}$ represents the proportional change in the methane ebullition per a $10\,^\circ\mathrm{C}$ change in the surface sediment temperature. It was calculated as Q$_{10} = 10^{10b}$, in which b is the slope of a linear fit between log$_{10}$-transformed ebullition and surface sediment temperature (DELSONTRO et al., 2016).

Temperature is a straightforward parameter to measure, yet it has a direct impact on ebullition and its controlling factors, including thermal stratification. Wupper and Passaúna reservoirs exhibited distinct temperature ranges, while ebullition varied within a similar magnitude, as shown in Figure 6. The sediment temperature at Wupper ranged from approximately $5\,^\circ\mathrm{C}$ to $17\,^\circ\mathrm{C}$, whereas the warmer temperatures at Passaúna spanned a narrower range of $17\,^\circ\mathrm{C}$ to $24\,^\circ\mathrm{C}$. The ecosystem-level Q$_{10}$ values for both Passaúna and Wupper were slightly lower than those reported for other lakes and reservoirs (DELSONTRO et al., 2016). When comparing the two study sites, the dependence of ebullition on

temperature was more pronounced in the colder temperate reservoir (Wupper), which exhibited a higher Q_{10} value compared to the warmer subtropical reservoir, Passaúna.

Although ebullition increased with rising temperatures in both reservoirs (with a similar slope), a noticeable offset was observed between the two study sites (Figure 6). This can be partly attributed to the fact that temperature alone explained a different portion of the mean ebullition variability. In the case of Wupper reservoir, temperature accounted for 89% of the reservoir-wide flux variability in a polynomial fit, whereas in Passaúna reservoir, temperature explained only 54% of the variability. As previously discussed and presented in Appendix C, additional environmental variables were required to explain the variability of ebullition in Passaúna reservoir, alongside temperature.
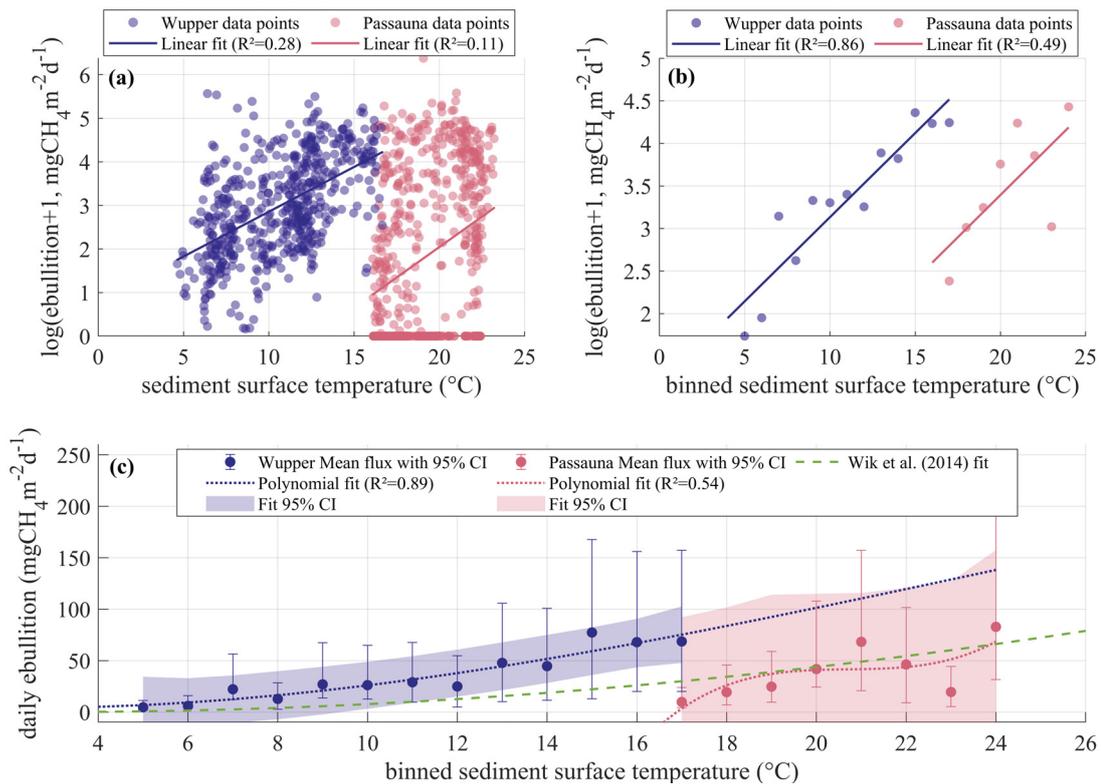
Figure 6 – (a) Scatter plot and linear regressions (solid lines) illustrating the relationship between CH_4 ebullition and sediment surface temperature at Wupper and Passaúna reservoirs. (b) Scatter plot and linear regressions (solid lines) depicting the relationship between mean CH_4 ebullition and binned sediment surface temperature (bin size: $1\,°C$) at Wupper and Passaúna reservoirs. (c) Mean CH_4 ebullition flux with 95% confidence interval plotted against binned sediment surface temperature. The dotted lines represent the respective polynomial fits between the two variables for each study site, while the green-dashed line corresponds to the curve proposed by Wik et al. (2014) for northern lakes, where mean ebullition is calculated as a function of binned sediment temperature. All panels display daily reservoir-wide ebullition flux, with colours indicating the study sites (refer to the legends). In panels (a) and (b), a constant value of 1 was added to the ebullition values, allowing for the inclusion of zero fluxes in the log-transformed data.

In order to further investigate the observed offset in reservoir-wide ebullition and surface sediment temperature between the study sites, the daily ebullition fluxes were normalized based on specific reservoir characteristics. This normalization involved dividing the fluxes by the mean reservoir depth, mean organic matter content in the sediment, and mean potential methane flux at the sediment-water interface (refer to values in Table 2). However, as demonstrated in Figure 7, these normalizations did not explain the observed offset between the two reservoirs when assuming a linear dependency between the variables. Although the offset remains unexplained in this study, it suggests the existence of one or a combination

of variables that could be utilized to parametrize ebullition flux across different reservoirs. This, in turn, could contribute to the transferability of empirical models for predicting ebullition in diverse reservoir settings.
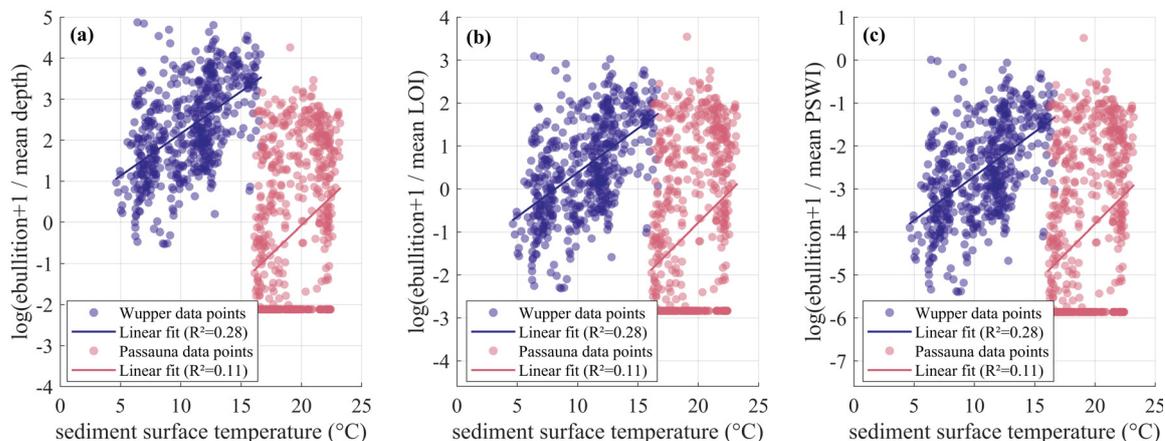
Figure 7 – (a) Scatter plot and linear regression (solid lines) between normalized ebullition by mean reservoir water depth and sediment surface temperature. (b) Scatter plot and linear regression (solid lines) between normalized ebullition by mean loss on ignition (LOI) as a proxy for organic matter content, and sediment surface temperature. (c) Scatter plot and linear regression (solid lines) between normalized ebullition by potential methane flux at the sediment-water interface (PSWI) and sediment surface temperature. In all panels, daily CH_4 ebullition values (in $mgCH_4\,m^{-2}\,d^{-1}$) are presented, with colours distinguishing Wupper and Passaúna reservoirs (refer to the legends). The values used for normalizing ebullition are provided in Table 2.

Given that this study was strongly based on in-situ measurements, several important aspects are further emphasised. Continuous and integrated monitoring of ebullition alongside environmental variables played a crucial role in this research, facilitating the understanding of ebullition dynamics at each study site. Additionally, the use of similar measurement techniques was vital for meaningful comparisons and interpretation of results between the two reservoirs. Nonetheless, several open questions still remain and warrant attention in future studies. Regarding gas content in the sediment, the vertical distribution of gas voids within the sediment could not be resolved using the acoustic method employed in this study. Therefore, further investigations are recommended, such as processing echo-sounder measurements to estimate the depth distribution of gas voids in the sediment aligning with the analysis conducted by (KATSNELSON et al., 2022).

As discussed previously, the parametrization of ebullition holds potential for enhancing the simulation of fluxes across diverse reservoirs. While the temporal variability of ebullition was analyzed in relation to various environmental variables, it is crucial to conduct continuous measurements of gas content in the sediment alongside ebullition flux under in-situ conditions. This integration would enable a better understanding of the interconnections between these two aspects.

Moreover, it is important to acknowledge that the empirical models tested in this study faced challenges in reproducing the temporal variability of ebullition on timescales shorter than one day. To address this limitation, a promising approach would be to combine empirical models with process-based models, which could improve the simulation of ebullition for shorter time intervals. In this way, future studies should prioritize the use of methods that enable continuous and high temporal resolution measurements of both ebullition and sediment gas content. Additionally, expanding these measurements to encompass a broader range of reservoirs would allow for generalizations regarding the spatial and temporal patterns of ebullition. This broader perspective is vital for advancing the understanding of ebullition

dynamics and improving predictive capabilities in various reservoir settings.

5 Conclusion

The research conducted in this study aimed to investigate the spatial-temporal variability of ebullition and sediment gas content in two contrasting freshwater reservoirs. Acoustic surveys showed that high sedimentation regions of the reservoir (near inflows, near the dam, and in the inner parts of bends) accumulate large amounts of free gas in the sediment matrix. Sediment thickness, organic matter content, and water depth in combination are good predictors of gas content in the sediment (could explain 89% of gas content variability at bottom sediment of Passaúna Reservoir in a trained ANN). A two-fold link was found between ebullition and gas content in the sediment, which was modulated by water depth and its associated effects (higher pressure, colder bottom temperature, and so forth). For the deeper reservoir (Passaúna with mean depth of $8.3\,\mathrm{m}$), ebullition was highest and less intermittent from the shallowest upstream region of the reservoir where the largest amount of gas content was detected in the sediment. With increasing water depths in the reservoir, the gas storage controlled the intermittency of ebullition, in which with increased hydrostatic pressure more gas was stored within the thicker sediment layer, but less gas could leave through ebullition events. In the shallower reservoir Wupper (mean depth of $2.0\,\mathrm{m}$), elevated CH_4 emissions (through ebullition, diffusion, degassing) and oxidation lead to depletion of gas content in the sediment. The gas storage in the sediment matrix acted as a buffer for CH_4 emissions, including CH_4 ebullition, which was recharged by production and depleted by various CH_4 efflux. The sediment matrix has the potential to store cumulative CH_4 production over several days, thereby sustaining ebullition fluxes for months, with longer turnover times in the deeper reservoir (Passaúna). Provided that there is gas being produced and stored in the sediment, the release of CH_4 from the sediment matrix through ebullition is shaped by triggers acting at different spatial and temporal scales. Factors such as thermal stratification, pressure changes (atmospheric and hydrostatic), sediment temperature, dissolved oxygen concentrations, and potential methane production in the sediment were significant drivers of ebullition, independent of the reservoir. However, the strength of the correlation between ebullition and these environmental controls varied between the study sites and over time within the same reservoir. While empirical models successfully simulated ebullition flux as a function of environmental variables for timescales greater than one day, the complex site-specific dependency of ebullition on its drivers makes it challenging to transfer these models across different systems to reproduce the temporal dynamics of ebullition accurately.

Lastly, the findings from this study contribute to the understanding of the spatial variability and temporal dynamics of ebullition in freshwater reservoirs. The novel aspects include insights into the relationship between ebullition and sediment gas storage, the influence of hydrodynamic processes (e.g., thermal stratification, bottom currents, dissipation rates) on ebullition dynamics, and the potential application of empirical models for estimating the timing and magnitude of ebullition events in impoundments. Nevertheless, several open questions remain to be addressed in further studies, including advances in methods for in-situ estimation of gas content in the sediment, parametrization of ebullition across different water bodies, and improvement in the capability to simulate ebullition flux on sub-daily timescales.

References

ABEN, R. C. et al. Cross continental increase in methane ebullition under climate change. *Nature Communications*, Springer US, v. 8, n. 1, p. 1–8, 2017. ISSN 20411723. Disponível em: <http://dx.doi.org/10.1038/s41467-017-01535-y>. 18, 21, 32, 69, 95, 96, 97, 111, 123, 125, 126, 136

ALGAR, C. K.; BOUDREAU, B. P. Transient growth of an isolated bubble in muddy, fine-grained sediments. *Geochimica et Cosmochimica Acta*, Elsevier Ltd, v. 73, n. 9, p. 2581–2591, 2009. ISSN 00167037. 21, 70

ALGAR, C. K.; BOUDREAU, B. P.; BARRY, M. A. Release of multiple bubbles from cohesive sediments. *Geophysical Research Letters*, v. 38, n. 8, p. 2–5, 2011. ISSN 00948276. 16

ALSHBOUL, Z. et al. Export of Dissolved Methane and Carbon Dioxide with Effluents from Municipal Wastewater Treatment Plants. *Environmental Science and Technology*, v. 50, n. 11, p. 5555–5563, 2016. ISSN 15205851. 95

ANDERSON, M. A.; MARTINEZ, D. Methane gas in lake bottom sediments quantified using acoustic backscatter strength. *Journal of Soils and Sediments*, v. 15, n. 5, p. 1246–1255, 2015. ISSN 16147480. 20, 22, 30, 55, 58, 59, 63, 64, 67, 71, 81, 85, 87, 94, 104

BALK, H.; LINDEM, T.; CARNERO, N. S. *Sonar4 and Sonar5 Pro post processing systems Operator manual*. [S.l.]: SonarX, 2011. 58, 73

BARTOSIEWICZ, M.; RZEPKA, P.; LEHMANN, M. F. Tapping Freshwaters for Methane and Energy. *Environmental Science & Technology*, v. 06210, p. acs.est.0c06210, mar 2021. ISSN 0013-936X. Disponível em: <https://pubs.acs.org/doi/10.1021/acs.est.0c06210>. 112

BASTVIKEN, D. Methane. In: *Encyclopedia of Inland Waters*. [S.l.]: Oxford: Elsevier, 2009. p. 783–805. ISBN 978-01-2088462-9. 54, 69, 70, 81, 95

BASTVIKEN, D. et al. Methane emissions from lakes: Dependence of lake characteristics, two regional assessments, and a global estimate. *Global Biogeochemical Cycles*, v. 18, n. 4, p. 1–12, 2004. ISSN 08866236. 19, 81

BASTVIKEN, D.; EJLERTSSON, J.; TRANVIK, L. Measurement of methane oxidation in lakes: A comparison of methods. *Environmental Science and Technology*, v. 36, n. 15, p. 3354–3361, 2002. ISSN 0013936X. 95

BASTVIKEN, D. et al. Low-cost methane (CH4) sensors for use in in flux chambers. In: *AGU General Assembly 2020*. Virtual meeting.: European Geosciences Union, 2020. 20

BAZHIN, N. Theory of methane emission from wetlands. *Energy & Environmental Science*, v. 3, n. 8, p. 1057, 2010. ISSN 1754-5692. Disponível em: <http://xlink.rsc.org/?DOI=b923456j>. 111

BAZHIN, N. M. Theoretical consideration of methane emission from sediments. *Chemosphere*, v. 50, n. 2, p. 191–200, 2003. ISSN 00456535. 69

BEAULIEU, J. J. et al. Effects of an Experimental Water-level Drawdown on Methane Emissions from a Eutrophic Reservoir. *Ecosystems*, Springer US, v. 21, n. 4, p. 657–674, 2018. ISSN 14350629. 32, 111

BEAULIEU, J. J.; DELSONTRO, T.; DOWNING, J. A. Eutrophication will increase methane emissions from lakes and impoundments during the 21st century. *Nature Communications*, Springer US, v. 10, n. 1, p. 3–7, 2019. ISSN 20411723. Disponível em: <http://dx.doi.org/10.1038/s41467-019-09100-5>. 54

BEAULIEU, J. J.; MCMANUS, M. G.; NIETCH, C. T. Estimates of reservoir methane emissions based on a spatially balanced probabilistic-survey. *Limnology and Oceanography*, v. 61, n. Thornton 1990, p. S27–S40, 2016. ISSN 19395590. 54

BECK, H. E. et al. Present and future köppen-geiger climate classification maps at 1-km resolution. *Scientific Data*, The Author(s), v. 5, p. 1–12, 2018. ISSN 20524463. 56

BERBERICH, M. E. et al. Spatial variability of sediment methane production and methanogen communities within a eutrophic reservoir: Importance of organic matter source and quantity. *Limnology and Oceanography*, v. 65, n. 6, p. 1336–1358, 2020. ISSN 19395590. 93

BERNARDO, J. W. Y. et al. A method for the assessment of long-term changes in carbon stock by construction of a hydropower reservoir. *Ambio*, v. 46, n. 5, p. 566–577, 2017. ISSN 16547209. 13

BOSSARD, V. P.; JOLLER, T.; SZABO, E. Die quantitative Erfassung von Methan im Seewasser. *Birkhäuser Verlag Basel*, v. 43, n. 1, p. 200–211, 1981. 57, 100

BOUDREAU, B. P. *Diagenetic Models and Their Implementation: Modelling transport and reactions in aquatic sediments.* 1. ed. Heidelberg: Springer Berlin Heidelberg, 2003. 428 p. ISBN 978-3-642-64399-6. Disponível em: <http://link.springer.com/10.1007/978-3-642-60421-8>. 19

BOUDREAU, B. P. The physics of bubbles in surficial, soft, cohesive sediments. *Marine and Petroleum Geology*, Elsevier Ltd, v. 38, n. 1, p. 1–18, 2012. ISSN 02648172. Disponível em: <http://dx.doi.org/10.1016/j.marpetgeo.2012.07.002>. 16

BOUDREAU, B. P. et al. Bubble growth and rise in soft sediments. *Geology*, v. 33, n. 6, p. 517–520, 2005. ISSN 00917613. 54, 70, 128

BRANCO, C. W. et al. Impact of climate on the vertical water column structure of Lajes Reservoir (Brazil): A tropical reservoir case. *Lakes and Reservoirs: Research and Management*, v. 14, n. 3, p. 175–191, 2009. ISSN 13205331. 85, 115

BRESLIN, M. C.; BELWARD, J. A. Fractal dimensions for rainfall time series. *Mathematics and Computers in Simulation*, v. 48, n. 4-6, p. 437–446, 1999. ISSN 03784754. 128

CAREY, C. C. et al. Chaoborus spp. Transport CH4 from the Sediments to the Surface Waters of a Eutrophic Reservoir, but Their Contribution to Water Column CH4 Concentrations and Diffusive Efflux Is Minor. *Environmental Science and Technology*, v. 52, n. 3, p. 1165–1173, 2018. ISSN 15205851. 15

CARNEIRO, C.; KELDERMAN, P.; IRVINE, K. Assessment of phosphorus sediment–water exchange through water and mass budget in Passaúna Reservoir (Paraná State, Brazil). *Environmental Earth Sciences*, Springer Berlin Heidelberg, v. 75, n. 7, p. 564, 2016. ISSN 1866-6280. 56

CASPER, P. et al. Fluxes of methane and carbon dioxide from a small productive lake to the atmosphere. *Biogeochemistry*, v. 49, n. 1, p. 1–19, 2000. ISSN 01682563. 18, 70, 111, 125

CAVIGLIONE, J. H. et al. *Cartas Climáticas do Paraná.* Londrina, 2010. Disponível em: <http://www.iapar.br/modules/conteudo/conteudo.php?conteudo=597>. 26

CHAPRA, S. C. *Surface water quality modeling.* Illinois: Waveland Press, 2008. 844 p. ISBN 978-1-57766-605-9. 15, 18

COLE, J. J. et al. Plumbing the global carbon cycle: Integrating inland waters into the terrestrial carbon budget. *Ecosystems*, v. 10, n. 1, p. 171–184, 2007. ISSN 14329840. 13

CRUSIUS, J.; WANNINKHOF, R. Gas transfer velocities measured at low wind speed over a lake. *Limnology and Oceanography*, v. 48, n. 3, p. 1010–1017, 2003. ISSN 00243590. 100

DALE, A. W. et al. Seasonal dynamics of the depth and rate of anaerobic oxidation of methane in Aarhus Bay (Denmark) sediments. *Journal of Marine Research*, v. 66, n. 1, p. 127–155, 2008. ISSN 00222402. 62

DEEMER, B. R. et al. Greenhouse Gas Emissions from Reservoir Water Surfaces: A New Global Synthesis Manuscript. *BioScience*, v. 66, n. 11, p. 949–964, 2016. ISSN 0006-3568. 16, 34, 54, 81, 96, 111, 125, 128

DELSONTRO, T.; BEAULIEU, J. J.; DOWNING, J. A. Greenhouse gas emissions from lakes and impoundments: Upscaling in the face of global change. *Limnology and Oceanography Letters*, v. 3, n. 3, p. 64–75, 2018. ISSN 2378-2242. 21, 54, 111

DELSONTRO, T. S. *Quantifying Methane Emissions from Reservoirs : From Basin-scale to Discrete Analyses with a Focus on Ebullition Dynamics.* 168 p. Tese (Doutorado) — ETH Zurich, 2011. 81

DELSONTRO, T. S. et al. Methane ebullition and diffusion from northern ponds and lakes regulated by the interaction between temperature and system productivity. *Limnology and Oceanography*, v. 61, p. S62–S77, 2016. ISSN 19395590. 18, 35, 97, 123, 125, 135

DELSONTRO, T. S. et al. Spatial heterogeneity of methane ebullition in a large tropical reservoir. *Environmental Science and Technology*, v. 45, n. 23, p. 9866–9873, 2011. ISSN 0013936X. 17, 70, 93

DELSONTRO, T. S. et al. Size does matter: Importance of large bubbles and small-scale hot spots for methane transport. *Environmental Science and Technology*, v. 49, n. 3, p. 1268–1276, 2015. ISSN 15205851. 22, 111, 122, 128

DELWICHE, K.; HEMOND, H. F. An enhanced bubble size sensor for long-term ebullition studies. *Limnology and Oceanography: Methods*, v. 15, n. 10, p. 821–835, 2017. ISSN 15415856. 20, 99

DELWICHE, K.; SENFT-GRUPP, S.; HEMOND, H. A novel optical sensor designed to measure methane bubble sizes in situ. *Limnology and Oceanography: Methods*, v. 13, n. 12, p. 712–721, 2015. ISSN 15415856. 99

DELWICHE, K. B. et al. Estimating Driver and Pathways for Hydroelectric Reservoir Methane Emissions Using a New Mechanistic Model. *Journal of Geophysical Research: Biogeosciences*, v. 127, n. 8, p. 1–24, 2022. ISSN 2169-8953. 16, 21, 96

DELWICHE, K. B.; HEMOND, H. F. Methane Bubble Size Distributions, Flux, and Dissolution in a Freshwater Lake. *Environmental Science and Technology*, v. 51, n. 23, p. 13733–13739, 2017. ISSN 15205851. 17

DESHMUKH, C. et al. Physical controls on CH4 emissions from a newly flooded subtropical freshwater hydroelectric reservoir: Nam Theun 2. *Biogeosciences*, v. 11, n. 15, p. 4251–4269, 2014. ISSN 17264189. 111, 112, 122, 123, 135, 138

DIAMOND, J. S. et al. Light and hydrologic connectivity drive dissolved oxygen synchrony in stream networks. *Limnology and Oceanography*, p. 322–335, 2022. ISSN 19395590. 116, 117

DÜCK, Y. et al. A novel freeze corer for characterization of methane bubbles and assessment of coring disturbances. *Limnology and Oceanography: Methods*, v. 17, n. 5, p. 305–319, 2019. ISSN 15415856. 20, 71

DÜCK, Y. et al. Laboratory and field investigations on freeze and gravity core sampling and assessment of coring disturbances with implications on gas bubble characterization. *Limnology and Oceanography: Methods*, v. 17, n. 11, p. 585–606, 2019. ISSN 15415856. 55, 71, 94

ESTEVES, F. d. A. *Fundamentos de Limnologia*. 3. ed. Rio de Janeiro: Interciência, 2011. 826 p. ISBN 978-85-7193-271-5. 13, 14, 15

ETMINAN, M. et al. Radiative forcing of carbon dioxide, methane, and nitrous oxide: A significant revision of the methane radiative forcing. *Geophysical Research Letters*, v. 43, n. 24, p. 12,614–12,623, 2016. ISSN 19448007. 54

EUGSTER, W.; DELSONTRO, T.; SOBEK, S. Eddy covariance flux measurements confirm extreme CH 4 emissions from a Swiss hydropower reservoir and resolve their short-term variability. *Biogeosciences*, v. 8, n. 9, p. 2815–2831, 2011. ISSN 17264170. 20

FAUSETT, L. *Fundamentals of neural networks: architctures, algorithms, and applications*. [S.l.]: Prentice-Hall, 1994. 461 p. ISBN 9780133341867. 71

FISCHER, H. B. et al. *Mixing in inland and coastal waters*. Nova York: Academic Press Inc, 1979. 483 p. 19, 85, 115

FONSECA, L. et al. The high-frequency backscattering angular response of gassy sediments: Model/data comparison from the Eel River Margin, California. *The Journal of the Acoustical Society of America*, v. 111, n. 6, p. 2621–2631, 2002. ISSN 0001-4966. 60

FRANGIPANE, G. et al. Comparison of loss on ignition and thermal analysis stepwise methods for determination of sedimentary organic matter. *Aquatic Conservation: Marine and Freshwater Ecosystems*, v. 19, n. 1, p. 24–33, jan 2008. ISSN 10527613. Disponível em: <https://onlinelibrary.wiley-.com/doi/10.1002/aqc.970>. 60

FRIEDL, G.; WÜEST, A. Disrupting biogeochemical cycles - Consequences of damming. *Aquatic Sciences-Research Across Boundaries*, v. 64, p. 55–65, 2002. ISSN 1015-1621. 13

GERARDO-NIETO, O. et al. Initial report on methane and carbon dioxide emission dynamics from sub-Antarctic freshwater ecosystems: A seasonal study of a lake and a reservoir. *Science of the Total Environment*, Elsevier B.V., v. 593-594, p. 144–154, 2017. ISSN 18791026. Disponível em: <http://dx.doi.org/10.1016/j.scitotenv.2017.02.144>. 85, 115

GOLDENFUM, J. A. *GHG measurement guidelines for freshwater reservoirs*. London, 2010. 138 p. 57, 83, 99, 100

GOLDENFUM, J. A. Challenges and solutions for assessing the impact of freshwater reservoirs on natural GHG emissions. *Ecohydrology and Hydrobiology*, Elsevier, v. 12, n. 2, p. 115–122, 2012. ISSN 20803397. Disponível em: <http://dx.doi.org/10.2478/v10104-012-0011-5>. 16, 20

GRASSET, C. et al. Large but variable methane production in anoxic freshwater sediment upon addition of allochthonous and autochthonous organic matter. *Limnology and Oceanography*, 2018. ISSN 19395590. 17, 35, 54, 111

GRASSET, C. et al. An empirical model to predict methane production in inland water sediment from particular organic matter supply and reactivity. *Limnology and Oceanography*, n. Middelburg 1989, p. 1–13, 2021. ISSN 0024-3590. 69, 93, 125

GRINHAM, A.; DUNBABIN, M.; ALBERT, S. Importance of sediment organic matter to methane ebullition in a sub-tropical freshwater reservoir. *Science of the Total Environment*, Elsevier B.V., v. 621, p. 1199–1207, 2018. ISSN 18791026. Disponível em: <https://doi.org/10.1016/j.scitotenv.2017.10.108>. 17, 18, 111

GUÉRIN, F. et al. Effect of sporadic destratification, seasonal overturn, and artificial mixing on CH4 emissions from a subtropical hydroelectric reservoir. *Biogeosciences*, v. 13, n. 12, p. 3647–3663, 2016. ISSN 17264189. 19

GURSKI, L. K. K. *Optimal resolutions for modeling and monitoring the water quality dynamics of Passaúna's reservoir*. 198 p. Tese (PhD dissertation) — Karlsruhe Institute of Technology (KIT) and Federal University of Paraná (UFPR), 2022. 27, 138

GUSEVA, S. et al. Multimodel simulation of vertical gas transfer in a temperate lake. *Hydrology and Earth System Sciences*, v. 24, n. 2, p. 697–715, feb 2020. ISSN 1607-7938. Disponível em: <https://hess.copernicus.org/articles/24/697/2020/>. 32, 97

HEIRI, O.; LOTTER, A. F.; LEMCKE, G. Loss on Ignition as a Method for Estimating Organic and Carbonate Content in Sediments : Reproducibility and Comparability of Results. *Journal of Paleolimnology*, v. 25, n. DECEMBER, p. 101–110, 2001. 102

HILGERT, S. *Analysis of spatial and temporal heterogeneities of methane emissions of reservoirs by correlating hhydro-acoustic with sediment parameters*. Tese (phD) — Karlsruhe Institute of Technology, 2014. 57, 60

HILGERT, S. et al. Development of a flexible dialysis pore water sampler placement system: Easy handling and related error sources. *Journal of Limnology*, v. 74, n. 2, p. 414–420, 2015. ISSN 11295767. 20

HILGERT, S.; SOTIRI, K.; FUCHS, S. Advanced Assessment of Sediment Characteristics Based on Rheological and Hydro-Acoustic Measurements in a Brazilian Reservoir. *38th IAHR World Congress - "Water: Connecting the World"*, v. 38, n. September, p. 61–70, 2019. 16, 20, 70, 81

HILGERT, S. et al. Resolving spatial heterogeneities of methane ebullition flux from a Brazilian reservoir by combining hydro-acoustic measurements with methane production potential. In: *38 IAHR World Congress Water - connecting the world*. Panamá: [s.n.], 2019. 55, 57, 62

HILGERT, S. et al. Investigation of echo sounding parameters for the characterisation of bottom sediments in a sub-tropical reservoir. *Advances in Oceanography and Limnology*, v. 7, n. 1, p. 93–105, 2016. ISSN 1947-5721. 58, 71, 73, 74

HOFMANN, H.; FEDERWISCH, L.; PEETERS, F. Wave-induced release of methane: Littoral zones as a source of methane in lakes. *Limnology and Oceanography*, v. 55, n. 5, p. 1990–2000, 2010. ISSN 00243590. 19

HÖLZLWIMMER, S. *Analysis of the relationship between sediment composition and methane concentration in sediments of subtropical reservoirs using sediment peepers.* 85 p. Tese (Doutorado) — Weihenstephan-Triesdorf University of Applied Sciences, 2013. 57

IPCC. *Climate Change 2021: The Physical Science Basis. Contribution of Working Group I to the Sixth Assessment Report of the Intergovernmental Panel on Climate Change.* Cambridge, United Kingdom and New York (USA): Cambridge University Press, 2021. 2391 p. 13, 81

ISHIKAWA, M.; BLENINGER, T.; LORKE, A. Hydrodynamics and mixing mechanisms in a subtropical reservoir. *Inland Waters*, Taylor & Francis, v. 11, n. 3, p. 286–301, 2021. ISSN 2044205X. Disponível em: <https://doi.org/10.1080/20442041.2021.1932391>. 26, 27, 30, 32, 56, 113, 114, 115, 125

ISHIKAWA, M. et al. Effects of dimensionality on the performance of hydrodynamic models for stratified lakes and reservoirs. *Geoscientific Model Development*, v. 15, n. 5, p. 2197–2220, 2022. ISSN 19919603. 115

ISHIKAWA, M. et al. Hydrodynamic Drivers of Nutrient and Phytoplankton Dynamics in a Subtropical Reservoir. *Water (Switzerland)*, v. 14, n. 10, 2022. ISSN 20734441. 27, 112, 115, 125

ISIDOROVA, A. et al. Methane formation in tropical reservoirs predicted from sediment age and nitrogen. *Scientific Reports*, v. 9, n. 1, p. 1–9, 2019. 68, 95, 111

JAIN, A. K.; JUANES, R. Preferential mode of gas invasion in sediments: Grain-scale mechanistic model of coupled multiphase fluid flow and sediment mechanics. *Journal of Geophysical Research: Solid Earth*, v. 114, n. 8, p. 1–19, 2009. ISSN 21699356. 96

JANSEN, J. et al. Drivers of diffusive CH4 emissions from shallow subarctic lakes on daily to multi-year timescales. *Biogeosciences*, v. 17, n. 7, p. 1911–1932, apr 2020. ISSN 1726-4189. Disponível em: <https://bg.copernicus.org/articles/17/1911/2020/>. 54

JOYCE, J.; JEWELL, P. W. Physical controls on methane ebullition from reservoirs and lakes. *Environmental and Engineering Geoscience*, 2003. ISSN 10787275. 19, 70, 111, 125

KATSMAN, R. Correlation of shape and size of methane bubbles in fine-grained muddy aquatic sediments with sediment fracture toughness. *Journal of Structural Geology*, v. 70, p. 56–64, 2015. ISSN 01918141. 21, 96

KATSMAN, R.; OSTROVSKY, I.; MAKOVSKY, Y. Methane bubble growth in fine-grained muddy aquatic sediment: Insight from modeling. *Earth and Planetary Science Letters*, Elsevier B.V., v. 377-378, p. 336–346, 2013. ISSN 0012821X. Disponível em: <http://dx.doi.org/10.1016/j.epsl.2013.07.011>. 54, 111, 128

KATSNELSON, B. et al. Acoustical methodology for determination of gas content in aquatic sediments, with application to Lake Kinneret, Israel, as a case study. *Limnology and Oceanography: Methods*, v. 15, n. 6, p. 531–541, 2017. ISSN 15415856. 20, 22, 30, 55, 67, 71, 81, 94

KATSNELSON, B. et al. Characterization of the gassy sediment layer in shallow water using an acoustical method: Lake Kinneret as a case study. *Limnology and Oceanography: Methods*, v. 20, n. 9, p. 581–593, sep 2022. ISSN 1541-5856. Disponível em: <https://onlinelibrary.wiley.com/doi/10.1002/lom3.10506>. 30, 37, 94, 97

KELLER, M.; STALLARD, R. F. Methane emission by bubbling from Gatun Lake, Panama. *Journal of Geophysical Research*, v. 99, n. D4, p. 8307–8319, 1994. ISSN 0148-0227. 111

KLEIN, S. Sediment porewater exchange and solute release during ebullition. *Marine Chemistry*, v. 102, n. 1-2, p. 60–71, 2006. ISSN 03044203. 17

KURAMOTO, Y. Self-entrainment of a population of coupled non-linear oscillators. In: *International Symposium on Mathematical Problems in Theoretical Physics. Lecture Notes in Physics, vol 39.* Berlin/Heidelberg: Springer-Verlag, 1975. p. 420–422. Disponível em: <http://link.springer.com/10-.1007/BFb0013365>. 117

LANGENEGGER, T. et al. What the bubble knows: lake methane dynamics revealed by sediment gas bubble composition. *Limnology and Oceanography*, n. February, 2019. ISSN 00243590. 19, 21, 31, 32, 69, 70, 97, 111, 125

LAUERWALD, R. et al. Inland Water Greenhouse Gas Budgets for RECCAP2: 1. State-of- the-Art of Global Scale Assessments. *Global Biogeochemical Cycles*, 2023. 13, 112

LEHNER, B. et al. Global Reservoir and Dam (GRanD) database. *European Environment*, n. March, p. 12, 2011. Disponível em: <http://www.gwsp.org/85.html>. 13

LEONTE, M. et al. Rapid rates of aerobic methane oxidation at the feather edge of gas hydrate stability in the waters of Hudson Canyon, US Atlantic Margin. *Geochimica et Cosmochimica Acta*, Elsevier Ltd, v. 204, p. 375–387, 2017. ISSN 00167037. Disponível em: <http://dx.doi.org/10.1016/j.gca.2017.01.009>. 101

LINKHORST, A. et al. Comparing methane ebullition variability across space and time in a Brazilian reservoir. *Limnology and Oceanography*, p. 1623–1634, 2020. ISSN 19395590. 22, 33, 122

LINKHORST, A. et al. Spatially Resolved Measurements in Tropical Reservoirs Reveal Elevated Methane Ebullition at River Inflows and at High Productivity. *Global Biogeochemical Cycles*, v. 35, n. 5, p. 1–16, 2021. ISSN 19449224. 54, 70, 93

LISS, P. S.; SLATER, P. G. Flux of gases across the Air-Sea interface. *Nature*, v. 247, n. 5438, p. 181–184, 1974. ISSN 00280836. 20, 83, 99

LIU, L. et al. Methane Bubble Growth and Migration in Aquatic Sediments Observed by X-ray μcT. *Environmental Science and Technology*, v. 52, n. 4, p. 2007–2015, 2018. ISSN 15205851. 16, 54, 67, 81, 94

LIU, L. et al. The control of sediment gas accumulation on spatial distribution of ebullition in Lake Kinneret. *Geo-Marine Letters*, Geo-Marine Letters, 2019. ISSN 14321157. 55, 71, 81

LIU, L. et al. The role of sediment structure in gas bubble storage and release. *Journal of Geophysical Research: Biogeosciences RESEARCH*, n. August, p. 1–14, 2016. 16, 19, 20, 21, 30, 68, 70, 81, 94, 96, 111

LORKE, A. et al. Effect of ship locking on sediment oxygen uptake in impounded rivers. *Water Resources Research*, v. 48, n. 12, p. 1–7, 2012. ISSN 00431397. 95

LORKE, A. et al. Breathing sediments: The control of diffusive transport across the sediment-water interface by periodic boundary-layer turbulence. *Limnology and Oceanography*, v. 48, n. 6, p. 2077–2085, 2003. ISSN 00243590. 19

LORKE, A. et al. Dynamics of turbulence in low-speed oscillating bottom-boundary layers of stratified basins. *Environmental Fluid Mechanics*, v. 2, n. 4, p. 291–313, 2002. ISSN 15677419. 125

LUNKOV, A. A.; KATSNELSON, B. G. Using discrete low-frequency components of shipping noise for gassy sediment characterization in shallow water. *The Journal of the Acoustical Society of America*, Acoustical Society of America, v. 147, n. 5, p. EL428–EL433, 2020. ISSN 0001-4966. 55

MA, S. et al. Evaluating alternative ebullition models for predicting peatland methane emission and its pathways via data–model fusion. *Biogeosciences*, v. 19, n. 8, p. 2245–2262, apr 2022. ISSN 1726-4189. Disponível em: <https://bg.copernicus.org/articles/19/2245/2022/>. 96

MAAVARA, T. et al. River dam impacts on biogeochemical cycling. *Nature Reviews Earth & Environment*, Springer US, v. 1, n. 2, p. 103–116, 2020. ISSN 0028-0836. 13, 81

MAAVARA, T. et al. Global perturbation of organic carbon cycling by river damming. *Nature Communications*, Nature Publishing Group, v. 8, n. May, p. 1–10, 2017. ISSN 20411723. Disponível em: <http://dx.doi.org/10.1038/ncomms15347>. 81

MAECK, A. et al. Sediment trapping by dams creates methane emission hot spots. *Environmental Science and Technology*, v. 47, n. 15, 2013. ISSN 0013936X. 16, 17, 54, 81

MAECK, A.; HOFMANN, H.; LORKE, A. Pumping methane out of aquatic sediments - ebullition forcing mechanisms in an impounded river. *Biogeosciences*, v. 11, n. 11, p. 2925–2938, 2014. ISSN 17264189. 16, 18, 19, 20, 22, 33, 34, 54, 69, 70, 97, 99, 111, 112, 124, 125, 126

MANNICH, M.; FERNANDES, C.; BLENINGER, T. Uncertainty analysis of gas flux measurements at air-water interface using floating chambers. *Ecohydrology and Hydrobiology*, n. 2016, 2017. ISSN 20803397. 20

MARCON, L. et al. High-frequency measurements of gas ebullition in a Brazilian subtropical reservoir—identification of relevant triggers and seasonal patterns. *Environmental Monitoring and Assessment*, v. 191, n. 6, p. 357, jun 2019. ISSN 0167-6369. Disponível em: <http://link.springer.com-/10.1007/s10661-019-7498-9>. 33, 34, 57, 69, 97, 114, 124, 127

MARCON, L. et al. *Date set for the manuscript: Exploring the temporal dynamics of methane ebullition in a subtropical freshwater reservoir*. [S.l.]: Repository Zenodo, 2023. 116, 117

MARCON, L. et al. *Date set for the manuscript: The Role of Sediment Gas Storage in the Methane Dynamics of a Shallow Freshwater Reservoir*. Online: Zenodo, 2022. 84

MARCON, L. et al. Acoustic Mapping of Gas Stored in Sediments of Shallow Aquatic Systems Linked to Methane Production and Ebullition Patterns. *Frontiers in Environmental Science*, v. 10, n. April, p. 1–17, 2022. ISSN 2296665X. 81, 93, 94, 114

MARTINEZ-CRUZ, K. et al. Ubiquitous and significant anaerobic oxidation of methane in freshwater lake sediments. *Water Research*, Elsevier Ltd, v. 144, n. 2, p. 332–340, 2018. ISSN 18792448. Disponível em: <https://doi.org/10.1016/j.watres.2018.07.053>. 15, 70

MARTINEZ, D.; ANDERSON, M. A. Methane production and ebullition in a shallow, artificially aerated, eutrophic temperate lake (Lake Elsinore, CA). *Science of the Total Environment*, Elsevier B.V., v. 454-455, p. 457–465, 2013. ISSN 00489697. Disponível em: <http://dx.doi.org/10.1016/j.scitotenv-.2013.03.040>. 81

MCCLURE, R. P. et al. The Magnitude and Drivers of Methane Ebullition and Diffusion Vary on a Longitudinal Gradient in a Small Freshwater Reservoir. *Journal of Geophysical Research: Biogeosciences*, v. 125, n. 3, p. 0–18, 2020. ISSN 21698961. 21, 22, 33, 111, 112, 120, 122, 123, 127, 128, 136, 137

MCCLURE, R. P. et al. Iterative Forecasting Improves Near-Term Predictions of Methane Ebullition Rates. *Frontiers in Environmental Science*, v. 9, n. December, p. 1–16, 2021. ISSN 2296665X. 112, 127

MCGINNIS, D. F. et al. Porewater methane transport within the gas vesicles of diurnally migrating Chaoborus spp.: An energetic advantage. *Scientific Reports*, Nature Publishing Group, v. 7, n. July 2016, p. 1–7, 2017. ISSN 20452322. 15, 111

MCGINNIS, D. F. et al. Fate of rising methane bubbles in stratified waters: How much methane reaches the atmosphere? *Journal of Geophysical Research: Oceans*, v. 111, n. 9, p. 1–15, 2006. ISSN 21699291. 16, 19, 54

MENDONÇA, R. et al. Organic carbon burial in global lakes and reservoirs. *Nature Communications*, Springer US, v. 8, n. 1, p. 1–6, 2017. ISSN 20411723. Disponível em: <http://dx.doi.org/10.1038-/s41467-017-01789-6>. 14

MORANA, C. et al. Methane paradox in tropical lakes? Sedimentary fluxes rather than pelagic production in oxic conditions sustain methanotrophy and emissions to the atmosphere. *Biogeosciences*, v. 17, n. 20, p. 5209–5221, 2020. ISSN 17264189. 69

MORRIS, G. Classification of Management Alternatives to Combat Reservoir Sedimentation. *Water*, v. 12, n. 3, p. 861, mar 2020. ISSN 2073-4441. Disponível em: <https://www.mdpi.com/2073-4441/12-/3/861>. 82

MULLIGAN, M.; SOESBERGEN, A. van; SÁENZ, L. GOODD, a global dataset of more than 38,000 georeferenced dams. *Scientific Data*, v. 7, n. 1, p. 1–8, 2020. ISSN 20524463. 13

MUSTASAAR, M.; COMAS, X. Spatiotemporal variability in biogenic gas dynamics in a subtropical peat soil at the laboratory scale is revealed using high-resolution ground-penetrating radar. *Journal of Geophysical Research: Biogeosciences*, v. 122, n. 9, p. 2219–2232, sep 2017. ISSN 2169-8953. Disponível em: <https://onlinelibrary.wiley.com/doi/10.1002/2016JG003714>. 20, 94

NATCHIMUTHU, S. et al. Spatio-temporal variability of lake CH4 fluxes and its influence on annual whole lake emission estimates. *Limnology and Oceanography*, v. 61, p. S13–S26, 2016. ISSN 19395590. 18, 21, 32, 70, 97, 111, 125

NETO, A. A. et al. Seismic peak amplitude as a predictor of TOC content in shallow marine sediments. *Geo-Marine Letters*, Geo-Marine Letters, v. 36, n. 5, p. 395–403, 2016. ISSN 14321157. Disponível em: <http://dx.doi.org/10.1007/s00367-016-0449-3>. 55

OSTROVSKY, I. et al. Quantifying gas ebullition with echosounder: the role of methane transport by bubbles in a medium-sized lake. *Limnology and Oceanography: Methods*, v. 6, p. 105–118, 2008. ISSN 15415856. 16, 20

OSTROVSKY, I.; TEGOWSKI, J. Hydroacoustic analysis of spatial and temporal variability of bottom sediment characteristics in Lake Kinneret in relation to water level fluctuation. *Geo-Marine Letters*, v. 30, n. 3-4, p. 261–269, 2010. ISSN 02760460. 55

PAUL, L. Nutrient elimination in pre-dams: Results of long term studies. *Hydrobiologia*, v. 504, p. 289–295, 2003. ISSN 00188158. 82

PEACOCK, M. et al. Global importance of methane emissions from drainage ditches and canals. *Environmental Research Letters*, v. 16, n. 4, 2021. ISSN 17489326. 54

PEKEL, J. F. et al. High-resolution mapping of global surface water and its long-term changes. *Nature*, Nature Publishing Group, v. 540, n. 7633, p. 418–422, 2016. ISSN 14764687. 54

PELTOLA, O. *Field intercomparison of four methane gas analysers suitable for eddy covariance flux measurements*. 80 p. Tese (Master) — University of Helsinki, 2011. 21

PELTOLA, O. et al. Technical note: Comparison of methane ebullition modelling approaches used in terrestrial wetland models. *Biogeosciences*, Copernicus GmbH, v. 15, n. 3, p. 937–951, feb 2018. ISSN 1726-4189. Disponível em: <https://bg.copernicus.org/articles/15/937/2018/>. 81, 96, 111

PILGRIM, I.; P. Taylor, R. Fractal Analysis of Time-Series Data Sets: Methods and Challenges. In: *Fractal Analysis*. IntechOpen, 2019. Disponível em: <https://www.intechopen.com/books/fractal-analysis/fractal-analysis-of-time-series-data-sets-methods-and-challenges>. 128

PRAETZEL, L. S. E. et al. Organic matter and sediment properties determine in-lake variability of sediment CO2 and CH4 production and emissions of a small and shallow lake. *Biogeosciences Discussions*, n. August, p. 1–39, 2019. 15, 17, 18, 21, 69

PRAETZEL, L. S. E.; SCHMIEDESKAMP, M.; KNORR, K.-h. Temperature and sediment properties drive spatiotemporal variability of methane ebullition in a small and shallow temperate lake. *Limnology and Oceanography*, v. 66, n. 7, p. 2598–2610, jul 2021. ISSN 0024-3590. Disponível em: <https://onlinelibrary.wiley.com/doi/10.1002/lno.11775>. 111, 123, 137

PRAIRIE, Y. T. et al. A new modelling framework to assess biogenic GHG emissions from reservoirs: The G-res tool. *Environmental Modelling and Software*, Elsevier Ltd, v. 143, p. 105117, 2021. ISSN 13648152. Disponível em: <https://doi.org/10.1016/j.envsoft.2021.105117>. 21, 97, 111

RAUEN, W. B.; CASTRO, C. O. D.; SILVA, M. G. D. Caracterização hidrossedimentológica do Rio Passaúna, PR, Brasil, a partir de dados históricos. *XX Simpósio Brasileiro de Recursos Hídricos*, n. 2, p. 8, 2017. 26, 112

ROSA, L. P. et al. *Emissões de Dióxido de Carbono e de Metano pelos Reservatórios Hidrelétricos Brasileiros*. Brasília, 2006. 118 p. 20

ROSENTRETER, J. A. et al. Half of global methane emissions come from highly variable aquatic ecosystem sources. *Nature Geoscience*, v. 14, n. April, 2021. ISSN 1752-0908. Disponível em: <http://dx.doi.org/10.1038/s41561-021-00715-2>. 13, 15, 16, 54, 81, 96, 111, 124

RUDD, J. W. M. et al. Are hydroelectric reservoirs significant sources of greenhouse gases. *Ambio*, v. 22, n. 4, p. 246–248, 1993. ISSN 0044-7447. 13

SANTOS, M. A. dos et al. Gross greenhouse gas fluxes from hydro-power reservoir compared to thermo-power plants. *Energy Policy*, v. 34, n. 4, p. 481–488, 2006. ISSN 03014215. 16

SAUNOIS, M. et al. The global methane budget 2000-2012. *Earth System Science Data*, v. 8, n. 2, p. 697–751, 2016. ISSN 18663516. 13

SAUNOIS, M. et al. The Global Methane Budget 2000–2017. *Earth System Science Data*, v. 12, n. 3, p. 1561–1623, jul 2020. ISSN 1866-3516. Disponível em: <https://essd.copernicus.org/articles/12/1561-/2020/>. 54, 81

SAWAKUCHI, H. O. et al. Oxidative mitigation of aquatic methane emissions in large Amazonian rivers. *Global Change Biology*, v. 22, n. 3, p. 1075–1085, 2016. ISSN 13652486. 83, 84, 95, 101, 111

SCANDELLA, B. P. *Numerical modeling of methane venting from lake sediments*. Tese (Master) — Massachusetts Institute of Technology, 2010. 16

SCANDELLA, B. P. et al. Persistence of bubble outlets in soft, methane-generating sediments. *Journal of Geophysical Research: Biogeosciences*, v. 122, n. 6, p. 1298–1320, 2017. ISSN 21698961. 16

SCANDELLA, B. P. et al. Ephemerality of discrete methane vents in lake sediments. *Geophysical Research Letters*, v. 43, n. 9, p. 4374–4381, 2016. ISSN 19448007. 16

SCANDELLA, B. P. et al. A conduit dilation model of methane venting from lake sediments. *Geophysical Research Letters*, v. 38, n. 6, p. 1–6, 2011. ISSN 00948276. 16, 18, 54, 70, 111, 128

SCHMID, M.; OSTROVSKY, I.; MCGINNIS, D. F. Role of gas ebullition in the methane budget of a deep subtropical lake: What can we learn from process-based modeling? *Limnology and Oceanography*, v. 62, n. 6, p. 2674–2698, 2017. ISSN 19395590. 21, 111

SCHMIEDESKAMP, M. et al. Whole-lake methane emissions from two temperate shallow lakes with fluctuating water levels: Relevance of spatiotemporal patterns. *Limnology and Oceanography*, v. 66, n. 6, p. 2455–2469, 2021. ISSN 19395590. 54

SCHWARZ, M.; MARCON, L.; LORKE, A. Quantifying bubble-mediated transport by ebullition from aquatic sediments. *Frontiers in Earth Science*, v. 11, n. April, p. 1–7, apr 2023. ISSN 2296-6463. Disponível em: <https://www.frontiersin.org/articles/10.3389/feart.2023.1113349/full>. 17

SEEBERG-ELVERFELDT, J. et al. Rhizon sampling of porewaters near the sediment-water interface of aquatic systems. *Limnology and Oceanography: Methods*, v. 3, n. 8, p. 361–371, 2005. ISSN 15415856. 20

SHOTBOLT, L. A.; THOMAS, A. D.; HUTCHINSON, S. M. The use of reservoir sediments as environmental archives of catchment inputs and atmospheric pollution. *Progress in Physical Geography: Earth and Environment*, v. 29, n. 3, p. 337–361, sep 2005. ISSN 0309-1333. Disponível em: <http://journals.sagepub.com/doi/10.1191/0309133305pp452ra>. 30

SILLS, G. C. et al. Behaviour of offshore soils containing gas bubbles. *Geotechnique*, v. 41, n. 2, p. 227–241, 1991. ISSN 17517656. 96

SMITH, K. A. et al. Exchange of greenhousegases between soil and atmosphere: interactions of soil physical factors and biological processes. *European Journal of Soil Science*, v. 54, n. December, p. 779–791, 2003. 15, 20, 81

SOBEK, S. et al. Extreme organic carbon burial fuels intense methane bubbling in a temperate reservoir. *Geophysical Research Letters*, v. 39, n. 1, p. 2–5, 2012. ISSN 00948276. 17, 69

SOCOLOFSKY, S. A.; JIRKA, G. H. Equations. 2004. 19

SOTIRI, K. *Integrated Sediment Yield and Stock Assessment for the Passaúna Reservoir, Brazil*. 220 p. Tese (Doctorate) — Karlsruher Instituts für Technologie (KIT), 2020. 55, 58, 59, 64, 65, 70

SOTIRI, K.; HILGERT, S.; FUCHS, S. Derivation of a Hydro-Acoustic Sediment Classification Methodology From an Extensive Dataset of Sixreservoirs. *38th IAHR World Congress - "Water: Connecting the World"*, v. 38, n. September, p. 51–60, 2019. 27, 55, 58, 67, 71

SOTIRI, K. et al. Implementation of comparative detection approaches for the accurate assessment of sediment thickness and sediment volume in the Passaúna Reservoir. *Journal of Environmental Management*, Elsevier Ltd, v. 287, n. January, p. 112298, 2021. ISSN 10958630. Disponível em: <https://doi.org/10.1016/j.jenvman.2021.112298>. 25, 26, 27, 35, 55, 58, 59, 60, 63, 64, 68, 113, 114, 138

STEPANENKO, V. M. et al. Numerical modeling of methane emissions from lakes in the permafrost zone. *Izvestiya, Atmospheric and Oceanic Physics*, v. 47, n. 2, p. 252–264, 2010. ISSN 0001-4338. 17

STERNLICHT, D. D.; MOUSTIER, C. P. de. Time-dependent seafloor acoustic backscatter (10–100 kHz). *The Journal of the Acoustical Society of America*, v. 114, n. 5, p. 2709, 2003. ISSN 00014966. 58, 60, 71

STOLAROFF, J. K. et al. Review of Methane Mitigation Technologies with Application to Rapid Release of Methane from the Arctic. *Environmental Science & Technology*, v. 46, n. 12, p. 6455–6469, jun 2012. ISSN 0013-936X. Disponível em: <https://pubs.acs.org/doi/10.1021/es204686w>. 112, 128

TANG, K. W. et al. Paradox reconsidered: Methane oversaturation in well-oxygenated lake waters. *Limnology and Oceanography*, v. 59, n. 1, p. 275–284, 2014. ISSN 00243590. 15

TEGOWSKI, J. Acoustical classification of the bottom sediments in the southern Baltic Sea. *Quaternary International*, v. 130, n. 1, p. 153–161, 2005. ISSN 10406182. 55

TEODORU, C. R. et al. The net carbon footprint of a newly created boreal hydroelectric reservoir. *Global Biogeochemical Cycles*, v. 26, n. 2, p. 1–14, 2012. ISSN 08866236. 14

THOTTATHIL, S. D. et al. The Extent and Regulation of Summer Methane Oxidation in Northern Lakes. *Journal of Geophysical Research: Biogeosciences*, v. 123, n. 10, p. 3216–3230, 2018. ISSN 21698961. 15

TRANVIK, L. J. et al. Lakes and reservoirs as regulators of carbon cycling and climate. *Limnology and Oceanography*, v. 54, n. 6 PART 2, p. 2298–2314, 2009. ISSN 00243590. 14, 111

TUŠER, M. et al. Seasonal and Spatial Dynamics of Gas Ebullition in a Temperate Water-Storage Reservoir. *Water Resources Research*, v. 53, n. 10, p. 8266–8276, 2017. ISSN 19447973. 122

UZHANSKY, E. et al. Spatial and temporal variability of free gas content in shallow sediments: Lake Kinneret as a case study. *Geo-Marine Letters*, Geo-Marine Letters, v. 40, n. 4, p. 491–505, 2020. ISSN 14321157. 22, 30, 31, 55, 67, 68, 71, 81, 94

VACHON, D. et al. Influence of water column stratification and mixing patterns on the fate of methane produced in deep sediments of a small eutrophic lake. *Limnology and Oceanography*, p. 1–15, 2019. ISSN 0024-3590. 19, 32, 69, 97, 124

VACHON, D. et al. Methane emission offsets carbon dioxide uptake in a small productive lake. *Limnology and Oceanography Letters*, n. June, p. lol2.10161, jun 2020. ISSN 2378-2242. Disponível em: <https://onlinelibrary.wiley.com/doi/abs/10.1002/lol2.10161>. 13

VACHON, D.; PRAIRIE, Y. T.; COLE, J. J. The relationship between near-surface turbulence and gas transfer velocity in freshwater systems and its implications for floating chamber measurements of gas exchange. *Limnology and Oceanography*, v. 55, n. 4, p. 1723–1732, 2010. ISSN 00243590. 20

VALENTINE, D. L. et al. Carbon and hydrogen isotope fractionation by moderately thermophilic methanogens. *Geochimica et Cosmochimica Acta*, v. 68, n. 7, p. 1571–1590, 2004. ISSN 00167037. 15, 54

Van Kessel, T.; Van Kesteren, W. G. Gas production and transport in artificial sludge depots. *Waste Management*, v. 22, n. 1, p. 19–28, 2002. ISSN 0956053X. 67, 70, 79

VARADHARAJAN, C.; HEMOND, H. F. Time-series analysis of high-resolution ebullition fluxes from a stratified, freshwater lake. *Journal of Geophysical Research: Biogeosciences*, v. 117, n. G02004, p. n/a–n/a, jun 2012. ISSN 01480227. 54, 111, 112, 127

VARADHARAJAN, C.; HERMOSILLO, R.; HEMOND, H. F. A low-cost automated trap to measure bubbling gas fluxes. *Limnology and Oceanography: Methods*, v. 8, p. 363–375, 2010. ISSN 15415856. 20

VESALA, T. et al. Eddy covariance measurements of carbon exchange and latent and sensible heat fluxes over a boreal lake for a full open-water period. *Journal of Geophysical Research Atmospheres*, v. 111, n. 11, p. 1–12, 2006. ISSN 01480227. 20

VÖRÖSMARTY, C. J. et al. Anthropogenic sediment retention: Major global impact from registered river impoundments. *Global and Planetary Change*, v. 39, n. 1-2, p. 169–190, 2003. ISSN 09218181. 13

WALTER, K. M. et al. Methane production and bubble emissions from arctic lakes: Isotopic implications for source pathways and ages. *Journal of Geophysical Research: Biogeosciences*, v. 113, n. 3, 2008. ISSN 01480227. 95

WANG, B.; SOCOLOFSKY, S. A. A deep-sea, high-speed, stereoscopic imaging system for in situ measurement of natural seep bubble and droplet characteristics. *Deep-Sea Research Part I: Oceanographic Research Papers*, Elsevier, v. 104, p. 134–148, 2015. ISSN 09670637. Disponível em: <http://dx.doi.org/10.1016/j.dsr.2015.08.001>. 20

WANNINKHOF, R. Relationship between wind speed and gas exchange over the ocean revisited. *Limnology and Oceanography: Methods*, v. 12, n. JUN, p. 351–362, 2014. ISSN 15415856. 100

WELCH, E.; NACZK, F. *Ecological Effects of Waste Water*. 2nd. ed. CRC Press, 1992. ISBN 9781134991389. Disponível em: <https://www.taylorfrancis.com/books/9781134991389>. 85, 115

WEST, W. E.; COLOSO, J. J.; JONES, S. E. Effects of algal and terrestrial carbon on methane production rates and methanogen community structure in a temperate lake sediment. *Freshwater Biology*, v. 57, n. 5, p. 949–955, 2012. ISSN 00465070. 69, 71

WETZEL, R. G. *Limnology*. 2. ed. Orlando: Saunders College, 1983. 753 p. ISBN 0-03-057913-9. 15

WETZEL, R. G. *Limnology: Lake and River Ecosystems*. 3. ed. [S.l.]: Academic Press Inc, 2001. 1014 p. ISBN 978-0-12-744760-5. 82

WHEELER, S. J. The undrained shear strength of soils containing large gas bubbles. *Geotechniqueorechnique*, n. 3, p. 399–413, 1988. 96

WIK, M. et al. Multiyear measurements of ebullitive methane flux from three subarctic lakes. *Journal of Geophysical Research: Biogeosciences*, v. 118, n. 3, 2013. ISSN 21698961. 18, 33, 69, 124

WIK, M. et al. Energy input is primary controller of methane bubbling in subarctic lakes. *Geophysical Research Letters*, v. 41, n. 2, p. 555–560, jan 2014. ISSN 00948276. Disponível em: <http://doi.wiley.com/10.1002/2013GL058510>. 21, 22, 34, 36, 111, 120, 122, 123, 126, 135

WILKENS, R. H.; RICHARDSON, M. D. The influence of gas bubbles on sediment acoustic properties: in situ, laboratory, and theoretical results from Eckernförde Bay, Baltic sea. *Continental Shelf Research*, v. 18, n. 14-15, p. 1859–1892, 1998. ISSN 02784343. 55, 71

WILKINSON, J.; BODMER, P.; LORKE, A. Methane dynamics and thermal response in impoundments of the Rhine River, Germany. *Science of the Total Environment*, Elsevier B.V., v. 659, p. 1045–1057, 2019. ISSN 18791026. Disponível em: <https://doi.org/10.1016/j.scitotenv.2018.12.424>. 20, 58, 69, 84, 95, 96, 97, 101

WILKINSON, J. et al. Measuring CO2 and CH4 with a portable gas analyzer: Closed-loop operation, optimization and assessment. *PLoS ONE*, v. 13, n. 4, p. 1–16, 2018. ISSN 19326203. 57, 87, 99, 102

WILKINSON, J. et al. Correction: Measuring CO2 and CH4 with a portable gas analyzer: Closed-loop operation, optimization and assessment. *PLoS ONE*, v. 14, n. 3, p. 29617382, 2019. ISSN 19326203. 57

WILKINSON, J. et al. Continuous Seasonal River Ebullition Measurements Linked to Sediment Methane Formation. *Environmental Science and Technology*, v. 49, n. 22, p. 13121–13129, 2015. ISSN 15205851. 54, 58, 68, 69, 71, 84, 93, 94, 95, 102, 125

WOOD, S. N. Stable and efficient multiple smoothing parameter estimation for generalized additive models. *Journal of the American Statistical Association*, v. 99, n. 467, p. 673–686, 2004. ISSN 01621459. 129

WÜEST, A.; LORKE, A. Small-scale hydrodynamics in lakes. *Annual Review of Fluid Mechanics*, v. 35, n. 1, p. 373–412, 2003. ISSN 0066-4189. 19, 32

XAVIER, C. d. F.; DIAS, L. N.; BRUNKOW, R. F. *Qualidade das águas dos reservatórios do estado do Paraná*. Curitiba, 2017. 56

YVON-DUROCHER, G. et al. Methane fluxes show consistent temperature dependence across microbial to ecosystem scales. *Nature*, Nature Publishing Group, v. 507, n. 7493, p. 488–91, 2014. ISSN 1476-4687. 18, 35, 71

ZHAO, K.; TEDFORD, E. W.; LAWRENCE, G. A. Ebullition Regulated by Pressure Variations in a Boreal Pit Lake. *Frontiers in Earth Science*, v. 10, n. June, p. 1–7, 2022. ISSN 22966463. 21, 111, 112, 123, 126, 127, 137

ZHAO, K. et al. Impact of atmospheric pressure variations on methane ebullition and lake turbidity during ice-cover. *Limnology And Oceanography Letters*, v. 6, n. 5, p. 253–261, 2021. ISSN 23782242. 22, 127

ZHOU, Y. et al. Autochthonous dissolved organic matter potentially fuels methane ebullition from experimental lakes. *Water Research*, Elsevier Ltd, v. 166, p. 115048, 2019. ISSN 0043-1354. Disponível em: <https://doi.org/10.1016/j.watres.2019.115048>. 18

ZIMMERMANN, M. et al. Microbial methane oxidation efficiency and robustness during lake overturn. *Limnology and Oceanography Letters*, 2021. ISSN 2378-2242. 97

Appendix

APPENDIX A – Acoustic Mapping of Gas Stored in Sediments of Shallow Aquatic Systems Linked to Methane Production and Ebullition Patterns

Lediane Marcon, Klajdi Sotiri, Tobias Bleninger, Andreas Lorke, Michael Männich, and Stephan Hilgert

Abstract

Bubble-mediated transport is the predominant pathway of methane emissions from inland waters, which are a globally significant sources of the potent greenhouse gas to the atmosphere. High uncertainties exist in emission estimates due to high spatial and temporal variability. Acoustic methods have been applied for the spatial mapping of ebullition rates by quantification of rising gas bubbles in the water column. However, the high temporal variability of ebullition fluxes can influence estimates of mean emission rates if they are based on reduced surveys. On the other hand, echo sounding has been successfully applied to detect free gas stored in the sediment, which provide insights into the spatial variability of methane production and release. In this study, a subtropical, midsize, mesotrophic drinking water reservoir in Brazil was investigated to address the spatial and temporal variability of free gas stored in the sediment matrix. High spatial resolution maps of gas content in the sediment were estimated from echo-sounding surveys. The gas content was analyzed in relation to water depth, sediment deposition, and organic matter content (OMC) available from previous studies, to investigate its spatial variability. The analysis was further supported by measurements of potential methane production rates, porewater methane concentration, and ebullition flux. The largest gas content (above average) was found at locations with high sediment deposition, and its magnitude depended on the water depth. At shallow water depth (<10

m), high methane production rates support gas-rich sediment, and ebullition is observed to occur rather continuously. At larger water depth (>12 m), the gas stored in the sediment is released episodically during short events. An artificial neural network model was successfully trained to predict the gas content in the sediment as a function of water depth, OMC, and sediment thickness ($R^2 = 0.89$). Largest discrepancies were observed in the regions with steep slopes and for low areal gas content ($<4\,\mathrm{L\,m^{-2}}$). Although further improvements are proposed, we demonstrate the potential of echo-sounding for gas detection in the sediment, which combined with sediment and water body characteristics provides insights into the processes that regulate methane emissions from inland waters.

Introduction

Methane (CH_4) is a potent atmospheric greenhouse gas, whose concentration has increased nearly three-fold since pre-industrial times, primarily due to anthropogenic activity (IPCC, 2013; Saunois et al., 2020). Although CH_4 emissions represent only 3% of the anthropogenic carbon dioxide emissions in units of carbon mass flux, the increase in atmospheric CH_4 concentrations contribute $\sim$23% ($\sim 0.62\,\mathrm{W\,m^{-2}}$) to the additional radiative forcing during the last century (ETMINAN et al., 2016). Recent estimates suggest that emissions from inland waters contribute nearly half of the total current CH_4 emissions from natural and anthropogenic sources (ROSENTRETER et al., 2021). These emissions represent the largest uncertainty in current CH_4 budgets (SAUNOIS et al., 2020). Although freshwater CH_4 emissions are considered as natural sources, they are expected to increase in response to climate warming and to anthropogenic activities including cultural eutrophication and modifications of aquatic ecosystems (PEKEL et al., 2016; DELSONTRO; BEAULIEU; DOWNING, 2018; BEAULIEU; DELSONTRO; DOWNING, 2019; PEACOCK et al., 2021). Manmade reservoirs have been estimated to contribute 2–8% to freshwater CH_4 emissions (DEEMER et al., 2016).

The estimation of methane emissions from inland waters is sensitive to the upscaling method and on accounting for spatial variability and temporal dynamics occurring within and among different systems (SCHMIEDESKAMP et al., 2021). In lakes and reservoirs, methane is mainly produced in the bottom sediment by methanogenic archaea and bacteria during the process of anoxic organic matter degradation (VALENTINE et al., 2004; BASTVIKEN, 2009). The buildup of methane in the sediment matrix can lead to the formation of gas voids if the dissolved gas pressure exceeds the ambient hydrostatic pressure. Gas voids have complex shapes (BOUDREAU et al., 2005; LIU et al., 2018), growth dynamics, and mobility (SCANDELLA et al., 2011; KATSMAN; OSTROVSKY; MAKOVSKY, 2013).

In shallow waters, bubble mediated transport is the most efficient way of transferring methane to the atmosphere, bypassing methane oxidation in the oxic water column (MCGINNIS et al., 2006). Its temporal variability is a result of changes in local net methane production and accumulation in the sediment, and the episodic occurrence of triggers for bubble release (VARADHARAJAN; HEMOND, 2012; MAECK; HOFMANN; LORKE, 2014; JANSEN et al., 2020). Whereas, spatial variability of ebullition in lakes and reservoirs results from variations of methane production rates in the sediment, which depend on sediment temperature (WILKINSON et al., 2015), sediment thickness (MAECK et al., 2013) and organic matter content (GRASSET et al., 2018). Shallow areas with high deposition rates of organic matter, such as river inflow regions, have been identified as ebullition hot spots (BEAULIEU; MCMANUS; NIETCH, 2016; LINKHORST et al., 2021).

Only few existing studies related ebullition rates to measured distributions of gas voids in the sediment of inland waters. First, because of the lack of a robust and accurate method for assessing the distribution of gas voids in the sediment. Second, there are still uncertainties around methods based on the extraction of sediment cores (DÜCK et al., 2019b) and the large temporal variability of ebullition adds additional uncertainties to the flux estimation. Uzhansky et al. (2020) applied an inverse geoacoustic technique to derive the sound speed in the sediment for estimating sediment gas content. Katsnelson et al. (2017) applied a similar inverse geoacoustic technique for the estimation of gas content in the sediment and to investigate its spatial variability in lake Kinneret, Liu et al. (2019) correlated CH4 pore water concentrations to acoustically derived parameters for that lake.

Nevertheless, acoustic remote sensing has been widely used in aquatic systems for obtaining information on sediment properties, such as wet bulk density and organic matter content (SOTIRI; HILGERT; FUCHS, 2019), grain size distribution (TEGOWSKI, 2005), sound velocity in gassy sediments (LUNKOV; KATSNELSON, 2020), and total organic carbon (NETO et al., 2016). Echo sounders have also been used to quantify the ebullition flux through the detection of rising bubbles in the water column (OSTROVSKY; TEGOWSKI, 2010). Wilkens and Richardson (1998) pointed out that the acoustic propagation of soundwaves in gassy sediment depends on how sediment particles and gas voids are distributed and suggested the application of acoustic methods for obtaining bubble size distribution in the sediment. Katsnelson et al. (2017) found that the distribution of gas content in the sediment derived from an inverse geoacoustic technique agreed with sediment organic content and methane ebullition. In another study, Anderson and Martinez (2015) proposed the maximum backscatter strength at a frequency of 201 kHz to obtain gas volume distribution in the sediment per unit area, which was applied to two lakes and a reservoir in the United States.

In this study, we aim to analyze the spatial and temporal variability of gas content in the sediment of a freshwater reservoir and to investigate its relation to sediment properties and methane ebullition. Acoustic parameters derived from echo-sounding surveys are used to obtain estimates of sediment-gas-contents with the method proposed by Anderson and Martinez (2015). We then combine the estimated gas content distribution with available data on sediment properties, potential of methane production, and continuous ebullition measurements to 1) map and analyze the spatial distribution of gas content in the sediment; 2) to test different models for the prediction of gas content in the sediment from bulk properties; and 3) to investigate temporal variations of gas content in the sediment.

Material and methods

In our analysis, we combine the results from intensive field measurements and monitoring campaigns that were conducted at Passaúna Reservoir between 2016 and 2019 and have partially been analyzed in former studies, but with different objectives. Reanalysis of echo-sounding surveys from Sotiri, Hilgert and Fuchs (2019) and Sotiri et al. (2021) are used to derive maps of gas content in the sediment. These results are related to new data on methane porewater concentration and ebullition flux, and to existing data on sediment thickness distribution estimated by Sotiri et al. (2021), loss on ignition (LOI 550 °C) mapping from Sotiri (2020), and potential methane production rates reported by Hilgert et al. (2019).

Study site

Passaúna Reservoir is located at the Passaúna River in the southern part of Brazil, near to the city of Curitiba (25.53°S and 49.39°W, Figure 8). The reservoir was constructed in 1989 for drinking water

supply. Passaúna is a polymictic and mesotrophic reservoir (XAVIER; DIAS; BRUNKOW, 2017), with an average depth of 8.3 m. It is elongated in the North-South direction with approximately 10 km length and 0.6 km width. Its main inflow is the Passaúna river with an average annual discharge of $2\,m^3\,s^{-1}$ (CARNEIRO; KELDERMAN; IRVINE, 2016).
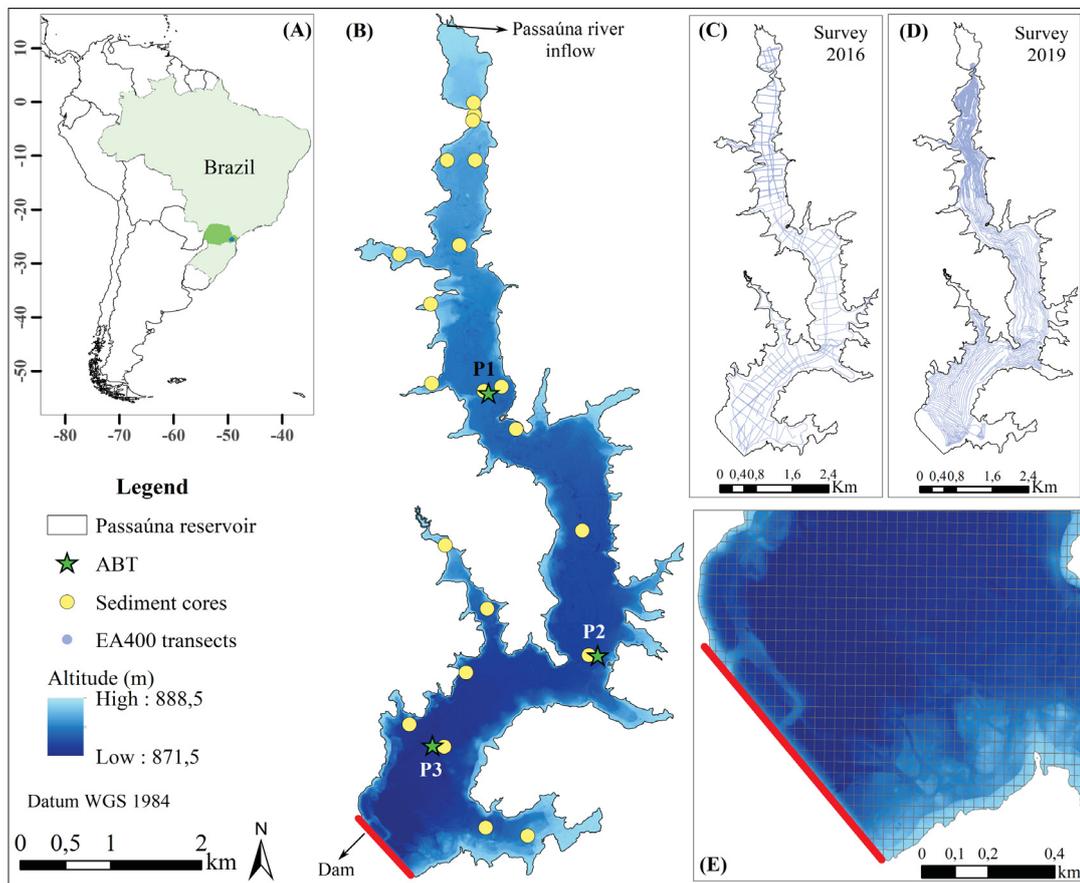
Figure 8 – **(A)** Location of the study site Passaúna Reservoir in South America; **(B)** Bathymetric map of Passaúna Reservoir and measurement locations (see legend); **(C)** echo-sounding transects during the survey in 2016; **(D)** echo-sounding transects during the 2019 survey; **(E)** Zoom to the dam area with overlaid analysis grid.

According to the updated Köppen climate classification, the region is characterized by temperate oceanic climate (Cfb), with monthly mean temperatures below 22 °C for all months and no significant precipitation difference between seasons (BECK et al., 2018). The mean annual precipitation in the region ranges between 1,400 and 1,600 mm. During measurements covering a full annual cycle conducted in 2018–2019, the reservoir water temperature ranged from 16 to 28 °C, with August being the coldest month with an averaged bottom temperature of 16.5 °C (ISHIKAWA; BLENINGER; LORKE, 2021). Meteorological data for this study was provided by the company SANEPAR which manages the reservoir. Weather data is logged at a station installed near to the dam.

Ebullition flux and pore water methane concentration measurements

Ebullition flux and pore water methane concentration were measured at three sampling sites distributed along the reservoir (Figure 8B). The site P1 is located most closely to the main river inflow (Passaúna River) at a water depth of 8 m. The site P2 was placed in the central region of the reservoir,

near to the water intake facility, where the water depth is 12.5 m. Site P3, was placed in the deepest region of the reservoir, approximately 810 m upstream of the dam, at a water depth of 14 m.

The ebullition measurements analyzed in the present study are a continuation of the measurements that started in 2017 and were described by Marcon et al. (2019). The ebullition flux was monitored continuously by automated bubble traps (ABT, Senect GmbH, Germany) from January to March 2019. The ABT were attached to a surface buoy and deployed at a depth of approximately 4–5 m above the sediment surface. The device consists of a 1 m diameter funnel, which collects rising gas bubbles, and a differential pressure sensor to monitor the gas volume that accumulated during fixed time intervals (30 s). The device also measured water temperature and pressure, which were used to convert the collected gas volume to standard pressure and temperature (1013.25 mbar and 20 °C). In addition, bubbles were collected from the sediment near to the ABT's location to estimate the methane fraction within the bubbles. The captured gas was transferred to vials with saturated salt solution until its analysis in the laboratory with an Ultraportable Greenhouse Gas Analyzer (UGGA, Los Gatos Research Inc.).

Dissolved methane concentration in the sediment pore water was measured with a dialysis pore water sampler (DPS) as described by Hilgert (2014) and Hölzlwimmer (2013). The DPS is a perforated aluminum frame of 70 cm height divided into 15 chambers of 4 cm width each. A cellulose membrane bag of 50 ml filled with ultra-pure water was added to each chamber. On 02 February 2019 three DPS's were deployed by divers in the bottom sediment at each ABT location (P1, P2, and P3) and positioned vertically such that seven chambers were inside the sediment and eight chambers in the overlaying water column. The devices were deployed for 5 days, to allow the ultra-pure water of the bags to equilibrate with the ambient water or pore water. Directly after recovery, a sample of 5 ml was extracted from each bag with a plastic syringe, a headspace of 5 ml was created in the syringe and after rigorous shaking, the headspace gas was transferred to vials containing saturated salt solution, previously sealed with a rubber stopper and crimp-capped. The vials were stored upside-down until analysis in the laboratory, where the methane concentration was measured with an Ultraportable Greenhouse Gas Analyzer (UGGA, Los Gatos Research Inc.) in a closed loop arrangement, as described by Wilkinson et al. (2018); Wilkinson et al. (2019). The corresponding methane concentration in the water sample (C_{CH4} in mol L^{-1}) was calculated as proposed by Bossard, Joller and Szabo (1981) as:

$$\text{CH}_4 = \left(\frac{V_{Hs}}{V_W} \frac{(X_{eq} - X_{back})}{RT} + X_{eq}K_H \right) \times P_{atm},$$

where V_{Hs} is the headspace volume in L, V_W is the water sample volume in L, X_{eq} and X_{back} are the methane mole fractions measured with the gas analyzer after equilibration and in the initial headspace in ppm respectively. K_H is the temperature dependent Henry gas solubility coefficient, which was calculated according to Goldenfum (2010) in mol L^{-1} atm^{-1}, T is temperature in K, R is the gas constant ($R = 0.082\,05$ L atm mol^{-1} K^{-1}), and P_{atm} is the atmospheric pressure in atm.

Data re-analyses

The following sections describe the re-analysis and additional processing of data from acoustic surveys conducted in Passaúna Reservoir during former studies.

Potential methane production

The potential methane production (PMP) in sediment samples collected at the ABT deployment locations (P1, P2, and P3, Figure 8) was analyzed in Hilgert et al. (2019). The potential production

rates were obtained for samples from different sediment layers, that were anaerobically incubated under laboratory conditions as described by Wilkinson et al. (2015). The potential methane production was calculated for in-situ sediment temperature by the relationship proposed by Wilkinson, Bodmer and Lorke (2019)

$$\mathrm{PMP_T = PMP_{20}10^{\theta(T-20)}},$$

where PMP_T (in $\mathrm{mgCH_4\ L^{-1}\ d^{-1}}$) is the potential methane production rate at in-situ temperature T (in °C), and PMP_{20} is the rate measured during laboratorial incubations at 20 °C. We used a value of the temperature coefficient θ of 0.045, as suggested by Wilkinson, Bodmer and Lorke (2019) for incubated freshwater sediments.

The PMP was integrated over the top 10 cm sediment layer by multiplication of the averaged PMP_T with layer thickness to provide a potential areal flux (in $\mathrm{mgCH_4\ m^{-2}\ d^{-1}}$) at the sediment water interface (WILKINSON; BODMER; LORKE, 2019).

Acoustic parameters and mapping of gas content in the sediment

The analysis of gas content in the sediment conducted in the present study is based on echo-sounding surveys with a dual frequency (38 and 200 kHz) echo-sounder EA400 (Kongsberg Inc. 2006). The surveys have been analyzed for different aspects before (SOTIRI; HILGERT; FUCHS, 2019; SOTIRI, 2020; SOTIRI et al., 2021). For the measurements, the echo-sounder was fixed 0.45 m below the water surface to an aluminum vessel, and zigzag transects weremeasured along and across the reservoir (Figure 8 panels (C) and (D)). The surveys were conducted from 26 February to 07 March 2016, and from 04 February to 07 February 2019 and covered approximate distances of 75 km in 2016 and 219 km in 2019. The echo-sounder was operated with an output power of 100 W, and pulse lengths of 0.512 and 0.128 ms for the 38 and 200 kHz channels, respectively, resulting in vertical resolutions of 0.096 and 0.024 m for the two frequencies. For an average water depth of 8.3 m, the footprint area of the acoustic beams were $5.0\,\mathrm{m^2}$ (38 kHz with opening angles of 13°for the longitudinal and 21°for the transversal direction) and $0.8\,\mathrm{m^2}$ (200 kHz with longitudinal and transversal opening angle of 7°). The measurement positions during the surveys were recorded using a Leica 1200 DGPS (Differential Global Positioning System) system. Vertical temperature profiles for sound speed correction were measured with a CTD-Conductivity-Temperature-Depth (CastAway-CTD) probe.

For this study, the conversion and processing of the acoustic data was done using the Sonar5-Pro software (Lindem Data Acquisition, Oslo, Norway). Two main acoustic parameters of the first bottom echo from the 200 kHz measurements exported from the software were considered: attack and maximum backscatter strength. The values are defined for each ping (sound pulse). The envelope of the backscatter profile across the sediment-water interface is generally characterized by an increase of the backscatter strength at the sediment surface, reaching a peak amplitude (maximum backscatter), and followed by a decay with increasing depth (STERNLICHT; MOUSTIER, 2003) (see Supplementary Figure 14). Attack is defined as the vertically integrated backscatter strength values occurring over a duration of one pulse length from the bottom detection point (HILGERT et al., 2016) and was used to estimate the organic content in the sediment (see below). The maximum backscatter (named as bottom peak in Sonar5-Pro), is the maximum value (dB) of the backscatter that occurred starting from the detected bottom downward and searched by the software until three transmitted pulse lengths (BALK; LINDEM; CARNERO, 2011).

Anderson and Martinez (2015) analyzed the acoustic parameters from three productive lakes in Southern California (United States). The authors established a relationship between maximum backscat-

ter (measurements at 201 kHz frequency) and gas volume in the sediment (corrected to the local hydrostatic pressure) per unit area:

$$\mathrm{gc} = \mathrm{e}^{0.327 \times S_{ymax} + 3.48},$$

where gc is gas content per unit area in $\mathrm{L m^{-2}}$ and S_{ymax} is the maximum backscatter strength in dB. The maximum backscatter was found to explain 93% of the variance in estimated gas content ($R^2 = 0.93$) (ANDERSON; MARTINEZ, 2015). We adopted the proposed equation to estimate the gas content per unit area, hereinafter also referred to as gas content, in the sediment of Passaúna Reservoir, which is justified by the similar conditions in respect to water depths, trophic state, bottom sediments, and acoustic measurements in comparison to the study of Anderson and Martinez (2015) (Table 1). Although the pulse lengths differed between the studies, the maximum backscatter values are expected to be unaffected, and thus the application of Anderson and Martinez (2015) relationship is expected to be a valid estimate for addressing the spatial variability of sediment gas content in Passaúna Reservoir during both echo-sounding surveys (2016 and 2019). The gas content estimated for the higher-resolution survey conducted in 2019 was then analyzed in relation to organic matter content in the sediment (LOI at 550 °C), sediment magnitude distribution, and bathymetry.

Table 3 – Summary of the study site characteristics and echo-sounder details of the study by Anderson and Martinez (2015) for which an empirical relationship between maximum backscatter strength and sediment gas content was established, and the corresponding information for Passaúna Reservoir.

| Name | Anderson and Martinez (2015) | | | This study |
	Elsinore	Hodges	Skinner	Passaúna
Type	lake	reservoir	lake	reservoir
Mean depth (m)	7.5	7.5	11.2	8.3
Maximum depth (m)	11	35	24	17
Trophic state	eutrophic	eutrophic	*	mesotrophic
Echo-sounder	BioSonics DTX-200			Kongsberg EA 400
Frequency (kHz)	201			200
Pulse length (ms)	0.4			0.13

* Trophic state of lake Skinner was not reported by the authors, nevertheless, the lake is described to have better water quality as Elsinore and Hodges, as it is used for water supply purposes.

Organic matter, sediment thickness, and bathymetry

Information on the reservoir bathymetry, organic matter content in sediments, and sediment thickness distribution were taken from Sotiri et al. (2021). The reservoir bathymetry was measured with a multibeam echo sounder (WASSP F3Xi) measuring with a frequency of 160 kHz. The bathymetric map was then used in this study to derive the bottom slope.

Sediment distribution and magnitude in the reservoir was measured by Sotiri et al. (2021) with a dynamic free-fall penetrometer. The mapping of the organic matter content was derived from a former study conducted by Sotiri (2020) at Passaúna Reservoir, which was based on measurements of loss on ignition at 550 °C (LOI 550 °C) for more than 20 sediment cores with echo-sounding measurements at each core location. The empirical relationship proposed by Sotiri (2020) had a R^2 of 0.66, in which LOI is calculated from a polynomial equation as a function of the acoustic parameter Attack (Att),

$$\text{LOI550}^\circ\text{C} = -44.6 + (-10.4\text{Att}) + (-0.6\text{Att}^2) + (-0.01\text{Att}^3),$$

where Att is derived from the echo-sounder EA400 measurements at 200 kHz frequency.

The LOI is widely applied as a proxy for quantifying organic matter content in the sediment, nevertheless for clay rich sediments LOI is reported to overestimate the organic matter content, as during the burning at 550 °C the loss of clay structural water and breakdown of carbonates have a share on the weight loss in addition to the organic matter (FRANGIPANE et al., 2008). Therefore, although LOI is adopted as a proxy for organic matter distribution, its absolute values might differ from organic matter measured by other methods. However, for sediment samples from two reservoirs in a neighboring watershed, (HILGERT, 2014) found strong significant correlation (Pearson correlation 0.76) between LOI and organic carbon, which showed the potential to consider LOI for representing organic matter distribution as the organic carbon was not directly measured at Passaúna reservoir.

Statistical models for predicting the sediment gas content

We developed statistical and data driven models to predict the spatial distribution of the estimated sediment gas content from maps of water depth, sediment thickness, and organic matter content (LOI 550 °C) as predictor variables. The input variables and the prediction of gas content were analyzed within a spatial grid created for the reservoir based on the acoustic survey conducted in 2019. The analysis grid was created using the Geographical Information System (GIS) software ArcGIS (v. 10.2.2) with the geoprocessing tool Fishnet, in which we divided the surface area of Passaúna reservoir in 8454 rectangular grid cells with dimensions of 33 m by 33 m (Figure 8E). Additional information about the grid selection is provided in the supplementary material (Supplementary Figure 15). The size of the grid cells was chosen to be sufficiently small to resolve the spatial heterogeneities of the measured parameters occurring in the sediment (longitudinal and transversal variations), and large enough to analyze all parameters in terms of spatial averages, that integrate small-scale (unresolved) structures. Mean values of all parameters (water depth, bottom slope, sediment thickness, organic content through LOI 550 °C, and gas content) were calculated for all grid cells for which survey data are available.

To reduce the uncertainty of parameters derived from acoustic measurements, we excluded grid cells with an average bottom slope larger than 10° from all subsequent analysis. This is justified by the fact that the acoustic backscatter strength of sediment surfaces and sediment layers depends on the grazing angle of the soundwave (angle between incident wave and the tangent to the surface). For incidence angles of the soundwave near to the normal direction in relation to the sediment surface, scattering (attack values) dominate the backscattering, in contrast for inclined conditions (i.e., grazing angles in the range 30-60°) the volume scattering dominates (FONSECA et al., 2002). Sternlicht and Moustier (2003) showed that the effect of slopes is lengthening the echo, resulting in prolongated rising and decaying parts of the echograms, leading to a reduction of the maximum backscatter independent from the sediment composition.

Steep slopes in Passaúna Reservoir occurred mainly near the banks or along the old Thalweg of the Passaúna River as described by Sotiri et al. (2021). The slope threshold resulted in removal of 1034 grid cells, thus 4651 grid cells were classified as valid cells (with data of all parameters measured and in agreement with the slope criterion).

The potential CH_4 production (PMP), dissolved CH_4 concentration in pore water, and ebullition were not extrapolated to the entire reservoir, as they were measured at only three locations. Nevertheless,

the measurements are used to support our discussion on the spatial distribution and dynamics of the estimated sediment gas content.

Three multiple linear regression models were tested for gas content prediction in which the water depth, sediment thickness, and LOI 550 °C were the predictors. The first model (MLR I) was a simple multiple linear regression, for the second model (MLR II) the predicted value (gas content) was log transformed, and for the third statistical model a stepwise multiple regression (SMR) with untransformed values was performed. The main difference of the stepwise multiple regression to the two other models is that predictors are included sequentially in the model and accepted if a *p-value* criterion is met for a significance level of 5%. Furthermore, interactions of the input variables are tested in this model as predictors.

The data driven model is a supervised artificial neural network (ANN). The ANN architecture had three layers, one input layer with three neurons, one hidden layer with 10 neurons, and one output layer with one neuron (Figure 9). The input variables were water depth, sediment thickness, and LOI 550 °C. For improving the performance of the ANN, the input variables were normalized to range from 0 to 1. The Hidden layer is a processing layer where the transfer function was a hyperbolic tangent sigmoid function, in which the values transferred to the output layer will vary between -1 to 1. The output layer is the gas content per unit area in L m^{-2}.
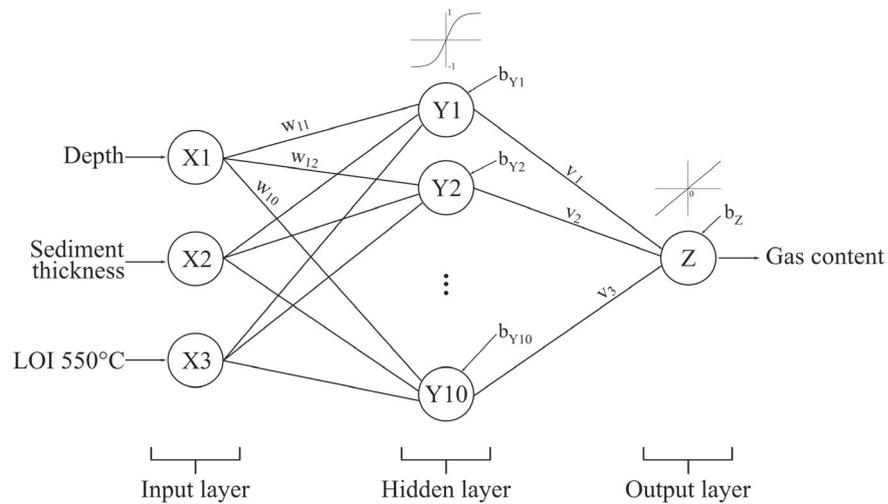
Figure 9 – Architecture of the artificial neural network implemented in this study for the prediction of gas content in sediment. X1, X2, and X3 are the neurons in the input layer, Y1 to Y10 are the neurons in the hidden, Z is the neuron at the output layer. w denotes the weight of each neuron connection from the input to the hidden layer, v are the weights of hidden layer connections to the output layer, and b are the bias for each neuron in the hidden and output layers.

We used the Levenberg—Marquardt backpropagation for training of the ANN. During the training step, the algorithm randomly divided the data into three parts. 70% of the data points are used for the actual training of the neural network, 15% are used for the validation of the ANN during the training calculations to avoid overfitting, and the remaining 15% are not included for the training and are used for testing the trained model.

The model's result for gas content prediction were evaluated considering the coefficient of determination (R^2) between observed and predicted gas content and through the relative error. The relative error, which was expressed in percentage, was calculated for each grid cell as

$$\text{Error}_{\text{relative}} = \left(\frac{|\ y_{predicted} - y_{observed}\ |}{y_{observed}} \right) \times 100,$$

where $y_{predicted}$ and $y_{observed}$ are the predicted and estimated gas content, respectively.

Lastly, the gas content in the sediment derived from the hydro-acoustic surveys performed in 2016 and in 2019 was compared to analyze the temporal changes in different regions of the reservoir and to check the application of the prediction model from 2019 against the measurements of 2016. The temporal change in gas content between 2016 and 2019 was tested for each valid grid cell using a non-parametric hypothesis test (Wilcoxon rank sum test), considering only cells that contained 30 or more pings (sound pulses), which resulted in 1321 cells for the comparison.

Results

PMP, porewater CH$_4$, and ebullition gas flux

The highest values of potential methane production for all three sampling locations were found in the top 10 cm sediment layer. The maximum PMP values ranged from $3.4 \, \text{mgCH}_4 \, \text{L}^{-1} \, \text{d}^{-1}$ at P3 to $5.9 \, \text{mgCH}_4 \, \text{L}^{-1} \, \text{d}^{-1}$ at P2. From the near-surface layer, PMP decayed approximately exponentially with increasing depth in the sediment (Figure 10A). The integrated temperature corrected PMP for the top 10 cm resulted in a potential methane flux at the water-sediment interface of 306.4, 450.2, and $91.1 \, \text{mgCH}_4 \, \text{m}^{-2} \, \text{d}^{-1}$ at locations P1, P2, and P3 respectively.
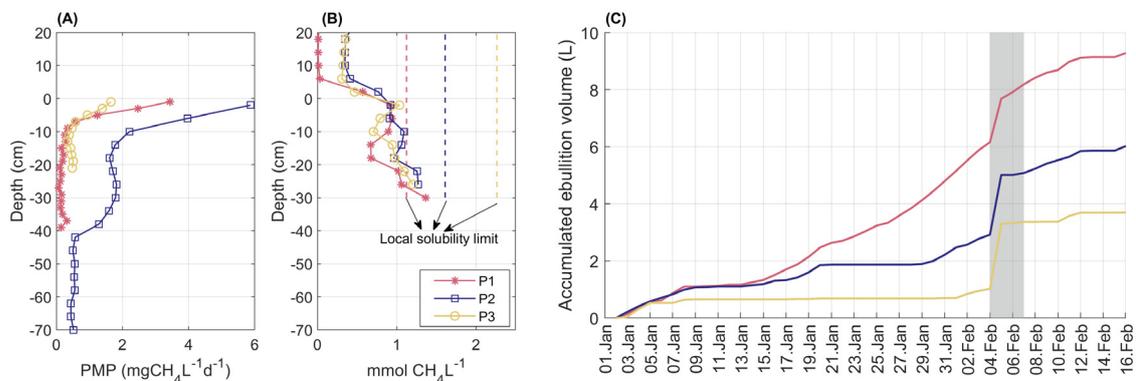
Figure 10 – **(A)** Depth profiles of potential methane production (PMP) in the sediment [data from Hilgert et al. (2019)]. **(B)** dissolved methane concentration in the pore water and overlaying water at the sediment-water interface measured in 2019. The origin of the depth-axis is at the water-sediment interface. The dashed lines show the respective CH$_4$ solubility limit for each location, calculated as a function of temperature, salinity, and hydrostatic pressure according to Dale et al. (2008). **(C)** Time series of accumulated gas volume recorded by the automated bubble traps (ABTs) from 1 January to 15 February 2019. The grey shaded area marks the days when the echo-sounding survey was conducted in 2019. All three panels show measurements at the three sampling locations in Passaúna Reservoir (P1, P2 and P3, see Figure 8.

Dissolved methane concentration was lowest in the overlaying water with a strong increase in concentration towards the water-sediment interface (Figure 10B). In the sediment, the dissolved methane concentration continued to increase with increasing depth with comparable vertical gradients at all three locations. The maximum porewater methane concentrations were measured in the deepest DPS chamber at 25-30 cm sediment depth ($1.4 \, \text{mmol} \, \text{L}^{-1}$ at location P1, $1.3 \, \text{mmol} \, \text{L}^{-1}$ at P2, and $1.2 \, \text{mmol} \, \text{L}^{-1}$ at P3).

Gas ebullition flux was continuously measured during 45 days, starting prior to the acoustic survey conducted in 2019. The largest amount of gas was collected by the bubble trap at location P1 (9.3 L), followed by locations P2 (6.0 L), and P3 (3.7 L) (Figure 10C). For the 45 measurement days, the recorded volume represents a methane ebullition flux of 118.1, 77.5, and 48.1 $mgCH_4\,m^{-2}\,d^{-1}$ at the locations P1, P2, and P3 respectively (with CH4 fraction in bubbles collected from the three locations of 68.9±6.8%).

At locations P2 and P3 (near to the water intake and in the dam region) the dynamics of gas accumulation is characterized by stepwise increases, in which periods of several days without ebullition are interrupted by ebullition events. At P1 in contrast, more continuous ebullition events occurred throughout the measurement period, as it can be observed by the prolonged rise of the accumulated gas volume curve (Figure10C). At all locations, pronounced ebullition was observed on February 5th during the period when the echo-sounding surveys were conducted. This ebullition event was associated with a weather change; from February 04th to February 07th, there was a reduction of the air temperature by approximately $10\,°C$ in comparison to the previous days (Supplementary Figure 16). Atmospheric pressure strongly decreased starting from February 05th. During the surveys, the water level in the reservoir decreased by 2 cm (from February 05th to February 07th) and the mean wind velocity was $1.6±0.4\,m\,s^{-1}$ (average±standard deviation).

Acoustic mapping of the reservoir sediment

According to Sotiri et al. (2021), the reservoir bottom is overlaid by an unconsolidated fine-grained low-density material layer. The analysis of the sediment cores showed that the bottom sediment is dominated by silt-clay grain sizes and an average loss on ignition (LOI) of 17±8.5%. The averaged LOI in the sediment estimated from the acoustic parameter attack (Figure 11C) was 14.7±4.9% for the whole reservoir, in which 3.9% of the valid grid cells had LOI of less than 10% and a minimum value of 1.8%.

The sediment magnitude estimated by Sotiri et al. (2021) varied from 0 to a maximum of 1.8 m, with highest sediment accumulation in the upstream region near to the river inflow and in the region near to the dam (see Figure 11B), where the water depth varies from 10 to 15 m. Average sediment thickness in the analysis grid ranged from 0 to 1.5 m, with a mean value of 0.5±0.2 m.

The overall mean value of the maximumacoustic backscatter in the analyzed grid cells was $-6.6±2.0\,dB$. According to the empirical relationship proposed by Anderson and Martinez (2015), this corresponds to a mean sediment gas content for the whole reservoir of $4.6±3.2\,L\,m^{-2}$. The largest values of sediment gas content were estimated for the upstream region of the reservoir, whilst the smallest values were found near the banks and in the deepest region of the reservoir in front of the dam (Figure 11D). Elevated (above average) gas content was also estimated for the central part of the deeper region near the dam. At the locations where the automated bubble traps were deployed, the averaged gas content in the sediment was $6.2±2.1\,L\,m^{-2}$, $4.1±1.6\,L\,m^{-2}$, and $5.6±2.0\,L\,m^{-2}$, for the P1 to P3 respectively (Table 4).

Models for the prediction of gas content in the sediment

The variables water depth, which ranged from 1.4-15.35 m (8.9±3.3 m), sediment thickness with values in the range of 0.03–1.5 m (0.5±0.2 m), and LOI 550 °C varying from 1.8–53.5% (14.7±4.9%) were tested as predictor variables for the gas content in the sediment, which varied from 0.1 to $40.4\,L\,m^{-2}$ ($4.6±3.2\,L\,m^{-2}$). In an exploratory analysis of the variables, a Spearman rank correlation test was applied to check statistical correlation among the parameters (see Supplementary Figure 17). Considering the
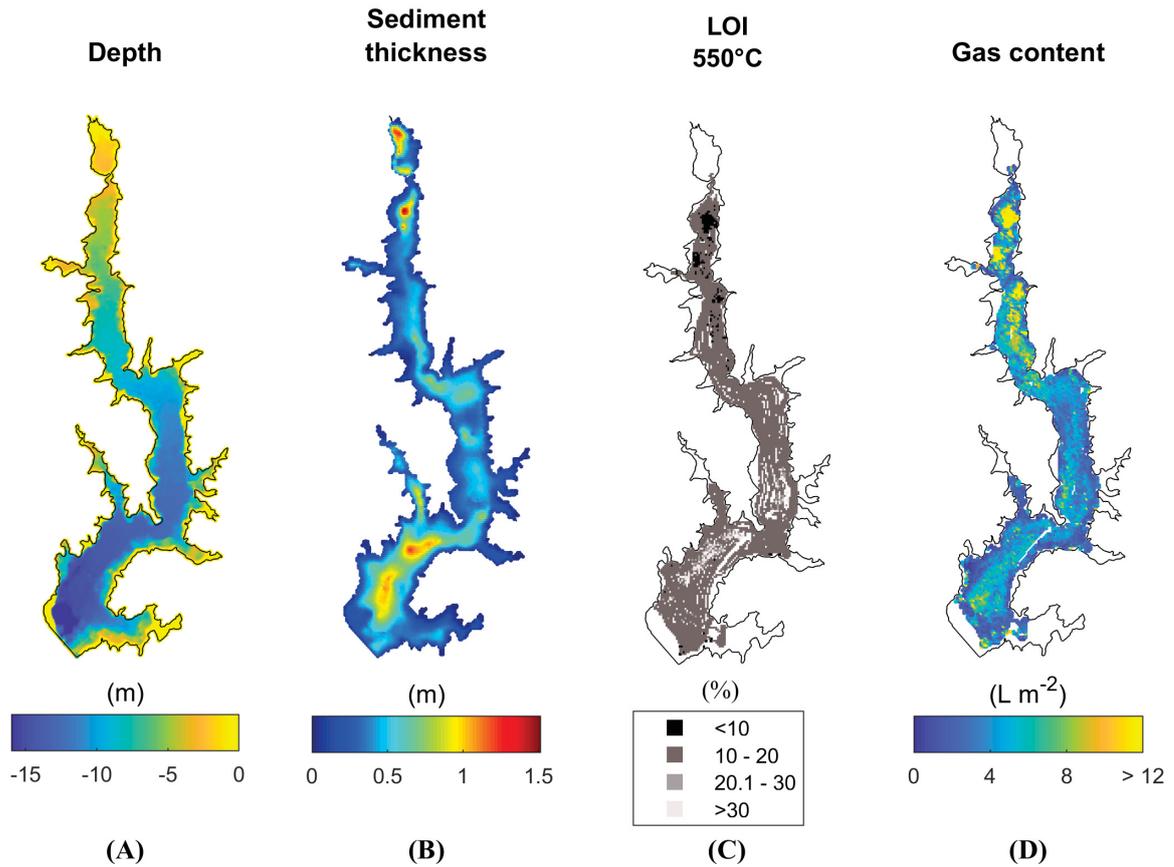
Figure 11 – **(A)** Passaúna Reservoir water depth and **(B)** sediment thickness distribution from Sotiri et al. (2021). **(C)** LOI 550 °C extrapolated to the entire reservoir as a function of the acoustic parameter Attack with the relation proposed by Sotiri (2020). **(D)** Distribution of estimated gas content in the sediment estimated from the equation proposed by Anderson and Martinez (2015). All data are averaged for individual cells of the analysis grid. Blank areas in **(C)** and **(D)** indicate missing data and grid cells with high bottom slope (>10°).

individual correlations between gas content and the predictor variables, the strongest correlation was found between gas content and LOI (Spearman correlation rs $= -0.58$ and $p = 0$), whereas weaker, yet significant, correlations were found between gas content and water depth (rs $= -0.12$, $p <0.05$) and gas content and sediment thickness (rs $= -0.18$ $p < 0.05$).

Multiple linear regression (model MLR I) resulted in a coefficient of determination (R^2) of estimated gas content of 0.24 ($p < 0.05$ for the F-test on the model). As the distribution of gas content in the sediment deviates from a normal distribution (Supplementary Figure 17), a multiple linear regression with log transformed gas content (MLR II) was tested, resulting in a R^2 of 0.16 ($p < 0.05$ for the F-test on the model). The stepwise multiple regression (SMR) resulted in a R2 of 0.54 ($p = 0$ for the F-test on the model). The full model equations are presented in Table 5. The trained artificial neural network (ANN) reproduced 89% of the gas content variance ($R^2 = 0.89$ for all data points). Comparable coefficients of determination were obtained for the test data set which was not included during the training of the ANN ($R^2 = 0.91$, Supplementary Figure 18).

The largest relative errors (>80%) for all models occurred near the banks at deepest region near to the dam (Figure 12 panels (B), (C), and (D)). The averaged relative error for the 4651 grid cells was 42.5, 61.2, and 72.96% for the ANN, SMR, and MLR I model, respectively. In addition, the linear regressions applied to the predicted and estimated gas content indicate a systematic underestimation

Table 4 – Parameters at the three monitoring sites P1, P2, and P3. Loss on ignition (LOI) from sediment cores were provided by Sotiri (2020); the PMP was integrated for the top 10 cm sediment layer; methane ebullition was calculated with the measured methane fraction in the gas bubbles of 68.9%; and the estimated gas content in the sediment was acoustically derived and averaged for the areas surrounding the location of each bubble trap deployment.

Site	Water depth (m)	LOI 550 °C (%)	PMP integrated (mgCH$_4$ m^{-2} d^{-1})	Methane ebullition	Ebullition total volume (L)	Estimated gas content in sediment (L m^{-2})
P1	8	15	306.4	118.1	9.3	6.2
P2	12.5	22	450.2	77.5	6	4.1
P3	14	16	91.1	48.1	3.7	5.6

Table 5 – Summary of the three statistical models (MLR I, MLR II, and SMR) and the data driven model (ANN) tested for the prediction of sediment gas content (y) from the variables X1 = water depth, X2 = sediment thickness, and X3 = LOI at 550 °C. For the trained ANN y_{in_k} denotes the input value for neuron Y_k, b_{Y_k} is the bias of neuron Y_k of the hidden layer, and x_i is the value of the predictor i. y_{out_k} is the value calculated by the transfer function and b_z is the bias of the output neuron. w_{ij}, and v_i are the weights of the neurons connecting the input to the hidden layer and the hidden layer to the output neuron, respectively.

Model	Prediction model for gas content	R^2	Relative error (%)
Multiple linear regression I (MLR I)	y=7.35+(−0.30×X1)+(5.41×X2)+(−0.19×X3)	0.24	73
Multiple linear regression II (MLR II)	ln(y)=1.63+(−0.05×X1)+(1.06×X2)+(−0.03×X3)	0.16	58.7
Stepwise multiple regression (SMR)	y= 27.604+(−2.39×X1)+(6.51×X2)+(−1.60×X3)+ (0.26×X1×X2)+(0.15×X1×X3)+(−0.43×X2×X3)	0.54	61.2
Artificial Neural Network (ANN)	i. $y_{in_k} = b_{Y_k} + \sum_j x_i w_{ij}$ ii. $y_{out_k} = \frac{2}{(1+e^{-2xy_{in_k}})-1}$ iii. $Z_{in} = b_Z + \sum_i y_{out_i} v_i$ iv. $y = Z_{in}$	0.89	42.5

of all three models compared to observations (Figure 12A). The frequency distributions of the relative error showed that for all models the most frequent relative errors obtained were smaller than 25% (see Supplementary Figure 19 panels (A) and (B)). On the other hand, the largest relative errors values (above 500%) occurred for the grid cells with gas content per unit area of less than 4 L m^{-2}.

Temporal variability of gas distribution in the sediment

The gas content in the sediment was also calculated with the hydro acoustic data recorded during the 2016 survey. In both surveys (March 2016 and February 2019), the water column was thermally stratified, with a warmer top layer of ∼26 °C and colder bottom water with the lowest temperature of ∼21 °C at location P3 (Supplementary Figure 20 panels (A) to (C)). Small variations of the reservoir water level were recorded during the hydro acoustic surveys of both years (3 cm in 2016 and 2 cm in 2019). However, for the 2016 survey the water level was ∼1 m higher than the water level recorded during the survey of 2019.
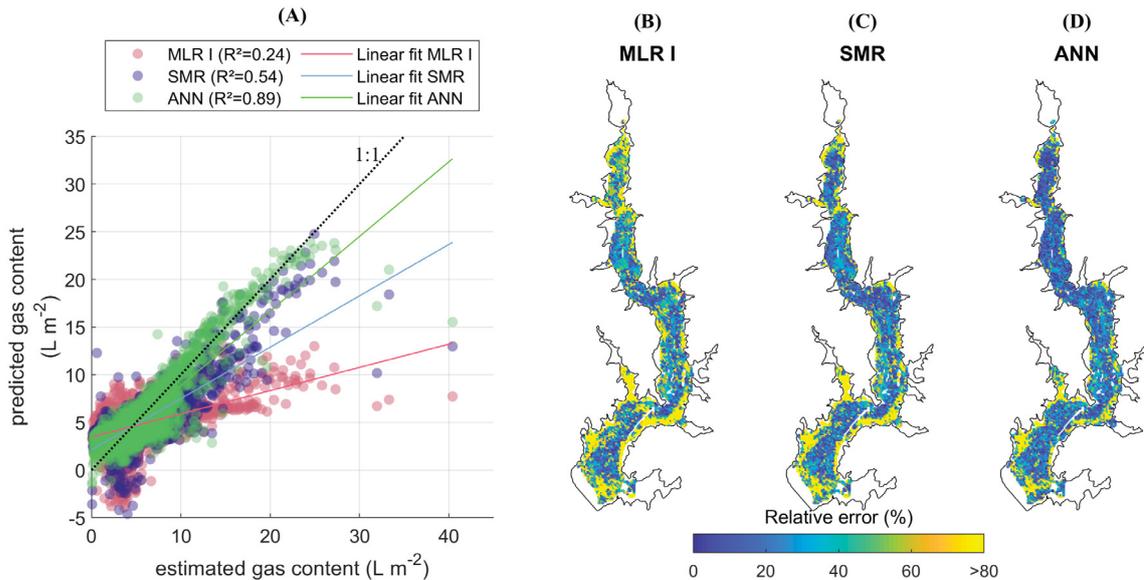
Figure 12 – **(A)** Scatter plot of predicted vs. estimated gas content and gas content for the survey in 2019 using three different empirical models (model MLR I are pink dots, SMR are the purple dots, and ANN are the green dots). Colored solid lines show linear regressions for each model with the following regression equations: MLR I y=3.46+0.24x (pink line); SMR y=2.11+0.54x (blue line), and ANN y=1.02+0.78x (green line). The dotted black line shows a 1:1 (y=x) relationship. **(B)** Spatial distribution of the relative error between predicted and estimated gas content from the multiple linear regression I (MLR I) in which 21.6% of the grid cells had errors larger than 80%. **(C)** Relative error of the predicted gas content from the stepwise multiple regression (SMR) in which 17.7% of the grid cells had errors larger than 80%. **(D)** relative error of the gas content predicted by the artificial neural network (ANN) in which 10.7% of the grid cells had error larger than 80%.

In both years, the estimated gas content in the sediment of the reservoir was similar with mean values of $4.4\pm3.1\,\mathrm{L\,m^{-2}}$ in 2016 and $4.6\pm3.2\,\mathrm{L\,m^{-2}}$ in 2019. Nevertheless, the range of the spatial variation of the gas content was slightly different with larger values in 2016 (2016: $0.1\text{-}57.0\,\mathrm{L\,m^{-2}}$; 2019: $0.1\text{-}40.4\,\mathrm{L\,m^{-2}}$). In both years, the largest gas content was estimated for sediments in the upstream part of the reservoir. Nevertheless, the coarser spatial resolution of the echo-sounding transects conducted in 2016 (partial loss of data) did not allow for capturing the spatial structure of the gas content hotspots in this region (Figure 13A).

As the spatial coverage of the acoustic transects during the 2016 survey was coarser than in the 2019 measurements, only 1321 grid cells could be considered for comparing the gas content between both years. A non-parametric hypothesis test was performed for each grid cell to verify the occurrence of a significant difference in the median gas content between both years (Figure 13). 48% of the cells had no significant difference in the median gas content and 52% were found to have different median gas content. Significant differences between both years occurred mainly at the shallower upstream part of the reservoir (near monitoring location P1), where the gas content was lower in 2019 compared to 2016 (Supplementary Figure 21). Higher gas content was detected in the reservoir stretch between the monitoring locations P1 and P3.

Lastly, we compared the predicted gas content from the artificial neural network model, which was based on 2019 data, with estimated gas content in 2016 and 2019. The gas content in the sediment in 2016 agreed with the predicted and estimated gas content of 2019, as shown in Figure 13D ($R^2 = 0.45$ for a linear fit with no intercept between predicted gas content from the ANN model and estimated gas content in 2016, $p = 0$ for the estimated coefficient). As previously mentioned, the upstream areas of
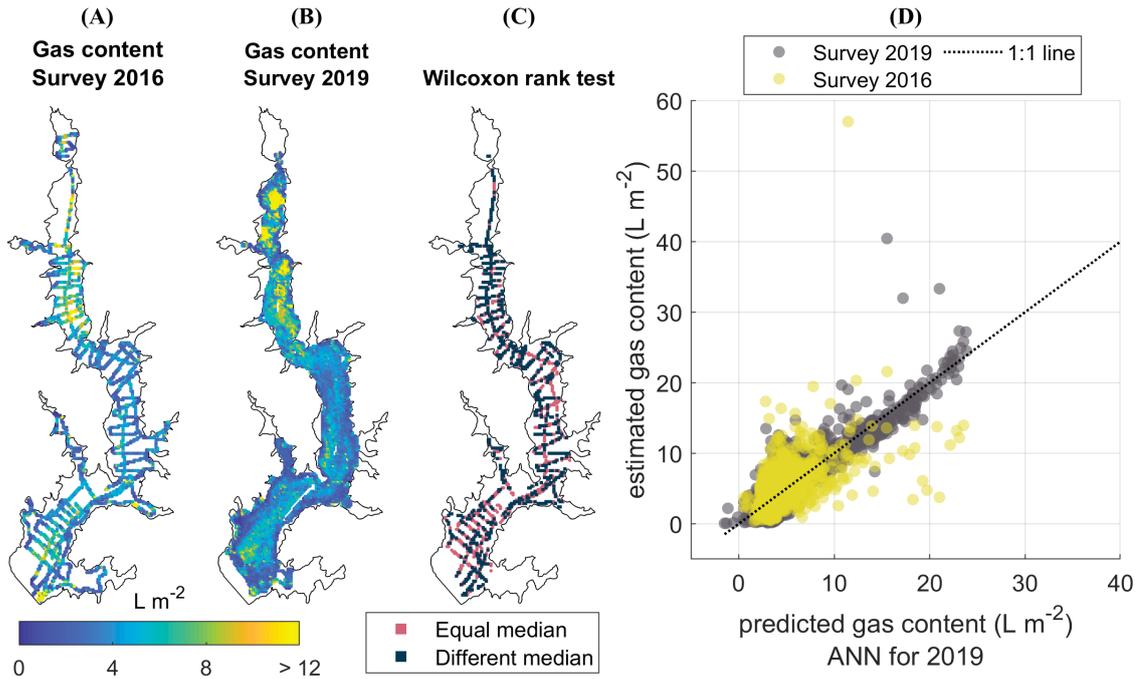
Figure 13 – **(A)** Areal gas content in the sediment for the 2016 acoustic survey. **(B)** Gas content in the sediment for the 2019 survey. **(C)** Results of the Wilcoxon rank test comparing the median gas content from both years, in which pink dots mark grid cells for which the null hypothesis of data from both years having the same distribution and equal median is accepted, and the dark blue dots mark the grid cells where the null hypothesis was rejected. **(D)** Scatter plot of observed vs. predicted gas content by the artificial neural network model with data from 2016 (yellow dots) and 2019 (grey dots). The dotted black line shows a 1:1 relationship.

potential high gas content in the sediment were not resolved in the 2016 survey. Nevertheless, grid cells with higher gas content in 2016 were observed in the vicinity of that region.

Discussion

Spatial-temporal mapping of sediment gas content

A high spatial resolution sediment gas content mapping was obtained as a function of the acoustic parameter maximum backscatter using the empirical relationship proposed by Anderson and Martinez (2015). The average maximum backscatter in Passaúna Reservoir ($-6.6\pm2.0\,\mathrm{dB}$) is in the range of the values obtained by Anderson and Martinez (2015) for the eutrophic reservoir Hodges. The gas content ranged between 0.1 and $40.4\,\mathrm{L\,m^{-2}}$, which for a 10 cm sediment layer represents a volumetric gas content of 0.1–40.4% (vol). The addition of gas voids to the sediment matrix results in a decrease in the sediment wet bulk density leading to instability of the sediment matrix and release of gas bubbles (Van Kessel; Van Kesteren, 2002; LIU et al., 2018). Van Kessel and Van Kesteren (2002) found that for muddy sediments, gas fraction in the range of 25–37% results in instabilities in the sediment matrix. For Passaúna reservoir less then 1% of the cells had gas content larger than 25% (Supplementary Figure 22). Moreover, considering the sediment wet bulk density mapped by Sotiri, Hilgert and Fuchs (2019), the regions with lower wet bulk density had relatively less gas content.

For lake Kinneret the upper limit of gas fraction in the sediment from acoustic measurements were 0.2% (KATSNELSON et al., 2017) and 3.8% (UZHANSKY et al., 2020). Nevertheless, for laboratory

conditions Liu et al. (2016) found a maximum gas content in incubated clay sediment of 46.8% with a depth-average of 18.8% for this fine sediment. Thus, the few highest fractions of gas content found (<1% cells) at Passaúna are in the same range as the values reported by Liu et al. (2016), whereas the averaged values of gas content are one order the values found in Lake Kinneret (UZHANSKY et al., 2020).

Transversal and longitudinal variation of gas content in the sediment were observed along the reservoir. Longitudinally, the largest amount of free gas in the sediment was detected in the upstream part of the reservoir, closest to the main inflow (Figure 11D), in a region with the largest sediment thickness and low water depth. We found that the gas content in the sediment tended to be higher in regions of preferred sedimentation (i.e. large sediment thickness), nevertheless with gas content magnitude being additionally affected by the water depth. For instance, at the deepest region of the reservoir where elevated sediment deposition was also mapped, the gas content was lower (up to $10\,\mathrm{L\,m^{-2}}$) compared to the shallow upstream region (up to $30\,\mathrm{L\,m^{-2}}$, Supplementary Figure 23C).

The occurrence of temporal change in gas content in the sediment was verified by analyzing two available echo-sounding surveys conducted 3 years apart from each other. The two surveys were done during summer at comparable water temperature and thermal stratification, and with small water level variation during both surveys, see Supplementary Figure 20. The mean sediment gas content was similar during both surveys ($4.4\pm3.1\,\mathrm{L\,m^{-2}}$ in 2016 and $4.6\pm3.2\,\mathrm{L\,m^{-2}}$ in 2019). The range of its spatial variability, however, differed and the maximum gas content in 2016 ($56.9\,\mathrm{L\,m^{-2}}$) was almost 50% higher than the maximum value in 2019 ($40.4\,\mathrm{L\,m^{-2}}$). We found that 52% of the analyzed sediment area had statistically different gas content between both surveys and lower gas content in 2019 was mainly estimated for the shallower upstream region (around location P1) (see Supplementary Figure 21). The lower gas content can be related to the 1m higher water level in 2016. Higher water level would represent additional hydrostatic pressure at the water-sediment interface, and thus increases the burden for bubble formation. A strong linear decrease of sediment gas content with increasing water level has been observed in Lake Kinneret, where acoustic surveys were conducted across several years (UZHANSKY et al., 2020). In addition to water depth, the proximity to the main inflow Passaúna river makes this region more affected by floods events which can alter the bottom sediment conditions.

Although small-scale variability of gas content in the sediment is not resolved in this study, either due to the echo response which is resulting from a bottom area ($0.8\,\mathrm{m^2}$ at $8.3\,\mathrm{m}$ depth) and from the averaging with the grid cell; measurements with closer distributed hydro acoustic transects were important for detecting spatial patterns in the gas content. For instance, in the 2016 survey, which covered a distance 3 times shorter than the survey performed in 2019, the areas of high gas content located at the upstream region of the reservoir were not captured due to missing data points.

Methane production, concentration, and ebullition

The results from the incubated sediment cores showed that the top sediment layer has the largest potential for methane production (PMP). The finding that the top $10\,\mathrm{cm}$ sediment layer is most productive is in agreement with Isidorova et al. (2019), who considered sediment within the range of sediment age (<6–12 years) as still active for methane production. In Passaúna, the first $10\,\mathrm{cm}$ of sediment have an age of 5 years, based on the findings of Sotiri et al. (2021), who estimated a sedimentation rate of $1.9\,\mathrm{cm\,yr^{-1}}$.

The integrated PMP over the $10\,\mathrm{cm}$ depth resulted in a potential methane flux at the sediment water interface of 306, 450, and $91\,\mathrm{mgCH_4\,m^{-2}\,d^{-1}}$ at the locations P1, P2, and P3 respectively at an average sediment temperature. The PMP of Passaúna sediment is within the range found in sediments from impoundments in Germany (WILKINSON et al., 2015) and the potential fluxes at the water-sediment interface are higher than the values reported for tropical lakes in Uganda (15.4–$144\,\mathrm{mgCH_4\,m^{-2}\,d^{-1}}$)

(MORANA et al., 2020). The largest integrated PMP value at location P2 coincided with the highest organic matter content (indicated by LOI 550 °C) from sediment cores (LOI 550 °C 15% at P1, 22% at P2, and 16% at P3), which is in agreement with other studies that reported enhanced methane production for sediments with higher organic matter content (WEST; COLOSO; JONES, 2012; GRASSET et al., 2021).

The averaged methane ebullition fluxes were 2.6, 5.8, and 1.9 times smaller than the corresponding potential flux at the water-sediment interface estimated from the integrated PMP at the three locations (see Table 4). The lower emission rates compared to sediment CH_4 production differ from observations by Wilkinson et al. (2015), in which the measured ebullition flux was comparable to the potential methane flux from PMP of shallow (<4 m) impoundments. We attribute this difference to the higher water depths of Passaúna Reservoir (average of 8.3 m), which can favour the diffusive flux of methane from the sediment (LANGENEGGER et al., 2019). The transported methane can accumulate in the overlaying water where it is susceptible to oxidation or release to the atmosphere during mixing events (VACHON et al., 2019). In fact, from the dissolved methane concentrations in the water overlaying the sediment, the shallowest upstream location, which is more likely to have mixing due to its lower water depth, had methane concentrations that were one order of magnitude smaller than at the other two sites (0.02, 0.36, and 0.33 mmolCH_4 L^{-1} for locations P1, P2, and P3).

Furthermore, although location P1 had a lower integrated PMP than location P2, the methane ebullition flux was 1.5 times higher, which we attribute in addition to the enhanced diffusion of CH4 to the water, to the larger water depth and thus, to the total pressure at the water-sediment interface. As the solubility limit of methane in the porewater increases with higher hydrostatic pressure (Figure 10B), larger dissolved gas concentrations are required for gas bubble formation (BAZHIN, 2003; LANGENEGGER et al., 2019). As shown in Figure 10, the methane concentration measured in sediment porewater at locations P2 and P3 were lower than the methane saturation limit considering the local water depth at these two sites. On the other hand, at the shallower location P1, the methane concentration in the sediment porewater was above the saturation limit for the deeper sediment layers. Lastly, an important aspect to consider, is that the PMP was obtained for laboratory conditions which may differ from the dynamic environmental conditions in the reservoir.

Ebullition is widely characterized in the literature as being highly variable in space and in time (WIK et al., 2013; MAECK; HOFMANN; LORKE, 2014). For Passaúna Reservoir, it was previously observed that ebullition events at the three monitoring locations where synchronized on a daily basis in which the ebullition events were triggered by large-scale forcing, such as drops in the atmospheric pressure (MARCON et al., 2019). For the 45-days time-series analyzed in the present study, a larger release of gas from the sediment was observed for February 4th to February 7th, which we could associate with the beginning of a period of decreasing atmospheric pressure (Supplementary Figure 16). We suggest that the drop in atmospheric pressure during the echo-sounding survey in 2019 potentially triggered gas release from the bottom sediment. Nevertheless, considering the elevated potential methane production of the bottom sediments, we assumed that the spatial patterns of gas in the sediment estimated from the echo-sounding was valid, as the ebullition trigger, in this case the atmospheric pressure drop, acted over the whole reservoir area.

Heterogeneities in gas distribution in the sediment are caused by different mutually influencing factors. Methane production in the sediment is driven by organic matter supply (GRASSET et al., 2021) and its degradability (SOBEK et al., 2012; WEST; COLOSO; JONES, 2012; PRAETZEL et al., 2019), as well as by temperature (ABEN et al., 2017; WILKINSON; BODMER; LORKE, 2019) and the presence of alternate electron acceptors (BASTVIKEN, 2009). Nevertheless, not all the produced methane escapes the sediment as ebullition, as also observed at Passaúna. The methane accumulation in the sediment

is affected by CH_4 oxidation (BASTVIKEN, 2009; MARTINEZ-CRUZ et al., 2018) and its transport out of sediment by diffusive fluxes (LANGENEGGER et al., 2019). Once the methane concentration in porewater reaches saturation gas voids are formed. The distribution and persistence of gas voids is further dependent on sediment properties such as grain size (BOUDREAU et al., 2005; ALGAR; BOUDREAU, 2009) and the sediment capacity to hold the free gas (Van Kessel; Van Kesteren, 2002; LIU et al., 2016). The ebullition flux (i.e., release of free gas from the sediment matrix as gas bubbles), is then a result of triggers facilitating gas release provided that there is free gas accumulated in the sediment. Drops in hydrostatic (SCANDELLA et al., 2011; MAECK; HOFMANN; LORKE, 2014) and atmospheric pressure (CASPER et al., 2000; NATCHIMUTHU et al., 2016) and bottom currents (JOYCE; JEWELL, 2003) have been reported as ebullition triggers.

The hotspot of gas content acoustically detected at the upstream region of Passaúna Reservoir indicates a higher potential for methane ebullition, which is confirmed by the highest ebullition flux recorded at the location P1. This is in accordance with numerous other studies, reporting high CH_4 fluxes in regions near to the main inflow river with high sedimentation rates (DELSONTRO et al., 2011; HILGERT; SOTIRI; FUCHS, 2019; LINKHORST et al., 2021). Whereas in the deeper locations of the reservoir (monitoring sites P2 and P3), higher methane partial pressure is required for bubble formation, Figure 10B, which combined with the deposition of finer sediment particles may increase sediment cohesivity and capacity to hold the produced gas in the sediment, and thus, would explain the observed dynamics of cumulative ebullition fluxes (Figure 10C) at locations P2 and P3 with longer periods (days) of no ebullition.

Prediction of gas content in the sediment

The capability of predicting gas content in the sediment is a useful tool for estimating methane ebullition from inland water. Large parts of the spatial variations in the estimated sediment gas content in Passaúna Reservoir could be explained by variations in more readily accessible characteristics of the reservoir and its sediment, including water depth, sediment thickness, and organic matter content of the sediment. The latter was estimated from the attack phase of the bottom echo.

Considering the relationships between gas content and individual parameters, the gas content was positively correlated with sediment thickness (rs = 0.2 $p = 3.4 \times 10^{-36}$) which may serve as a proxy for the deposition rate of fresh sediment (Supplementary Figure 17). Water depth was negatively correlated with gas content (rs = -0.1 $p = 4.7 \times 10^{-17}$), and accounts for hydrostatic pressure, as well as an indirect measure of sediment temperature (colder at largest depths), dissolved oxygen concentration in the hypolimnion (formation of bottom anoxic layer is favored during periods of stratification). Surprisingly, LOI was negatively correlated to gas content (rs = -0.6 $p = 0$). However, the correlation varied with water depth (Supplementary Figure 23) and the negative correlation was mainly caused by data from the upstream region of the reservoir, where large sediment thickness with high gas content occurred together with lowest LOI values (<10%) were found. Gas content and LOI were acoustically derived. Although they are calculated from different parameters (maximum backscatter and attack), there is a strong dependency between maximum backscatter and attack (Spearman correlation rs = 0.9 $p = 0$). On the other hand the acoustic derived LOI values agreed with the measurements from sediment samples (SOTIRI, 2020). In addition, in this study the available data set didn't allow to verify the relationship of LOI and organic matter content for the sediment characteristics of Passaúna Reservoir.

As discussed above, the gas content in the sediment depends on a combination of different parameters, thus the combination of available information was tested as predictors of gas content. The multiple regression (MR) models resulted in a lower agreement between predicted and estimated gas

APPENDIX A. Acoustic Mapping of Gas Stored in Sediments of Shallow Aquatic Systems Linked to Methane Production and Ebullition Patterns

71

content in comparison to the artificial neural network (ANN) model ($R^2 < 0.55$ for MR and $R^2 = 0.89$ for the ANN). The ANN model has the capability of accounting for nonlinearities among the variables and to handle high-dimensional multi-scale systems, thus identifying hidden patterns in the data set (FAUSETT, 1994). In the present application, this was observed in the contrasting magnitude of gas content for comparable sediment thickness regions with differing water depths.

The largest relative errors between the predicted and estimated sediment gas content were found for low gas content ($<4\,\mathrm{L\,m^{-2}}$), at the deepest region of the reservoir near to the dam, and towards the reservoir banks. Steep slopes are known to affect acoustic backscatter measurements of bottom sediments (STERNLICHT; MOUSTIER, 2003). This supports the application of a slope threshold in our spatial analyses. On the other hand, no evident dependence of the relative error on the average slope of the respective grid cell was observed for slopes smaller than the threshold (Supplementary Figure 19C). In addition, compact sediments are reported to have higher maximum backscatter comparable to the acoustic response of gassy sediments (HILGERT et al., 2016; SOTIRI; HILGERT; FUCHS, 2019).

We contrasted the predicted gas content from the trained artificial neural network for 2019 with the estimated gas content derived from the 2016 and 2019 hydroacoustic surveys and found good agreement between both years (Figure 13D). In this way, we denote that even though small spatial scale heterogeneities occur, which were averaged within grid cells, the main underlying spatial variability of gas content was maintained between the years and that the trained artificial neural network (ANN) model for gas content prediction is valid for both years. The prediction of the ANN model can be complemented and tested further with a stricter slope criterion and with the inclusion of additional relevant parameters. For instance, the origin of the organic matter (WEST; COLOSO; JONES, 2012), sediment exposure to dissolved oxygen concentrations (YVON-DUROCHER et al., 2014), and potential of methane production in the sediment (WILKINSON et al., 2015) were reported to be relevant to methane ebullition. However, mapping of such parameters for the whole reservoir would require the combination of the in-situ measurements complemented with modelling or upscaling techniques.

Further considerations and limitations

In this study, we derived gas content in the sediment from acoustic measurements and investigate its spatial-temporal variability in a subtropical reservoir. The analysis was supported by comparing gas content estimates with spatial maps of sediment thickness, loss on ignition, and bathymetry and considering the three locations with estimated potential methane production, dissolved methane concentration in the pore water, and continuously measured ebullition flux.

The potential of using the echo-sounding approach for detecting gas content in the sediment and the need for further investigations of its spatial distribution and relation to methane fluxes was highlighted in previous studies (ANDERSON; MARTINEZ, 2015; KATSNELSON et al., 2017; UZHANSKY et al., 2020) and corroborated in this study. One remaining challenge is the lack of direct measurements of sediment gas content under in-situ conditions that can serve for testing and calibration of acoustic approaches. Anderson and Martinez (2015) collected gas that was released from the sediment upon mechanical disturbance, which can be difficult when applied from a boat at larger water depth where an accurate definition of the disturbed area that contributes to the collected volume of gas is not possible. More recent studies analyzed sediment cores frozen under in-situ conditions [freezed cores (DÜCK et al., 2019a)], which are analyzed in an X-ray CT scanner to quantify the amount of free gas (DÜCK et al., 2019b; LIU et al., 2019). However, freezing of the sediment cores is also reported to cause mechanical disturbances in the sediment core and result in additional bubble formation (DÜCK et al., 2019b). Sampling of pressurized sediment cores (e.g., Wilkens and Richardson (1998)) certainly allow for most

APPENDIX A. Acoustic Mapping of Gas Stored in Sediments of Shallow Aquatic Systems Linked to Methane Production and Ebullition Patterns

72

accurate estimates of column-integrated gas content in the laboratory, yet they require the support of divers for sediment sampling and are also affected by bubbles that escape during corer penetration.

The understanding of spatial variability and temporal dynamics of methane fluxes from inland waters can be improved by knowing the process that affect the production, transport, oxidation, and emission of CH_4, which include storage of free gas in the sediment. High resolution acoustic surveys can provide estimates of sediment gas content and its spatial and temporal dynamics. Nevertheless, additional sampling locations for echo-sounding and ebullition monitoring would be required to explore relationships between gas storage and ebullition. A main advantage of acoustic gas content measurements as a proxy for ebullition flux is the high potential areal coverage of echo-sounding in comparison to the limited area sampled by bubble traps (funnel diameter of 1 m) and the possibility to measure transects covering the entire reservoir. As an additional aspect, it remains to be investigated if the uncertainties of flux measurements that are associated with temporal variability of ebullition can be reduced by accessing the gas stored in the sediment.

Conclusion

In this study, we used data from echo-sounding surveys with high spatial resolution to analyze the distribution of free gas in the sediments of a freshwater reservoir and discussed the observed spatial heterogeneity. The gas content mapping for the entire reservoir provided improved understanding of the environmental factors that regulate methane production and emission in reservoirs and other inland waters. We demonstrate a shift of the drivers of spatial variability in ebullition fluxes from proximity to the main inflow in the upstream part, to water depth and its associated effects (in deeper water occurs colder temperature at the bottom, water stratification, and higher total pressure at the water-sediment interface) in the downstream part of the reservoir. In the shallower upstream part, where the observed ebullition fluxes were the highest, the sediment gas content was highest, and the ebullition gas flux was rather continuous. In the deeper downstream sections of the reservoir, the sediment gas storage became more relevant in controlling the intermittent ebullition dynamics. The spatial variations of the estimated sediment gas content could be well predicted by sediment thickness, water depth, and sediment organic matter content (here inferred from loss on ignition) with an artificial neural network model. The largest discrepancies between estimated and predicted gas content were found for low gas content ($<4\,\mathrm{L\,m^{-2}}$). Finally, the comparison of gas content estimates derived from acoustic surveys conducted in two different years suggested that the main pattern of the spatial variability of gas content was similar, while the total amount of gas stored in the sediment was higher during the year with higher water level. Improved sampling techniques for undisturbed measurements of gas content in aquatic sediments are required to validate and to further improve acoustic sampling techniques.

Supplementary material

In this section is presented the supplementary material for the paper 'Acoustic Mapping of Gas Stored in Sediments of Shallow Aquatic Systems Linked to Methane Production and Ebullition Patterns'. It is presented Figures SI 14 to 23. The publication can be accessed online at `https://www.frontiersin.org/articles/10.3389/fenvs.2022.876540/full#supplementary-material`.

Acoustic parameters and spatial grid selection

The main acoustic parameters exported from Sonar5-Pro software from the echo-sounding surveys were acoustic attack, acoustic decay, and maximum backscatter. Attack is calculated as the vertically integrated backscatter strength over the duration of one pulse length from the detected bottom surface and represents the energy scattered at the sediment surface (HILGERT et al., 2016). Decay is defined as the energy of the backscattered sound from within the sediment. It is obtained by integrating the backscatter intensities over the decaying part of the signal below the maximum backscatter (BALK; LINDEM; CARNERO, 2011; HILGERT et al., 2016).

The acoustic parameters Attack (Att) and Decay (Dec) are calculated by the software Sonar5-Pro as:

$$\text{Att(dB)} = 10 \times log \left(\frac{1}{N} \sum_{i=Bi}^{As} (10^{Sv_i/10}) \right)$$

$$\text{Dec(dB)} = 10 \times log \left(\frac{1}{N} \sum_{i=As+1}^{Ds} (10^{Sv_i/10}) \right)$$

in which Bi is the starting backscatter strength samples and As is the end of the attack samples. In which the attack samples are defined as the samples occurring within the duration of 1 pulse length, as represented by Hilgert et al. (2016). The Decay is then computed as the integrated backscatter strength samples from $As + 1$ until the Decay samples (Ds), which has the duration of three pulse lengths, showed in Figure 14. The maximum backscatter which is applied for the estimation of gas content in the sediment, is the maximum backscatter value detected below the sediment water interface.

The selection of the spatial grid for this study was done based on the coefficient of variation of the acoustic parameters attack and decay calculated for 6 tested grids. For each cell of the spatial analysis grid, and for each field survey (2016 and 2019), the data variability within the grid cell was evaluated considering the coefficient of variation (CV) calculated as CV $= \sigma/\mu$, in which σ is the standard deviation and μ is the mean value. After calculated for each grid cell, mean values for the whole reservoir were calculated as the weighted average of the CV by the number of points (sound pulses) within each grid cell. The spatial grid was selected as the one with the lowest weighted CV.
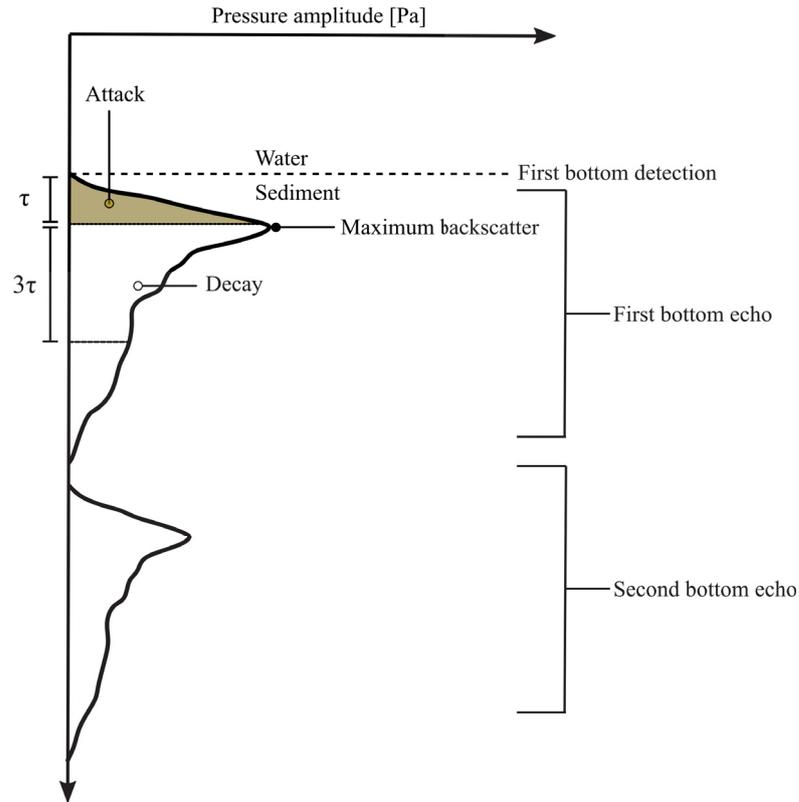
Figure 14 – Representation of the echo envelope as it penetrates the bottom sediment according to the first division method, adopted from Hilgert et al. (2016). The integrated area in orange represents the energy of the attack phase (integration of backscatter samples over the duration of one pulse length from the detected bottom), which is followed by the identification of the maximum backscatter value (used in this study for the estimation of gas content in the sediment), and the decay phase. The symbol τ denotes the pulse length. A second echo can also be found on the echograms, which results from the sound wave that is reflected by the water surface back to the sediment and then recorded by the transceiver, however, the second bottom echo was not analysed in this study.
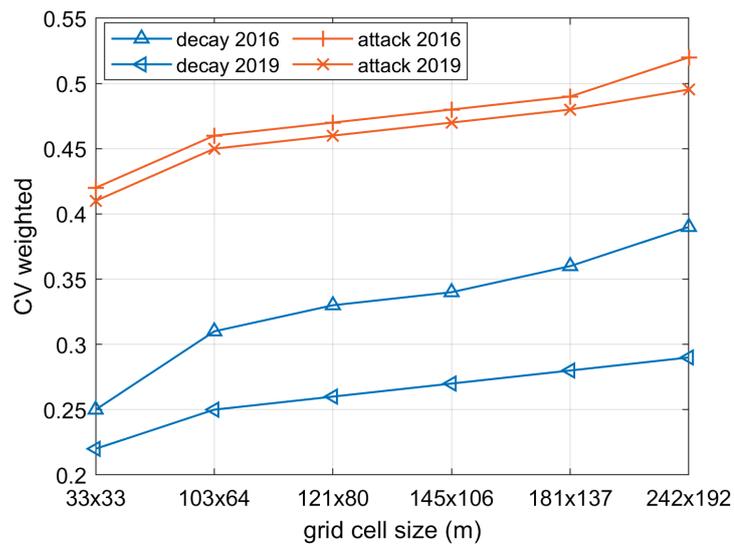
Figure 15 – Weighted averaged coefficient of variation for the entire reservoir for the echo-sounding measurements performed in 2016 and 2019, for the acoustic decay (blue line) and acoustic attack (orange) against different grid cell sizes.
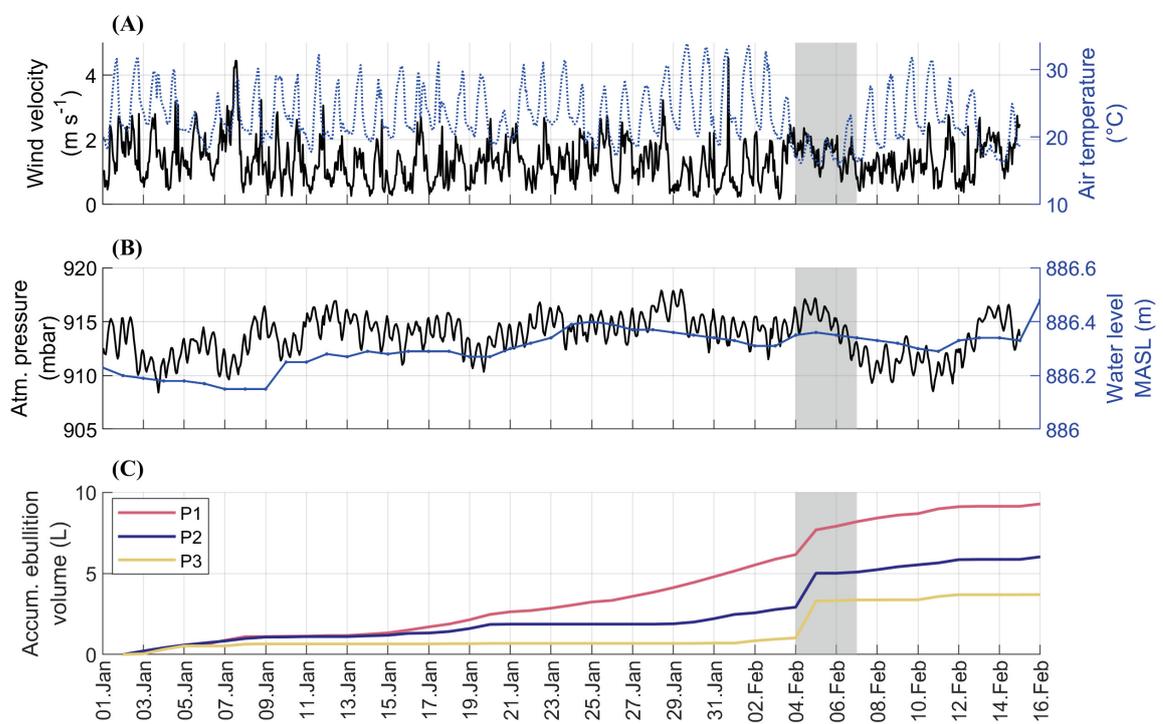
Figure 16 – Time series of **(A)** wind velocity and air temperature measured by a weather station located near to the dam of Passaúna Reservoir, and **(B)** atmospheric pressure and reservoir water level. Data showed in **(A)** and **(B)** are provided by SANEPAR). **(C)** Accumulated gas emitted through ebullition, recorded by automated bubble traps deployed at the monitoring locations P1 (red line), P2 (dark blue line), and P3 (yellow line).
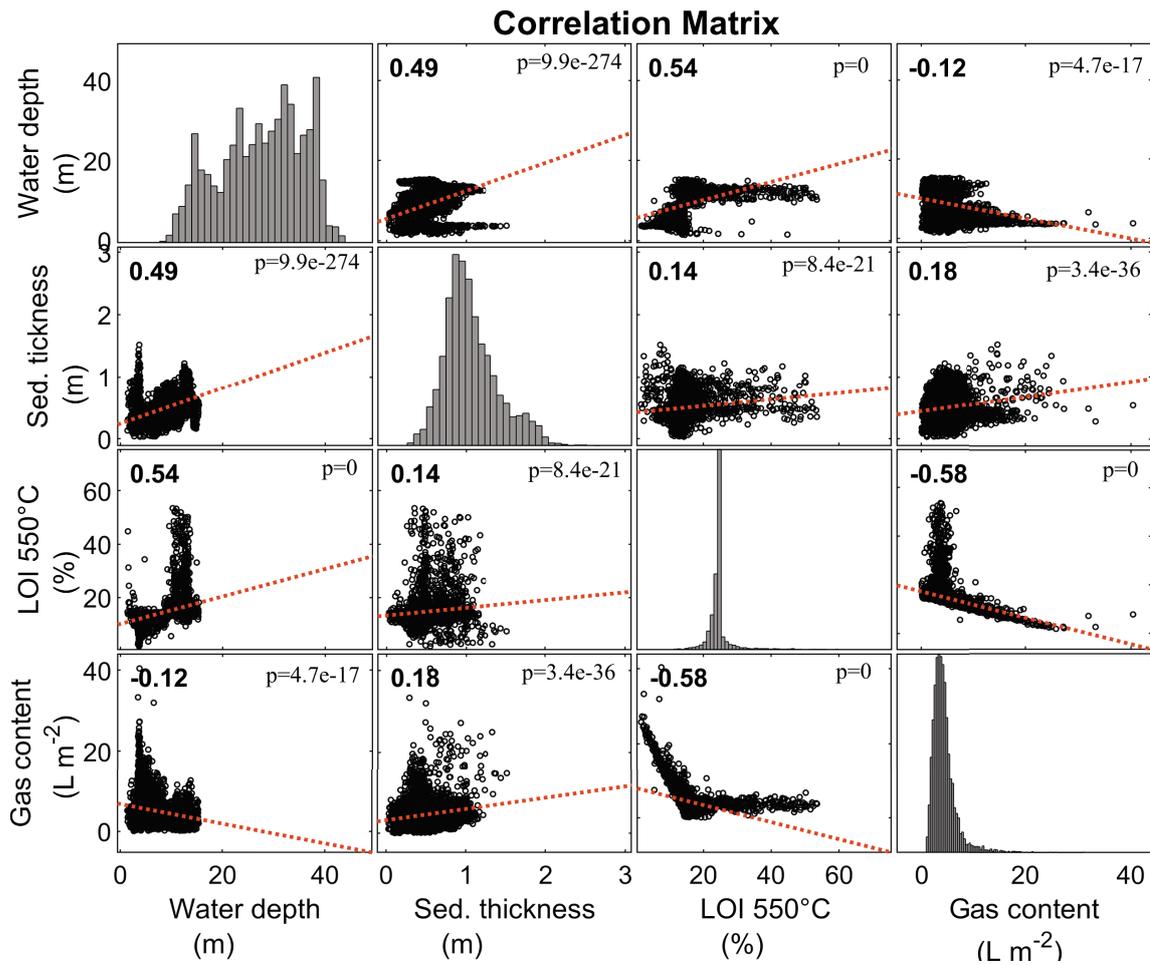
Figure 17 – Correlation matrix among the estimated gas content in the sediment, water depth, organic matter content (LOI 550 °C), and sediment thickness. All numbers represent mean values for individual grid cells. The diagonal elements of the matrix show the frequency distributions of the respective data. Numbers inside the panels denote the Spearman correlation coefficient (which tests for monotonical relationship between variables) and the corresponding p-value. The orange dotted lines are linear fits between the two respective variables.
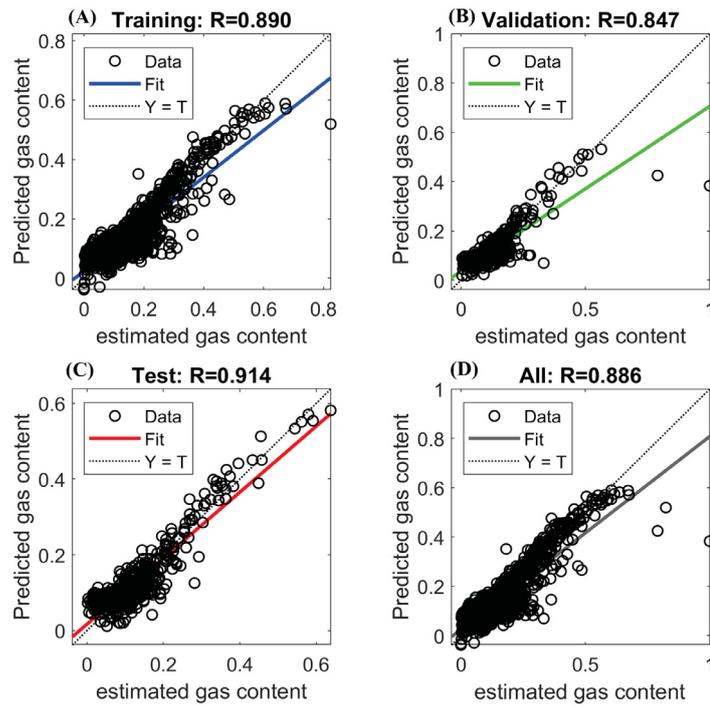
Figure 18 – **(A)** Scatter plot (black circles) of predicted versus estimated gas content for the predictions from the artificial neural network model using the training data set (3255 grid cells). The blue solid line is a linear regression. **(B)** Scatter plot (black circles) of predicted versus estimated gas content by the artificial neural network using the validation data set (698 grid cells). The green solid line shows a linear fit. **(C)** Scatter plot (black circles) of predicted versus estimated gas content by the artificial neural network model using the test data set (698 grid cells not included during training). The red solid line is the linear fit. **(D)** Scatter plot (black circles) and linear fit (grey solid line) for the entire data set (4651 grid cells), The dotted black line in all panels shows a 1:1 relationship. All panels show dimensionless gas content which was scaled to vary between 0 and 1.
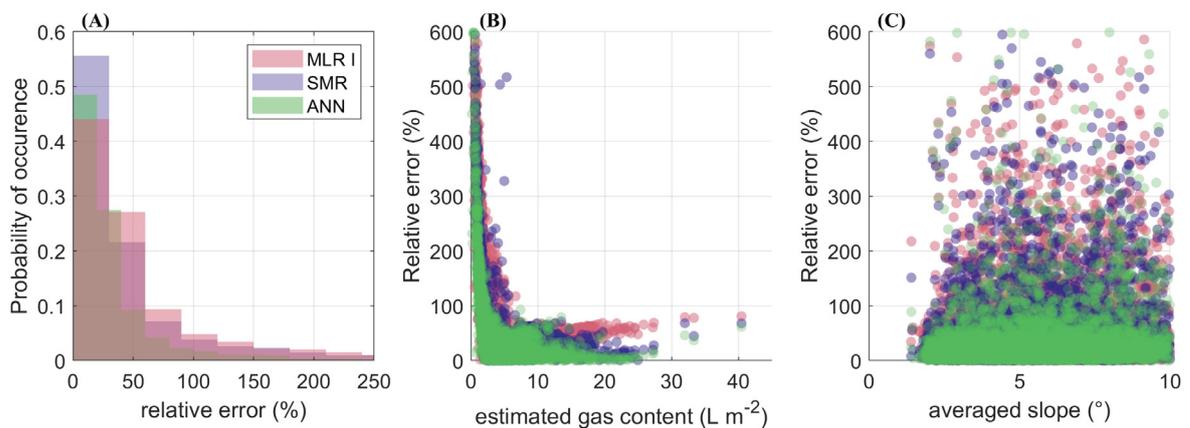
Figure 19 – **(A)** Probability of occurrence of relative errors of the three models applied for the prediction of the gas content. **(B)** Scatter plot of the relative error of the three models versus estimated gas content derived from the echo-sounding survey. **(C)** Scatter plot of the relative error of the three models for gas content prediction versus mean bottom slope for each grid cell. In all panels the pink color represents the multiple linear regression model (MLR I), the purple color is the Stepwise multiple regression (SMR), and the green color is the artificial neural network model (ANN).
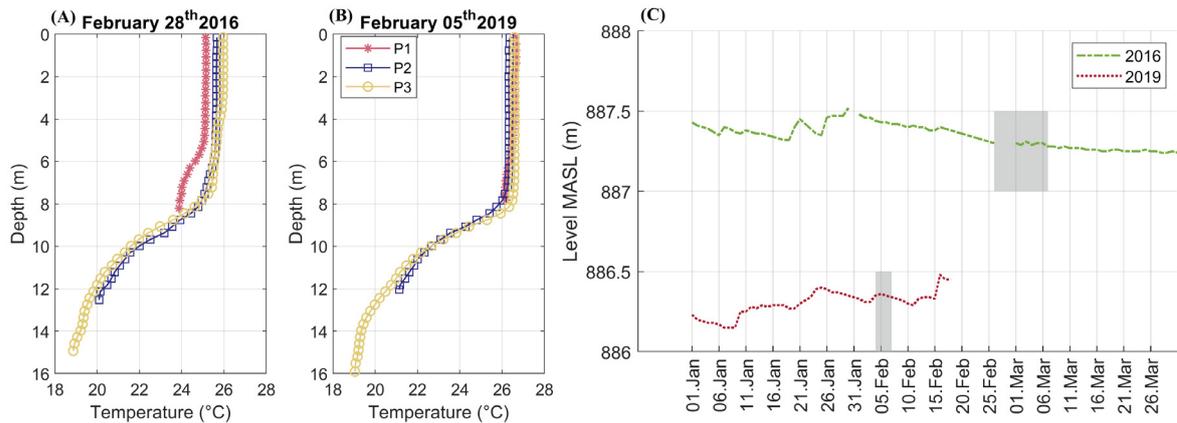
Figure 20 – Vertical profiles of water temperature measured with a CTD – Conductivity-Temperature-Depth (CastAway-CTD) probe at the three monitoring locations at Passaúna Reservoir (P1, P2, and P3, see legend for color assignment) during the echo-sounding surveys conducted in 2016 **(A)** and 2019 **(B)**. **(C)** Time series of water level in the reservoir for 2016 (green dashed line) and 2019 (dotted dark red line). The two grey shaded areas indicate the days when the echo-sounding surveys were performed in each year. The water level data were provided by the reservoir operator (SANEPAR).
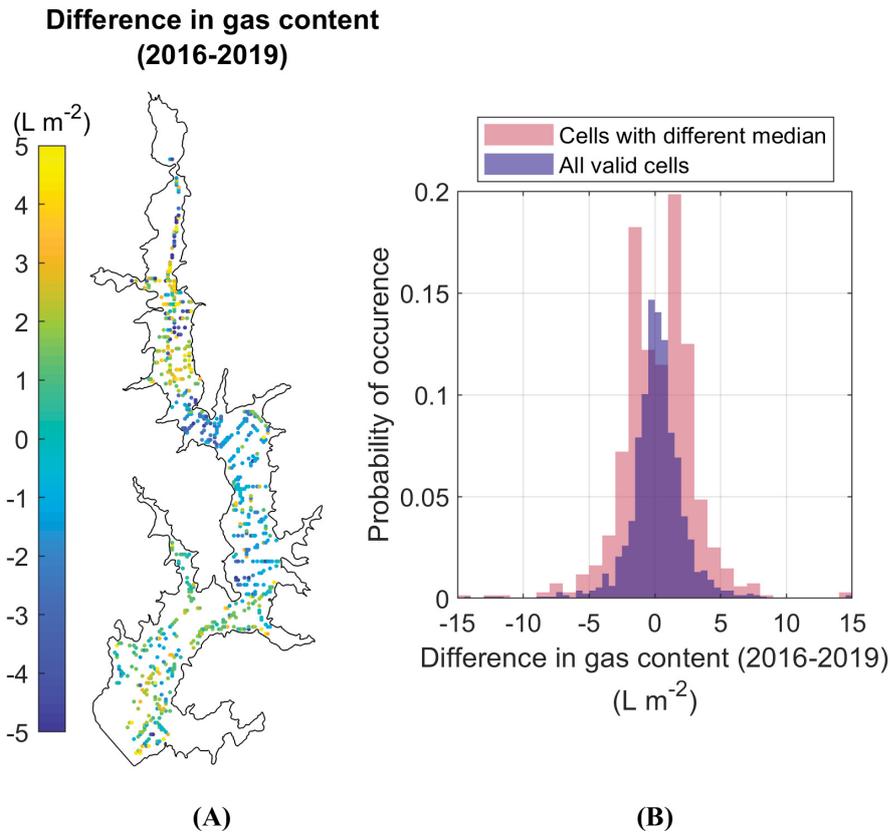
Figure 21 – **(A)** Difference in estimated sediment gas content for the years 2016 and 2019 for grid cells for which the median values from both years differed significantly (Wilcoxon rank test). **(B)** Probability of occurrence of differences in estimated gas content between both years considering all grid cells (pink bars), and only the grid cells with significant differences in the median gas content (purple bars).
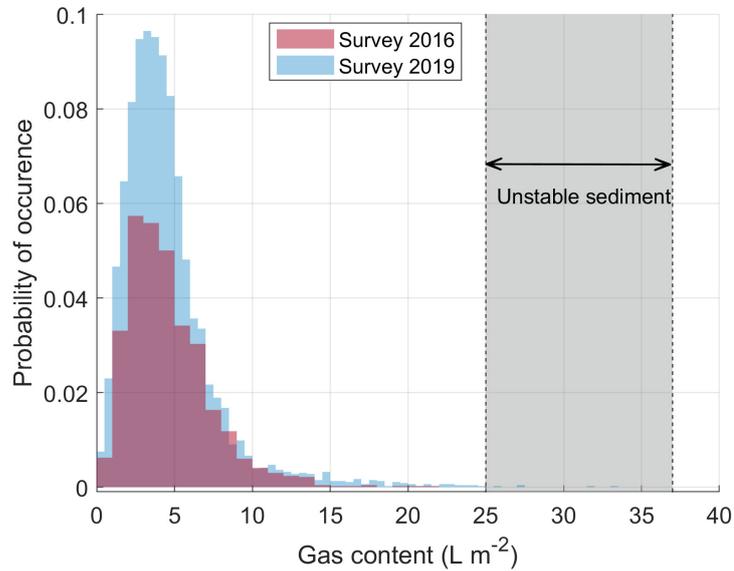
Figure 22 – Probability of occurrence of estimated gas content in the sediment from echo-sounding survey conducted in 2016 (pink bars) and in 2019 (blue bars). Considering a 10 cm sediment layer the gas content values in L m^{-2} correspond to the gas volume fraction in the sediment in %. The grey shaded area is the gas fraction range $(25 - 37\%)$ reported by Van Kessel and Van Kesteren (2002) in which the sediment matrix (muddy sediment) would become unstable due to buoyancy forces.
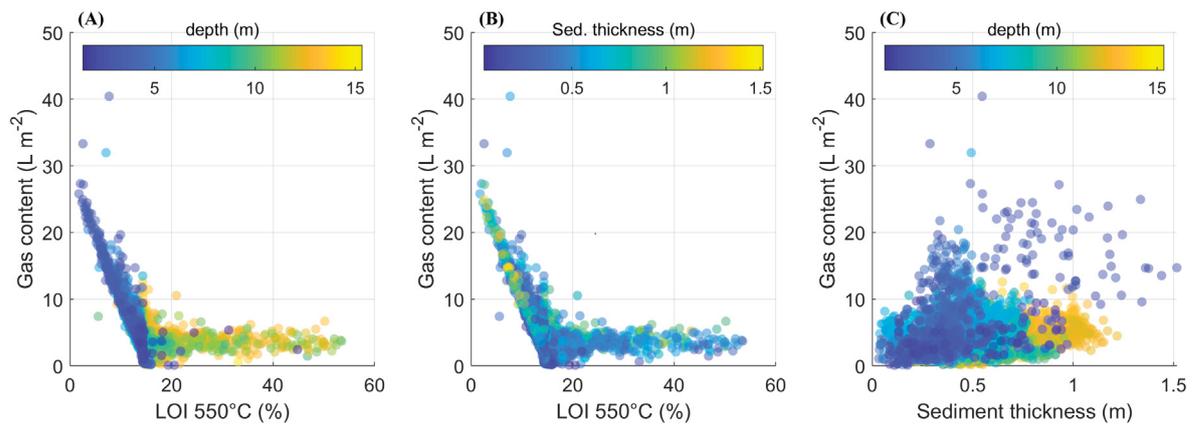
Figure 23 – **(A)** Scatter plot of estimated gas content and loss on ignition (LOI 550 °C) with symbol color representing the water depth for each grid cell. **(B)** Scatter plot of estimated gas content and LOI 550 °C with symbol color according to sediment thickness for each grid cell. **(C)** Scatter plot of estimated gas content and sediment thickness with symbol color denoting water depth for each grid cell.

APPENDIX B – Linking sediment gas Storage to the methane dynamics in a shallow freshwater reservoir

Lediane Marcon, Michael Schwarz, Laura Backes, Mara Offermann, Felix Schreiber, Stephan Hilgert, Klajdi Sotiri, Christian Jokiel, and Andreas Lorke

Abstract

Freshwater reservoirs are globally relevant sources of the greenhouse gas methane. Organic matter rich sediments are hot spots of methane production and can store large amounts of methane dissolved in porewater and as free gas. Yet, in-situ data on the gas storage as free gas (bubbles) in freshwater sediments are scarce. Here, an acoustic approach was tested and used to map the gas content in the sediment of a shallow temperate reservoir. The sediment gas storage was linked to the methane budget obtained from almost two years of in-situ monitoring. The emission fluxes were dominated by ebullition and degassing at the reservoir outlet, which combined accounted for 93% of the total methane emissions. 66% of the ebullition variability was explained by a combination of environmental parameters. Mappings of sediment gas content using echo sounder surveys revealed the accumulation of free gas in regions of elevated sediment deposition. Temporally, the gas storage in the sediment was related to methane emissions, in which a period of intensified emissions resulted in a reduction of sediment gas storage. The sediment could store an equivalent of four to thirteen days of accumulated potential methane production, which could supply the mean ebullition flux for more than two months. We suggest that sediment gas storage plays an important role in buffering and modulating methane emissions in aquatic systems and need to be accounted for in process-based models.

Introduction

Freshwater aquatic ecosystems are a relevant source of atmospheric methane (CH_4), an important greenhouse gas contributing 16% to the effective radiative forcing (IPCC, 2021). Manmade reservoirs are estimated to emit 18–24 $TgCH_4$ per year to the atmosphere, corresponding to 2.2–3% of anthropogenic sources (DEEMER et al., 2016; ROSENTRETER et al., 2021). Nevertheless, the magnitude of methane emissions from reservoirs as well as from other inland waters (i.e., rivers, lakes, and wetlands) is still highly uncertain (SAUNOIS et al., 2020).

The damming of rivers is often associated with a change from lotic to lentic ecosystem characteristics, including changes in sediment retention, flow velocity, as well as thermal and chemical conditions (MAAVARA et al., 2017). Combined they favor the production of CH_4 and its emission to the atmosphere (MAAVARA et al., 2020). The spatial and temporal dynamics of CH_4 emission from these aquatic systems have been increasingly investigated with the aim to understand and to identify the governing processes. Improved mechanistic understanding is key for upscaling of flux measurements in space and time, for making predictions of ongoing and future changes, and to develop mitigation strategies together with optimized management strategies.

In freshwater reservoirs, CH_4 is mostly formed during the anaerobic degradation of organic matter (BASTVIKEN, 2009; SMITH et al., 2003). Deposition zones of sediments being rich in organic matter are hotspots of CH_4 production (DELSONTRO, 2011; HILGERT; SOTIRI; FUCHS, 2019; MAECK et al., 2013), while the fate of the produced CH4 is determined by the prevailing environmental conditions. In the sediment CH_4 can be oxidized by bacteria, which can consume up to 95% of the methane produced (BASTVIKEN, 2009); CH_4 can be transported into the surface water by diffusion; If the net CH_4 production in the sediment results in dissolved gas pressure exceeding the ambient hydrostatic pressure, gas voids can form, from which events of bubble release (ebullition flux) can transport CH_4 out of the sediment matrix. In shallow reservoirs, ebullition fluxes, which bypass CH_4 oxidation, can dominate the emissions (BASTVIKEN et al., 2004).

The bottom sediment plays an important role for CH4 dynamics in water reservoirs. In addition to its influence on the production and transport, the sediment matrix can store CH_4 dissolved in the pore water or as free gas. The gas void fraction in the sediment has being reported in the range from <1% (UZHANSKY et al., 2020) for in-situ measurements to up to 18% under laboratory conditions (LIU et al., 2016). The sediment storage capacity for free gas depends on ambient conditions, such as temperature and pressure, and on the mechanical properties of the sediment (LIU et al., 2018; LIU et al., 2019).

Recent models for CH_4 emissions from wetland have introduced gas storage for predicting ebullition dynamics (PELTOLA et al., 2018). Yet data on gas storage and its spatial and temporal variability in other inland waters are scarce. Katsnelson et al. (2017) estimated the gas content in the sediment of lake Kinneret based on measurements of the reflection coefficient of low-frequency sound and found that spatial patterns of sediment reflectance coincided with the distribution of organic matter. At the same lake, Uzhansky et al. (2020) showed that the gas content in the sediment was lower during periods of higher water level. Martinez and Anderson (2013) measured the areal sediment gas content in a eutrophic reservoir and identified it as a driver of ebullition. In a follow-up study, Anderson and Martinez (2015) proposed an empirical calibration to estimate the areal gas content based on the maximum acoustic backscatter observed in the bottom echo of high-frequency echo-sounders. This calibration curve was also applied to estimate gas content in another aquatic system (MARCON et al., 2022b).

In this study we estimated the free gas stored in the sediment of a freshwater reservoir in Germany with the use of an echo-sounder and the method proposed by Anderson and Martinez (2015), which we validated using in-situ measurements. For the first time, we relate the sediment gas content to

the reservoir CH_4 budget, which we derived from extensive field measurements of fluxes and potential production rates. Our analysis follows three main objectives: 1) to establish a methane budget for a shallow freshwater reservoir; 2) to evaluate the spatio-temporal dynamics of methane emissions from the system; and 3) to link the spatial and temporal dynamics of sediment gas storage to the methane budget.

Material and methods

Study site and sampling overview

This study was conducted in the Wupper-Vorsperre, which is the main pre-dam of the Wupper reservoir. The reservoir is located in the western part of Germany (coordinates 51.16°N and 7.33°E). It was built in 1976 primary for flood control, but it is also used for energy generation, with an installed capacity of 1.25 MW. Reservoir pre-dams, also known as check dams, are often built for controlling sediment input (MORRIS, 2020) and water quality (PAUL, 2003) in the main reservoir. The Wupper pre-dam (hereafter also referred as reservoir) in which our sampling was conducted, has a surface area of 150 000 m^2, an average depth of 2 m, and a maximum depth of 5.5 m close to the dam. It has an elongated, curved shape with approximately 2.4 km length from the inflow to the dam and an average width of 77 m. The bathymetry clearly shows the location of the talweg of the former river course, and a preference of sediment accumulation at the inner curves of the reservoir, similar to sediment deposition patterns typically described in rivers bends (WETZEL, 2001), as well as in the shallow upstream regions near to the inflow (Figure 24).
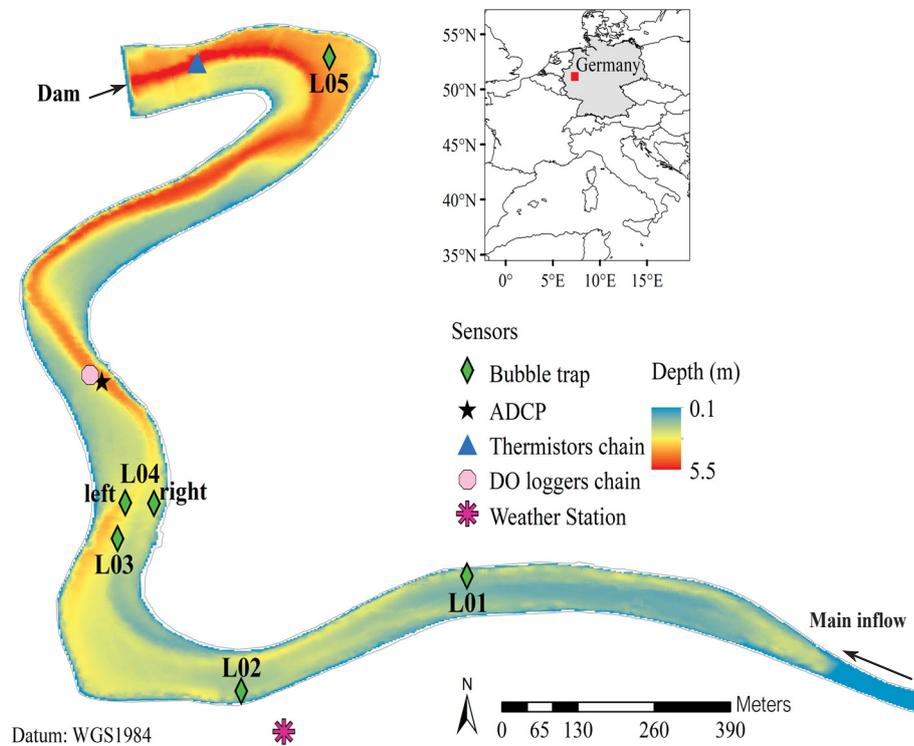
Figure 24 – Map of the study site, Wupper pre-dam, located in the western region of Germany (see inset map). The location of the monitoring sites is marked by symbols indicating the different measuring device deployed and the color shows the reservoir bathymetry, see Figure legend.

The main inflow to the reservoir is the Wupper River. The river discharge is monitored by a

gauging station approximate 1.5 km upstream of the reservoir entrance (operated by Wupperverband). From March 2020 to December 2021, the average daily inflow discharge was $3.3 \pm 4.0 \, \text{m}^3 \, \text{s}^{-1}$ (average $\pm$ standard deviation), nevertheless peak discharges exceeding $30 \, \text{m}^3 \, \text{s}^{-1}$ were recorded in mid March 2020 and mid July 2021 (see supporting information Figure SI 31). In July 2021, a major flood event occurred in the region, causing a significant increase in the water level overflowing the reservoir banks. A wastewater treatment plant (WTP) is located near the upper part of the reservoir, with an effluent discharge location upstream of the monitoring site L02.

The monitoring in the reservoir was conducted from March 2020 to November 2021 with a combination of continuous sensor measurements and monthly field campaigns. The measurements comprised methane fluxes and concentrations, and relevant environmental parameters detailed on the following sections. Data gaps in continuous measurements and in monthly samplings were caused by sensor failure, logistic limitations, or weather and hydrological conditions, such as floods.

Methane fluxes

We measured CH_4 fluxes by ebullition, diffusive gas exchange at the water surface, advective fluxes with inflows and outflows, degassing at the outflow spillway, and ecosystem CH_4 oxidation rates. The measurements and respective flux calculation are outlined below, and more detailed information are provided in the supporting information (Text SI B).

Gas ebullition was continuously monitored using bubble traps with logging capabilities, which were deployed at five monitoring locations (from L01 to L05, see Figure 24). Detailed description of the devices and ebullition calculation is provided in supporting information (Text SI B). Depending on location, valid ebullition fluxes were recorded for a total of 85 days (at L05) up to 362 days (at L03) for the monitoring period from March 18th 2020 to November 28th 2021. At each monitoring site, gas bubbles from the sediment were monthly captured and analyzed for the methane fraction within the gas samples, which was used for the calculation of the CH_4 ebullition fluxes. Daily CH_4 ebullition fluxes were obtained for each monitoring site. The daily fluxes were then used to obtain the mean and median fluxes at each monitoring site to evaluate its spatial distribution. In addition, daily values of spatially averaged fluxes (average of all monitoring sites) were used to analyze the temporal dynamics of reservoir-wide ebullition fluxes.

The diffusive CH_4 flux at the air-water interface was estimated for 14 months from monthly measured dissolved CH_4 concentrations in the surface water and by applying the thin boundary layer method. The CH_4 diffusive flux crossing the air-water interface was calculated from the difference between the dissolved concentration and the atmospheric equilibrium concentration at in-situ water temperature, and the gas transfer velocity, which was estimated from wind speed (LISS; SLATER, 1974).

The water outflow from the pre-dam to the main reservoir is through a spillway overflow at the dam and from two bottom outlets controlled by gates. The passage of water over the spillway enhances the release of the dissolved methane to the air (degassing flux). The degassing flux was calculated for 10 months during the monitoring period as proposed by Goldenfum (2010), as the product of the difference in dissolved CH_4 concentration upstream and downstream the dam, and the water discharge. Despite being rather a point source, the degassing flux is normalized by the reservoir surface area to facilitate comparison with other fluxes. The difference between the dissolved CH_4 exported and imported by water leaving and entering the reservoir was used to calculate a net advective CH_4 flux, which was available for 8 months and also normalized by reservoir surface area.

Lastly the CH_4 oxidation rate was estimated as proposed by Sawakuchi et al. (2016). In sum-

mary, the fraction of CH_4 oxidized was calculated by applying the Rayleigh isotopic fractionation model (Langrangian, closed system model) using measurements of the isotopic ratios of methane carbon (δ^{13}C-CH_4) in bubbles stirred from the sediment and in dissolved CH_4 in the surface water. The underlying assumption of this method is that the diffusive CH_4 flux at the water-air interface represents the total dissolved CH_4 that escaped oxidation, while the input of methane into the water column is the sum of the diffusive flux at the water surface and the fraction of the input that is oxidized (SAWAKUCHI et al., 2016). For further details, see Text SI B. Oxidation rates were estimated based on monthly measurements for 13 months of the monitoring period.

Sediment sampling

Sediment cores with 6 cm diameter were sampled at all sites (L01 to L05) in May, July, and September 2020 using a gravity corer (Uwitec). The length of the sampled sediment cores varied from ∼32 cm to ∼42 cm. After retrieval, the sediment cores were transported to the laboratory and kept at a temperature of ∼4 °C) until analysis. In the laboratory, the sediment cores were analysed for dissolved CH_4 concentration in the porewater, potential methane production (PMP), and organic matter content. An extended explanation of the sampling procedure is provided in the supporting information (Text SI B).

Sediment porewater was extracted from sediment layers (3 cm vertical spacing at the top 15 cm and at 10 cm spacing for the remaining of the core) using Rhizon tubes inserted into pre-drilled holes, as described by Wilkinson, Bodmer and Lorke (2019). The porewater was transferred to pre-evacuated glass vials, and the dissolved CH_4 concentration in porewater was calculated from the CH_4 headspace concentration measured in the vials. The sediment cores were then sliced into 3 to 10 cm layers in a nitrogen flushed glove box, transferred to 120 mL nitrogen flushed serum bottles, and incubated under dark conditions at a constant temperature of 20 °C for the estimation of potential methane production (PMP) rates in the sediment. The volumetric PMP rates from the individual incubated sediment layers of the top 30 cm of each core, were then vertically integrated to obtain the potential methane flux at the sediment water interface (PSWI) in units of mgCH$_4$ m^{-2} d^{-1}, which was adjusted to in situ sediment temperature (WILKINSON et al., 2015; WILKINSON; BODMER; LORKE, 2019).

The remaining sediment from each core layer was transferred to falcon tubes, freeze-dried, and stored for measurement of organic matter content. The organic matter content in the sediment was estimated from Loss on Ignition (LOI). In addition to the LOI, the carbon and nitrogen content in the sediment samples were estimated using a CHNS elemental analyzer (Vario MicroCUBE, Germany).

Echo-sounding and estimation of sediment gas content

An initial echo-sounding survey for obtaining the reservoir bathymetry was conducted in May 2021 with a GSD 26 echo-sounder (Garmin) and a Airmar CM599LH transducer with a frequency of 180 to 210 kHz. Two additional surveys with a dual frequency (38 and 200 kHz) single beam echo-sounder (EA400, Kongsberg Inc. 2006) were conducted for estimating the amount of free gas (bubbles) in the sediment (sediment gas content). The first survey was conducted on July 1st of 2020 and covered the entire pre-dam. The second survey was conducted on June 11th 2021, but restricted to the upstream region of the pre-dam (from monitoring site L04 towards the upstream site L01, see map at Figure 24 for the monitoring locations) due to logistic reasons.

The areal gas content in the sediment was estimated from the EA400 echo-sounder data following Marcon et al. (2022a). The 200 kHz measurements were processed using the Sonar5-Pro software (Lindem

Data Acquisition, Oslo, Norway), in which the magnitude of the maximum acoustic backscatter near the sediment surface is exported together with its geographic coordinates for each ping (sound pulse). A spatial grid of 5 m by 5 m was created for the pre-dam and the average maximum backscatter was calculated with the available measurements for each grid cell. Anderson and Martinez (2015), proposed an empirical relationship between the areal gas content in the sediment (in L m^{-2}) and the maximum backscatter strength at a frequency of 200 kHz. We validated and applied this relationship for mapping the gas content in the sediment of the reservoir.

The calibration equation from Anderson and Martinez (2015) was tested with four in-situ measurements in a cross-section of the reservoir with water depth varying from 2 to 3.5 m (see Figure SI 32 and SI 33). The measurements were conducted on June 17th, 2021. A rope fixed to trees at both banks of the cross-section was used to maintain the boat at a fixed position during the measurements. At each location, stationary echo-sounder measurements with the EA400 were conducted for 1 min. After these measurements, a self-made device was used to capture the gas stored in the sediment by inserting an aluminum cylinder with an inner moving mesh (24.5 cm diameter and 35 cm length) into the sediment. The upper 30–39 cm of the sediment were mechanically disturbed using the vertically moving mesh, and the volume of gas that was released during the disturbance was measured. A detailed description of the cylinder is provided in the supporting information (Text SI B). A sediment depth of 30 cm was adopted to calculate the volumetric gas fraction from the estimated gas content. This sediment thickness was selected based on the vertical profiles of potential methane production obtained from incubated sediment cores, as we expect that the largest part of gas content in the sediment matrix is from the top productive sediment layer.

Auxiliary measurements

Temperature in the surface sediment was recorded at locations L01, L03, and L05 in 4 h time intervals by temperature loggers (HOBO loggers). The loggers were attached to the lower side of anchor weights used for bubble trap deployments. Water temperature was monitored at depth increments of 0.5 m by thermistors (RBR TR-1050) at 1 min time intervals. The thermistor chain was deployed downstream of location L05, closer to the dam (Figure 24). Vertical thermal stratification was assessed in terms of the relative water column stability (RWCS) also referred to as the relative thermal resistance to mixing (WELCH; NACZK, 1992):

$$\text{RWCS} = \frac{\rho_{bottom} - \rho_{surface}}{\rho_{4^\circ C} - \rho_{5^\circ C}},$$

in which ρ_{bottom} and $\rho_{surface}$ are the water densities at the bottom and at the surface respectively, $\rho_{4^\circ C}$ and $\rho_{5^\circ C}$ are the water densities at temperatures of 4 °C and 5 °C. The water density as a function of temperature was calculated using the UNESCO equation (FISCHER et al., 1979). For RWCS > 56.5 the reservoir is considered as stratified, RWCS < 16.3 indicates a mixed water column, and 16.3 < RWCS < 56.5 indicates partial stratification (BRANCO et al., 2009; GERARDO-NIETO et al., 2017).

Dissolved oxygen (DO) concentration was continuously monitored near the bottom (0.3 m above the sediment) and near the water surface (0.5 m depth). The oxygen loggers (MiniDot, PME) were deployed near the monitoring site L04 and recorded at 5 min intervals. Near the oxygen loggers, an upward-looking Acoustic Doppler Current Profiler (ADCP, Nortek AS – Signature 1000) was deployed from August 24th 2020 to July 13th 2021 at the bottom for recording vertical profiles of flow velocity (from approximately 0.6 m above the sediment to approximately 0.5 m below the water surface). The ADCP recorded vertical profiles of all three velocity components with a vertical resolution of 0.2 m and

a temporal resolution of 5 min. In addition, the ADCP also recorded bottom water temperature and pressure.

Time series of discharge and atmospheric pressure were available for the sampling period from stations maintained by the reservoir operator Wupperverband. Inflow discharge was recorded at 20 s time interval by a gauging station in the Wupper River, approximately 1.5 km upstream the reservoir. Atmospheric pressure was measured at 30 min time intervals by a weather station located 2 km from the reservoir. In addition, a weather station (MWS 9-5, Reinhardt System und Messelectronic GmbH) was installed next to the reservoir (approx. 70 m from monitoring location L02, see Figure 24 for location) for recording meteorological data at 3 m height above ground. Air temperature, barometric pressure, wind direction and velocity, and solar radiation are available from August 2020 to May 2021 with 15 min resolution.

Results

Reservoir conditions

The current velocities in the reservoir were correlated with inflow discharge (Spearman correlation rs $= 0.82$) with a mean values of $2.9\pm2.1\,\mathrm{cm\,s^{-1}}$ (average $\pm$ standard deviation). No significant correlation was found between wind velocity and current, nevertheless, periods were observed in which increased variability in the flow velocity were observed at high wind speed (see Figure S31).

The dissolved oxygen (DO) concentration near the bottom was found to be similar to the concentration recorded at the water surface for most of the monitoring period. For 76% of the time, the difference between surface and bottom DO was smaller than $1\,\mathrm{mg\,L^{-1}}$, except from February 2021 to July 2021, when the DO concentration at the bottom decreased to $0.22\,\mathrm{mg\,L^{-1}}$ (Figure S31). On average, the DO concentrations were $8.7\pm1.7\,\mathrm{mg\,L^{-1}}$ and $9.6\pm1.2\,\mathrm{mg\,L^{-1}}$ at the bottom and surface respectively. This weak vertical stratification or lack thereof was also observed for the vertical distribution of flow velocity and water temperature and can be attributed to the shallow depth of the reservoir.

Top sediment temperature from three different locations along the reservoir were similar and indicated a nearly homogeneous longitudinal sediment temperature distribution (Figure SI 31). The difference between daily mean sediment temperature at the shallowest (L01) and at the deepest (L05) sampling sites, was smaller than 1 °C during 88% of the time. The maximum sediment temperature of 17.4 °C was recorded at the deepest monitoring site (location L05) in August 2020, the lowest temperature of 1.6 °C was recorded in February 2021 at the shallowest sampling location (L01). The temporal dynamics of sediment temperature was similar to that in the overlaying water column. The relative water column stability indicates that the reservoir was thermally stratified (RWCS > 56.5) for 8% of the monitored period, particularly during the warmer months. For 59% of the time the reservoir was fully mixed (RWCS < 16.3), and in the remaining time the reservoir was classified as partially stratified (Figure SI 31).

Methane in the sediment: vertical profiles and spatial distribution of gas content

The potential methane production (PMP) from incubated sediment samples was generally higher in the top sediment layers and decreased towards deeper sediment layers. Most of the methane production occurred within the top 20 cm layer (Figure 25a). In deeper, less productive sediment layers, the incubations resulted in near-zero and sometimes slightly negative production rates. Although, the sediment preparation and incubation were conducted in a sealed, nitrogen-flushed glovebox, any remaining oxygen

concentration in the incubation glass vials may have influenced the estimates, particularly for low production rates. Furthermore, the closed-loop measurements in the gas analyzer, which have been reported to have an uncertainty range of 6–10% (WILKINSON et al., 2018), could also have contributed to a high relative uncertainty in low production rates, including also negative values. Longitudinally, slight variations were observed in PMP with higher production rates on the reservoir stretch between sites L02 and L04.

Loss on Ignition (LOI), which was used as a proxy for the distribution of organic matter in the sediment, was highest in the top sediment layers with a maximum value of 14.9% measured at monitoring location L04 (L04 right - Figure 25a and 25b). The carbon content (C) in the sediment had a significant positive correlation with LOI (Spearman correlation rs = 0.84 and $p = 9.3 \times 10^{-13}$). Spatially, both the C content and LOI in the sediment from the deeper monitoring site near the dam (L05), was higher than in the upstream locations closer to the river inflow (L01 and L02, Figure 25d). Furthermore, the PMP was positively corelated with LOI (rs = 0.3 and $p = 0.01$), nevertheless, no significant correlation was found between PMP and carbon content and PMP and carbon to nitrogen ratio (C:N) in the sediment (Figure SI 34).

Dissolved CH_4 concentration in the pore water slightly increased with increasing depth into the sediment, with the lowest values measured in the top 5 cm (Figure 25c). No consistent longitudinal pattern was observed in porewater dissolved CH_4 concentration.
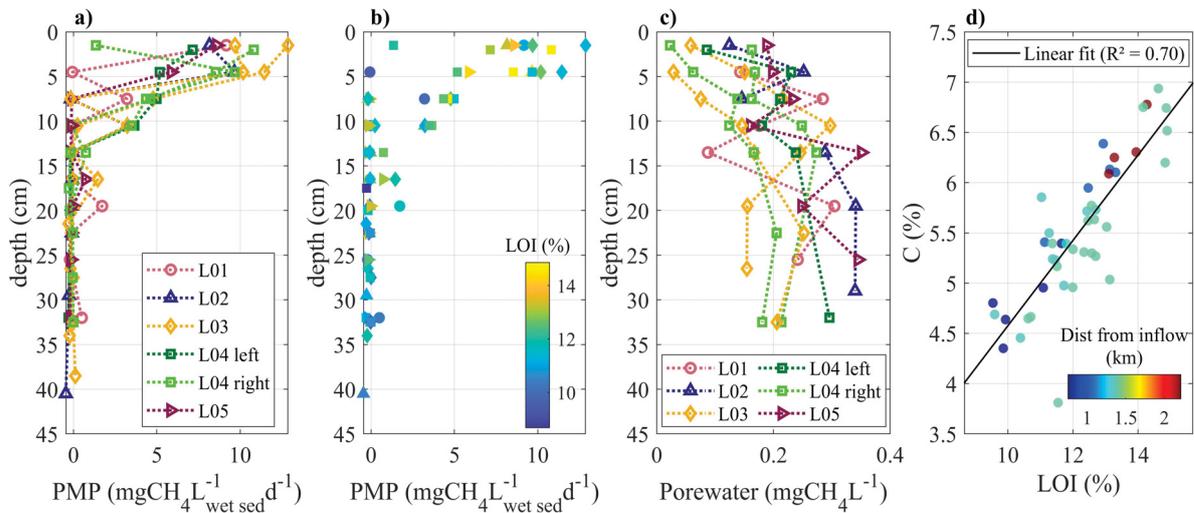
Figure 25 – **(a)** Vertical profiles of Potential Methane Production (PMP) in the sediment at the different monitoring locations (see legend for explanation of symbols and colors). **(b)** Vertical profile of PMP combined with the Loss on Ignition (LOI) for the sediment samples. Symbols represent the monitoring locations, see legend in **(a)**, and the color shows the LOI range. **(c)** Vertical profiles of dissolved methane concentration in the porewater in the sediment cores. **(d)** Comparison of carbon content (C) and LOI for all sediment samples. The symbol color scales with the distance of the sampling location from the river inflow and the solid line is the linear fit $C = 0.425 \times LOI + 0.326$.

The content of free gas in the sediment from the manual sampling ranged from $2.5 - 9.2\,\mathrm{L\,m^{-2}}$, with the lowest value found near the reservoir bank in the former riverbed where steeper slopes were found. The data from the manual gas volume sampling and maximum acoustic backscatter were at the upper end of the data reported by Anderson and Martinez (2015). A linear regression between the logarithm of the gas content and maximum acoustic backscatter including the data from the published study and our own estimates, had a coefficient of determination (R^2) of 0.91, which is comparable to the R^2=0.93 obtained by Anderson and Martinez (2015)(Figure SI 33). By applying the updated calibration curve,

spatial maps of gas content in the sediment were obtained for both surveys carried out in the reservoir in 2020 and 2021 (Figure 26a and 26b).

The mapping of gas content in 2020 revealed gas accumulation in locations near to the inner regions of the reservoir bends and coincide with regions of preferred sediment deposition. Comparing the estimated gas content in both surveys, it was found that on average the sediment contained $1.5\pm2.2\,\mathrm{L\,m^{-2}}$ gas in 2020, whereas in 2021 for the same area, the estimated gas content was $5.1\pm3.6\,\mathrm{L\,m^{-2}}$ (see selected areas in Figure 26a and 26b). This represents an average CH_4 content in free gas of $1.27\,\mathrm{gCH_4\,m^{-2}}$ and $4.42\,\mathrm{gCH_4\,m^{-2}}$, respectively in both years (assuming a CH_4 fraction of 58% within the free gas). The spatial distribution of sediment gas content differed between both surveys (Figure 26c and 26d). Grid cells with the highest gas content in 2020 did not have the highest gas content in 2021. In particular, the number of cells with high gas content (up to $10\,\mathrm{L\,m^{-2}}$) increased in 2021, indicating gas storage in the sediment in regions where no or less gas was detected in 2020. Longitudinal and transversal distribution of gas content in the sediment was analysed based on the more extensive survey conducted in 2020. Longitudinally, the averaged gas content increased towards the dam, and ranged from 0.7 to $5.8\,\mathrm{L\,m^{-2}}$ (see Figure SI 35). In the transversal direction, the gas content was more variable than in the longitudinal direction, especially in the deeper areas, where the gas content ranged from 1.4 to $11.4\,\mathrm{L\,m^{-2}}$ within a single cross section.
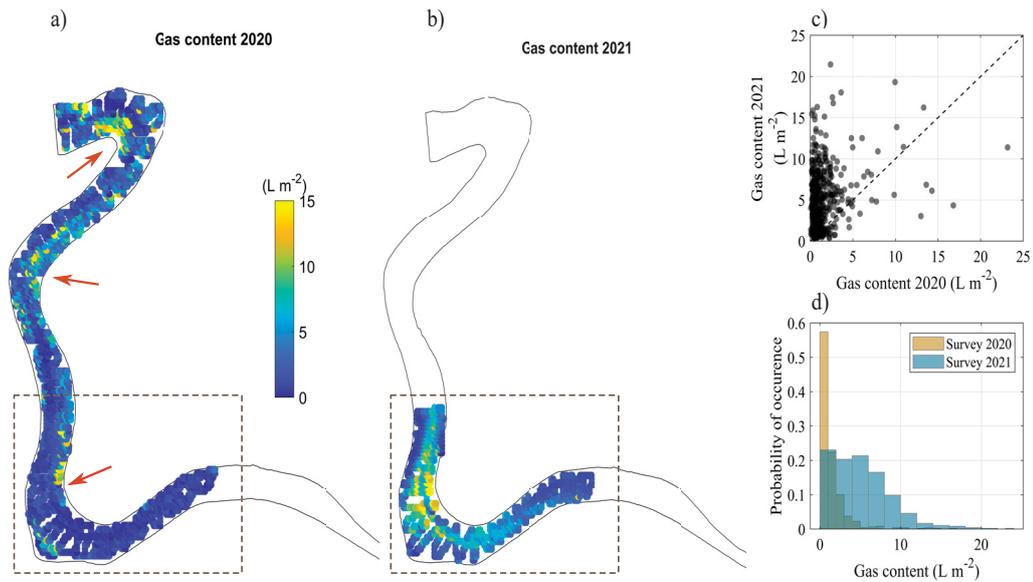
Figure 26 – Sediment gas content estimated from echo-sounder surveys conducted in **(a)** June 11th 2020 and (b) July 1st 2021, respectively. The solid black line shows the outline of the reservoirs and colored symbols show the mean gas content within 5 m by 5 m grid cells along the tracks of echo-sounding surveys. The red arrows in **(a)** point to regions of high gas accumulation. The dashed box shows the region where measurements are available from both years. **(c)** Scatter plot of gas content measurements in individual grid cells made in both years with the dashed black line indicating a 1:1 relationship. **(d)** Probability of occurrence histograms of estimated gas content in the sediment, with colors indicating the year of measurement.

Spatial variability and temporal dynamics of methane budget components

The CH_4 fraction within gas bubbles sampled during the monitoring period varied from 39% to 94% with a mean value of 58 ± 13%, which was then adopted in this study to calculate CH_4 ebullition fluxes and CH_4 content in the sediment. Temporally averaged ebullition fluxes were highest at the middle location L03 and lower at the upstream location L01, near to the dam (L05), and at the left side of

location L04 (L04 left) (average ebullition in mgCH$_4$ m^{-2} d^{-1}: L01 = 16.9 < L04 left = 17.6 < L05 = 21.5 < L02 = 39.2 < L04 right = 40.4 < L03 = 45.2). Combining the flux measurements from all monitoring sites (see Figure 27b), the range of ebullition fluxes was from 0–399.8 mgCH$_4$ m^{-2} d^{-1}, with a mean value of 31.5±45.3 mgCH$_4$ m^{-2} d^{-1} and a median flux of 12.6 mgCH$_4$ m^{-2} d^{-1}.
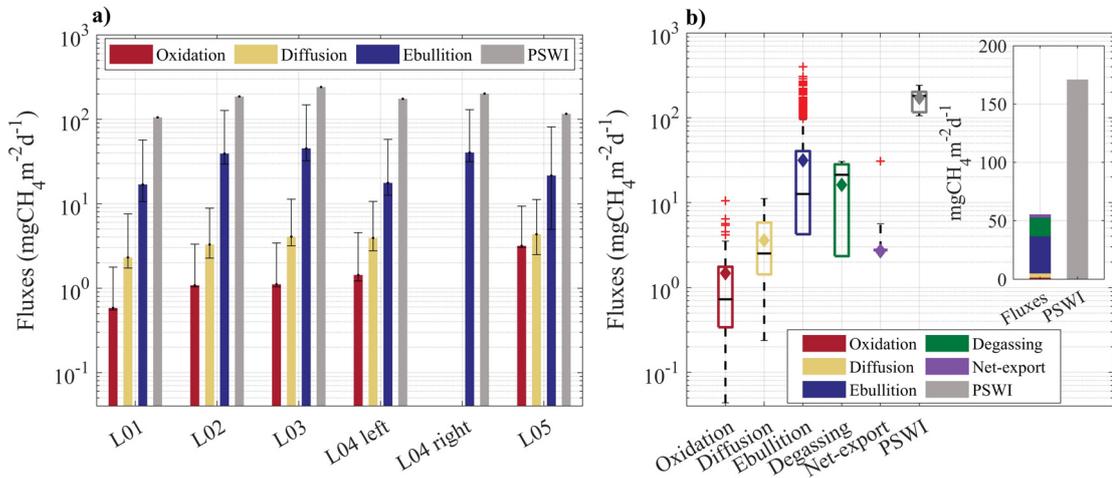
Figure 27 – **(a)** Temporal average of different methane fluxes monitored at the sampling sites along the reservoir. PSWI is the potential methane flux at the sediment water interface, calculated as the vertically integrated potential methane production rates and corrected to in-situ sediment temperature. Different flux components are shown by different color (see legend) and the vertical error-bars show flux standard deviation. **(b)** Boxplots of different flux components for the whole reservoir. The horizontal lines inside the boxes are the median values, whereas the mean is showed by the diamond symbol. The upper and lower limits of the boxes represent the 75th and 25th percentiles, respectively. The whiskers show the maximum and minimum values, and the red crosses are outliers. The inset figure with colored bar plot shows the mean fluxes stacked and the grey bar is the average PSWI from the monitoring locations in a linear scale.

The isotopic analysis showed that CH4 in gas bubbles collected near the bottom was consistently more depleted in 13C (mean δ^{13}C-CH$_4$ varied from −65.1‰ to −61.5‰, than in dissolved CH$_4$ in surface water (−57.5‰ to −53.8‰). The resulting mean oxidation fraction ranged from 0.23±0.12 at upstream location L01 to 0.38±0.16 at the deepest location L05 near the dam (Figure SI 36). The flux of CH$_4$ presumably lost to oxidation (hereafter referred to as the oxidation flux) strongly increased along the reservoir from negligible rates (0.6 mgCH$_4$ m^{-2} d^{-1}) near the inflow (L01), to 5 times higher fluxes (3.2 mgCH$_4$ m^{-2} d^{-1}) near the dam (L05, Figure 27a). No such longitudinal gradient was observed in the diffusive fluxes at the air-water interface. The mean diffusive flux was 3.6±2.8 mgCH$_4$ m^{-2} d^{-1}, about two times higher than the oxidation flux (1.5±1.9 mgCH$_4$ m^{-2} d^{-1}) (Figure 27b). Over the monitored period, both diffusion flux and oxidation flux were higher during the warmer months (Figure SI 37).

The mean degassing flux at the outflow spillway was 16.2±13.1 mgCH$_4$ m^{-2} d^{-1}. The largest fluxes were measured in 2020 during the warmer months from June to October, when the dissolved CH$_4$ concentration at the dam was highest (Figure SI 38). During May and June 2021, the water level in the main downstream reservoir was above the dam wall due to a flood, and therefore no degassing occurred. After June 2021 degassing measurements could not be continued due to access restrictions at the sampling locations.

The reservoir had a net export flux (difference between inflowing and outflowing dissolved load) ranging from −4.3 mgCH$_4$ m^{-2} d^{-1} to 30.7 mgCH$_4$ m^{-2} d^{-1} (mean value 2.7±11.7 mgCH$_4$ m^{-2} d^{-1}, Figure 27b). The downstream export flux was strongly affected by degassing as the dissolved CH$_4$ concen-

tration in the outflow was reduced during periods of intensified degassing (Figure SI 38). In contrast, when degassing was reduced, the net methane export reached $30.7\,\mathrm{mgCH_4\,m^{-2}\,d^{-1}}$.

The PMP was mostly restricted to the top 20 cm of the sediment (Figure 25a). The vertically integrated production rates (integrated over the top 30 cm layer) provided an estimate of the potential CH_4 flux at the sediment water interface (PSWI). The variations of mean PSWI among the monitoring locations were similar to those described above for PMP. When extrapolated to the entire reservoir, PSWI was ∼3 times greater than the sum of the monitored fluxes (ebullition + diffusion + degassing + oxidation + net export), see Figure 27b. When the median fluxes are considered, the difference between the PSWI and the observed methane fluxes increased further (median PSWI ∼5 times higher than the sum of median fluxes).

In terms of total CH_4 emissions (ebullition + diffusion + degassing), the reservoir emits on average $51.3\,\mathrm{mgCH_4\,m^{-2}\,d^{-1}}$, in which ebullition had the largest share (61.4%), followed by the degassing (31.6%), and lastly by the diffusive flux (7.0%). However, when the median fluxes are considered, the total CH_4 fluxes are estimated as $36.3\,\mathrm{mgCH_4\,m^{-2}\,d^{-1}}$, with degassing being the most important flux contributing with 58.4% to the total emissions, followed by ebullition (34.7%), and diffusion (6.9%). One important aspect of the studied reservoir is the presence of the wastewater treatment plant (WTP) with its effluent discharge located upstream of monitoring site L02. From our dataset, it was challenging to isolate any specific impact of the WTP discharge on CH_4 emissions. Dissolved CH_4 concentrations, as well as CH_4 fluxes, carbon and nitrogen content in the sediment, and PMP measured at L02 were not particularly different from the other monitoring sites (see in Figure 27a).

All components of the CH_4 budgets showed pronounced seasonal variations (Figure 28). The total emissions were lower during the colder months (December to May), which coincides with lower PMP. Over all seasons, PSWI and ebullition fluxes were significantly correlated (rs = 0.8). Similarly, a positive correlation was found between diffusive and ebullition fluxes (rs = 0.7, see Figure SI 39). For the mean fluxes, degassing was more important than ebullition during periods when ebullition flux was low, for instance in January 2021 F_{ebul} $13.2\,\mathrm{mgCH_4\,m^{-2}\,d^{-1}}$ < F_{deg} $20.6\,\mathrm{mgCH_4\,m^{-2}\,d^{-1}}$.
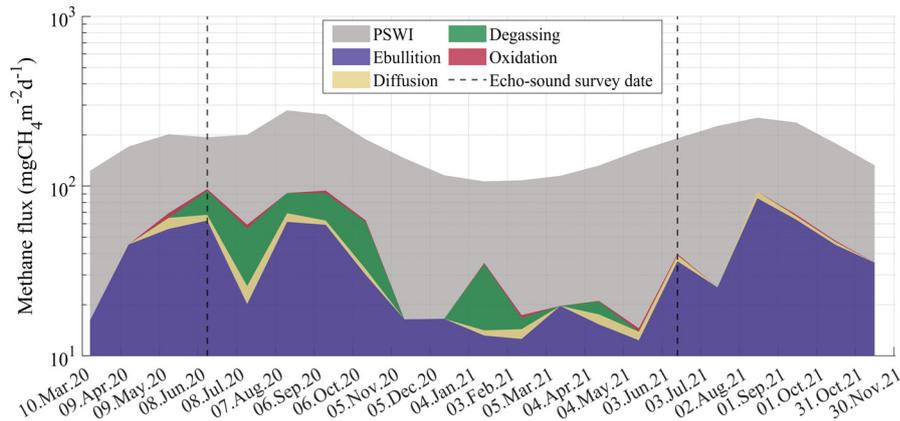
Figure 28 – Seasonal variations of the measured components of the methane budget with monthly resolution. PSWI is the potential methane flux at the sediment water interface shown as the grey area at the background. Ebullition, diffusion, degassing, and oxidation fluxes are stagged values. The advective fluxes (net export) were for most of the time negative, which indicates to accumulation of CH_4 in the reservoir or its release to the atmosphere through degassing in the dam. Therefore, the next export of CH_4 was not included in the stagged values. However, they are shown in Figure SI 38. The vertical dashed lines indicate the dates when the echo-sound surveys for the estimation of gas content in the sediment were conducted.

Methane budget and CH4 storage in the sediment

We compared the CH_4 budget components for the two months when the acoustic surveys were conducted (June 2020 and June 2021) to the estimated sediment gas content for the reservoir region marked in Figure 26, (detailed information are summarized in Table 6). The estimated gas volume was converted to CH_4 mass using the ideal gas law with the locally measured environmental parameters and assuming a fraction of 58% CH_4. In June 2020 and 2021, the average CH_4 as free gas in the sediment matrix was $0.7 \, gCH_4 \, m^{-2}$ and $2.6 \, gCH_4 \, m^{-2}$.

For both months (June 2020 and June 2021) similar temperatures were recorded, nevertheless in 2021 the water level was $0.5 \, m$ higher than in 2020. In terms of the CH_4 budget components, all fluxes were higher in 2020, resulting in higher total CH_4 emissions from the reservoir in that month ($93.8 \, mgCH_4 \, m^{-2}$ in June 2020 and $39.1 \, mgCH_4 \, m^{-2}$ in June 2021).

The ratio of the areal CH_4 content as free gas in the sediment and measured fluxes represent mean turnover times that are associated with a recharge of the sediment with newly produced gas (PSWI), or by releasing the stored gas by ebullition. According to these ratios, the free CH_4 gas measured in the sediment matrix represents the cumulative potential CH_4 production of 3.8 and 13.4 days and can support 11.7 and 70.9 days of average ebullition flux in the two years, respectively (Table 6).

Table 6 – Summary of the environmental parameters, measured methane fluxes, estimated gas content in the sediment, and calculated ratios between gas content in the sediment and relevant CH_4 fluxes (representing turnover time scales) for June 2020 and June 2021. P_{atm} is the mean atmospheric pressure recorded by the weather station installed near the reservoir, $P_{hydrostatic}$ is the mean hydrostatic pressure calculated using water depth, PSWI is the potential methane flux at the sediment water interface, and Total Emissions is the sum of ebullition, degassing, and diffusion CH_4 fluxes. When available we also provide the values' standard deviation. The advective CH_4 flux in 2021 was not measured (NA – Not Available).

	June 2020	June 2021
Environmental parameters		
Water depth (m)	2.5	3
P_{atm} (kPa)	98.4±0.7	98.8±0.43
$P_{hydrostatic}$ (kPa)	24.5	29.4
Bottom sediment temperature (° C)	12.1±0.4	11.9±0.7
Methane Fluxes		
PSWI ($mgCH_4 \, m^{-2} \, d^{-1}$)	194.1±54.7	191.3±55.4
Ebullition ($mgCH_4 \, m^{-2} \, d^{-1}$)	62.7±84.9	36.1±49.3
Diffusion ($mgCH_4 \, m^{-2} \, d^{-1}$)	5.0±2.1	3.0±0.6
Degassing ($mgCH_4 \, m^{-2} \, d^{-1}$)	26.1	0
Net-export (advection) ($mgCH_4 \, m^{-2} \, d^{-1}$)	−0.9	NA
Oxidation ($mgCH_4 \, m^{-2} \, d^{-1}$)	2.2±1.9	0.7±0.4
Total Emissions ($mgCH_4 \, m^{-2} \, d^{-1}$)	*93.8*	*39.1*
Free gas in the sediment: echo-sound estimation		
Gas content in the sediment ($L \, m^{-2}$)	1.5±2.2	5.1±3.6
Methane free gas in the sediment ($mgCH_4 \, m^{-2}$)	735.9	2561.3
Turnover time		
CH_4 free gas in the sediment / PSWI (d)	3.8	13.4
CH_4 free gas in the sediment / Ebullition (d)	11.7	70.9

Temporal variability of ebullition

As pointed out above, the ebullition flux was a relevant CH_4 emission pathway in the reservoir, which affects the gas content in the sediment while also being highly variable in time (Figure 27b). High-resolution (daily) mean values of spatially averaged ebullition fluxes were further analyzed to investigate the main controls on ebullition dynamics. Initially, a correlation matrix with the Spearman rank correlation was calculated for all monitored variables, (Figure SI 40). Ebullition flux had a significant positive correlation (for a significance level of 5%) with variables related to temperature (water temperature rs = 0.55, sediment temperature rs = 0.54) and thermal stratification (RWCS, rs = 0.45). On the other hand, significant negative correlations were observed between ebullition and total pressure at the bottom (rs = −0.49), dissolved oxygen concentration at bottom (rs = −0.36), current speed (rs = −0.20), atmospheric pressure (rs = −0.24), atmospheric pressure change (rs = −0.30), and discharge (rs = −0.22).

A principal component analysis (PCA) was then performed, in which the main aforementioned parameters were considered with the data points seasonally grouped (Figure 29a). Seasonally influenced variables (sediment temperature, bottom velocity, discharge, and dissolved oxygen), mostly contributed to the first PCA component, whereas the pressure related terms (total pressure, atmospheric pressure change, and rainfall) were more aligned with the second principal component. Moreover, the approximate angle of 45° of ebullition with the two principal components suggests that ebullition is affected by both components.
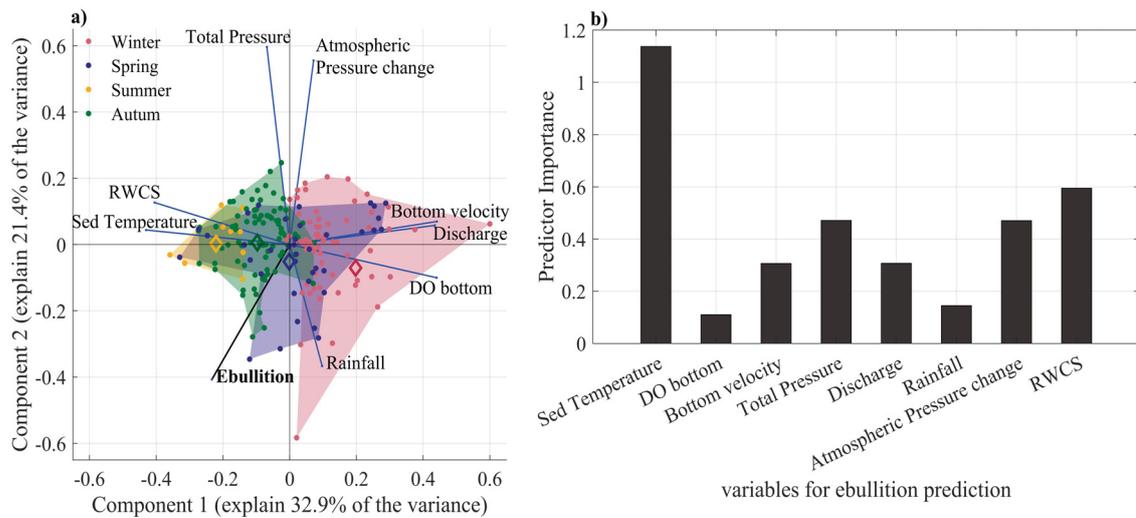
Figure 29 – **(a)** Results of a Principal Component Analysis (PCA) with the first two principal components. The dots showdaily values, which were seasonally grouped by different colors (see legend) as: winter (December–February), Spring (March–May), Summer (June–August), and Autum (September–November). **(b)** Importance of each variable on the prediction of methane ebullition flux from a decision tree model.

A decision tree classification model was applied to analyse the relative importance of ebullition predictors, in which the input variables were the same as in the PCA. According to the results, the most important predictor for variations in daily mean ebullition rates was sediment temperature, followed by relative water column stability (RWCS), total pressure, and atmospheric pressure change. Dissolved oxygen concentration at the bottom (DO bottom) and rainfall were classified as the least important ebullition predictors (Figure 29b).

Lastly, three statistical models were applied to test whether and how well ebullition variability could be explained by variations in the observed environmental variables presented in Figure 29. A

multiple linear regression with log transformed daily ebullition flux resulted in a R^2 of 0.49 and a stepwise linear regression with log transformed daily ebullition flux resulted in a R^2 of 0.47. For the stepwise linear regression, four variables were maintained in the model based on the p-value (sediment temperature, DO at bottom, total pressure, and atmospheric pressure change). The decision tree model resulted in the best coefficient of determination ($R^2 = 0.66$) between measured and predicted ebullition flux (Figure 30a). The statistical models could well represent the main temporal patterns of the measured ebullition flux, nevertheless, the greater ebullition peaks were underestimated by the models applied (Figure 30b).
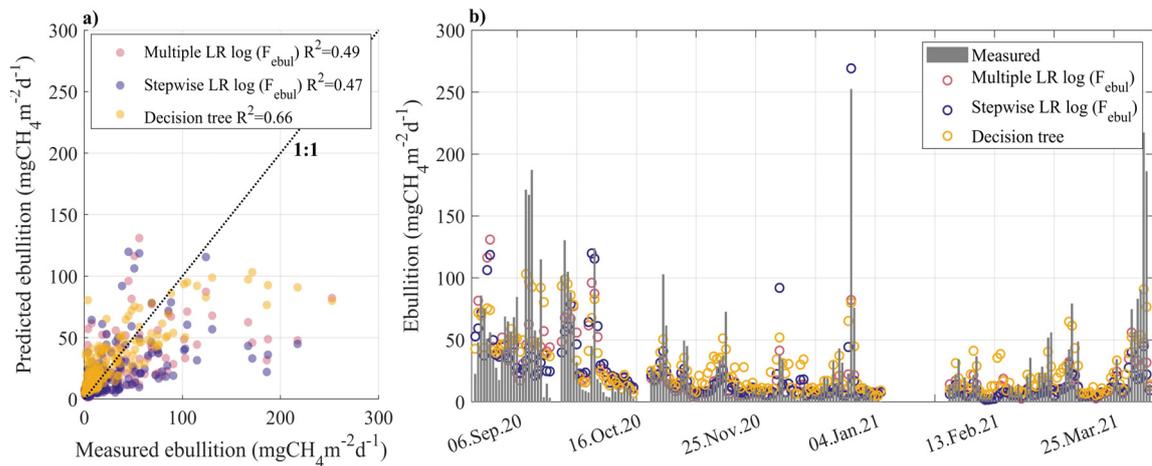
Figure 30 – **(a)** Comparison of measured and predicted daily mean ebullition flux for three statistical models indicated by the different color (see legend for model name and coefficient of determination (R^2). The black dotted line shows a 1:1 relationship. **(b)** Daily fluxes of measured and predicted ebullition fluxes from the three models tested.

Discussion

Spatial distribution of methane in the sediment

The range of potential methane production (PMP) rates in the sediment of the reservoir (up to $12.8\,\mathrm{mgCH_4\,L^{-1}\,d^{-1}}$) was lower than the range reported for other impoundments in the same region (up to $25.0\,\mathrm{mgCH_4\,L^{-1}\,d^{-1}}$ in Wilkinson et al. (2015)) and higher than the values reported for a subtropical reservoir in Brazil (up to $6.0\,\mathrm{mgCH_4\,L^{-1}\,d^{-1}}$ in Marcon et al. (2022b)). The highest PMP rates were measured in the top sediment layers, which had higher organic matter content (LOI). This suggests that methanogenesis in the reservoir was fuelled by the supply of fresh organic matter to the sediment surface, as other studies showed that the input of both terrestrial and phytoplankton organic matter enhances CH_4 production (BERBERICH et al., 2020; GRASSET et al., 2021).

Longitudinal variations in PMP were mainly linked to sediment deposition patterns, as in our shallow system the sediment temperature was nearly homogenous across the monitoring sites. Reservoir geomorphology and sedimentation dynamics are key aspects for methane emission hot-spots in reservoirs (DELSONTRO et al., 2011; LINKHORST et al., 2021). The narrow-elongated shape of the reservoir with one main inflow led to sediment accumulation in the upstream regions near the inflow and in the regions outside the former river Talweg (mostly in the inner parts of the reservoir bends), which explains the slightly lower PMP at monitoring sites in the old riverbed (L01, L04 left, and L05). The free gas in the sediment estimated from echo-sounder measurements followed similar longitudinal patterns. The

higher spatial resolution measurements showed preferred accumulation of free gas in the inner parts of the reservoir bends (Figure 26a).

The mapping of gas content in the sediment also revealed strong temporal heterogeneity. We expected that the amount of free gas in the sediment depends on sediment mechanical properties, and on the sources and sinks of methane (i.e. CH_4 production and emission pathways). Temporally, we attribute the variability mainly to the fluxes transporting methane out of the sediment matrix, which is further discussed in a following section.

The average gas content in the sediment ($1.5\pm2.2\,L\,m^{-2}$ in 2020 and $5.1\pm3.6\,L\,m^{-2}$ in 2021) was in the same range as the average reported for a subtropical reservoir ($4.4\,L\,m^{-2}$ and $4.6\,L\,m^{-2}$ Marcon et al. (2022b). By assuming that the gas content is mainly distributed over the most productive top 30 cm of the sediment, the corresponding volumetric gas fraction were 0.5% and 1.7% in 2020 and 2021 respectively. These fractions are similar to the fraction estimated for Lake Kinneret ($< 1\%$ and up to 3.8% Katsnelson et al. (2017), Uzhansky et al. (2020)), and one order of magnitude smaller than the volumetric gas content reported for different sediment types under laboratory conditions (LIU et al., 2016). Nevertheless, in this study the depth in which the gas voids are distributed could not be derived from our echo-sounder data set, as there is still no well-established direct method. In this way the actual gas fraction may differ, depending on how the gas voids are vertically distributed in the sediment. Other studies reported the depth distribution of gas voids is various depths of the sediment. Dück et al. (2019b) detected the presence of bubbles starting from 4 cm below the sediment surface in freeze-cores. Under laboratory conditions, Liu et al. (2018) observed gas voids in sediment depths smaller than 4 cm, which originated from local methane production or vertical migration. For lake Kinneret, Katsnelson et al. (2022) estimated the thickness of the gassy sediment layer to be in the range of 20–40 cm.

We highlight the potential of echo-sounder techniques to remotely access gas distribution in the sediment without disturbing the sediment. Only few studies addressed the gas content in sediment of freshwater ecosystems under in-situ conditions. Katsnelson et al. (2017) and Katsnelson et al. (2022) determined the gas fraction and the thickness of the gassy sediment layer based on sound velocity, amplitude and frequency analysis of the bottom reflection in lake Kinneret. Anderson and Martinez (2015) proposed a calibration curve for echo-sounder measurements at the 200 kHz frequency, in which the volumetric gas content per unit area is simply estimated based on the maximum backscatter. Our in-situ measurements of gas content fitted well to the calibration curve from Anderson and Martinez (2015) and were within the upper region of the calibration curve (Figure SI 33), close to the data points from the Hodges Reservoir studied by the authors. This could indicate that both reservoirs have similar sediment properties, but also to the potential of stablishing an extensive procedure for measuring in-situ sediment gas content in inland waters. The latter is a crucial aspect, as the alternative methods currently available depend on extraction of sediment cores combined with x-ray Computed Tomography (x-ray CT) scanning (DÜCK et al., 2019b), or ground penetrating radar, which is restricted to shallow freshwater (MUSTASAAR; COMAS, 2017).

Spatial and temporal variations of methane budget components

Considering a CH_4 balance for the reservoir we initially hypothesised that the potential methane flux at the sediment water interface (PSWI, which is the vertically integrated PMP) was in the same order as the sum of CH_4 fluxes, including the oxidation flux. Nevertheless, on a monthly basis, the mean PSWI was a factor of 3 (5 for median) greater than all CH_4 sinks to the water column combined (ebullition + diffusion + degassing + oxidation + net export). This is contrasting to the findings from Wilkinson et al. (2015) who found comparable PSWI to the measured ebullition flux in a similarly shallow (4 m water

depth) river impoundment.

The sediment cores sampled had a maximum length of 40.5 cm, which is relatively short compared to other studies (e.g., Wilkinson et al. (2015) sampled cores up to 90 cm in length). The shorter length was considered because of lower sedimentation rates in the studied reservoir, which received a mean inflow discharge that is one order of magnitude smaller than in the river impoundments studied by Wilkinson et al. (2015). Nonetheless, it is expected that the deeper sediment layers (beyond 40 cm) would have lower potential methane production (PMP), aligning with the vertical trends observed in our sediment cores (Figure 25a) and supported by findings from other studies (ISIDOROVA et al., 2019; WILKINSON et al., 2015).

We suggest that the gap in the CH_4 budget can be explained by variable sediment gas storage (discussed below), as well as a potential underestimation of CH_4 oxidation rates. In lakes it has been found that 50 to 95% of the produced CH_4 can be oxidized in the oxic upper sediment layers (BASTVIKEN, 2009), which is high compared to the oxidized fraction estimated for the reservoir studied here (0.8±0.6%). For 88% of the monitored period, the dissolved oxygen (DO) concentrations near the bottom were higher than $7\,mg\,L^{-1}$ (Figure SI 31) and potentially supported a sufficient oxygen flux into the sediment. The sediment-water oxygen fluxes in areas of sediment deposition and intense CH_4 ebullition in an impounded river of comparable water depth have been found to be around $0.5\,gO_2\,m^{-2}\,d^{-1}$ during low-flow conditions (LORKE et al., 2012). If exclusively used for CH_4 oxidation, this flux can support an oxidation flux of $125\,mgCH_4\,m^{-2}\,d^{-1}$, which is in the order of the budget gap ($111.9\pm38.2\,mgCH_4\,m^{-2}\,d^{-1}$. Moreover, the average stable carbon isotopic composition of CH_4 ($\delta^{13}C$-CH_4, see Figure SI 36) measured in bubbles collected near the bottom was less depleted in comparison to bottom waters of lakes in Sweden (down to −80.6‰Bastviken, Ejlertsson and Tranvik (2002)) and in gas bubbles from bottom sediments in arctic lakes (down to −79.7‰Walter et al. (2008)). The comparably low depletion found in bubbles at our study sites suggest that CH_4 oxidation in the sediment has caused a change in $\delta^{13}C$-CH_4 in gas bubbles, as oxidation of CH_4 leads to an increase in the $\delta^{13}C$-CH_4 signature (BASTVIKEN; EJLERTSSON; TRANVIK, 2002; SAWAKUCHI et al., 2016). These oxidative losses were not accounted for in the oxidation rates estimated from the difference of $\delta^{13}C$-CH_4 in bubbles and at the water surface and may have caused severe underestimation of the oxidation fluxes. Additionally, the data gaps or limitations in the temporal-spatial resolution of sampling may have affected the flux estimates by not capturing hot moments of ebullition, diffusion, or degassing emissions. However, we also acknowledged that uncertainties in the estimated PMP and fluxes might have contributed to the imbalance in the CH_4 budget.

Consistent longitudinal gradients were detected in diffusive and oxidation CH_4 fluxes, in which both increased towards the dam (Figure 27a and Figure SI 37), probably due to the accumulation of dissolved CH_4 in the water along the reservoir. In contrast, CH_4 ebullition was larger at the monitoring sites located at the mid-stretch of the reservoir (from sites L02 to L04) where higher PSWI was also detected (significant correlation found, rs = 0.79, between Ebullition and PSWI, Figure SI 39). The effect of the wastewater treatment plant (WTP) discharge on CH_4 fluxes could not be disentangled from the general longitudinal trends. Nevertheless, we cannot exclude the possibility that WTP discharge influences CH_4 dynamics in water bodies. In smaller streams, Alshboul et al. (2016) observed increased dissolved CH_4 concentrations from effluent discharge, in which the CH_4 concentration had a linear dependence on the organic load of the wastewater.

Unfortunately, due to depth restrictions for the deployment of bubble traps, ebullition could not be measured at the shallow (water depth <1.0 m) upstream regions of the reservoir, and therefore, these regions had to be excluded from the CH_4 budget. Temporal variability was found in all measured CH_4 budget components. The largest fluxes were recorded during the warmer months, which is explained by the exponential dependence of CH_4 production on temperature (ABEN et al., 2017; WILKINSON;

BODMER; LORKE, 2019). The high frequency variation of ebullition flux is analysed below.

Taking into account the CH_4 budget for the entire reservoir, represented on Figure 27b, the total CH_4 emissions (ebullition + diffusion + degassing) of the reservoir ($51.3\,mgCH_4\,m^{-2}\,d^{-1}$ mean fluxes and $36.3\,mgCH_4\,m^{-2}\,d^{-1}$ median fluxes) was 3–5 times lower than the average areal emissions reported for reservoirs worldwide (DEEMER et al., 2016; ROSENTRETER et al., 2021). In our study, ebullition and degassing had the main share accounting for 93% of the total CH_4 emissions, contributing respectively to 61.4% (34.7% median fluxes) and 31.6% (58.4% median fluxes). Both degassing and ebullition fluxes are variable across different reservoirs. Median degassing flux was reported as one order magnitude lower than ebullition flux (DEEMER et al., 2016), however, a modelling approach showed that for stratified hydropower reservoirs the degassing can be up to four times higher than ebullition (DELWICHE et al., 2022). Temporally, considering monthly fluxes, the share of ebullition and degassing to the total CH_4 emissions was variable. In July 2020 and January 2021, when there was a reduction of ebullition, degassing was the dominant CH_4 emission pathway.

Linking methane budget components to gas storage in the sediment

To the best of our knowledge, this is the first time that temporal variability of in-situ gas content in the sediment was linked to the CH_4 balance in an aquatic ecosystem. The average gas content in the sediment was remarkably different between both surveys (by a factor of $\sim$3.5 between 2020 to 2021). Differences in sediment temperature between both years could not explain the change ($0.2\,°C$ between the years). We hypothesize that the dynamics in processes removing CH_4 from the reservoir (ebullition + diffusion + oxidation + degassing) lead to a reduction of free gas in the sediment matrix. Consequently, the gas storage in the sediment increases when the efflux of CH_4 is diminished (see Figure 28 and Table 6 for contrasting CH_4 fluxes for the two periods when gas content in the sediment was estimated).

The ratio between estimated gas content in the sediment and the PSWI revealed that the sediment had stored an amount of CH_4 potentially produced in $\sim$4 days in June 2020 up to 13 days in June 2021. The gas stored in the sediment for both periods (June 2020 and June 2021), represented 12 to 71 days of averaged ebullition flux respectively, and therefore, even without production, the sediment could potentially supply gas for the mean ebullition flux of more than two months.

The gas storage in the sediment matrix (such as found in June 2021), suggests that temporarily reduced CH_4 fluxes do not necessarily decrease the reservoir's potential contribution to the CH_4 emissions, as the stored gas can later be released to the water column, depending on external triggers. The gas retention capacity of the sediment matrix can affect the CH_4 balance by affecting oxidation and diffusion, which in turn can impact the CH_4 content in the bubbles leaving the sediment, the sediment mechanical properties (SILLS et al., 1991; WHEELER, 1988), and the timing of ebullition events. Our findings suggest that the gas storage in the sediment was connected to the CH_4 fluxes from the reservoir, emphasizing its significance as a component of the CH_4 budget and a potential contributor to the observed mismatch in the balance of production and emission rates (Table 6). Moreover, it may mask the dependence of ebullition on the environmental variables, which are discussed in the following section.

We suggest that gas storage in the sediment should be considered in modelling approaches of CH_4 dynamics and emissions from lakes and reservoirs, similar to ebullition models for terrestrial wetlands (MA et al., 2022; PELTOLA et al., 2018). Sediment gas storage can be described as a buffer with a maximum holdup capacity for gas, which is recharged by production and depleted by various outflows (i.e., ebullition, diffusion, and oxidation). In turn, it is controlled by sediment properties such as grain size distribution (JAIN; JUANES, 2009; LIU et al., 2016), sediment bulk density and fracture toughness (KATSMAN, 2015), and environmental conditions of temperature and pressure. Peltola et al. (2018)

tested different model approaches for estimating CH_4 ebullition from boreal wetlands and showed that adding a volume threshold for gas in the sediment led to improved simulation results of ebullition fluxes.

In our study, the areal gas content was converted to a volumetric content based on the depth of PMP. In a recent study Katsnelson et al. (2022) proposed a method to determine the thickness of the gassy layer of the sediment from measurements combining a sound transducer and a hydrophone with sound pulses in the frequency range of 0.3–3.5 kHz. Nevertheless, obtaining in-situ vertical distribution of gassy sediment layers is still an open issue.

Controls on methane ebullition and temporal dynamics

Since ebullition flux serves as the primary pathway for CH_4 outflow from the sediment, it directly affects the dynamics of gas storage in the sediment. The quasi-continuous time-series of ebullition rates measured by automatic bubble traps were used to analyze the drivers of their temporal variations. Principal component analysis (PCA) showed that the drivers of ebullition fluxes can be classified into two groups: one related to temperature and another linked to pressure. While the sediment temperature enhances ebullition flux due to its relationship to methane production (ABEN et al., 2017; WILKINSON; BODMER; LORKE, 2019), the decrease in pressure at the sediment water interface can trigger bubble release from the sediment, such pressure reductions can be due to water level oscillations (MAECK; HOFMANN; LORKE, 2014) or atmospheric pressure variations (MARCON et al., 2019; NATCHIMUTHU et al., 2016). The significance of sediment temperature, relative water column stability (RWCS), total pressure, and pressure change in explaining the temporal variability of ebullition was further confirmed by a decision tree model. These parameters were found to be most important for explaining the observed variability of ebullition compared to the other environmental variables.

We observed intensified ebullition during periods of more stable density stratification (higher RWCS). Density stratification attenuates the vertical transport and the exchange of gases and substances through the water column (GUSEVA et al., 2020; VACHON et al., 2019). The increased CH_4 concentration in the water column leads to a reduction of CH_4 diffusion from the sediment (LANGENEGGER et al., 2019) and increased oxidation rates (VACHON et al., 2019; ZIMMERMANN et al., 2021). In the case of the pre-dam, the RWCS was controlled by temperature, but also affected by the inflow discharge (see Figure SI 40 — RWCS was negatively correlated to discharge). Higher discharge from the inflow river led to an increase in the current velocity, which contributes to water column mixing.

The tested regressions and decision tree models could explain 47% to 66% of ebullition variability with a better performance of the decision tree model (Figure 30a). This better performance of the decision tree can be mostly attributed to the model's capability of considering non-linear relationships between the variables. Using a multiple regression model, DelSontro et al. (2016) explained 52% of ebullition variability from different ponds and lakes based on sediment temperature and total phosphorous. Whereas for a larger data set of different reservoirs, Prairie et al. (2021) predicted ebullition flux as a function of reservoir littoral area and global horizontal radiance explaining 26% of its variability. Our results suggest that the inclusion of other parameters such as atmospheric pressure and water column stability can improve the prediction of ebullition even further.

Conclusions

Based on extensive field monitoring, we analyzed the CH_4 budget of a small and shallow temperate reservoir. From the vertical profiles of potential methane production (PMP) and LOI, we showed that

the top organic matter rich sediment layers had the greatest PMP. A large gap between potential methane fluxes at the sediment water interface (PSWI) and measured fluxes was identified, which could be caused by a combination of factors including sediment gas storage and the underestimated CH_4 oxidation in the sediment.

Longitudinally, diffusive and oxidation CH_4 fluxes strongly increased towards the dam, whereas ebullition was larger at the mid-stretch of the reservoir at locations with higher PMP. Considering the total CH_4 emissions from the reservoir, ebullition and degassing accounted for 93% of the emissions. The relative share of each flux to the emissions varied with time. The combination of different data analysis methods confirmed the complex nature of ebullition and its dependence on several parameters. Sediment temperature, total pressure (hydrostatic + atmospheric), atmospheric pressure change, relative water column stability, and bottom velocity were the main controlling factors for the temporal variations in daily ebullition rates. The combination of environmental parameters in a decision tree model explained 66% of ebullition variability.

The gas content in the sediment could be estimated from an acoustically derived parameter (maximum backscatter), in which a previously reported empirical relationship was validated and adopted. Gas accumulation of up to $15\,\mathrm{L\,m^{-2}}$ were observed in regions of preferred sediment deposition. The temporal variability of gas content in the sediment could be linked to the monitored methane budget components, in which periods of intensified emissions resulted in depletion of the gas stored in the sediment. Nonetheless, when emissions are damped, the sediment matrix can store the cumulative CH_4 production of several days, which in turn can maintain mean ebullition fluxes over months. We discussed the possible effect of sediment gas storage on the CH_4 budget in the shallow lakes and reservoirs and we suggest that its implementation in process-based model can improve predictions of CH_4 emissions from these aquatic ecosystems.

In addition, we confirmed the potential of echo-sounding to access the gas content in the sediment matrix, which contributes to the understanding of methane spatial variability and its temporal dynamics in inland waters. However, further investigations and calibrations are still necessary for the application of the echo-sounder for different systems and for describing the vertical distribution of gas voids in the sediment matrix.

Supplementary material

In this section it is presented the supplementary material for the paper 'Linking Sediment Gas Storage to the Methane Dynamics in a Shallow Freshwater Reservoir'. The publication was submitted to the *Journal of Geophysical Research: Biogeosciences* and is currently under review.

This Supporting Information contain supporting text and figures for the main manuscript. It includes a detailed explanation of in-situ measurements and methane flux calculations for the Wupper pre-dam (Text S1), the procedures followed for sediment analysis (Text S2), and a description of gas sampling in the sediment for determining areal gas content (Text S3). Figures SI 31– SI 40 present data, measurement details and statistical analysis results. Descriptions are provide in each figure caption.

Text S1: calculation of methane fluxes

In this section we present extended information on in-situ measurements and calculation of methane (CH_4) ebullition, diffusive gas exchange at the water surface, advective fluxes, degassing at the outflow spillway, and oxidative rates.

Methane ebullition was continuously monitored by bubble traps deployed at five monitoring locations (from L01 to L05, see Figure 24 in the main document). The bubble traps had a funnel diameter of 1 m, were submerged, maintained vertically suspended in the water column by a surface buoy and two side buoys attached to anchor weights to fix the instrument location.

At each monitoring site, an optical bubble trap (OBT) was deployed. The device was described in Delwiche, Senft-Grupp and Hemond (2015) and Delwiche and Hemond (2017). In summary, three pairs of optical sensors controlled by an Arduino microcontroller are used to detect individual bubbles that were funneled through a glass tube (0.5 cm inner diameter). The start and end time of bubbles passing by the sensors were recorded and used to calculate the rise velocity of each bubble. The bubble volume is then calculated from the rise velocity and the tube diameter.

In addition to the OBTs, at locations L01 and L03 automatic bubble traps (ABT–Senect GmbH, Germany) were deployed. The ABTs were deployed with buoys in the same arrangement as the OBTs. In the ABTs, the gas volume collected by the funnel is accumulating over time and vented, if the collection cylinder is filled. The stored gas volume is measured at fixed time intervals (from 1 to 60 seconds) by a differential pressure sensor (MAECK; HOFMANN; LORKE, 2014).

For both the OBT and the ABT, methane ebullition rate (F_{ebul}) in $mgCH_4$ m^{-2} d^{-1} was calculated by applying the ideal gas law, knowing the methane fraction in the bubbles (f_{CH_4}), the funnel area ($A_{funnel} = 0.78\,m^2$), and the time interval ($\Delta t = 1$ day):

$$F_{ebul} = M_{CH_4} \frac{PV}{RT} f_{CH_4} \frac{1}{A_{funnel} \Delta t} 1000,$$

where M_{CH_4} is methane molar mass ($16\,g\,mol^{-1}$), P is pressure in Pa, V is the total gas volume in m^3 captured within the time interval Δt, R is the gas constant ($8.31\,J\,mol^{-1}\,K^{-1}$, T is temperature in K, and the value 1000 is a factor for unit conversion from g to mg. The methane fraction within the gas bubbles (f_{CH_4}), was measured monthly for gas samples captured during maintenance of the bubble traps. For that, a weight attached to a rope was used to disturb the bottom sediment causing the release of bubbles from the sediment matrix. The rising bubbles were captured near to the water surface using a plastic funnel fitted to an initially water-filled glass vial, that was kept completely submerged. The gas captured inside the glass vial, was then transferred to 10 ml glass vials pre-filled with saturated salt solution. Approximately 5 ml of gas was transferred using a syringe and an additional needle placed in the butyl stopper of the vial to allow water drainage. The vials containing the gas samples were kept upside-down to avoid leakage. In the laboratory, the methane concentration in the headspace gas was measured using the Los Gatos (UGGA, Los Gatos Research Inc.) gas analyzer, in a closed-loop arrangement as described by Wilkinson et al. (2018).

The diffusive flux of CH_4 at the air-water interface was estimated from monthly measured dissolved CH_4 concentrations in the surface water using the thin boundary layer (TBL) method. For the TBL a two layer system (water-air) is considered and the diffusive flux of methane (F_{dif}) crossing the interface can be calculated according to Liss and Slater (1974) as:

$$F_{dif} = k(C_{CH4,W} - C_{CH4,eq}),$$

in which k is the gas transfer velocity; $C_{CH4,W}$ is the dissolved concentration of methane measured in the water; $C_{CH4,eq}$ is the methane concentration at the interface when in equilibrium with the atmosphere and was calculated considering the Henry's Law as $C_{CH4,eq} = K_h X_{CH4} P_{atm}$, in which K_h is the Henry's gas constant calculated as a function of temperature according to Goldenfum (2010); X_{CH4} is the mean mol

fraction of methane fraction in the air measured in-situ during the sampling; and P_{atm} the atmospheric pressure obtained from a nearby weather station.

The gas transfer velocity (k) is gas specific and can be converted to a standardized value expressed as k_{600}, using the Schmidt number of water. According to Crusius and Wanninkhof (2003) for wind speed at 10 m height as $U_{10} < 3.7\,\mathrm{m\,s^{-1}}$ the dependency of gas transfer velocity to wind speed is reduced and k_{600} can be assumed as constant around $1\,\mathrm{cm\,hr^{-1}}$. Considering hourly wind speeds (U_{10}), at $\sim$25% of the time the wind speed exceeded $3.7\,\mathrm{m\,s^{-1}}$ (Figure SI 31). The daily average wind speed measured at the pre-dam of Wupper reservoir converted to 10 m height was $1.9\,\mathrm{m\,s^{-1}}$, and thus the transfer velocity for methane was calculated as $k_{CH4} = \frac{k_{600}}{(\frac{600}{Sc})^{-2/3}}$ where the Schmidt number (Sc) was obtained as function of water temperature as proposed by Wanninkhof (2014).

The dissolved methane concentration in water ($C_{CH4,W}$) was measured from water samples collected at the monitoring sites into 1 L Schott bottles. At the shore, a headspace ($\sim$420 mL) with ambient air was created in the bottles. The bottles were closed with an adapted cap and after shaking for obtaining gas equilibration, the bottles were connected to the gas analyser (Ultra-portable Greenhouse Gas Analyzer, Los Gatos Research Inc., Mountain View, Calif., USA) for measuring the methane mol fraction within the headspace gas. From the mol fraction in the headspace, the concentration of methane dissolved in the water was calculated as proposed by Bossard, Joller and Szabo (1981) as:

$$C_{CH4,W} = \left(\frac{V_{HS}}{V_W} \frac{(X_{eq} - X_{back})}{RT} + X_{eq}K_{H,CH4} \right) P_{atm},$$

in which $\frac{V_{HS}}{V_W}$ is the ratio of headspace and water volume during equilibration, X_{eq} is the methane fraction measured by the gas analyser in the headspace in ppmv, X_{back} is the background methane fraction that was initially present in the headspace in ppmv, $K_{H,CH4}$ is the Henry's gas solubility coefficient for methane in $\mathrm{mol\,L^{-1}\,atm^{-1}}$, it is temperature dependent and was calculated as proposed by Goldenfum (2010), and P_{atm} is the local barometric pressure in atm. The water sample temperature (T) was measured using a multiparameter probe (WTW–Xylem analytics).

According to Goldenfum (2010), degassing methane flux (F_{deg}) can be calculated from the difference of dissolved methane concentration upstream ($C_{CH4,up}$) and downstream ($C_{CH4,down}$) the dam, multiplied by the discharge (Q) as:

$$\mathrm{F}_{deg} = (C_{CH4,up} - C_{CH4,down}) \times Q.$$

The dissolved methane concentration in water was measured through the headspace technique as previously described. As the water level in the pre-dam did not show abrupt changes over the sampling days, the outflow discharge was assumed to be equal to the inflow discharge from the Wupper River, thus the average inflow discharge of the sampling day was used to calculate the methane degassing flux. Lastly, we divided the degassing flux (F_{deg}) by the surface area of the reservoir ($150\,000\,\mathrm{m^2}$) to obtain the flux per unit area of the pre-dam ($\mathrm{mgCH_4\ m^{-2}\ d^{-1}}$).

The net-export of methane ($\mathrm{F}_{netexport}$ in $\mathrm{mgCH_4\ m^{-2}\ d^{-1}}$) was calculated as the difference between outflow rate of methane ($C_{CH4,out} \times Q_{out}$) and inflow rate ($C_{CH4,in} \times Q_{in}$) divided by the water surface area (Area = $150\,000\,\mathrm{m^2}$) as:

$$\mathrm{F}_{netexport} = \frac{(C_{CH4,out} \times Q_{out}) - (C_{CH4,in} \times Q_{in})}{\mathrm{Area}},$$

in which $C_{CH4,out}$ and $C_{CH4,in}$ are the dissolved methane concentration in mgCH$_4$ L^{-1} measured downstream the dam and from the upstream monitoring location closest to the inflow (L01), Q_{out} and Q_{in} were the outflow and inflow discharge respectively in L d^{-1} and considering to be the same over the measurement day.

The methane oxidation rate was estimated assuming that the diffusive flux at the water-air interface represents the total amount of dissolved CH$_4$ that escaped oxidation in the water column and that the input of methane in the water column is the sum of the diffusive flux at the water surface and the fraction of input CH$_4$ flux that is oxidized (SAWAKUCHI et al., 2016). In this way, the oxidation flux of methane (F$_{ox}$) was calculated as

$$F_{ox} = \frac{f}{1-f} F_{dif},$$

where F$_{dif}$ is the diffusive flux at water-air interface and f is the fraction of methane oxidized (SAWAKUCHI et al., 2016).

The fraction of methane oxidized (f) was calculated applying a Rayleigh isotopic mass-balance model considering the water column as a closed system, which is a Lagrangian approach assuming that oxidation is a first order reaction and that mixing is negligible (LEONTE et al., 2017). The model proposed by Sawakuchi et al. (2016) was applied,

$$\ln(1-f) = \frac{ln(\delta_b + 1000) - ln(\delta_w + 1000)}{\alpha - 1},$$

in which δ_b and δ_w are the isotopic ratios of methane carbon (δ^{13}C-CH$_4$) of bubbles stirred from the sediment and from gas samples of CH$_4$ dissolved in surface water respectively, and α is the isotope fractionation factor adopted to be 1.025 (SAWAKUCHI et al., 2016).

The potential methane flux at the sediment water interface (PSWI) was obtained by depth integration of the potential methane production rates. The PMP was integrated over a depth of 30 cm. This depth was defined so all the sediment cores are integrated over the same depth (as the cores had various length). In addition, the manual sampling of gas volume in the sediment was also done for the top sediment layer between 30–39 cm. The PSWI was adjusted to in situ sediment temperature with the following expression:

$$PSWI_{in-situ} = PSWI\, 10^{\theta(T_{in-situ} - T_{incubation})},$$

where $T_{in-situ}$ is the in-situ measured sediment temperature, $T_{incubation}$ is the temperature the samples were exposed during incubation (20 °C), and the coefficient θ was assumed as 0.045 as proposed by Wilkinson, Bodmer and Lorke (2019) for incubated sediments.

Text S2: sediment cores analysis

The sediment cores sampled at the monitoring site by the Uwitec gravity corer had 6 cm diameter and length varying ~32 cm to ~42 cm. The cores were kept stored at a temperature of ~4 °C. The night before the analysis, the sediment cores were removed from the storage for its temperature to equilibrate with the room temperature.

Sediment porewater was extracted from sediment layers using Rhizon tubes inserted into pre-drilled holes, as described by Wilkinson, Bodmer and Lorke (2019). The porewater was collected in 10 mL

pre-evacuated glass vials allowing for a headspace volume. After shaking the vials for gas equilibration, $100\,\mu L$ of headspace gas was extracted using a gas-tight glass syringe (Hamilton) and the methane mol fraction was measured with a gas analyser (UGGA, Los Gatos Research Inc.) in a closed-loop arrangement (WILKINSON et al., 2018). The dissolved CH_4 concentration in porewater was calculated from the headspace concentration.

The potential methane production (PMP) in the sediment was estimated during laboratory incubation of sediment samples following the procedure described by Wilkinson et al. (2015). The sediment cores were sliced into 3 to 10 cm layers in a nitrogen flushed glove box with low oxygen concentration ($<$ 10%). The sediment from each layer was first homogenized and 3 mL of sediment were then transferred to 120 mL serum bottles. The bottles were flushed with nitrogen to guarantee anoxic conditions, closed with butyl stoppers, and crimped. The bottles were maintained in dark conditions at a constant temperature of $20\,°C$. The CH_4 concentration in the headspace was measured weakly for four weeks and the PMP was obtained from the slope of a linear fit of the increase in CH_4 concentration in the headspace over time.

The remaining sediment from each core layer was transferred to falcon tubes, freeze-dried, and stored for measurement of organic matter content. The organic matter content in the sediment was estimated from Loss on Ignition (LOI), in which 3 to 5 g of sediment were weighted, dried at a temperature of $105\,°C$ and burned at a temperature of $550\,°C$ afterwards. The loss of mass during the burning process is proportional to the organic content (HEIRI; LOTTER; LEMCKE, 2001). In addition to the LOI, the carbon and nitrogen content in the sediment samples were estimated using a CHNS elemental analyzer (Vario MicroCUBE, Germany).

Text S3: manual sampling of gas content in the sediment

A self-made device built with aluminium and polyvinyl chloride (PVC) pipe was used to measure gas volume within a defined sediment area (see Figure SI 32 for the device).

A cylinder of 24.5 cm diameter and 35 cm length was built with the aluminium sheet. The upper opening of the cylinder was closed with a funnel-shaped PVC cap with an outlet to collect rising gas bubbles from inside the cylinder. The cylinder was mounted to a hollow a metal handle with extendable length. The handle was used to insert and keep the cylinder in the sediment. A second metal rod with smaller diameter was placed inside the handle and could be manually moved vertically to move a metal mesh which was attached to its end inside the aluminum cylinder. In this way, the sediment was disturbed causing the free gas to escape from the sediment matrix. At the sampled points (Figure SI 32, the maximum penetration depth of the mesh varied between 30 cm and 39 cm, depending on how compact the sediment was.

The collected gas was transported to the surface through low-permeability tubing (Tygon) fitted with a three-way valve and transferred to an acrylic cylinder with known diameter. The acrylic cylinder was kept upside down submerged in the water and used to measure the total volume of gas. The total captured gas volume was divided by the cylinder's base area ($0.047\,m^2$) to obtain the areal gas content.

Figures
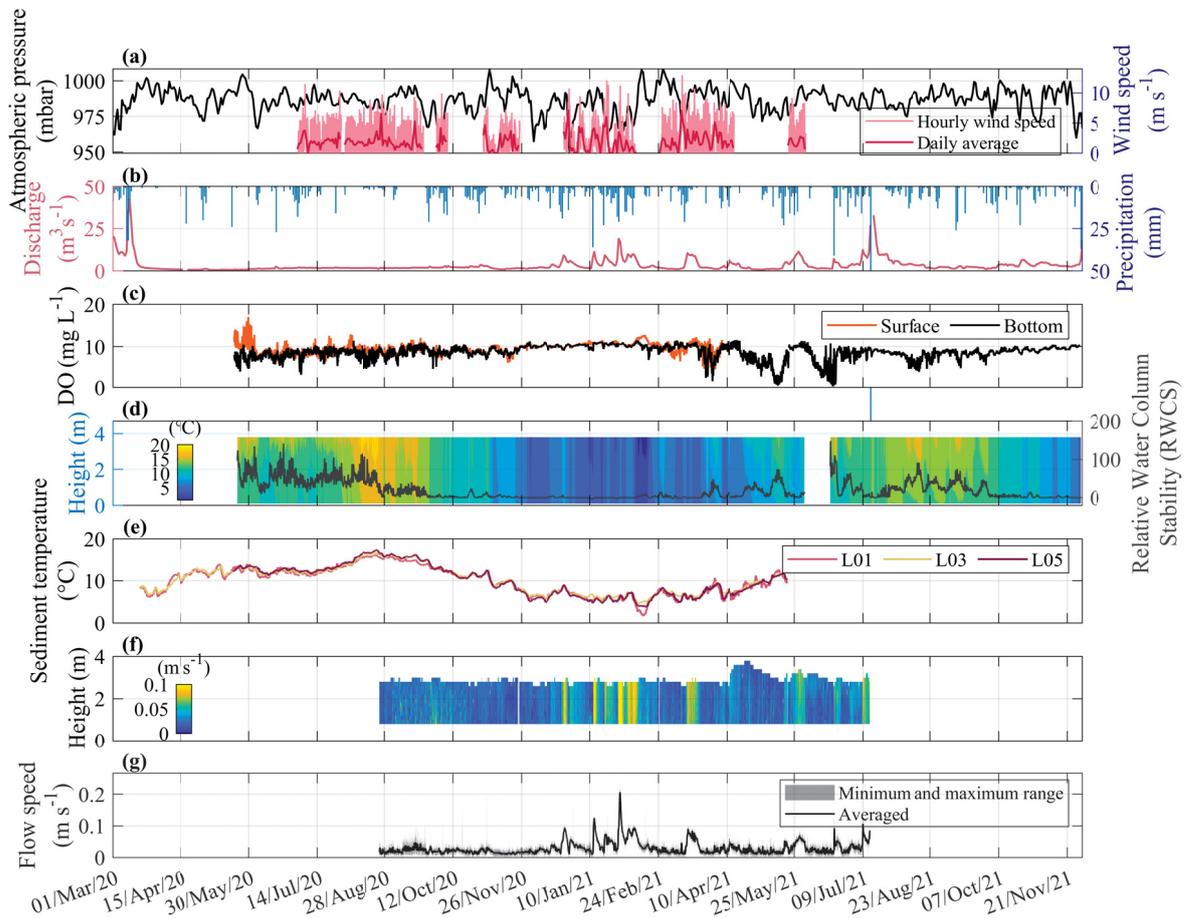
Figure 31 – Time series **(a)** Daily averaged atmosphetic pressure measured by a station in the reservoir vicinity (lat. 51.17° long 7.30°, left axis), and wind velocity (hourly values and daily averaged) observed at the weather station at the reservoir (see location on Figure 24 of main document) converted to 10 m height (right axis). It is showed hourly wind speeds and daily averages. **(b)** Daily averaged discharge from the inflow River Wupper (left axis) and daily accumulated precipitation measured upstream the reservoir (lat. 51.14° long. 7.37°, right axis). (c) Dissolved Oxygen (DO) concentrations at 5 min time intervals measured 30 cm above the sediment (bottom) and 50 cm below the water surface (surface). **(d)** Water temperature measured with thermistors chain deployed close to the dam (left axis)and relative water column stability (RWCS) calculated from water density (right axis), see main document for full explanation. **(e)** Sediment temperature at three different sampling locations (L01, L03, and L05 at time steps of 4 hours, 2 hours, and 2 hours respectively). **(f)** Current velocity measured by the Acoustic Doppler Current Profiler (ADCP) averaged over 30 min time intervals in which the color scales represent the velocity magnitude. **(g)** Vertically averaged horizontal flow speed measured with the ADCP (see location on Figure 24 of main document). Atmospheric pressure, discharge, and precipitation data were provided by the reservoir operator Wupperverband.
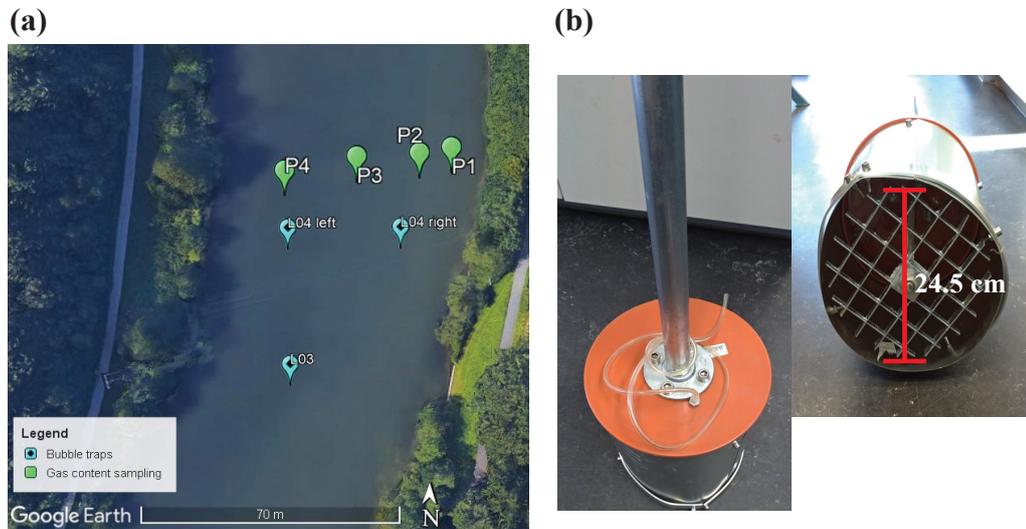
Figure 32 – **(a)** Sampling sites where the gas content in the sediment was measured along the cross section at the Wupper pre-dam. **(b)** self made device constructed for the measurement of gas volume in a defined sediment area. The device consisted in an aluminium cylinder of 24.5 cm diameter, an internal mesh which could be moved up and down for disturbing the sediment, and a Tygon tube attached to the top part of the device, allowing the collected gas to be transported to the water surface for measurement.
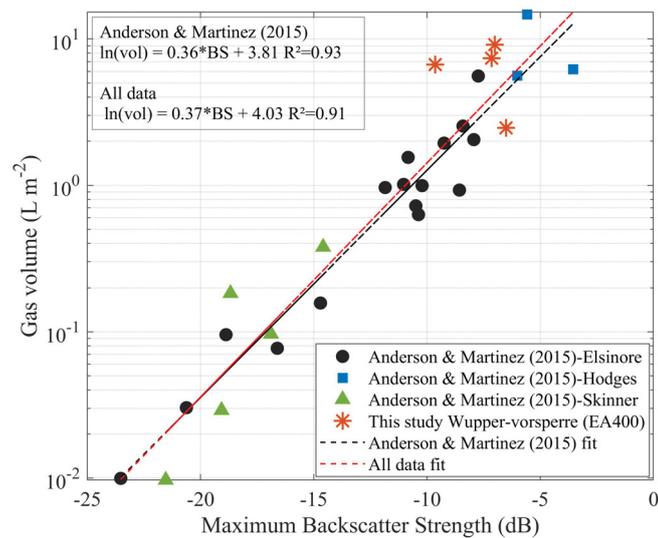
Figure 33 – Calibration curve for the estimation of gas content in the sediment as a function of the maximum acoustic backscatter (BS). Adapted from Anderson and Martinez (2015) with the addition of the data points from this study. The data from different water bodies are represented by different symbols and the dashed lines are linear fits proposed by Anderson and Martinez (2015) and for the extended data set including this study. See legends for details.
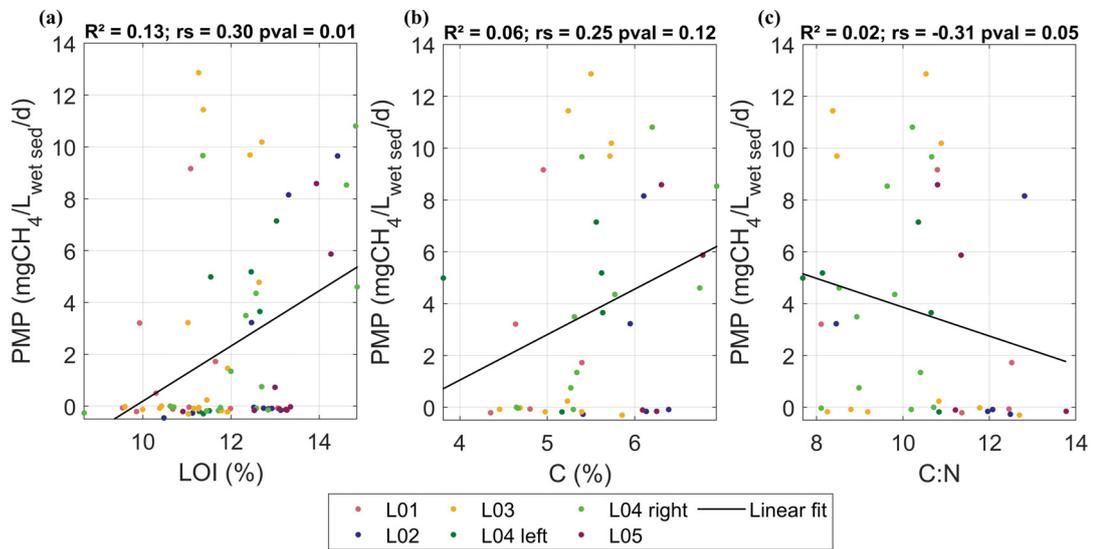
Figure 34 – **(a)** Scatter plot of potential methane production (PMP) and loss on ignition (LOI) with the linear fit PMP = 1.06LOI−10.45. **(b)** Scatter plot of potential methane production (PMP) and carbon (C) content with the linear fit PMP = 1.75C−5.97. **(c)** Scatter plot of potential methane production (PMP) and carbon to nitrogen ratio (C:N) with the linear fit PMP = −0.56C:N+9.42. In all graphs the data points colors indicate the monitoring site (see legend) and at the top are showed the coefficient of determination (R^2) of the linear fit, the Spearman correlation (rs) with the respective *p-value*.
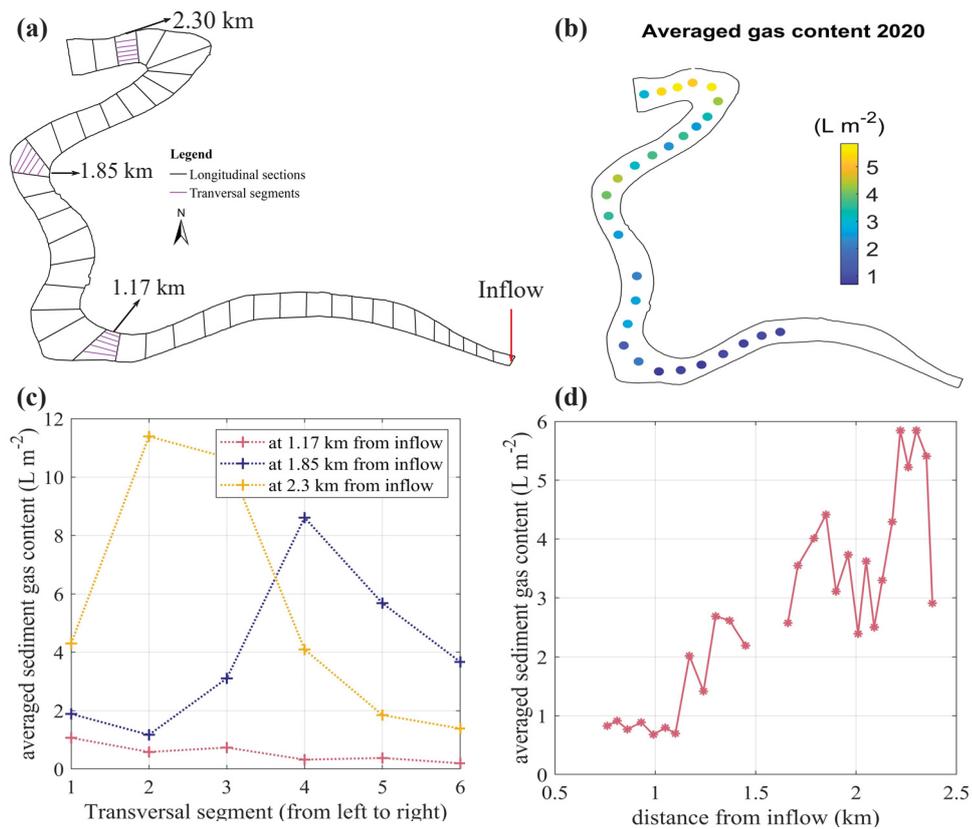
Figure 35 – **(a)** The Wupper reservoir divided into 42 longitudinal segments, in which the average gas content was calculated to obtain the values presented in panels **(c)** and **(d)**. Three segments were selected and divided into 6 transversal parts for calculating the average gas content. **(b)** Scatter plot of the averaged gas content for each longitudinal segment, with colors indicating the range of the calculated values. **(c)** Scatter plot of the average gas content for each transversal segment, t, with colors indicating the location in the reservoir (refer to the legend). **(d)** Scatter plot of gas content in the sediment averaged for each longitudinal segment.
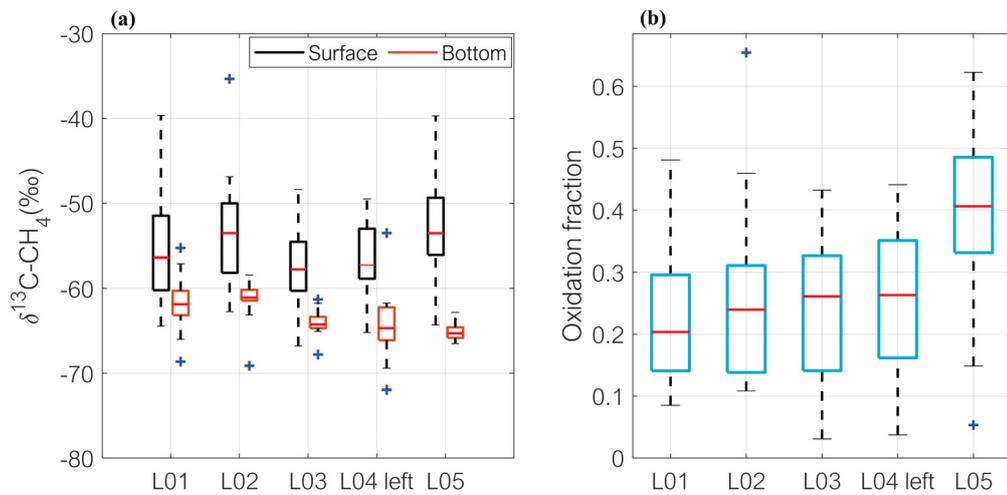
Figure 36 – **(a)** Boxplots of stable carbon isotopic composition of CH_4 ($\delta^{13}C$-CH_4) in the standard delta (δ) notation expressed in ‰relative to the standard Vienna Pee Dee Belemnite at the four monitoring locations. Black boxplots show data for the surface water (from headspace gas sample), red boxplots (bottom) show data from bubbles collected from the bottom sediment. **(b)** Boxplots of the methane oxidation fraction calculated based on the isotopic composition for each monitoring location. It represents the fraction of CH_4 diffusive flux at the air-water interface that was oxidized. On both graphs, the horizontal red lines inside the boxes are the median values, the upper and lower limits of the boxes represent the 75th and 25th percentiles, respectively, the whiskers show the maximum and minimum values, and the blue crosses are outliers.
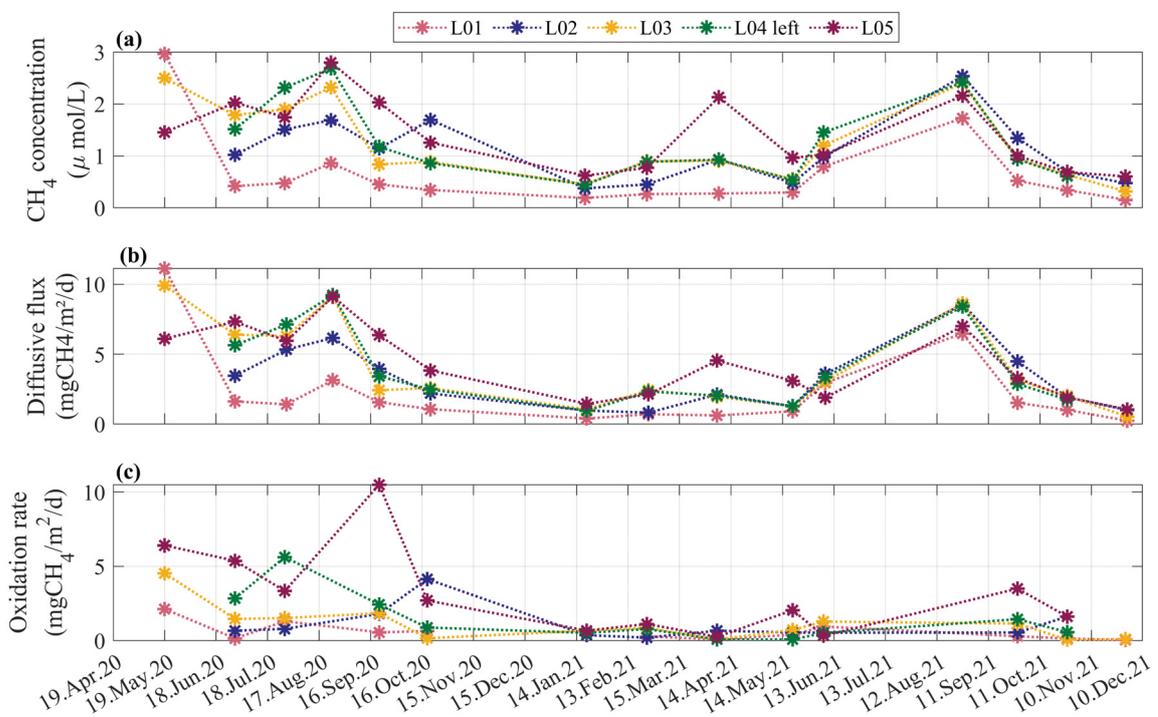
Figure 37 – **(a)** Dissolved CH_4 concentration measured at each location during the monthly field campaigns. **(b)** Diffusive flux of methane at the water-air interface calculated with the thin boundary layer model. **(c)** Oxidative CH_4 flux. The colors in all graphs represent the monitoring location, see legend for detail. Details on dissolved concentration and fluxes calculation are provided on Text S1 of the supporting information.
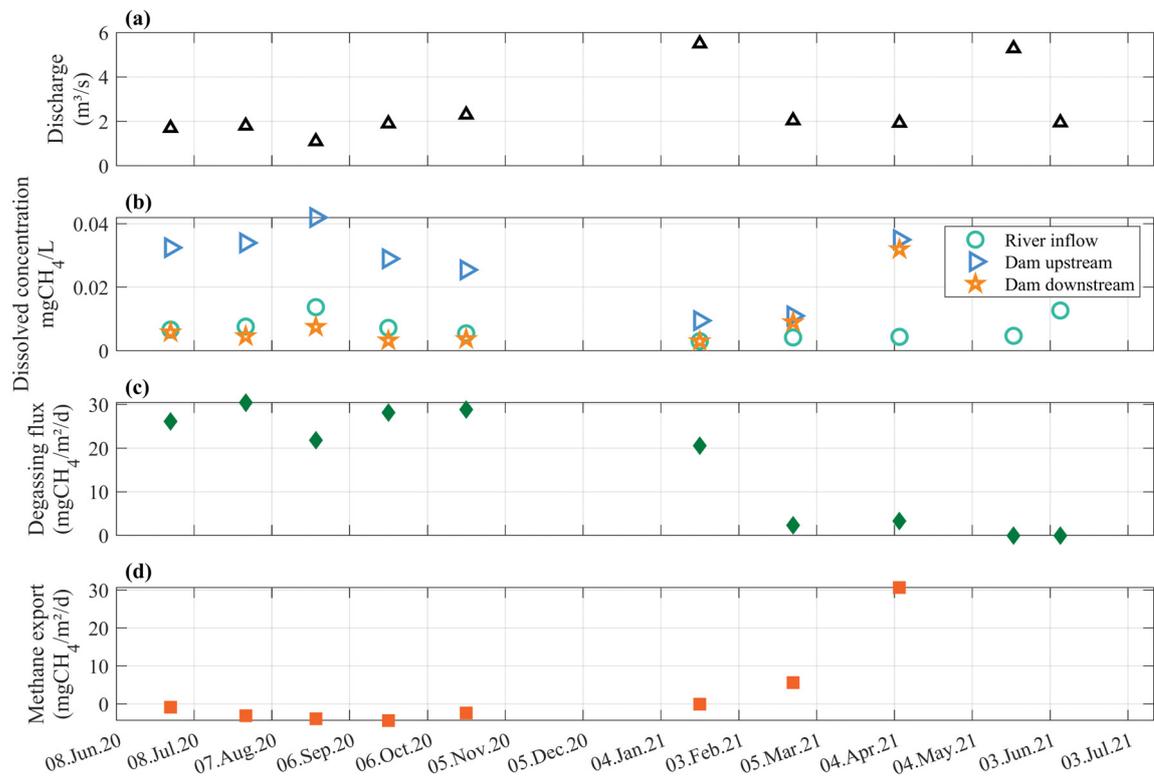
Figure 38 – **(a)** Daily average discharge of the inflow river Wupper measured by a gauge station 1.5 km upstream the reservoir. **(b)** Dissolved methane concentration in water see legend for the location of measurement. **(c)** Degassing flux at the pre-dam spillway, details on flux calculation are provided in the supporting information Text S1, **(d)** Net-export of methane, calculated as the difference between import of methane through the inflow river and the export by the outflow, Text S1 for details.
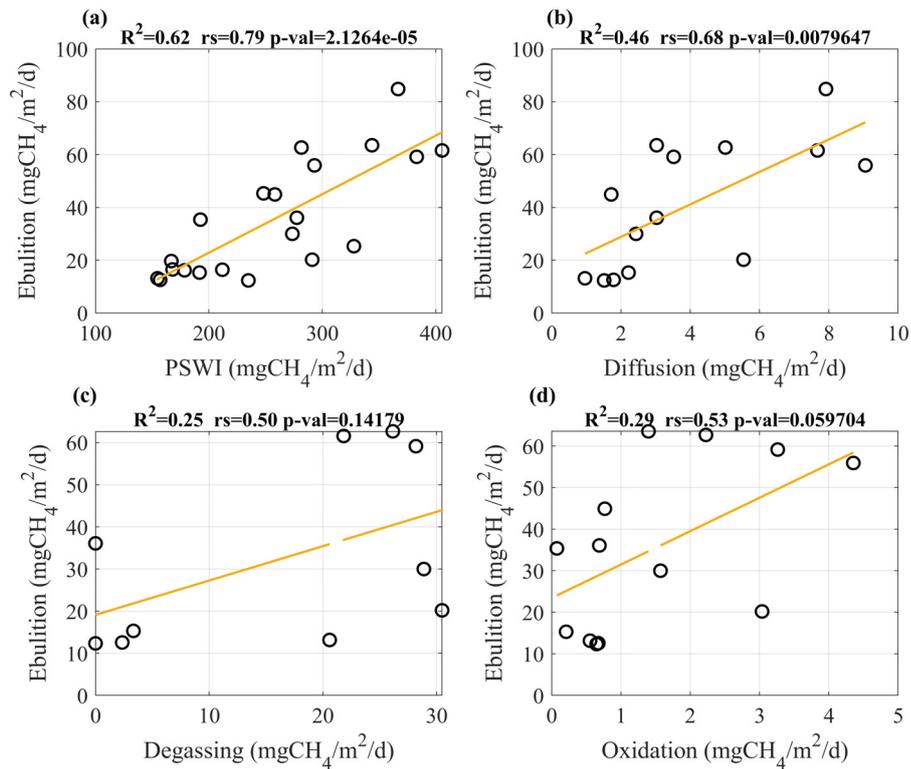
Figure 39 – Scatter plot of average ebullition and the different methane fluxes monitored considering monthly scale. The solid yellow line is a linear fit. At the top of the plots are showed the coefficient of determination (R^2) of the linear fit and the Spearman rank correlation (rs) with the respective *p-value* for a confidence level of 5%. The regression equations of the linear fit are as follows: **(a)** Ebullition = 0.32 PSWI−21.5; **(b)** Ebullition = 6.15 Diffusion+16.53; **(c)** Ebullition = 0.82 Degassing+19.11; and **(d)** Ebullition = 8.04 Oxidation+23.44.
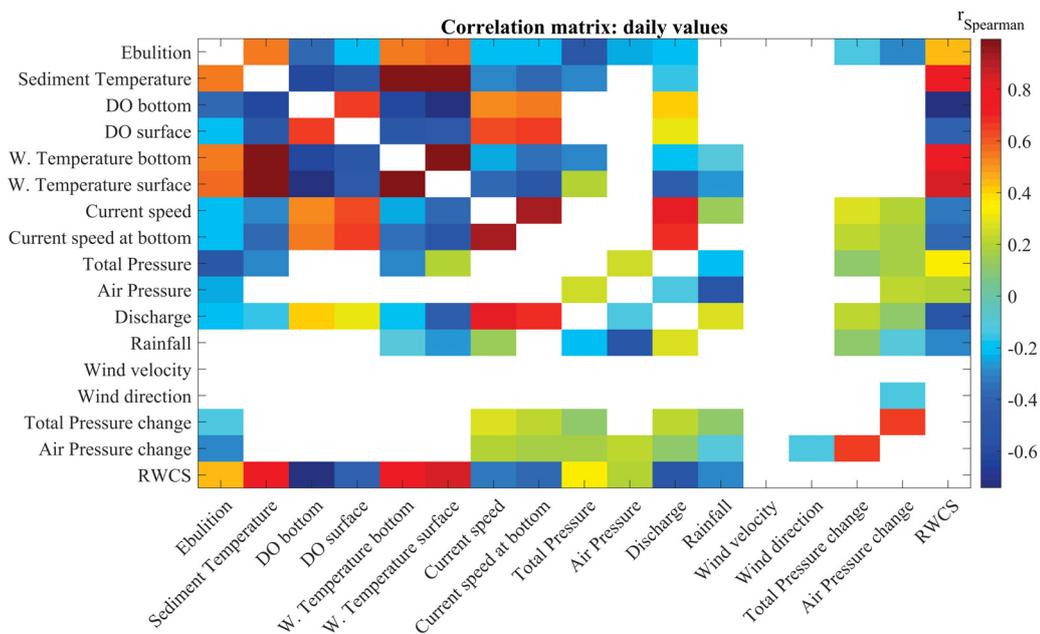
Figure 40 – Correlation matrix (Spearman correlation) of continuously monitored variables and spatially averaged methane ebullition rates (all data are considered with daily resolution). The color scales with the magnitude of the correlation coefficient (see legend) for a significance level of 0.05. The white boxes are for correlation with *p-value* > 0.05, whereas the autocorrelation of the variables (on the main diagonal) are omitted.

APPENDIX C – Exploring the temporal dynamics of methane ebullition in a subtropical freshwater reservoir

Lediane Marcon, Tobias Bleninger, Michael Männich, Mayra Ishikawa, Stephan Hilgert, Andreas Lorke

Abstract

The transport of methane from sediments to the atmosphere by rising gas bubbles (ebullition) can be the dominant, yet highly variable emission pathway from shallow aquatic ecosystems. Ebullition fluxes have been reported to vary in space and time, as methane production, accumulation, and bubble release from the sediment matrix is affected by several physical and bio-geochemical processes acting at different timescales. Time-series analysis and empirical models have been used for investigating the temporal dynamics of ebullition and its controls. In this study, we aim to better understand the factors governing the temporal dynamics of ebullition and to evaluate the application of empirical models to reproduce these dynamics across different timescales and across different aquatic systems. The study is based on continuous high frequency measurements of ebullition fluxes and environmental variables in a mesotrophic subtropical and polymictic freshwater reservoir. The synchronization of ebullition events across different monitoring sites, and the extent to which ebullition was correlated to environmental variables varied throughout three years of observations and were affected by thermal stratification in the reservoir. Empirical models developed for other systems could reproduce a limited fraction of the variability in observed ebullition fluxes ($R^2 < 0.3$), however the predictions could be improved by considering additional environmental variables. The model performance was depended on the timescale. For daily and weekly time intervals, a generalized additive model could reproduce 70 and 96% of ebullition variability, but could not resolve hourly fluxes ($R^2 = 0.19$). Lastly, we discuss the potential application of empirical models for filling gaps in ebullition measurements and for reproducing the main temporal dynamics of the fluxes. The results provide crucial

information for emission estimates, and for the development and implementation of strategies targeting at a reduction of methane emissions from inland waters.

Introduction

Freshwater reservoirs play a vital role in the global carbon cycle (TRANVIK et al., 2009) and emit large amounts of greenhouse gases, including methane, to the atmosphere (ROSENTRETER et al., 2021). Bubble mediated transport of methane, i.e. methane ebullition, is an important pathway of methane emissions in shallow lentic ecosystems (DEEMER et al., 2016). At the same time, ebullition is an episodic and highly variable process (KELLER; STALLARD, 1994; DELSONTRO et al., 2015).

Spatially, ebullition is reported to vary across different water bodies as well as within individual systems. Sediment deposition, quality and quantity of organic matter content, nutrients, and sediment temperature have been reported to affect methane production in bottom sediments (GRASSET et al., 2018; GRINHAM; DUNBABIN; ALBERT, 2018; ISIDOROVA et al., 2019). The accumulation of methane, the formation of gas voids, and the release of gas bubbles from the sediment matrix is controlled by the complex interplay of physical aspects, including grain size, total pressure and pressure changes at the sediment-water interface (LIU et al., 2016; BEAULIEU et al., 2018) and biochemical conditions, such as methane oxidation (SAWAKUCHI et al., 2016), or zooplankton migration (MCGINNIS et al., 2017).

In time, ebullition is highly variable at timescales ranging from minutes to seasons (VARADHARAJAN; HEMOND, 2012), as it is influenced by the dynamics of multiple environmental variables. Atmospheric conditions of low pressure and rapid decrease of hydrostatic pressure are known to promote bubble release from the sediment, as with reduced pressure the bubbles expand and gain buoyancy (CASPER et al., 2000; MAECK; HOFMANN; LORKE, 2014; NATCHIMUTHU et al., 2016). Other environmental variables, such as strong wind and high current velocities (KELLER; STALLARD, 1994; JOYCE; JEWELL, 2003), and warmer temperatures (ABEN et al., 2017) are also reported to enhance ebullition fluxes.

The overlapping and sometimes delayed (asynchronous) effects of the environmental variables on ebullition, make it challenging to predict the fluxes. Past studies proposed mechanistic approaches and empirical relationships to predict ebullition fluxes from aquatic systems. In mechanistic approaches, ebullition is simulated by resolving the methane transport-reaction equations with ebullition occurring above a threshold, commonly based on pressure, dissolved gas concentration, or volume of free gas (BAZHIN, 2010; SCANDELLA et al., 2011; PELTOLA et al., 2018). The process-based models have been developed in different ways, however, they commonly require information on methane production and loss (others than ebullition) from the sediment (SCHMID; OSTROVSKY; MCGINNIS, 2017; LANGENEGGER et al., 2019), while more complex models require additional information on sediment properties, such as porosity and effective stress (SCANDELLA et al., 2011; KATSMAN; OSTROVSKY; MAKOVSKY, 2013). The required input data (e.g., boundary conditions), and the availability of measurements for calibration make the application of mechanistic models for the simulation of ebullition challenging.

Statistical and data-driven models are less demanding in terms of input variables, however the quality and quantity of input data directly affect the model performance. These empirical models have been applied in previous studies for both testing the dependency of ebullition on diverse environmental variables and for estimating the ebullition flux, and considered temperature (WIK et al., 2014; ABEN et al., 2017), chlorophyll-a (DELSONTRO; BEAULIEU; DOWNING, 2018), littoral area and radiance (PRAIRIE et al., 2021), sediment organic matter content (PRAETZEL; SCHMIEDESKAMP; KNORR, 2021), wind speed (MCCLURE et al., 2020), pressure, and pressure changes (DESHMUKH et al., 2014;

MCCLURE et al., 2020; ZHAO; TEDFORD; LAWRENCE, 2022). Nevertheless, the applicability of these statistical and data-driven models across diverse systems and timescales for reproducing ebullition dynamics has rarely been addressed. Ebullition drivers were shown to change from one location to another of the same reservoir (MCCLURE et al., 2020), while iterative forecasting models with continuous update of model coefficients can potentially improve the prediction of ebullition dynamics at weekly time scales (MCCLURE et al., 2021). Additionally, a recent study (LAUERWALD et al., 2023) highlighted that advances are needed for the application of empirical models for the estimation of greenhouse gas emissions from inland waters.

The analysis of ebullition time-series provide important and useful insights into ebullition dynamics (VARADHARAJAN; HEMOND, 2012), while the use of ebullition time series in combination with time-series of environmental variables allows for the identification of main environmental drivers (DESH-MUKH et al., 2014; MCCLURE et al., 2020). At the same time, empirical models are powerful tools to fill measurement gaps, to support estimates of emissions from systems where mechanistic approaches are no available, and to potentially reproduce the short-term temporal dynamics of ebullition. The ability of predicting short-term temporal dynamics of ebullition, in contrast to mean fluxes, is important to identify patterns and trends that may have been missed by considering mean fluxes. Moreover, as ebullition is a highly dynamic process that can vary greatly at short timescales (VARADHARAJAN; HEMOND, 2012; MAECK; HOFMANN; LORKE, 2014), predicting mean fluxes alone may not accurately capture this variability. Lastly, the identification of hot moments in ebullition fluxes can guide practical applications targeting a reduction of methane emissions from freshwater reservoirs (STOLAROFF et al., 2012; BARTOSIEWICZ; RZEPKA; LEHMANN, 2021).

In the present study, we aim to improve the understanding of the temporal dynamics of ebullition and its main controls. We revisited and complemented high frequency ebullition measurements in a polymictic mesotrophic subtropical freshwater reservoir with an integrated measurement approach. We analysed ebullition time-series in combination with an extensive high temporal resolution dataset of environmental variables with the objectives (1) to evaluate the dependency of ebullition on different drivers over time; (2) to test to what extent empirical models can be applied across different systems to reproduce ebullition temporal dynamics; and (3) to verify the capabilities of empirical models to reproduce ebullition temporal dynamics at different timescales.

Material and methods

Study cite

We analyzed measurements from a subtropical drinking-water reservoir (Passaúna Reservoir), located in the southern part of Brazil (25.53°S and 49.39°W, Fig 1). The reservoir was created in 1989 by a dam constructed in the Passaúna River. It has a surface area of $8.5\,km^2$, an average water depth of $8.3\,m$, and maximum depth of $\sim 18\,m$ near the dam. The main water inflow to the Reservoir is the Passaúna River (average of $1.7\,m^3\,s^{-1}$ (RAUEN; CASTRO; SILVA, 2017)) and the main water outflows are the withdrawal at the water treatment plant (average of $1.8\,m^3\,s^{-1}$), a bottom outlet near the dam (with continuous discharge of $0.5\,m^3\,s^{-1}$), and a free overflow at the spillway (ISHIKAWA et al., 2022b).

Several environmental parameters were monitored in the reservoir from February 2017 to February 2020 and were reported in previous studies. The field monitoring was conducted in cooperation with the reservoir operator Sanepar (Sanitation Company of Paraná State), which granted access to the study site and provided relevant data. In years without severe droughts, the water level in the Reservoir fluc-
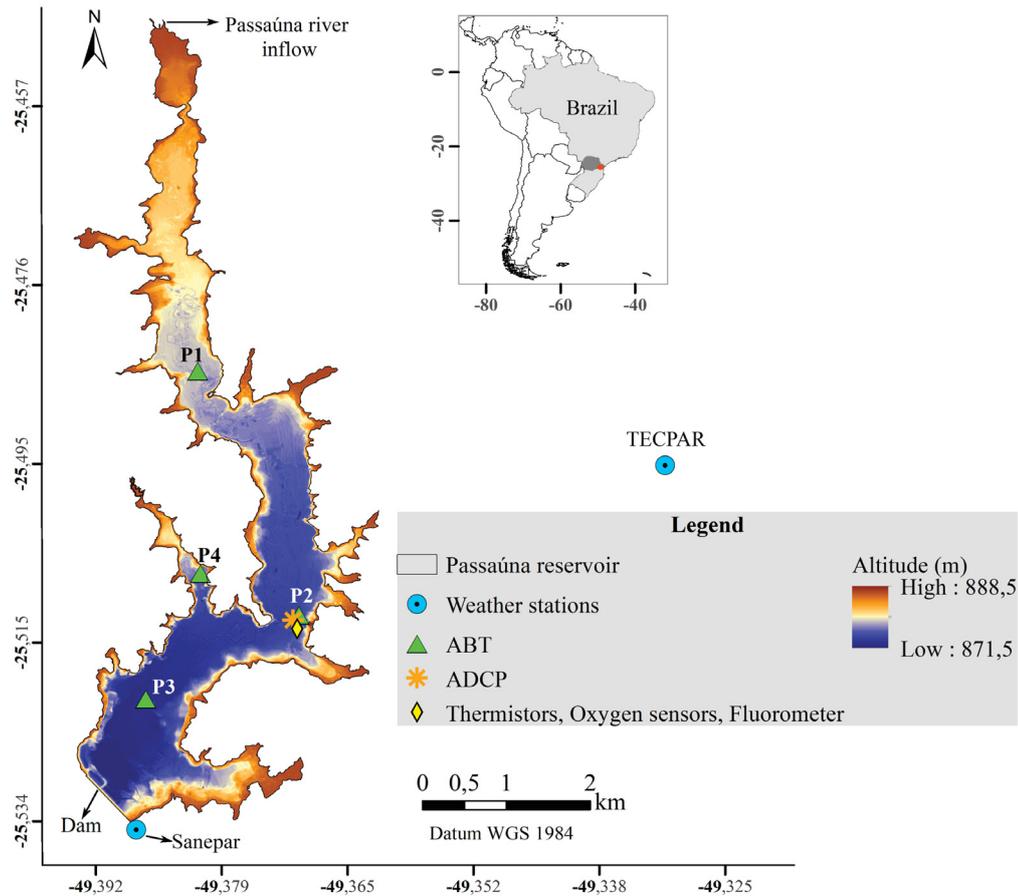
Figure 41 – Bathymetric map of Pasaúna Reservoir with the location of sampling sites. The inset map shows the location of the reservoir in Brazil and South America. The location of sensors in the reservoir is marked by different symbols (see legend) and the colour scale shows the reservoir bathymetry. Reservoir's bathymetric data and boundaries are republished from Sotiri et al. (2021) under a CC BY license, with permission from ELSEVIER, original copyright 2021.The measurement period of each sensor is provided in Figure SI 41. Ebullition was monitored at 4 sites using automated bubble traps (ABT). The shallowest (∼8 m depth) upstream site was labelled as P1 (also referred as Park, as there is a natural park at the left-hand reservoir bank), site P2 (Intake) at ∼12 m depth was placed in front of the water intake facility, site P3 (Dam) is at the deepest (∼14 m) region of the reservoir, and site P4 (Arm) was placed in a side-arm of the reservoir which has ∼10 m depth.

tuates only slightly (for instance, during the monitoring period, the maximum variation was 1.4 m over 3 months from July to September 2018). Passaúna is a polymictic mesotrophic reservoir, the maximum observed water temperature near the sediment was of 23.2 °C (in February 2019), whereas the coldest temperature of 16 °C occurred in June 2018 and July 2019 (ISHIKAWA; BLENINGER; LORKE, 2021). During warmer periods, when the reservoir was thermally stratified, the bottom water layer can become anoxic with dissolved oxygen concentrations less than $1\,\mathrm{mg\,L^{-1}}$. High-frequency internal waves with periods ranging from 2.1 to 17.1 minutes were also detected in the reservoir, in which short periods (< 6.2 minutes) internal waves were reported during stratified conditions, whereas internal waves with longer periods were detected during mixed conditions (ISHIKAWA; BLENINGER; LORKE, 2021).

The bottom sediment is characterized by unconsolidated fine-grained material with an average Loss on Ignition (LOI at 550 °C as an indicator for organic matter content) of 17.2% and a highest fraction (up to 50%) found on the deepest regions (SOTIRI et al., 2021). Within the reservoir, two main locations are preferred for sediment accumulation, upstream near to the main river inflow and in the

deepest region in front of the dam (SOTIRI et al., 2021). The top 10 cm of organic-rich sediment can produce and store methane. The average potential methane production for this top layer obtained from incubated sediments was $2.2 \, \text{mgCH}_4 \, \text{L}^{-1} \, \text{d}^{-1}$, while the mean gas content stored in the sediment matrix was acoustically estimated as $4.6 \, \text{L} \, \text{m}^{-2}$ in 2019 (MARCON et al., 2022b).

Measurements and data

Here we analyzed time series of ebullition fluxes in combination with additional data from previous studies, including dissolved oxygen concentration, water temperature, water level, flow velocity, acoustic backscatter in the water column, chlorophyll-a, and meteorological variables (solar radiation, wind velocity and direction, atmospheric pressure, air temperature, and humidity). All measurements and data are briefly described below and a summary of data availability throughout the analysis period is shown in supporting information Figure SI 47 (sensor locations are shown in Figure 41). Data gaps in the time series were caused by different issues, including sensor failure, battery shortage, and maintenance requirements. Monthly field campaigns were performed for data acquisition, sensor cleaning and maintenance.

Ebullition flux and potential methane production

Monitoring of ebullition fluxes in the reservoir started in February 2017 and the results from the first year of measurements were presented in Marcon et al. (2019). Here we continued the gas flux monitoring with measurements until February 2020 at four locations (P1 to P4, see Figure 41 with automated bubble traps (ABT, Senect GmBH, Germany). The bubble traps were fixed to buoys and submerged in the water column. Anchors weights attached to secondary buoys were used to keep the ABT position at 1.7–2.7 m bellow the water surface (6 to 11 m above the bed). The ABT collected rising bubbles with an inverse canvas funnel of 1 m diameter ($0.78 \, \text{m}^2$ opening area) attached to an aluminum frame. The gas was channeled into an acrylic tube where the volume was measured by a calibrated differential pressure sensor. The ABT recorded gas fill height, temperature, and pressure at 30 s time intervals in an internal data logger. The accumulated gas was flushed by a valve when the maximum fill height was reached, or every 12 hours.

The gas flux (in mL m^{-2} d^{-1}) was calculated for defined time intervals (5 min, 10 min, 1 hr, and 1 d) as the total gas volume at standard pressure (1 atm) and temperature (20 °C), as described in Marcon et al. (2019). To obtain the methane ebullition flux (in mgCH4 m^{-2} d^{-1}), the gas volume was converted to methane mass using the ideal gas law with in-situ temperature and pressure, and a mean constant methane fraction within the bubbles of 68.9% (MARCON et al., 2022b). During the monitoring period, we recorded valid data for 605 d at location P1, 680 d at P2, 549 d at P3, and 274 d at P4.

Time series at 5 min, 10 min, 1 hr, and 1 d time intervals of the potential methane flux at the sediment water interface (PSWI) as a function of in-situ temperature were obtained from Marcon et al. (2022b). The potential fluxes were estimated from depth-integrated production rates measured in laboratory incubations of sediment cores sampled near the ABT's locations, and corrected for water temperature at the respective sampling sites.

Velocity field and acoustic backscatter

Vertical profiles of flow velocity were adopted from Ishikawa, Bleninger and Lorke (2021). The measurements were conducted using an upward-looking Acoustic Doppler Current Profiler (ADCP Signature 1000, Nortek AS, Norway), which was deployed from February 2018 to February 2019 at the

reservoir bottom next to ABT P2 (Figure 41). Vertical profiles of the three components of the mean flow velocity were measured with 0.5 m vertical resolution over the entire water column and with a temporal resolution of 5 min. In addition, the ADCP recorded high resolution profiles (0.04 m vertical resolution and sampling frequency of 1–4 Hz) of the vertical velocity component (HR-Burst mode), and acoustic backscatter strength (full water column profile). The temporal variations in acoustic backscatter measured in Passaúna was previously used as an indicator of zooplankton migration in the water column (ISHIKAWA; BLENINGER; LORKE, 2021). The ADCP also recorded the pressure, which was used to calculate time series of water depth.

Here we used the velocity time series to calculate the variance and the magnitude of root-mean square fluctuations of the vector-averaged mean flow speed at the lowest sampling depth (1.2 m above the sediment) and of the high-frequency fluctuations in the vertical velocity (HR-Burst measurements for the water layer between 1 m to 3 m above the bed), respectively. The statistical properties were estimated for defined time intervals (mean horizontal current speed at 1 hr and 1 d and vertical velocity at 5 min, 10 min, 1 hr, and 1 d). The dissipation rate of turbulent kinetic energy near the bottom (0.64–0.68 m from the bottom) at 10 min time intervals was available from a previous study (ISHIKAWA; BLENINGER; LORKE, 2021).

Dissolved oxygen concentration, water temperature, chlorophyll-a, and inflow discharge

Dissolved oxygen concentration ($\sim$1 m below the water surface and 2 m above the bed) and water temperature near the sediment were obtained from Ishikawa, Bleninger and Lorke (2021). Dissolved oxygen was measured at 5 min time interval by optical sensors (miniDOT, Precision Measurement Engineering, Inc.) and the water temperature was measured by temperature loggers (Minilog-II-T, Vemco, Bedford, NS, Canada) at 1 min time intervals (ISHIKAWA; BLENINGER; LORKE, 2021). The difference in water temperature between the surface and the bottom were used to calculate the relative water column stability (RWCS), which represents the relative thermal resistance to mixing (WELCH; NACZK, 1992):

$$\text{RWCS} = \frac{\rho_{bottom} - \rho_{surface}}{\rho_{4^\circ C} - \rho_{5^\circ C}},$$

ρ_{bottom} and $\rho_{surface}$ are the water densities at the bottom and at the surface, respectively, $\rho_{4^\circ C}$ and $\rho_{5^\circ C}$ are the water densities at temperatures of 4 °C and 5 °C. The water density as a function of temperature was calculated using the UNESCO equation (FISCHER et al., 1979). For RWCS > 56.5, the reservoir is considered as thermally stratified, RWCS < 16.3 indicates a mixed water column, and 16.3 < RWCS < 56.5 indicates partial stratification (BRANCO et al., 2009; GERARDO-NIETO et al., 2017). In addition, the Schmidt stability (S_T) was also used as an indicator for mixed or stratified conditions (ISHIKAWA; BLENINGER; LORKE, 2021). Here we assumed that the sediment temperature was in equilibrium with the overlaying water, and therefore we adopted the bottom water temperature as the sediment surface temperature.

Time series of daily averaged chlorophyll-a concentration near the water surface were adopted from Ishikawa et al. (2022b) and were estimated from continuous measurements with a fluorometer (FluoroProbe III, bbe moldaenke GmbH, Germany) deployed at 1.4 m water depth at the monitoring site P2. The daily time-series of the Passaúna river inflow discharge was obtained from Ishikawa et al. (2022a).

Meteorological data

Wind velocity and direction, solar radiation, air temperature, relative humidity, and atmospheric pressure were recorded by two weather stations located near and at the reservoir, respectively (see Figure 41 for locations). A station at the reservoir dam was installed in May 2018 (by the reservoir operator Sanepar) and recorded data at 10 min time intervals. A second station was located at the Technology Institute of Parana (TECPAR) ~4 km away from the reservoir and recorded data at 1 min time intervals. Both data sets had frequent gaps exceeding 10 days. Therefore, we combined the measured variables from both weather stations (except for wind direction) to obtain a single continuous data set, in which the data of the Sanepar station was complemented with the TECPAR measurements using linear fits between data from both stations. For our analysis, the meteorological data were averaged over time intervals of 5 min, 10 min, 1 hr, and 1 d.

Data processing and analysis

Time series preparation

Several quality checks were applied to all time-series to remove spurious data (e.g. identify and exclude sensor failure and sensors readings during maintenance/deployment periods). The different environmental parameters were recorded at various discrete time intervals (e.g. 30 s, 1 min, or 10 min) with different starting and ending times. Therefore, after the data check and cleaning, time-series with regular and fixed time intervals (5 min, 10 min, 1 hr, 1 d) were created for each variable in which the time refers to the end of the considered intervals. Initially, high-resolution timetables (5 min and 10 min time steps) were created, and linear interpolation was used when necessary to calculate the values at the desired pre-defined timesteps (for instance, for adjusting the time-step from measured at 13:13 to pre-defined time at 13:15). In a second step, the 10 min time series were used to calculate hourly and daily timetables by averaging.

Some variables were originally monitored/calculated only at longer time-intervals (such as the velocity variance of horizontal currents, which were only available for time intervals > 1 hr, and Chlorophyll-a measurements were at daily time steps only). In these cases, we opted for not downscaling the values to shorter time intervals, as this could introduce artificial temporal dynamics and affect the subsequent analysis of the data. In total, daily time series of 30 environmental variables were obtained (excluding ebullition fluxes, all the variables are listed in Figure SI 50). The final time series are available in the Zenodo repository (MARCON et al., 2023).

Statistical analysis of ebullition time series

After data preparation, the temporal dynamics of environmental variables and ebullition fluxes were evaluated by basic statistics (averages ± standard deviations, median values, and boxplots). The normality of the time-series was checked using Kolmogorov-Smirnov tests. The coherence of ebullition fluxes at different monitoring sites and timescales was tested using Spearman rank correlations (rs, for significance level of 0.05) and the Kuramoto order parameter (r). As described by Diamond et al. (2022), the Kuramoto order parameter indicates synchrony among different oscillators, in which r ranges between 0 and 1, with r = 1 indicating perfect synchrony (oscillations in phase) and r = 0 perfect asynchrony (oscillations with opposing phase). Because the calculation of the Kuramoto order parameter requires continuous time series, we used daily ebullition time-series simultaneously recorded at study sites P1, P2, and P3 for two periods: December 13th 2018 – April 24th 2019 and June 05th 2019 – October 16th 2019. Location P4 was not included due to gaps in the measurements. For the Kuramoto order parameter, we

first filled missing values by linear interpolation (for gaps up to 8 data points), removed linear trends in the time-series, normalized them using z-scores, and finally calculated r for each time step based on the instantaneous phase of each oscillator in a complex plane (KURAMOTO, 1975; DIAMOND et al., 2022).

The frequency distribution of variance in ebullition time-series (linearly detrended 5 min time-series) was analyzed using power spectra. The spectra were estimated using the Welch's method with a Hamming window and 50% overlap. Wavelet analysis was used to locate the occurrence of any existing periodicity in time. The analytic Morse wavelet was used to obtain the continuous wavelet transforms.

Ebullition triggers and prediction

The relationship between methane ebullition flux and possible environmental drivers (or controls) was initially explored using Spearman rank correlations (for significance level of 5%) and Principal Component Analysis (PCA) with the main variables with significant correlation and grouped by reservoir mixing conditions (based on RWCS described above). The interrelation between methane ebullition and main (single) drivers was further evaluated with wavelet coherence analysis, which allows to evaluate when and at what frequencies the two time-series were correlated. The method is based on continuous wavelet transforms to calculate the wavelet cross-spectrum and to obtain the magnitude-squared coherence between two time-series. Values of magnitude-squared coherence range between 0 and 1, in which values equal to one indicate high coherence and values equal to 0 no coherence.

We tested eight empirical relationships (here also referred to as models or statistical models) proposed in previous studies in the last 10 years for calculating (methane) ebullition fluxes (or in some models log-transformed fluxes) as a function of environmental variables (such as temperature, pressure, and others). Our aim was to explore if the ebullition variability at Passaúna reservoir can be described by the same set of variables as in other systems and to analyze to what extent these models can be applied across different systems to reproduce the temporal dynamics of ebullition. In this step we tested the models in two ways: with the same coefficients from the original studies and by recalculating the models' coefficients based on our dataset for Passaúna reservoir. After that, we tested if the inclusion of additional environmental variables in different model set-ups can improve the models' capability to reproduce the temporal dynamics of ebullition. Finally, we selected the model with the best performance in reproducing daily ebullition fluxes to test at which timescales the model could resolve ebullition variability.

For applying the empirical models proposed in the literature, we used the time series at the same time interval as reported in each respective study. The time intervals of estimated ebullition fluxes ranged between daily to biweekly. The models were tested to predict the accumulated fluxes (as a representation for mean/seasonal ebullition) and to reproduce ebullition temporal dynamics. The model's capability to estimate the total accumulated methane flux was evaluated by calculating the relative error (Rel_{error}) between measured and simulated values, in which a negative Rel_{error} indicates an overestimation by the model and a positive Rel_{error} an underestimation of accumulated fluxes. As continuous data are required for calculating accumulated fluxes, we restricted the calculation of Rel_{error} to two periods of continuous measurements: June 26th 2018 – October 2nd 2018 and December 14th 2018 – February 05th 2019. The model's performance in reproducing ebullition temporal dynamics was evaluated through three metrics: coefficient of determination (R^2), root-mean-square error (RMSE), and Nash-Sutcliffe efficiency (NSE) of measured and estimated non-log transformed fluxes. *MatLab* codes of the empirical models tested and models' performance calculations are available in the Zenodo repository (MARCON et al., 2023).

Results

Temporal dynamics of time-series

The measured variables were characterized by temporal variations of different magnitudes and at different frequencies (Figure 42). Pronounced sub-daily variability was observed in velocity variance, DO at the bottom, and in RWCS, whereas variations in total pressure occurred mostly over days. Seasonal and other longer-term trends were present in total pressure, DO and RWCS. Inter-dependencies between parameters were also observed, for instance the concentration of DO near the bottom was negatively correlated to RWCS (Spearman rank correlation rs = −0.76 with *p-val* < 0.05). In periods when the reservoir was mixed, the DO near the bottom tended to be higher, whereas the bottom water layer became anoxic during strong stratification (see Figure 42b after end of November 2018).
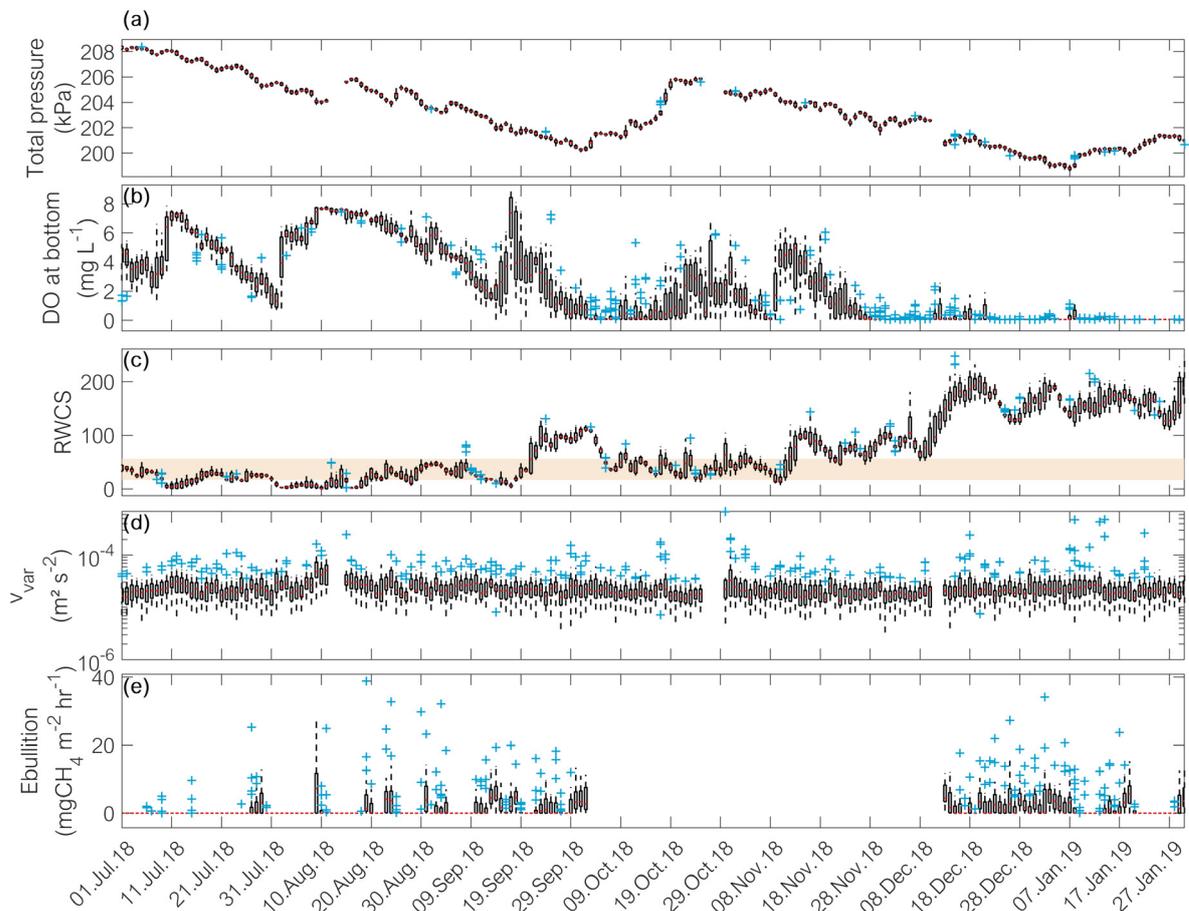
Figure 42 – Box plots of daily variations in observed hourly time-series. **(a)** Total pressure (hydrostatic + atmospheric pressure). **(b)** Dissolved oxygen concentration measured near the bottom. **(c)** Relative Water Column Stability (RWCS). The shaded area represents values when the reservoir was partially stratified whereas higher values indicate stratified conditions. **(d)** Velocity variance near the bottom. **(e)** Methane ebullition flux at location P2. In all time series the blank spaces represent data gaps. The upper and lower limits of the boxes represent the 75th and 25th percentiles, respectively. The whiskers show the maximum and minimum values, the red line represents the median, and the blue crosses are outliers.

The ebullition fluxes at Passaúna reservoir were episodic and zero inflated. The fluxes were not normally distributed (Kolmogorov-Smirnov test), which can also be observed in the boxplots (see Figure 42e and Figure SI 48), and thus, non-parametric methods were used for correlation analysis. The average ± standard deviation fluxes over the entire monitoring period at the monitoring loca-

tions were $24.2\pm47.0\,\mathrm{mgCH_4\,m^{-2}\,d^{-1}}$ (n = 605, median 0, range $0\text{--}264.1\,\mathrm{mgCH_4\,m^{-2}\,d^{-1}}$) at site P1, $33.8\pm49.3\,\mathrm{mgCH_4\,m^{-2}\,d^{-1}}$ (n = 680, median $3.8\,\mathrm{mgCH_4\,m^{-2}\,d^{-1}}$, range $0\text{--}238.7\,\mathrm{mgCH_4\,m^{-2}\,d^{-1}}$) at site P2, $18.9\pm43.4\,\mathrm{mgCH_4\,m^{-2}\,d^{-1}}$ (n = 549, median 0, range $0\text{--}587.1\,\mathrm{mgCH_4\,m^{-2}\,d^{-1}}$) at the deepest site P3, and $19.1\pm39.8\,\mathrm{mgCH_4\,m^{-2}\,d^{-1}}$ (n = 274, median 0, range $0\text{--}175.1\,\mathrm{mgCH_4\,m^{-2}\,d^{-1}}$) at site P4. Generally, ebullition was more frequent during summer and at the beginning of autumn (Dec–Apr), whereas during winter (Jun–Aug) the events of bubble release became less frequent, often resulting in daily median fluxes of zero during these months (see Figure SI 48).

Spectral analysis was applied to time-series of methane ebullition at site P1, for which the longest continuous record (of almost one year from December 13th 2018 to November 24th 2019) was obtained. Most of the variance of the time-series was associated with high frequencies ($> 10^{-4}$ Hz, S3 Figure SI 49), i.e. at time scales shorter than 3 hr. A minor peak of spectral variance was observed at frequencies corresponding to a 3 hr period, however, from the wavelet transform we observed that the periodicity was not evenly distributed throughout the year, instead it was present mostly in the summer months from December to February, which were the months with more frequent ebullition fluxes.

The correlation of ebullition among locations was weak at the shortest time intervals (5 min, Spearman correlation rs < 0.3 and $p < 0.05$). Nevertheless, for increasing averaging intervals (1 hr and 1 d), the correlation between fluxes increased (Figure 43). The maximum correlation (rs=0.65 *p-val* < 0.05) was observed between sites P1 and P4. For the periods with continuous and simultaneous measurements at locations P1, P2, and P3, the daily fluxes were highly synchronized with an average synchronization parameter r (Kuramoto order parameter) of 0.76 ± 0.23. The synchronization was highest from February to April 2019, whereas the lowest synchronization (mean r = 0.60) was in December 2018 (see Figure 43d).
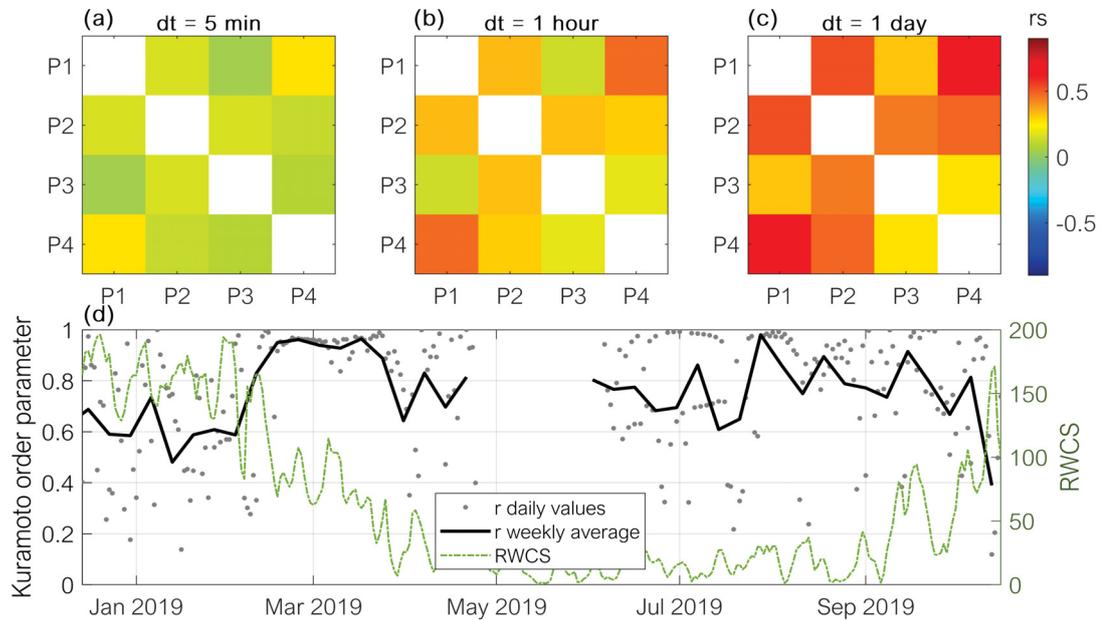
Figure 43 – Correlation of ebullition fluxes among monitoring sites for different timescales and synchronization of fluxes. Correlation matrix of methane ebullition fluxes observed at the four monitoring sites (P1–P4) at time intervals of 5 min **(a)**, 1 hr **(b)**, and 1 d **(c)** respectively. The colour indicates the Spearman rank correlation coefficient for a significance level of 5%. **(d)** Kuramoto order parameter (r, left-hand side axis) indicating the synchronization of daily ebullition fluxes at locations P1, P2, and P3 (grey dots) and weekly averaged r values (solid black line). Values of r = 1 indicate perfect synchrony whereas r = 0 indicates asynchrony of the fluxes. The green line shows the relative water column stability (RWCS, right-hand side axis).

The high degree of synchronization of the fluxes among locations suggests that ebullition was triggered by forcings acting over large spatial scales, which implies that the temporal dynamics of ebullition for time scales $\geq 1\,\mathrm{d}$ is similar among the monitoring locations. Therefore, for the statistical analysis of daily ebullition time-series in combination with environmental parameters described in the following sections, we only used the ebullition recorded at location P2, for which we had most valid data and for which most of the additional variables were measured in close vicinity (e.g., flow velocity, chl-a, water temperature, and DO).

Ebullition drivers

Methane ebullition flux was significant positively correlated (Spearman correlation rs) with bottom temperature (rs = 0.35), as well as to RWCS (rs = 0.45) and to Schmidt stability (rs = 0.41). In addition, we found positive correlations between ebullition and velocity variance near the bottom (rs = 0.37) and with the mean current speed (rs = 0.29). Significant negative correlations of ebullition were observed with air pressure (rs = −0.49), water depth (rs = −0.24), dissolved oxygen concentration at the bottom (rs = −0.35), chlorophyll-a (rs = −0.29), and backscatter intensity in the bottom layer (rs = −0.23) (see Figure SI 50 for correlation matrix). In the principal component analysis (PCA) of ebullition with eleven variables (see Figure SI 50) we observed two main groupings of the data points based on mixing conditions of the reservoir: mixed/partially stratified and stratified. Therefore, based on the PCA findings, the correlation analysis was additionally applied to subsets of the data, according to the prevailing stratification conditions (Figure SI 50).

When the reservoir was partially stratified, the dissipation rate of turbulent kinetic energy near the bottom was positively correlated with ebullition (rs = 0.31), whereas the bottom current velocity was positively correlated with ebullition when the reservoir was partially stratified (rs = 0.35) and stratified (rs = 0.30). Nevertheless, during the longest stratified period (December 2018 – February 2019), the wavelet coherence between time-series of methane ebullition and individual variables, such as total pressure and bottom current speed, varied with time and with the period. For the total pressure, there was high coherence with ebullition throughout the analysed time series for periods of approximately 8.5 d and 2.5 d, with the latter being more intensified between the end of December to the first week of January. Considering the bottom current, high coherence with ebullition was observed during short periods of less than 2.5 d. For both total pressure and bottom current the interrelation with ebullition occurred with a delay in respect to the variable (indicated by the left-up and right-down pointing arrows in Figure 44). In summary, the strength to which ebullition correlated with these environmental controls depended on the considered timescale and on time of the year.

Empirical models for ebullition prediction

Temperature (in the sediment or in water) and pressure (hydrostatic and atmospheric) were the most common ebullition predictors considered in empirical models presented in former studies (Table 7, and Table SI 8). In general, the empirical models from previous studies had a poor performance in reproducing ebullition fluxes at Passaúna ($R^2 < 0.5$ and Nash-Sutcliffe efficiency (NSE) < 0.3 between measured and simulated ebullition, Table 7). The best performance was achieved with the model that predicts mean ebullition fluxes solely as a function of binned sediment temperature (proposed by Wik et al. (2014), which could explain 47% of mean methane ebullition variability). Nevertheless, the temporal dynamics of ebullition was not captured by the model, as sediment temperature was changing only slowly and averaging of fluxes based on binned temperature smoothes ebullition variability (Figure 45). An autoregressive model proposed by McClure et al. (2020) for the simulation of reservoir-wide ebullition
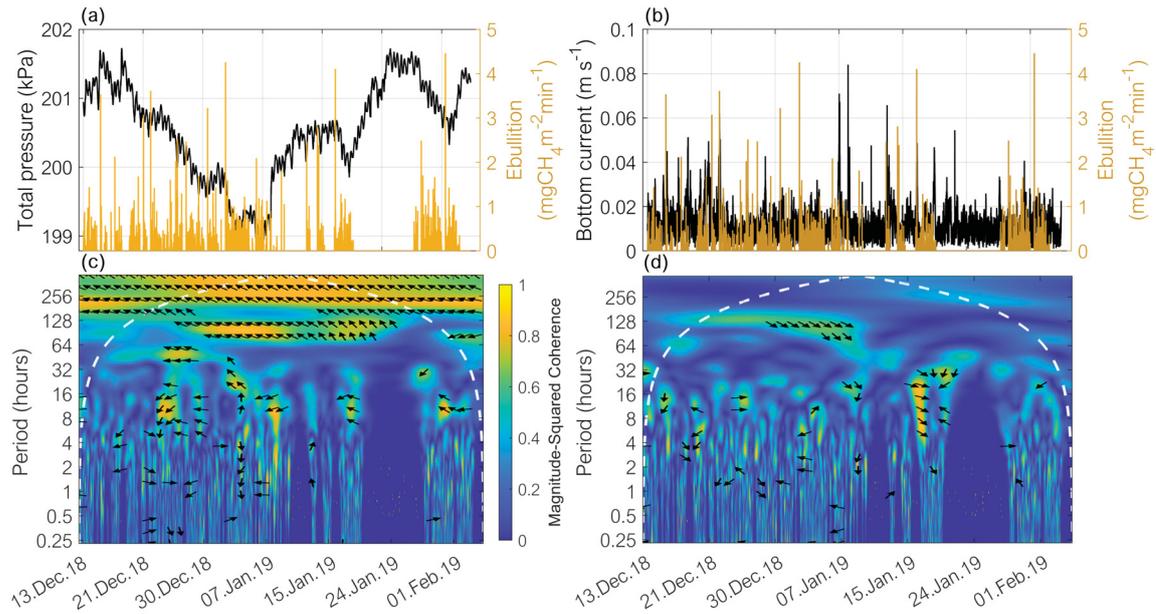
Figure 44 – Time series of methane ebullition, total pressure, bottom current speed and results of the wavelet coherence analysis. **(a)** Total pressure (hydrostatic + atmospheric, left hand axis) at the sediment surface at location P2 and methane ebullition rates measured at location P2 (right-hand axis). **(b)** Near-bottom current speed (left-hand axis) and methane ebullition rates measured at location P2. **(c)** and **(d)** show the squared wavelet coherence magnitude of total pressure and ebullition, and bottom current speed and ebullition, respectively. In both panels, the dashed white lines mark the cones of influence, in which the areas above the lines represent unresolved timescales. The yellow colour represents regions of high coherence, while blue colour represents lower dependence between the time-series; the left-up and right-down pointing arrows indicate that ebullition is occurring with a delay in respect to the controlling variable. In all panels the time series are at 5 min time intervals.

(average from different monitoring sites), which in addition to sediment temperature also considered wind speed, changes in atmospheric pressure, and ebullition from the previous time-step, could not well reproduce the flux variability of weekly-averaged fluxes ($R^2 = 0.25$, Figure 45b). The same combination of variables with recalculated model coefficients did not improve the model capability to explain the variability of ebullition fluxes ($R^2 = 0.24$), indicating that more variables, or different models are required for describing ebullition variability in Passaúna Reservoir. All the other literature models tested had worse performance in predicting the temporal dynamics of ebullition. Considering the models with recalculated coefficients (see first part of Table SI 9), the best performance ($R^2 = 0.32$ and NSE = 0.31) was obtained for an Artificial Neural Network (ANN) model, in which daily time series of ebullition was explained as a function of the change in total pressure, total pressure and bottom temperature.

The performance of new empirical models for the prediction of daily time-series of ebullition tested with various combinations of input variables, varied from a R^2 of 0.18 to 0.70 (see Table SI 9 for all the new models implemented). The best result was obtained from a generalized additive model (GAM, see Figure 46 and Table 7), in which methane ebullition was explained using a sum of univariate shape functions of predictors. The input predictors were bottom current, velocity variance at the bottom, energy dissipation rate near the bottom, sediment temperature, DO at the bottom, atmospheric pressure, wind speed, relative water column stability (RWCS) and total pressure. The same set of variables in a similar model could explain 96% (and NSE = 0.96) of the variability of weekly ebullition time series. Nevertheless, as we increased the temporal resolution of the time series (time steps of 1 hr and 10 min), the models could not reproduce most of the variability ($R^2 = 0.19$ NSE = 0.19 and $R^2 = 0.05$ NSE = 0.048 respectively). The predicted R-squared values were additionally calculated for the GAM models
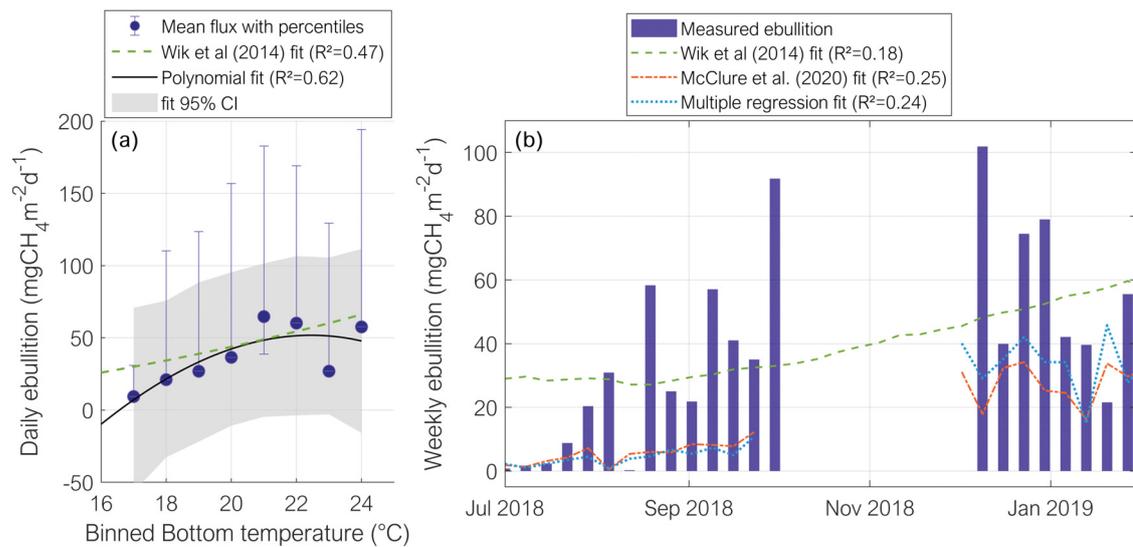
Figure 45 – Empirical models from the literature tested for the prediction of ebullition. **(a)** Application of an empirical model (dashed green line) for predicting mean ebullition flux as a function of binned (by $1\,°C$) sediment temperature (from Wik et al. (2014)). The blue circles are the mean methane ebullition fluxes for each temperature bin and the error bars are the 10th and 90th percentiles; the solid black line is a polynomial fit to the data and the 95% confidence interval (CI) of the fit is shown by the grey shaded area. **(b)** Weekly-averaged time-series of methane ebullition flux (blue vertical bars) and simulated ebullition predicted by the empirical equations from Wik et al. (2014) (dashed green line), from McClure et al. (2020) (orange dot-dash line), and from a multiple regression with the same input variables as McClure et al. (2020) (dotted blue line). The blank space between October and beginning of December 2018 is due to gaps in the measurements. The equations of all models are shown in Tables SI 8 and 9.

as an indicator of model overfitting. The values obtained for the predicted R-squared were below zero, which can be interpreted as equal to zero, indicating potential overfitting of the models (see Table SI 9).

        Considering the models for estimating the total accumulated methane flux (Tables SI 8 and 9), the models tested from the literature could be improved by recalculating the model coefficients for data from Passaúna Reservoir. For instance the polynomial fit proposed by Wik et al. (2014) had a Rel_{error} of -24.3% in reproducing accumulated ebullition, whereas with the recalculated polynomial fit we obtained a Rel_{error} of $2.06 \times 10^{-13}\%$ (see Figure 45a). Similarly, the artificial neural network originally trained in Deshmukh et al. (2014) resulted in an overestimation of 289.5% (Rel_{error}) of accumulated fluxes at our study site, however, with a retrained neural network using the same input variables the relative error was reduced to 4.4%. Rel_{error} could be further reduced in the new models developed for the Passaúna dataset, with the lowest error obtained also from the generalized additive model ($Rel_{error} = -0.28\%$, for daily time-series). For shorter time scales, the Rel_{error} of the generalized additive model increased to -1.4% and -1.2% for the hourly and 10 min resolution (Table 7).

Discussion

Ebullition temporal patterns and drivers

        Ebullition flux in freshwater reservoirs is considered as being stochastic in nature (DELSONTRO et al., 2015; TUŠER et al., 2017; LINKHORST et al., 2020), which turns both measurements and prediction of emissions challenging. At Passaúna Reservoir, ebullition fluxes were highly variable at different time-scales (minutes to months) with most of the temporal variance occurring at sub-daily timescales,

Table 7 – Results of empirical models tested from the literature and developed in this study (one selected model applied for different timescales) for the prediction of ebullition fluxes at Passaúna Reservoir. The timescales and predictor variables are provided. The model performance in reproducing the temporal dynamics of ebullition was evaluated using R^2, RMSE, and NSE. The model performance for estimating the accumulated flux was evaluated using the Relerror. Extended tables are provided in the supporting material (Tables SI 8 and 9) showing the equations of all models with additional information.

Reference	Timescale and variables	Performance for Passaúna
(WIK et al., 2014)	Temperature-binned daily ebullition Predictors: binned sediment temperature	$R^2 = 0.47$ $NSE = 0.23$ $Rel_{error} = -24.3\%$
(DESHMUKH et al., 2014)	Daily methane ebullition time series Predictors: change in total static pressure, total static pressure, and bottom temperature	$R^2 = 0.03$ $NSE = -6.06$ $Rel_{error} = 289.5\%$
(DELSONTRO et al., 2016)	Biweekly gas ebullition time-series Predictors: sediment temperature	$R^2 = 0.20$ $NSE = 0.09$ $Rel_{error} = 39.4\%$
(DELSONTRO et al., 2016)	Biweekly methane ebullition time-series Predictors: total phosphorous and sediment temperature	$R^2 = 0.19$ $NSE = 0.16$ $Rel_{error} = 30.1\%$
(ABEN et al., 2017)	Temperature-binned daily ebullition Predictors: methane ebullition at 20 °C, site-specific temperature coefficient, and binned sediment temperature	$R^2 = 0.39$ $NSE = 0.01$ $Rel_{error} = -17.5\%$
(MCCLURE et al., 2020)	Weekly methane ebullition time series Predictors: methane ebullition from the previous time step, sediment temperature, wind speed, and change in atmospheric pressure	$R^2 = 0.25$ $NSE = -0.11$ $Rel_{error} = 62.5\%$
(PRAETZEL; SCHMIEDESKAMP; KNORR, 2021)	Daily methane ebullition time-series Predictors: sediment temperature, sediment porosity, and organic matter content	$R^2 = 0.07$ $NSE = 0.06$ $Rel_{error} = 44.4\%$
(ZHAO; TEDFORD; LAWRENCE, 2022)	Daily methane ebullition time series Predictors: proportionality constant, pressure threshold, and total pressure	$R^2 = 0.12$ $NSE = -0.005$ $Rel_{error} = 9.8\%$
This Study	10-min methane ebullition time-series Predictors: bottom current, dissipation rate near the bottom, sediment temperature, DO near bottom, atmospheric pressure, wind speed, RWCS, and total pressure.	$R^2 = 0.05$ $NSE = 0.048$ $Rel_{error} = -1.2\%$
This Study	Hourly methane ebullition time-series Predictors: bottom current, velocity variance near the bottom, dissipation rate near the bottom, sediment temperature, DO near bottom, atmospheric pressure, wind speed, RWCS, and total pressure	$R^2 = 0.19$ $NSE = 0.19$ $Rel_{error} = -1.4\%$
This Study	Daily methane ebullition time-series Predictors: bottom current, velocity variance near the bottom, dissipation rate near the bottom, sediment temperature, DO near bottom, atmospheric pressure, wind speed, RWCS, and total pressure	$R^2 = 0.70$ $NSE = 0.69$ $Rel_{error} = -0.28\%$
This Study	Weekly methane ebullition time-series Predictors: bottom current, velocity variance near the bottom, dissipation rate near the bottom, sediment temperature, DO near bottom, atmospheric pressure, wind speed, RWCS, and total pressure	$R^2 = 0.96$ $NSE = 0.96$ $Rel_{error} = 0.01\%$
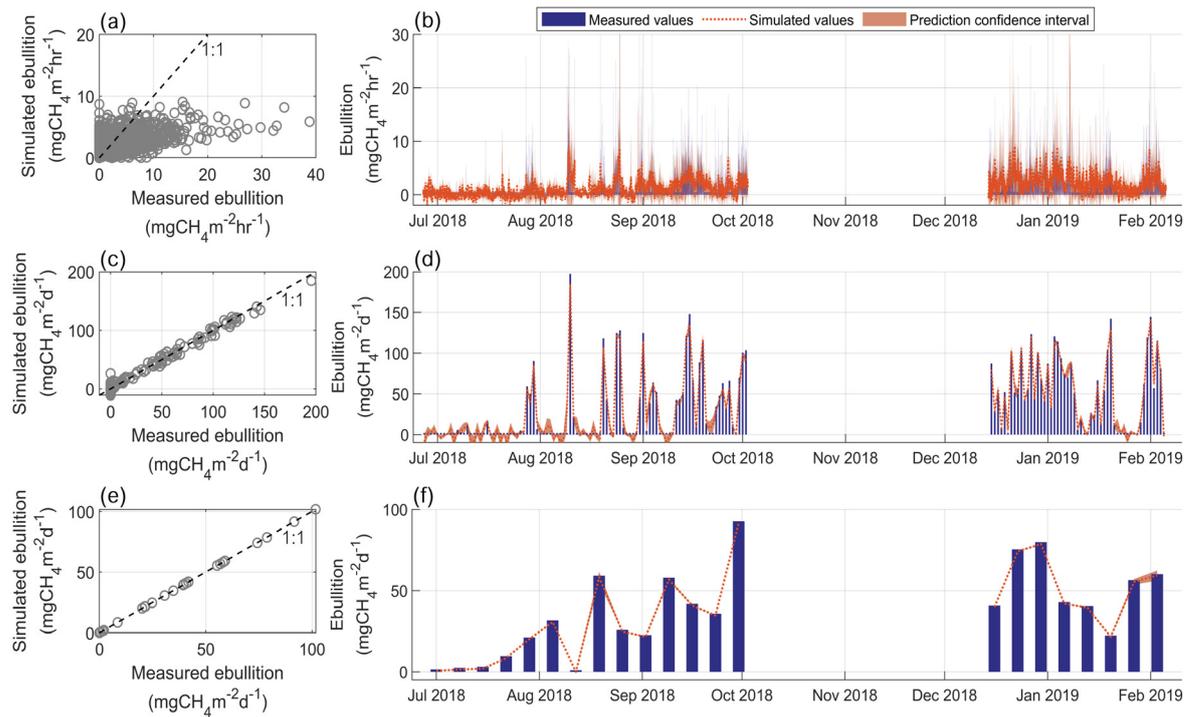
Figure 46 – Results of a generalized additive model (GAM) for reproducing methane ebullition at location P2 for hourly (**a** and **b**), daily (**c** and **d**), and weekly (**e** and **f**) time scales. The mean ebullition was predicted as a function of bottom current, velocity variance and energy dissipation rates near the bottom, sediment temperature, DO near the bottom, atmospheric pressure, wind speed, relative water column stability (RWCS), and total pressure. Model's equations and performance statistics are presented in S2 Table in the supporting material. Panels **a**, **c**, and **e** show scatter plots of simulated versus measured ebullition rates. Panels **b**, **d**, and **f** show time-series at the respective time steps (1 hr, 1 d, 1 week) of measured and simulated ebullition rates (as well as the prediction 95% confidence intervals, see legend).

as similarly reported for a river impoundment in Germany (MAECK; HOFMANN; LORKE, 2014). As a result of the episodic occurrence of ebullition, the time series were zero-inflated leading to frequent zero median fluxes throughout the monitoring period (from February 2017 to February 2020). On the one hand, median values are preferred over mean values for non-normally distributed data, such as ebullition (ROSENTRETER et al., 2021). On the other hand, median values lead to zero emissions estimates when using high temporal resolution measurements (time-scale $\leq$ 1 d). These results confirm that the use of cumulative fluxes is more appropriate for representing ebullition (WIK et al., 2013), and therefore, the importance of continuous measurements.

Considering seasonal variations, the extended time series of ebullition fluxes analyzed in the present study, confirm previous results (MARCON et al., 2019), showing that ebullition at Passaúna is intensified during periods when the reservoir is stratified (also confirmed by the PCA analysis, Figure SI 50). This can be explained by a combination of higher sediment temperature (up to 23 °C), reduced methane loss from the sediment due to diffusive transport (VACHON et al., 2019), and reduced methane oxidation as the water overlaying the sediment has lower dissolved oxygen concentrations ($<2\,\mathrm{mg\,L^{-1}}$) during stratification; all aspects favouring methane production and accumulation in the sediment.

The stochastic nature of ebullition fluxes is caused by the multitude of processes affecting the temporal and spatial dynamics of gas production, accumulation, and release from the sediment. In addition to stratification, other variables that have been reported for other water bodies were significant drivers of ebullition at Passaúna Reservoir, such as bottom water temperature (DELSONTRO et al.,

2016; ABEN et al., 2017), atmospheric and hydrostatic pressure (CASPER et al., 2000; MAECK; HOFMANN; LORKE, 2014; NATCHIMUTHU et al., 2016), and potential methane production (WILKINSON et al., 2015). Nevertheless, we would like to highlight interesting aspects found at Passaúna reservoir.

Surprisingly, ebullition was negatively correlated with chlorophyll-a concentrations (rs = −0.29). The presence of chlorophyll-a indicates fresh labile organic matter, which can enhance methanogenesis and sediment methane production (GRASSET et al., 2021), when deposited on the sediment. Other studies have found a positive relationship between ebullition and chlorophyll-a concentrations across different aquatic systems (DEEMER et al., 2016; DELSONTRO et al., 2016). At Passaúna reservoir, chlorophyll-a concentrations were reported to be higher after periods of mixing during autumn and winter (ISHIKAWA et al., 2022b), when sediment temperature was lower and the bottom water was oxic (see Figure SI 51). These conditions might lead to reduced methane production and enhanced methane oxidation. In addition, the diffusive transport of methane across the sediment water interface is enhanced during mixing conditions, resulting in lower ebullition fluxes (LANGENEGGER et al., 2019). In this way, the positive effect of higher chlorophyll-a could have been off-set by the combination of variables leading to a flux reduction. Two additional aspects are also important to be noted. First, correlations were calculated considering daily time-series, however the effects might be observed only for longer time intervals (months or seasons). Secondly, the chlorophyll measurements were done at 1.5 m below the water surface at site P2, and most of the chlorophyll deposition on the bed is expected to occur in the region around location P3 (ISHIKAWA et al., 2022b), nevertheless we also obtained significant negative correlation (rs = −0.15) between chlorophyll-a and ebullition flux measured at site P3.

Our extended set of variables facilitated analyses of ebullition fluxes in relation to the hydrodynamic conditions in the reservoir. Although stronger stratification (higher S_T and RWCS) occurred during the warmer summer months, the mixing periods at Passaúna reservoir were not restricted to one specific season, as the reservoir is classified as warm-polymictic (ISHIKAWA; BLENINGER; LORKE, 2021). Furthermore, according to Ishikawa, Bleninger and Lorke (2021), higher flow velocities associated with wind-driven currents were more frequent during stratified periods, whereas dissipation rates near the bottom were higher during mixed conditions. Consequently, we found that the effect of bottom currents and dissipation rates on ebullition were linked to the stratification conditions. During periods when the reservoir was stratified and partially stratified, the bottom currents were positively correlated to ebullition flux (rs = 0.36 and $p < 0.05$, Figure SI 50), in which ebullition events were occurring shortly after increased bottom currents (Figures 44b and 44d). A previous study showed that bottom currents can trigger bubble release, if the gas reservoir in the sediment is not depleted (JOYCE; JEWELL, 2003). When the amount of gas accumulated in the sediment was reduced, such as during mixing, bottom currents cannot trigger ebullition. We used the energy dissipation rates near the bottom as an indicator for the intensity of turbulence near the sediment (LORKE et al., 2002), and we expect a trade-off between two contrasting effects of turbulence on ebullition. On one hand, mechanical disturbances at the sediment surface can cause bubble release, whereas on the other hand, the increase in diffusive transport by near-bed turbulence can cause an increased loss of methane from the sediment by diffusive fluxes (LANGENEGGER et al., 2019). In fact, significant correlation (rs = 0.31) between ebullition and dissipation rates was only detected when the reservoir was partially stratified, mainly between July-August of 2018 (see details in Figure SI 52). During this period, the higher dissipation rates triggered ebullition, whereas during stratification, when the dissipation rates were generally lower, the negative sign of correlation suggests a dampening effect on ebullition.

Lastly, we found that the strength and direction of the effects of environmental variables on ebullition changed over time. Former studies proposed that the temporal dynamics of ebullition in different systems could be classified as controlled by forcing (ebullition triggers), or controlled by methane

production in the sediment (MAECK; HOFMANN; LORKE, 2014). In systems with continuously high methane production and high-frequency forcing, ebullition fluxes are continuously high. In systems with lower production and low frequency forcing, in contrast, ebullition dynamics is mainly controlled by the dynamics of the forcing. We argue that Passaúna Reservoir is switching between both states depending on stratification conditions. As the variation of sediment temperature at Passauna was relatively small (16–23 °C), temperature might not be the main control on methane production, but as discussed above, the loss of methane from the sediment (e.g. increased oxidation and diffusion) are expected to be the largest during the moments of reduced ebullition. Thus, during the periods with reduced methane accumulation in the sediment (e.g. during mixed conditions), ebullition dynamics is governed by the forcing, in which the high synchrony of ebullition among locations during this period suggests that large-scale forcings are dominant. However, during conditions favouring methane production and accumulation (e.g. with reduced losses other than ebullition), the site-specific characteristics (such as water depth and sediment properties) become also relevant in modulating ebullition dynamics, and thus reducing the synchrony of ebullition events among locations (see Figure 42, we obtained significant negative correlation rs = −0.37 between weekly values of RWCS and the Kuramoto order parameter characterizing the spatial synchrony of ebullition fluxes).

Empirical models for representing mean fluxes

The seasonal variations of mean ebullition fluxes could be well predicted by a simple empirical model considering binned sediment temperature proposed by Wik et al. (2014) ($R^2 = 0.47$ and $\text{Rel}_{error} = -24.3\%$ for the original polynomial fit and $R^2 = 0.62$ and $\text{Rel}_{error} = 2.06 \times 10^{-13}\%$ for the refitted model). The good fit of the model to our dataset from a subtropical man-made reservoir was surprising, as the model was originally obtained for data from subarctic postglacial lakes with contrasting characteristics. The model's capability of predicting ebullition across different systems, would point to the possibility of a universal model. Nevertheless, Aben et al. (2017) showed that a single model for predicting the varying magnitudes of ebullition across different systems as a function of temperature is not possible. However, the exponential dependence of ebullition on temperature is shared among the different systems (ABEN et al., 2017), which was also observed at Passaúna Reservoir. The mean fluxes for binned sediment temperature were minimum for temperatures lower than 18 °C (Figure 45a). Using the modified Arrhenius equation as proposed by Aben et al. (2017), we could explain 39% of mean ebullition as a function of binned temperature, however with an overestimation of accumulated fluxes by −17.5% (Table 7).

The difficulty in transferring models across systems was also observed for the prediction of accumulated fluxes. On overall, the models from previous studies failed in predicting the accumulated fluxes (Rel_{error} from −346.9% to 289.5%, Table SI 8). The model proposed by Zhao, Tedford and Lawrence (2022) based on total pressure could estimate the accumulated fluxes with an underestimation of 10%, however the model parameters were site specific (to Passaúna), which explain the improved model performance (Table 7). Nonetheless, the range of relative errors obtained from the prediction of accumulated fluxes were lower (from −2.8% to 48.1%) for the new models implemented, which can result from the combination of the addition of new ebullition predictors, the model's capability of capturing the short-term temporal dynamics of ebullition (and thus, reducing accumulated errors), and the tuning of model parameters to our data.

Empirical models for representing the temporal dynamics of ebullition

The characteristics of ebullition time-series of episodic/pulse events and being zero-inflated, in combination with the complex connection to various drivers, pose difficulties in reproducing the temporal

dynamics of ebullition fluxes and its magnitude using empirical approaches. Nevertheless, previous studies could successfully reproduce the temporal dynamics of ebullition by considering only atmospheric pressure ($R^2 = 0.87$) (ZHAO et al., 2021; ZHAO; TEDFORD; LAWRENCE, 2022), or a combination of more variables. For instance, McClure et al. (2020) reproduced ebullition time series with an autoregressive model using sediment temperature, wind speed, change in atmospheric pressure with good agreement ($R^2 = 0.86$). Eight models, proposed for other aquatic systems including lakes and reservoirs, were directly applied to Passaúna reservoir. The objective was to assess the extent to which these models can be employed across different systems to simulate ebullition fluxes, and to determine if they share similar controls on the fluxes. When applied to Passaúna reservoir, the empirical models from other systems resulted in a poor representation of ebullition variability, with the best results for reproducing ebullition temporal dynamics obtained by the equation proposed by McClure et al. (2020) ($R^2 = 0.25$ and NSE = -0.03 in Table 7 and Table SI 8).

Although the simulated fluxes were still within the range of the measured values (Figure 44b), the results indicated a weak transferability of empirical models from one system to another. In addition, other factors that may influence ebullition fluxes, such as mixing regimes, watershed area and characteristics, or the number of sampled sites, are commonly not considered in the different models. In a second step, the models proposed from the literature were refitted to our dataset. However, by readjusting the models' coefficients to the observations at Passaúna, the combination of the same variables could represent only a fraction of daily methane ebullition variability ($R^2 < 0.35$, see Table SI 9). Therefore, other factors are playing an important role in controlling ebullition dynamics in Passaúna Reservoir.

In a third step, new empirical models were implemented and tested for prediction of ebullition by including additional variables. A combination of nine input variables (including temperature, pressure, DO, velocity, and turbulence) in a generalized additive model could well capture the main temporal dynamics in daily ebullition time-series ($R^2 = 0.70$ and NSE = 0.69) and in weekly time-series ($R^2 = 0.96$ and NSE = 0.96), however, with poor performance for reproducing hourly time-series ($R^2 = 0.19$ and NSE = 0.19, Figure 46). The difficulty in reproducing ebullition with high temporal resolution is in part caused by the fact that with short time intervals the episodic behaviour of the time series is mostly pronounced, and also, because time mismatches when synchronizing several time-series measured by various devices are more likely to affect the results (VARADHARAJAN; HEMOND, 2012).

According to McClure et al. (2021), the transferability of empirical model for prediction of ebullition dynamics is likely to be weak even in the same system, whereas a continuous update of model constants by the inclusion of new measurements can improve the model performance in predicting ebullition. In this direction, we showed that ebullition was correlated with several parameters, however the strength of the correlation with each parameter was changing over time and was controlled by stratification conditions. For some variables, such as for the dissipation rate of turbulent kinetic energy, even the direction of the correlation was time dependent. Therefore, linear models will most likely fail in reproducing ebullition temporal patterns with a good performance, which can also result in a poor estimation of the accumulated fluxes and mean ebullition rates.

Broader implications, limitations, and further studies

Statistical analysis is a key approach for addressing highly variable processes, such as ebullition. Similar to rainfall, ebullition is characterized by episodic events of varying intensity, duration, and frequency of occurrence (VARADHARAJAN; HEMOND, 2012; MARCON et al., 2019). However, there is still no established and standard approach to measure and describe ebullition statistics in terms of long term and continuous measurements, timescales of analysis, and representation of fluxes. Time series

analysis can provide insights into the underlying processes and controls on methane ebullition in freshwater reservoirs and therewith improve the understanding of its temporal dynamics. Further analysis can bring additional insights into ebullition timescales, for instance by exploring the fractal dimensions in ebullition time series, similarly to analyses of rainfall data (BRESLIN; BELWARD, 1999). When applied to time series, fractal dimensions allow to connect information and to identify repeating complexities and patterns across different timescales (PILGRIM; P. Taylor, 2019), which in turn, might be useful for identifying the relevant time scales of ebullition across different systems.

Here we evaluated the temporal dynamics of ebullition mostly based on measurements from a single monitoring site (P2). We argued that it is representative for the other three monitoring sites in the Reservoir, as we found high synchronization of ebullition fluxes across the sites at daily timescales. However, it is important to mention that at shorter timescales ($< 1\,\mathrm{d}$), the degree of synchronization and the correlation of fluxes among the monitoring sites decreased. In addition, as found by McClure et al. (2020) for a shallow reservoir (maximum depth of $9.3\,\mathrm{m}$), the relevance of ebullition predictors differed between different regions of the reservoir, mainly longitudinally. Therefore, we speculate that for shorter timescales ($< 1\,\mathrm{d}$), shallow regions of the reservoir (upstream of site P1), and during periods when the fluxes among locations were asynchronous, the temporal variability of ebullition varied among locations, which could not be resolved in the available data.

The combination of different conditions (e.g., elevated methane production, higher temperature, reduction in water pressure) can culminate to hot moments and hot spots of methane emissions (DELSONTRO et al., 2015; DEEMER et al., 2016). Being able to predict the timing of such events is a basic initial step towards the development and implementation of methods for handling methane in water bodies. For instance, as summarized in Stolaroff et al. (2012), several of methane mitigation strategies rely on capturing and treating the methane, or are applicable only when methane gas fraction exceeds 1% (this methane fraction is easily found in rising bubbles). Empirical relationships can be fitted to capture and reproduce the temporal dynamics of ebullition as a function of a set of known variables and be applied to identify the hot moments of methane venting from aquatic systems. The advantages of data-driven models in comparison to mechanistic approaches, are that data-driven models generally require less computational power and are more flexible in terms of required input parameters, whereas process-based models might resolve complex physical and biogeochemical processes of methane formation and bubbles dynamics to simulate ebullition, which requires specific measurements for model calibration and validation (BOUDREAU et al., 2005; SCANDELLA et al., 2011; KATSMAN; OSTROVSKY; MAKOVSKY, 2013). In addition, statistical approaches and data-driven models are widely applied for filling measurement gaps in different fields, which can also be used for the case of ebullition for complementing existing measurements that are sparse in time.

We found that existing empirical models cannot be transferred across different systems. Similar to mechanistic approaches, model parameters need to be tuned to each system. The capability of empirical models for reproducing ebullition temporal dynamics was linked to the timescale under consideration. The models tested in this study had increasing difficulty in reproducing high temporal ($< 1\,\mathrm{d}$) variabilities of ebullition, since the randomness of the processes and uncertainties in the measurements increase with increasing temporal resolution. This is an important limitation because most of the ebullition variance was found at sub-daily timescales. In this regard, a mechanistic approach coupled with empirical models can potentially improve the predictions, which would have to be tested in future studies. Lastly, while a model based only on sediment temperature could estimated the total accumulated ebullition with a small relative error ($< 1\%$), a more complex model was necessary to capture the temporal dynamics of ebullition. Considering that ebullition does not respond linearly to its forcing, models that are capable of handling non-linearities among variables are better candidates to capture and to reproduce ebullition

flux dynamics. Nonetheless, it is important to note that in the case of the tested generalized additive models (GAM, see Table SI 9), the results indicated potential overfitting of the models to the data. Model overfitting is an important aspect, as it affects model's ability to generalize, consequently impacting its transferability. Therefore, model overfitting should be further investigated. For the case of GAM models, a penalty function can be used to the likelihood estimation to avoid overfitting (WOOD, 2004).

Furthermore, we identified that the strength of ebullition drivers was modulated by stratification conditions in the reservoir. Therefore, the implementation of different empirical models depending on the mixing conditions can potentially improve the prediction of ebullition fluxes, which can be investigated in futures studies.

Conclusion

We analysed high frequency ebullition measurements over three years of monitoring to understand the influence of various controls on its temporal dynamics and to evaluate the application of empirical models for reproducing the dynamics of ebullition fluxes across different aquatic systems and timescales. Vertical thermal stratification was an important modulator of the temporal dynamics of ebullition, impacting the strength and in some cases also the direction of the correlation between forcing and fluxes. The capability of reproducing and predicting ebullition fluxes from water bodies is relevant both in terms of estimating greenhouse gas budgets and for implementing mitigation strategies. Although empirical models are useful in understanding the drivers governing ebullition in aquatic system, to fill measurements gaps, and as a supporting tool for reservoirs management, they had a weak transferability from one system to another, which is caused by the complex interactions between ebullition and its controls. Weekly to daily temporal variability of ebullition could be well explained (R^2 = 0.96 and R^2 = 0.70) by a site-specific, generalized additive model considering nine input variables (bottom current, velocity variance at the bottom, dissipation rate near the bottom, sediment temperature, DO concentrations near the bottom, atmospheric pressure, wind speed, relative water column stability (RWCS) and total pressure). On longer time scales, the total accumulated ebullition flux could be well estimated by the generalized additive model (Rel_{error} = -0.28%). The relative error is further reduced (Rel_{error} = $2.06{\times}10^{-13}\%$) for a model based on sediment temperature only, however at the expense of not resolving temporal variability. Our results demonstrate that there is certainly no unique solution for predicting methane ebullition dynamics in aquatic systems, however, we suggest further studies to explore simplified approaches for reproducing ebullition temporal dynamics (such as exploring the fractal dimensions of ebullition), and to combine empirical models with mechanistic-based approaches.

Supplementary material

In this section are presented additional figures (Figure SI 47 to Figure SI 52) and tables (Table SI 8 and Table SI 9) supporting the manuscript 'Exploring the temporal dynamics of methane ebullition in a subtropical freshwater reservoir'.
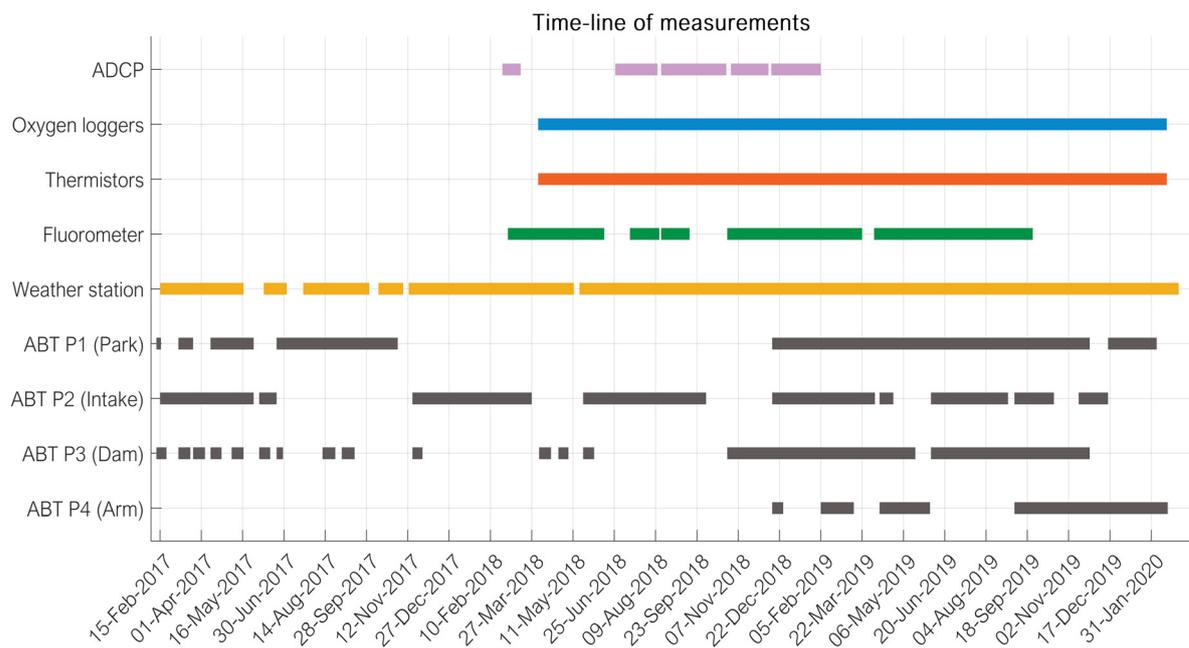
Figure 47 – Overview of measurements conducted at Passaúna reservoir during three years of monitoring. The Acoustic Doppler Current Profiler (ADCP) recorded velocity profiles, acoustic backscatter, and water depth; the dissolved oxygen loggers (near the bottom and near surface) recorded dissolved oxygen concentrations and water temperature; a chain of thermistors recorded the vertical distribution of water temperature; chlorophyll-a concentrations were recorded by a Fluorometer; the weather stations recorded wind velocity and direction, solar radiation, air temperature, atmospheric pressure, and humidity; and the Automated Bubble Traps (ABTs) recorded gas ebullition. The sensor locations are shown in Fig 1. The breaks within the horizontal lines indicate data gaps.
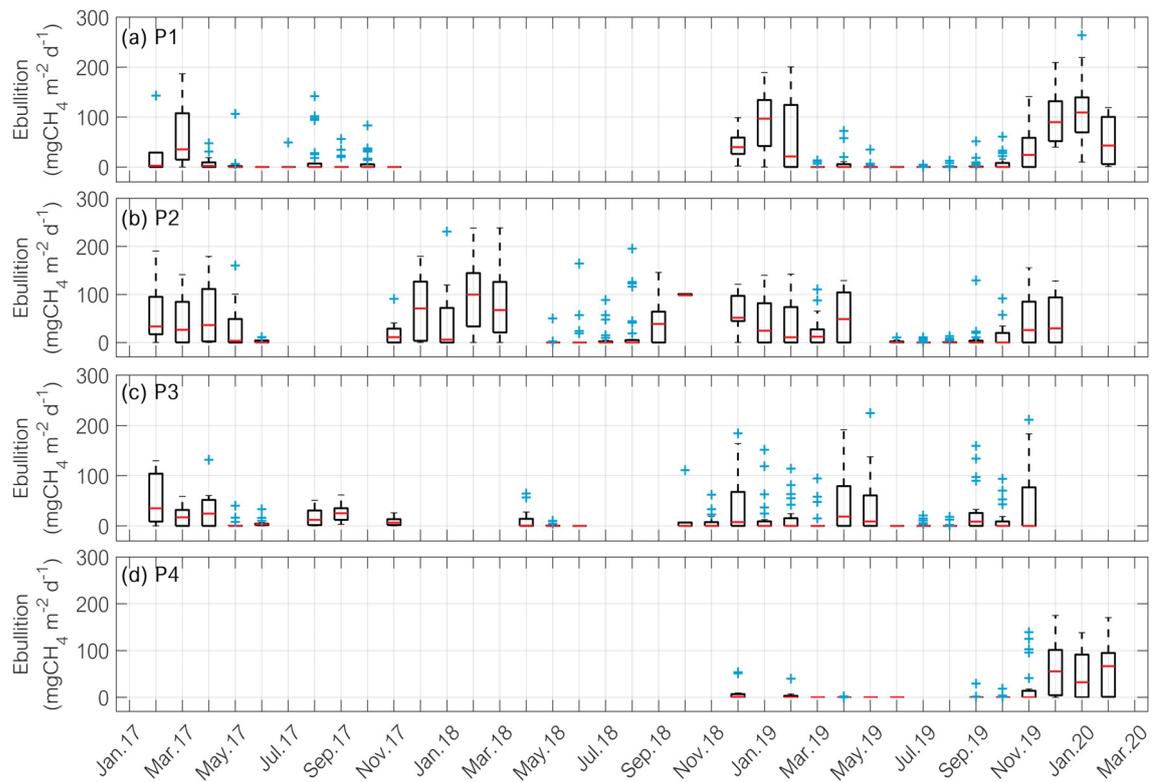
Figure 48 – Boxplots of monthly methane ebullition fluxes obtained from daily estimates at the four sampling locations between January 2017 and March 2020: **(a)** site P1 (Park); **(b)** site P2 (Intake); **(c)** site P3 (Dam); **(d)** site P4 (side arm). In all time series the blank spaces are data gaps. The upper and lower limits of the boxes represent the 75th and 25th percentiles, respectively. The whiskers show the maximum and minimum values, the red line represents the median, and the blue crosses are outliers.
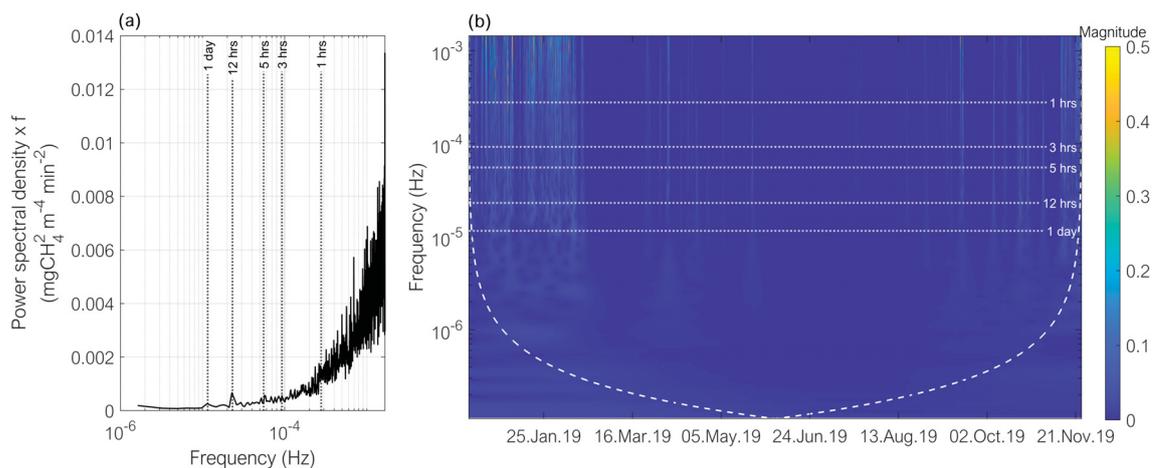
Figure 49 – **(a)** Variance-preserving power spectra of methane ebullition flux at site P1 with a sampling period of 5 min. **(b)** Wavelet transform of methane ebullition time-series at site P1. The colour represents the absolute value of the continuous wavelet transform in which the yellow colour indicates regions of periodic components and blue regions of low periodic components. The dashed white line shows the cone of influence, in which the areas below the line represent unresolved time scales. For both graphs the period of data used is from December 13th of 2018 to November 24th of 2019.
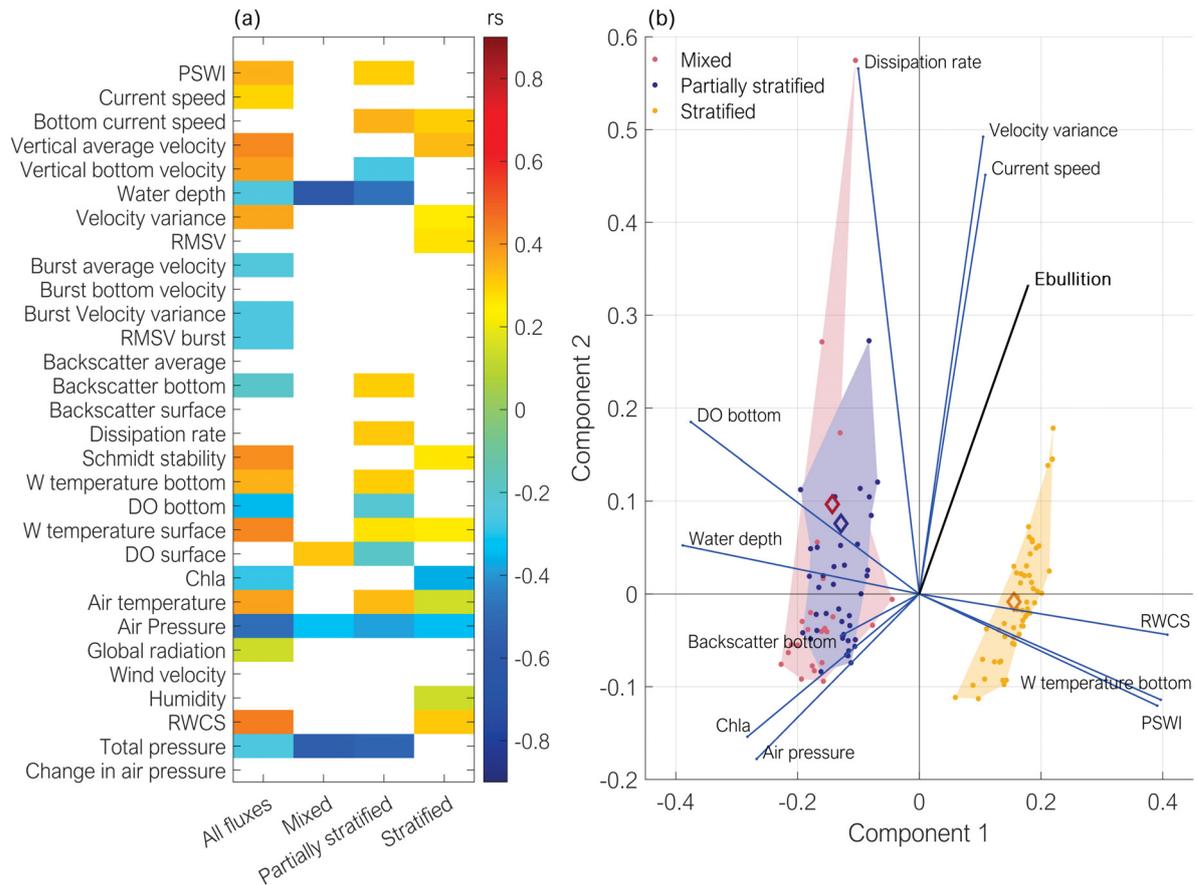
Figure 50 – **(a)** Correlation matrix (Spearman rank correlation) of daily methane ebullition fluxes at location P2 and daily averages of measured environmental parameters. The colour scales with the magnitude of the correlation coefficient (see legend) for a significance level of 0.05 (white boxes refer to no significance correlations with $p > 0.05$). The first column is the correlation with the complete data set whereas for the 3 other columns the data set was divided according to the prevailing stratification conditions. PSWI refers to the potential methane flux at sediment water interface; RMSV is the Root Mean Square Velocity ; W temperature (bottom or surface) is water temperature (near sediment bed or below the surface); and Chla is Chlorophyll-a concentration. Total pressure is the sum of hydrostatic and atmospheric pressure. **(b)** Results of a Principal Component Analysis (PCA) of selected variables with the first two principal components. The dots are data points (daily values) which were grouped based on the stratification conditions by different colours (see legend). Components 1 and 2 explain 47.8% and 15.5% respectively of the data set variability.
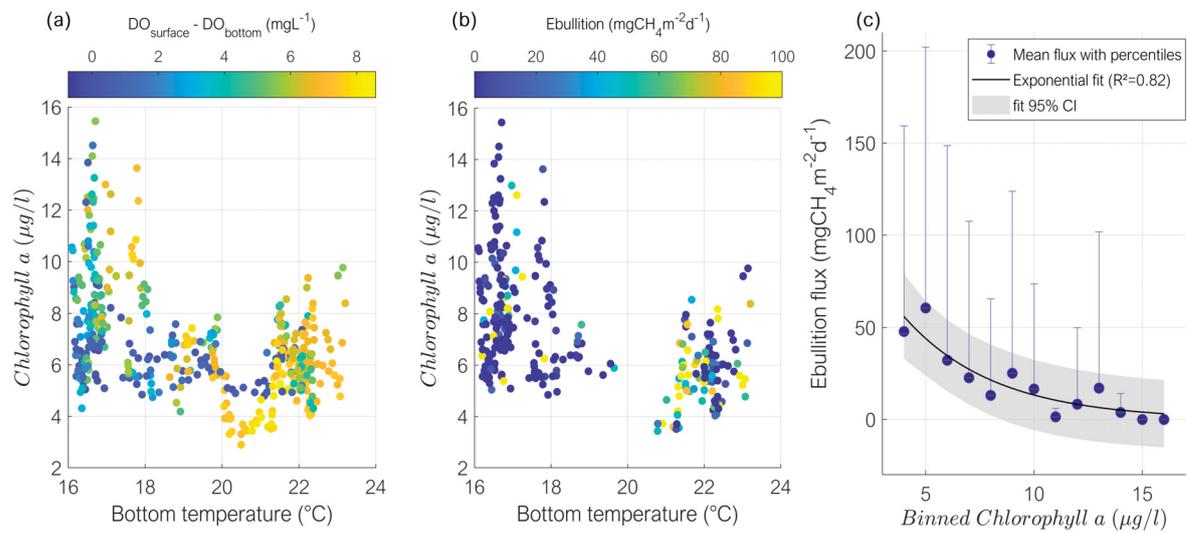
Figure 51 – **(a)** Scatter plot of chlorophyll-a and bottom temperature with the colour scale representing the difference of dissolved oxygen concentrations measured near the surface and near the bottom of the reservoir (see legend). **(b)** Scatter plot of chlorophyll-a and bottom temperature with the colour scale representing the methane ebullition flux (see legend). **(c)** Mean methane ebullition flux versus binned chlorophyll-a (by $1\,\mu\mathrm{g\,L}^{-1}$). The blue circles show the mean flux for each Chla bin and the error bars are the 10th and 90th percentiles; the solid black line is an exponential fit ($y = 145.7e^{(-0.24x)}$) to the data and the 95% confidence interval (CI) of the fit is shown by the grey shaded area. All plots are based on daily mean values at monitoring site P2.
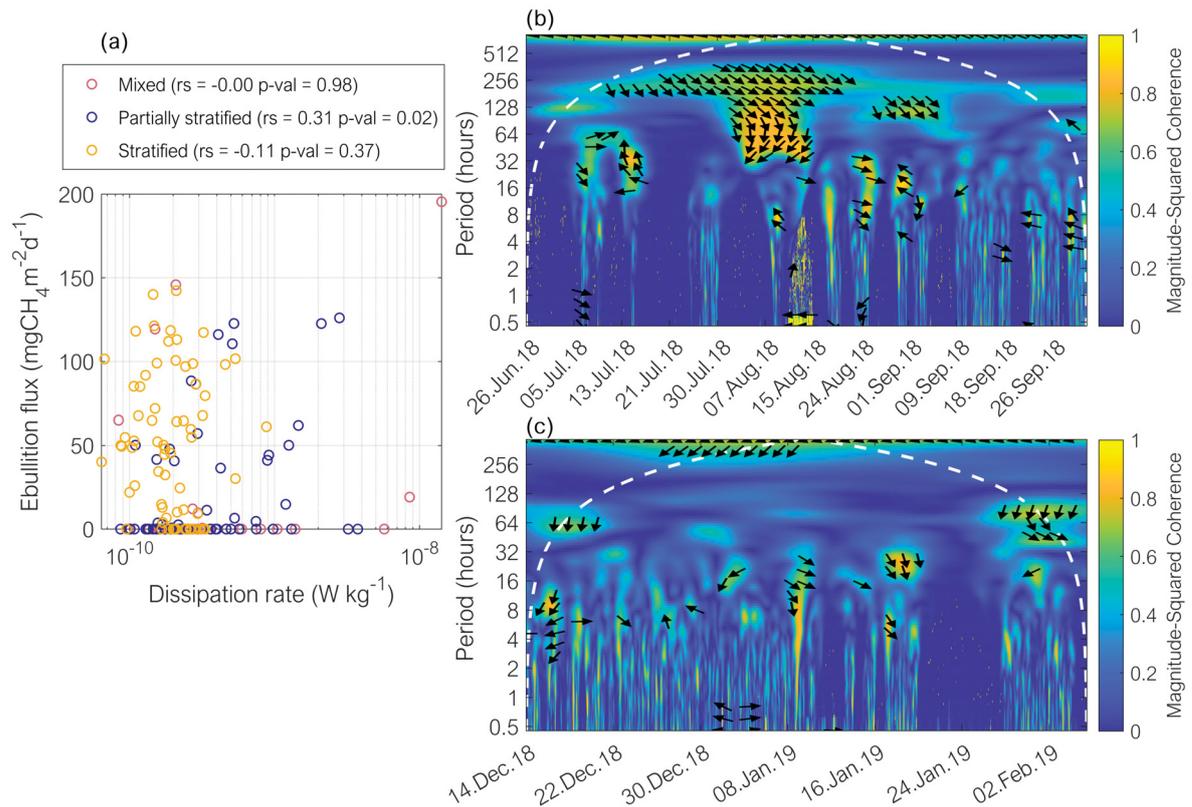
Figure 52 – **(a)** Scatter plot between daily methane ebullition and energy dissipation rates at location P2 grouped by the stratification classification (see colours and legend). Spearman correlation coefficients and significance levels between ebullition and $\log_{10}$-transformed dissipation rates are also shown in the legend. **(b)** and **(c)** shows the wavelet coherence analysis between total dissipation rates and ebullition for two intervals of measurements: mixed/partially stratified in **(b)** and stratified in **(c)**. In both figures, the dashed white lines are the cones of influence, in which the areas above the lines represent time and scales with no dependence in the series. The yellow colour represents regions with high coherence, while blue colour represents lower dependence between the time-series. For both panels the time series are at 10 minutes time intervals (as the highest time resolution available of dissipation rates are at 10 minutes time steps).

Table 8 – Summary of empirical models from other studies tested for the prediction of ebullition fluxes (y in ml m⁻²d⁻¹ or methane flux in mgCH$_4$m⁻²d⁻¹) at Passaúna reservoir. The timescale of each model is provided in the column 'Variables'. Additional information about the application of the models is provided as footnotes below the table. The model performance on predicting ebullition was evaluated considering the coefficient of determination (R²) of a linear fit between measured and simulated ebullition, the root-mean-square error (RMSE), and the Nash-Sutcliffe efficiency (NSE). The relative error (Rel$_{error}$) was calculated between measured and simulated total accumulated flux, in which negative values indicate an overestimation by the model and positive values an underestimation.

Reference	Empirical relationship	Variables	Performance for Passaúna
(WIK et al., 2014)	$y = -0.00036T_{sed}^3 + 0.16T_{sed}^2 - 0.94T_{sed} + 1.48$	Temperature binned time series y = mean methane ebullition in mgCH$_4$m⁻²d⁻¹ $Tsed$ = binned (1 °C) sediment temperature	R² = 0.47 RMSE = 16.79 NSE = 0.23 Relerror = −24.3%
(DESHMUKH et al., 2014) [1]	$yin_k = W_k + \sum_i WI_j v_i$ $y = W + \sum_{i=1}^{3} WS_i.tanh(yin_i)$	Daily time series yin_k = input value to each neuron W, WI, WS = are weights of the trained neural network v = normalized input variables (change in total static pressure in mH2O, total static pressure in mH2O, and bottom temperature in °C) y = normalized ebullition flux	R² = 0.03 (0.11) RMSE = 7.40 (18.85) NSE = −6.06 (−44.81) Rel$_{error}$ = 289.5% (770.8%)
(DELSONTRO et al., 2016) [2]	Ponds: $log_{10}(y) = 0.41 + 0.11T_{sed}$ Lakes: $log_{10} = 1.34 + 0.02T_{sed}$	Biweekly time-series y = gas ebullition in ml m⁻²d⁻¹ T_{sed} = sediment temperature in °C	Ponds: R² = 0.17 RMSE = 385.11 NSE = −57.68 Rel$_{error}$ = −346.9% Lakes: R² = 0.20 RMSE = 48.07 NSE = 0.09 Rel$_{error}$ = 39.4%
(DELSONTRO et al., 2016) [3]	$log_{10}(y) = -2.0 + 1.04 log_{10}TP + 0.06T_{sed} + 0.14(log_{10}TP - 1.26)(T_{sed} - 14.65)$	Biweekly time-series y = methane ebullition in mmol m⁻²d⁻¹ TP = total phosphorous (46 µg L⁻¹) T_{sed} = sediment temperature in °C	R² = 0.19 RMSE = 20.2 NSE = 0.16 Rel$_{error}$ = 30.1%

Reference	Equation	Description	Statistics
(ABEN et al., 2017) [4]	$y = E_{20} \times \theta^{(T-20)}$	Daily time series (Temperature binned data); y = methane ebullition in $\mathrm{mgCH_4m^{-2}d^{-1}}$; E_{20} = methane ebullition at 20 °C (36.48 $\mathrm{mgCH_4\,m^{-2}\,d^{-1}}$); θ = overall system temperature coefficient (1.22)	$R^2 = 0.01$ (0.39); RMSE = 38.73 (18.13); NSE = 0.01 (0.11); Rel_{error} = 5.1% (−17.5%)
(MCCLURE et al., 2020) [5]	All sites: $ln(y) = -5.11 + 0.37AR1 + 0.30T_{sed} + 1.14w_s - 0.53\Delta P$	Weekly time series; y = methane ebullition+0.1 in $\mathrm{mgCH_4m^{-2}d^{-1}}$; AR1 = log_e-transformed methane ebullition from the previous time step (previous week) in ln(in $\mathrm{mgCH_4m^{-2}d^{-1}}$); T_{sed} = sediment temperature in °C; w_s = log_e-transformed wind speed in $\ln(\mathrm{m\,s^{-1}})$; ΔP = change in atmospheric pressure in kPa	$R^2 = 0.25$; RMSE = 26.53; NSE = −0.03; Rel_{error} = 62.5%
(MCCLURE et al., 2020) [5]	Site T1: $ln(y) = -6.46 + 0.62AR1 + 0.39T_{sed} + 0.39w_s - 0.44\Delta P$	Weekly time series; y = methane ebullition+0.1 in $\mathrm{mgCH_4m^{-2}d^{-1}}$; AR1 = log_e-transformed methane ebullition from the previous time step (previous week) in ln(in $\mathrm{mgCH_4m^{-2}d^{-1}}$); T_{sed} = sediment temperature in °C; w_s = log_e-transformed wind speed in $\ln(\mathrm{m\,s^{-1}})$; ΔP = change in atmospheric pressure in kPa	$R^2 = 0.20$; RMSE = 26.62; NSE = −0.04; Rel_{error} = 59.70
(MCCLURE et al., 2020) [5]	Site T2: $ln(y) = -2.36 + 0.04AR1 + 0.16T_{sed} - 0.20Q$	Weekly time series; y = methane ebullition+ 0.1 in $\mathrm{mgCH_4m^{-2}d^{-1}}$; AR1 = log_e-transformed methane ebullition from the previous time step (previous week) in ln(in $\mathrm{mgCH_4m^{-2}d^{-1}}$); T_{sed} = sediment temperature in °C; Q = log_e-transformed inflow discharge in $\ln(\mathrm{m^3s^{-1}})$	$R^2 = 0.41$; RMSE = 37.83; NSE= −1.01; Rel_{error} = 94.09

Reference	Equation	Description	Statistics
(MCCLURE et al., 2020) [5]	Site T3: $ln(y) = -2.18 - 0.29AR1 - 0.60Q$	Weekly time series y = methane ebullition+ 0.1 in $mgCH_4m^{-2}d^{-1}$ $AR1$ = log_e-transformed methane ebullition from the previous time step (previous week) in ln(in $mgCH_4m^{-2}d^{-1}$) Q = log_e-transformed inflow discharge in $ln(m^3s^{-1})$	$R^2 = 0.13$ $RMSE = 55.47$ $NSE = -1.35$ $Rel_{error} = 100.12$
(MCCLURE et al., 2020) [5]	Site T4: $ln(y) = -3.21 + 0.23AR1 + 1.37Phyto$	Weekly time series y = methane ebullition+ 0.1 in $mgCH_4m^{-2}d^{-1}$ $AR1$ = log_e-transformed methane ebullition from the previous time step (previous week) in ln(in $mgCH_4m^{-2}d^{-1}$) T_{sed} = sediment temperature in °C w_s = log_e-transformed wind speed in $ln(m\ s^{-1})$ ΔP = change in atmospheric pressure in kPa	$R^2 = 0.01$ $RMSE = 41.69$ $NSE = -0.64$ $Rel_{error} = 97.52$
(PRAETZEL; SCHMIEDESKAMP; KNORR, 2021) [6]	$ln(y) = -13.79 + 0.25T_{sed} + 12.39\phi + 0.03OM$	Daily time-series y = methane ebullition in $mgCH_4m^{-2}d^{-1}$ T_{sed} = sediment temperature in °C ϕ = sediment porosity (0.9) OM = organic matter (Loss on Ignition 22.9%)	$R^2 = 0.07$ $RMSE = 37.87$ $NSE = 0.06$ $Rel_{error} = 44.4\%$
(ZHAO; TEDFORD; LAWRENCE, 2022) [7]	$y = \begin{cases} k(P_{th} - P), & P < P_{th} \\ 0, & P \geq P_{th} \end{cases}$ $P_{th}(t) = \frac{1}{\tau}\int_{\tau-t}^{t} P(t)dt$	Daily time series y = methane ebullition in $mgCH_4m^{-2}d^{-1}$ k = proportionality constant (94.9 $mgCH_4m^{-2}d^{-1}kPa^{-1}$) P_{th} = time dependent pressure threshold (in kPa) P = Total pressure (in kPa) τ = time-window over which the threshold is calculated (9 days)	$R^2 = 0.12$ $RMSE = 52.14$ $NSE = -0.005$ $Rel_{error} = 9.8\%$

[1] The model is Multilayer perceptron neural network (MLP) with 3 neurons in the hidden layer. The input variables are normalized to improve model performance. The weights trained by the neural network (W, WI, WS) and the coefficients for normalizing the input variables and the ebullition flux are provided by the authors (DESHMUKH et al., 2014). We tested the model with the input variables normalized as proposed by the author (adopting the provided coefficient for normalization) and by normalizing the data with the minimum and maximum values to obtain the data in the range between 0 and 1. The model performance for the last case is shown in parenthesis.

[2] Biweekly time-series were calculated as the average from the daily time series were, as the authors used measurements with a mean temporal resolution of 15 days.

[3] Mean TP from water samples at P2 of 13 $\mu g\,L^{-1}$ (GURSKI, 2022).

[4] E_{20} = mean ebullition flux from temperature-benned data at 1 °C. θ obtained as $Q_{10} = \theta^{10}$, in which the ecosystem level $Q_{10} = 10^{10 \times b}$ with b as the slope of a linear regression between $\log_{10}$(methane Ebullition flux) and (near) sediment temperature. The values in parentheses from the model application refer to the results using binned dataset.

[5] It was adopted weekly time-series of methane ebullition and environmental variables, which were calculated as the average from the daily time series.

[6] $\phi = 0.90$, porosity assumed as the reservoir sediment is composed mostly by clay and Loss on Ignition (LOI at 550 °C) for sediment core at location P2 of 22.9% (SOTIRI et al., 2021).

[7] The proportionality constant (k) and the time window (τ) were selected based on the best prediction of methane ebullition.

Table 9 – Empirical models tested for the prediction of ebullition flux (y in mL m^{-2}d^{-1} or methane flux in mgCH$_4$m^{-2}d^{-1}) based on data from Passaúna reservoir. The timescale of each model is provided in the column 'Variables'. Additional information about the application of the models are provided as footnotes below the table. The model performance in predicting ebullition was evaluated considering the coefficient of determination (R^2) of a linear fit between measured and simulated ebullition, the root-mean-square error (RMSE), and the Nash-Sutcliffe efficiency (NSE). The relative error (Rel$_{error}$) was calculated between measured and simulated total accumulated flux, in which negative values indicate an overestimation by the model and positive values an underestimation.

Method	Empirical equation	Variables	Performance for Passaúna
		Models from Table 8 with coefficients recalculated for Passaúna reservoir	
Polynomial fit	$y = -0.024T_{sed}^3 + 0.006T_{sed}^2 + 36.57T_{sed} - 496.7$	Temperature binned data y = mean methane ebullition in mgCH$_4$m^{-2}d^{-1} T_{sed} = binned (1 °C) sediment temperature	R^2 = 0.62 RMSE = 11.79 NSE = 0.62 Rel$_{error}$ = 2.06×10^{-13}%
Linear fit	$log_{10}(y) = -1.78 + 0.15T_{sed}$	Biweekly time series y= mean methane ebullition+0.1 in mgCH$_4$m^{-2}d^{-1} T_{sed} = sediment temperature in °C	R^2 = 0.16 RMSE = 22.73 NSE= −0.07 Rel$_{error}$ = 59.1%
Linear fit	$log_{10}(y) = -3.50 + 0.19T_{sed}$	Daily time series y= mean methane ebullition+0.1 in mgCH$_4$m^{-2}d^{-1} T_{sed} = sediment temperature in °C	R^2 = 0.06 RMSE = 43.86 NSE= −0.26 Rel$_{error}$ = 93.1%

Model	Equation	Description	Metrics
Multiple linear regression	$ln(y) = -8.48 + 0.20AR1 + 0.46T_{sed} + 2.92w_s - 0.24\Delta P$	Weekly time series y = methane ebullition+0.1 in $mgCH_4 m^{-2}d^{-1}$ $AR1$ = $\log_e$-transformed methane ebullition+0.1 from the previous time step (previous week) in $\ln$(in $mgCH_4 m^{-2}d^{-1}$) T_{sed} = sediment temperature in °C w_s = $\log_e$-transformed wind speed in $\ln(m\ s^{-1})$ ΔP = change in atmospheric pressure in kPa	$R^2 = 0.24$ RMSE = 25.74 NSE= 0.03 $Rel_{error} = 59.0\%$
Multiple linear regression	$ln(y) = -3.64 + 0.61AR1 + 0.19T_{sed} + 0.33w_s + 2.88\Delta P$	Daily time series y = methane ebullition+0.1 in $mgCH_4 m^{-2}d^{-1}$ $AR1$ = $\log_e$-transformed methane ebullition+0.1 from the previous time step (previous day) in $\ln$(in $mgCH_4 m^{-2}d^{-1}$) T_{sed} = sediment temperature in °C w_s = $\log_e$-transformed wind speed in $\ln(m\ s^{-1})$ ΔP = change in atmospheric pressure in kPa	$R^2 = 0.31$ RMSE = 38.47 NSE= 0.02 $Rel_{error} = 74.4\%$
Artificial neural network (ANN) [1]	$yin_k = b_{in,k} + \sum_i x_i w_{ij}$ $yout_k = \frac{2}{1+e^{-2\times yin_k}} - 1$ $y = b_{out} + \sum_i yout_i v_i$	Daily time series yin_k = values of each neuron in the hidden layer b_{in}, b_{out} = are the bias of hidden neurons and of output layer w, v = are weights of the trained neural network (hidden layer and output neuron) x = normalized input variables (change in total static pressure in Pa, total static pressure in Pa, and bottom temperature in °C) $yout_k$ = output value of the sigmoid transfer function y = normalized ebullition flux	$R^2 = 0.32$ RMSE = 0.31 NSE= 0.31 $Rel_{error} = 4.4\%$

New models developed based on Passaúna dataset

Model	Equation	Definitions	Statistics
Stepwise regression 2	$y = 1.79 \times 10^5 + 1976.7v_{bottom} - 194.21P_{air} - 0.85P_{total} + 9.26 \times 10^{-4}(P_{air} \times P_{total})$	Daily time series y= methane ebullition in mgCH$_4$m^{-2}d^{-1} v_{bottom} = bottom current speed in m s^{-1} P_{air} = atmospheric pressure P_{total} = total pressure (hydrostatic+atmospheric)	R^2 = 0.10 RMSE = 51.91 NSE= 0.004 Rel$_{error}$ = −2.31%
Stepwise regression (log-transformed) 2	$y = 1033.8 + 0.78v_{var} - 3.42T_{sed} - 206.75P_{air} - 77.81P_{total}$	Daily time series y= methane ebullition+1 in mgCH$_4$m^{-2}d^{-1} v_{var} = log$_{10}$-transformed velocity variance T_{sed} = log$_{10}$-transformed sediment temperature P_{air} = log$_{10}$-transformed atmospheric pressure P_{total} = log$_{10}$-transformed total pressure (hydrostatic+atmospheric)	R^2 = 0.26 RMSE = 41.94 NSE= 0.11 Rel$_{error}$ = 48.11%
Multiple linear regression 3	$y = 5.89 \times 10^3 + 1.58 \times 10^3 v_{bottom} + 1.18 \times 10^5 v_{var} - 2.45T_{sed} - 1.07DO_{bot} - 5.08P_{air} + 0.14w_s + 0.005RWCS - 0.006P_{total}$	Daily time series y= methane ebullition in mgCH$_4$m^{-2}d^{-1} v_{bottom} = bottom current in m s^{-1} v_{var} = velocity variance at bottom in m^{2}s^{-2} T_{sed} = sediment temperature in °C DO_{bot} = dissolved oxygen concentrations in mg L^{-1} P_{air} = air pressure in mbar w_s = wind speed in m s^{-1} $RWCS$ = relative water column stability P_{total} = total pressure (hydrostatic+atmospheric) in Pa	R^2 = 0.37 RMSE = 35.25 NSE= 0.37 Rel$_{error}$ = −1.89%

| Multiple linear regression with AR1 term [3] | $y = 4.46 \times 10^3 + 1.54 \times 10^3 v_{bottom} + 1.39 \times 10^5 v_{var} - 0.99 T_{sed} - 1.54 DO_{bot} - 3.78 P_{air} - 2.26 w_s - 0.06 RWCS - 0.005 P_{total} + 0.20 AR1$ | Daily time series
 $y=$ methane ebullition in mgCH$_4$m^{-2}d^{-1}
 v_{bottom} = bottom current in m s^{-1}
 v_{var} = velocity variance at bottom in m^{2}s^{-2}
 T_{sed} = sediment temperature in °C
 DO_{bot} = dissolved oxygen concentrations in mg L^{-1}
 P_{air} = air pressure in mbar
 w_s = wind speed in m s^{-1}
 $RWCS$ = relative water column stability
 P_{total} = total pressure (hydrostatic+atmospheric) in Pa
 $AR1$= log$_e$-transformed methane ebullition+1 from the previous time step (previous day) | R^2 = 0.37
 RMSE = 35.25
 NSE = 0.37
 Rel$_{error}$ = −1.89% |
| Multiple linear regression with AR1 term (log$_e$-transformed) [3] | $y = 608.00 + 0.48 v_{bottom} + 0.73 v_{var} + 0.045 \varepsilon - 4.45 T_{sed} - 0.26 DO_{bot} - 117.37 P_{air} + 0.14 w_s - 0.06 RWCS - 47.05 P_{total} + 0.36 AR1$ | Daily time series
 $y=$ methane ebullition+1 in mgCH$_4$m^{-2}d^{-1}
 v_{bottom} = log$_e$-transformed bottom current in m s^{-1}
 v_{var} = log$_e$-transformed velocity variance at bottom in m^{2}s^{-2}
 ε = log$_e$-transformed dissipation rates near the bottom in W kg^{-1}
 T_{sed} = log$_e$-transformed sediment temperature in °C
 DO_{bot} = log$_e$-transformed dissolved oxygen concentrations in mg L^{-1}
 P_{air} = log$_e$-transformed air pressure in mbar
 w_s = log$_e$-transformed wind speed in m s^{-1}
 $RWCS$ = log$_e$-transformed relative water column stability
 P_{total} = log$_e$-transformed total pressure (hydrostatic+atmospheric) in Pa
 $AR1$= log$_e$-transformed methane ebullition+1 from the previous time step (previous day) | R^2 = 0.28
 RMSE = 40.44
 NSE= 0.17
 Rel$_{error}$ = 40.8% |

Model	Equation	Description	Metrics
Generalized additive model (GAM) regression [4]	$y \sim N(\mu\sigma^2)$ for $g(\mu) = 45.18 + \sum_i f_i(x_i)$	Daily time series; y= methane ebullition in $mgCH_4m^{-2}d^{-1}$, assuming a normal distribution with mean μ and standard deviation σ; $g(\mu) = \mu$ = identity link function; $f_i(x_i)$ = is a univariate shape function for the ith predictor	$R^2 = 0.70$; RMSE = 27.34; NSE = 0.69; $Rel_{error} = -0.28\%$; Predicted-$R^2 = <0$
Artificial Neural Network (ANN) (9 input variables) [5]	$yin_k = b_{in,k} + \sum_i x_i w_{ij}$ $yout_k = \frac{2}{1+e^{-2\times yin_k}} - 1$ $y = b_{out} + \sum_i yout_i v_i$	Daily time series; yin_k = values of each neuron in the hidden layer; b_{in}, b_{out} = are bias of hidden neurons and of output layer newline u, v = are weights of the trained neural network (hidden layer and output neuron); x = normalized input variables (see bottom notes); $yout_k$ = output value of the sigmoid transfer function; y = normalized ebullition flux	$R^2 = 0.41$; RMSE = 0.29; NSE= 0.41; $Rel_{error} = 2.6\%$

Testing best model for prediction in different timescales

Model	Equation	Description	Metrics
Generalized additive model (GAM) regression [6]	$y \sim N(\mu\sigma^2)$ for $g(\mu) = 0.03 + \sum_i f_i(x_i)$	10-minutes time series; y= methane ebullition in $mgCH_4m^{-2}min^{-1}$, assuming a normal distribution with mean μ and standard deviation σ; $g(\mu) = \mu$ = identity link function; $f_i(x_i)$ = is a univariate shape function for the ith predictor	$R^2 = 0.05$; RMSE = 0.11; NSE= 0.049; $Rel_{error} = -1.2\%$; Predicted-$R^2 = <0$
Generalized additive model (GAM) regression [4]	$y \sim N(\mu\sigma^2)$ for $g(\mu) = 1.85 + \sum_i f_i(x_i)$	Hourly time series; y= methane ebullition in $mgCH_4m^{-2}hr^{-1}$, assuming a normal distribution with mean μ and standard deviation σ; $g(\mu) = \mu$ = identity link function; $f_i(x_i)$ = is a univariate shape function for the ith predictor	$R^2 = 0.19$; RMSE = 3.22; NSE= 0.19; $Rel_{error} = -1.24\%$; Predicted-$R^2 = <0$

Model	Equation	Description	Metrics
Generalized additive model (GAM) regression [4]	$y \sim N(\mu\sigma^2)$ $g(\mu) = 37.68 + \sum_i f_i(x_i)$	Weekly time series $y=$ methane ebullition in $mgCH_4m^{-2}d^{-1}$, assuming a normal distribution with mean μ and standard deviation σ $g(\mu) = \mu =$ identity link function $f_i(x_i) =$ is a univariate shape function for the ith predictor	$R^2 = 0.96$ $RMSE = 6.4$ $NSE = 0.96$ $Rel_{error} = 0.01\%$ Predicted-R^2 = < 0

[1] ANN: output layer with three inputs (normalized to range 0 and 1); one hidden layer with with five neurons and a sigmoid transfer function; and one output layer as the normalized daily methane ebullition flux (fluxes normalized to range between -1 and $+1$). The ANN was trained using the 'Neural Network Fitting' toolbox at MatLab 2023a. The toolbox uses the Levenberg—Marquardt training algorithm and the data points (n = 149) are randomly divided into training set (70%), validation (15%), and testing (15%). The validation dataset is used by the algorithm to stop training the ANN when the error in predicting the validation data continuously increases for more than 6 (Default) Epochs.

[2] For the Stepwise regression nine variables were potential ebullition predictors: bottom current, velocity variance at the bottom, dissipation rate near the bottom, sediment temperature, dissolved oxygen concentrations near bottom, atmospheric pressure, wind speed, relative water column stability (RWCS) and total pressure. Here, the predictors are included sequentially in the model and accepted if a p-value criterion is met for a significance level of 5%. Interactions among the input variables are also tested as potential predictors.

[3] For the multiple linear regression the same nine variables from the Stepwise regression were considered as potential predictor (adding ebullition with time-lag of 1 in the last 2 cases of the multiple linear regression). Here the main difference to the Stepwise linear regression is that interactions among the input variables are not considered as potential predictors.

[4] The model was created using the *fitrgam* function in MatLab. In the model methane ebullition is explained using a sum of univariate shape functions of predictors. The input predictors were the nine variables used on the Stepwise regression. The model can handle non-linear interactions between ebullition and each predictor. The shape function for each predictor in created using a boosted tree. The model was also tested with log-transformed variables, however no improvement was achieved. The predicted-R^2 was estimated as an indication for model overfitting. It was calculated applying the Leave One Out Cross-Validation method as $predR^2 = 1 - \frac{PRESS}{SSTO}$, where $PRESS$ is the prediction sum of squares calculated by omitting each observation individually and $SSTO$ is the total sum of squares considering all data points.

[5] ANN: output layer with the same nine inputs variables adopted for Stepwise regression (normalized to range 0 and 1); one hidden layer with twenty neurons and a sigmoid transfer function; and one output layer as the normalized daily methane ebullition flux (fluxes normalized to range between -1 and $+1$). The ANN was trained using the 'Neural Network Fitting' toolbox at MatLab 2023a. We adopted the Bayesian regularization training algorithm and the data points (n = 149) are randomly divided into training set (65%), validation (15%), and testing (20%). Different architectures of the ANN was tested, here we present the configuration with the best results. The validation dataset is used by the algorithm to stop training the ANN when the error in predicting the validation data continuously increases for more than 6 (Default) Epochs.

[6] For testing the GAM model with the 10 minutes timestep time series, the velocity variance wasn't included as a predictor, because it was only available for time intervals $\geq$ 1hr. Therefore, eight predictors were considered: bottom current, dissipation rate near the bottom, sediment temperature, dissolved oxygen concentrations near bottom, atmospheric pressure, wind speed, relative water column stability (RWCS) and total pressure.

Annex

ANNEX A – Author contributions

This thesis is based on three original research manuscripts provided in Appendix A, B, and C which were conceived by all of the authors. I am the lead author of all manuscripts. The contributions of all authors are explained in the following:

Acoustic mapping of gas stored in sediments of shallow aquatic systems linked to methane production and ebullition patterns

Lediane Marcon, Klajdi Sotiri, Tobias Bleninger, Andreas Lorke, Michael Männich, and Stephan Hilgert

> Conceptualization: TB, SH
>
> Field campaigns: LM, KS, MM, SH
>
> Formal analysis: LM, KS
>
> Writing the manuscript: LM
>
> Revising the manuscript: LM, KS, TB, AL, MM, SH

Linking sediment gas storage to the methane dynamics in a shallow freshwater reservoir

Lediane Marcon, Michael Schwarz, Laura Backes, Mara Offermann, Felix Schreiber, Stephan Hilgert, Klajdi Sotiri, Christian Jokiel, and Andreas Lorke

> Conceptualization: LM, AL
>
> Field campaigns: LM, MS, LB, MO, FS, SH, KS
>
> Formal analysis: LM, LB, MO
>
> Writing the manuscript: LM, AL
>
> Revising the manuscript: LM, MO, FS, SH, KS, CJ, AL
>
> Supervision: AL

Exploring the temporal dynamics of methane ebullition in a subtropical freshwater reservoir

Lediane Marcon, Tobias Bleninger, Michael Männich, Mayra Ishikawa, Stephan Hilgert, and Andreas Lorke

> Conceptualization: LM, TB, MM, AL
>
> Data acquisition: LM, MM, MI, SH
>
> Formal analysis: LM
>
> Writing the manuscript: LM
>
> Revising the manuscript: LM, TB, MM, MI, AL, SH

ANNEX B – Declaration

I hereby declare that the thesis entitled "Investigation of Spatial and Temporal Dynamics of Ebullition in Impoundments" is the result of my own work except where otherwise indicated. This approved dissertation thesis was completed under a double degree agreement, as the partial fulfilment of the requirements for the degree of Doctor in Philosophy in Water Resources and Environmental Engineering at Federal University of Paraná (Brazil) and in Natural Sciences at University of Kaiserslautern-Landau. The present thesis is original and is not being submitted elsewhere.

Landau, August 2023

. . . .
Lediane Marcon

ANNEX C – Curriculum Vitae

Lediane Marcon

Nationality	Brazilian and Italian
Languages	Portuguese (mother tongue), English, German (B1)

September of 2023

Academic Background

June 2018	**Ongoing Doctorate (Double degree Brazil-Germany)**
	Federal University of Paraná (UFPR) – Curitiba, Brazil. Postgraduate Program in Water Resources and Environmental Engineering – PPGERHA.
	RPTU Kaiserslauter-Landau – Landau, Germany. Natural and Environmental Sciences, Environmental Physics.
	Title: Spatial and temporal dynamics of methane ebullition in impoundments. **Supervisors**: Prof. Dr-Ing Tobias Bleninger, Prof. Dr. Michael Männich, and Prof. Dr. Andreas Lorke
2016 - 2018	**Master in Water Resources Engineering and Environmental Engineering**
	Federal University of Paraná (UFPR) – Curitiba, Brazil
	Title: High temporal resolution measurement of ebullition in a subtropical reservoir. **Supervisors**: Prof. Dr-Ing Tobias Bleninger and Prof. Dr. Michael Männich.
2013 – 2014	**Undergraduate sandwich in Environmental Engineering**
	Carleton University – Ottawa, Canada
	Department of Civil and Environmental Engineering
2009 – 2015	**Bachelor in Environmental Engineering**
	University of Vale do Itajaí (UNIVALI) – Itajaí, Brazil
	Center of Earth and Sea's Technological Sciences (CTTMar)

Skills

Softwares and programing	MatLab; ArcGis; Arduino; Office Package; Latex; Statistical analyses; Numerical models (HEC-Ras, Delft-3D, and ModFlow)
General	Environmental monitoring and sensors maintenance; Laboratorial and experimental work; Data analysis and processing; Reports preparation and presentations; Teamwork and international cooperations
Fields of interest	Water resources; Limnology; Greenhouse gases; Methane; Hydrodynamics; Hydrology; Fluid Mechanics; Freshwater reservoirs; Sediments; Acoustics; Time-series; Modelling.

Awards

2016	Academic Merit
	University of Vale do Itajaí (UNIVALI) – Itajaí, Brazil

Scientific Career

2020 - 2022	**Research assistant** University Koblenz-Landau, Environmental Physics working group Project Methane gas elimination, funded by Deutsche Bundesstiftung Umwelt (DBU)
2015 – 2016	**Scientific initiation** University of Vale do Itajaí (UNIVALI) – Itajaí, Brazil Topic: Jets and plumes classification from outfall discharge. Case study: Cartagena outfall.
2015	**Environmental Engineering Trainee program** Federal Public Ministry – Itajaí, Brazil Expert advisory department
2014	**Internship** University of Ottawa – Ottawa, Canada Hydraulics Laboratory Topic: Laboratory Investigations on Environmental Hydraulics and River Engineering.
2012 - 2013	**Scientific initiation** University of Vale do Itajaí (UNIVALI) – Itajaí, Brazil Topic: Experimental and numerical modeling of unidimensional channel flow.

Selected Talks

Marcon, L.; Sotiri, K.; Bleninger, T. ; Lorke, A.; Mannich, M. ; Hilgert, S. Acoustic mapping of internal sediment characteristics defining ebullition areas in impoundments. *ASLO Aquatic Science Meeting*, Jun. 2021. Virtual.

Marcon, L.; Ishikawa, M.; Bleninger, T.; Mannich, M.; Lorke, A. Methane ebullition predictors for reservoir emissions combining modeling and machine learning. *XXIV Simpósio Brasileiro de Recursos Hídricos*, Nov. 2021. Virtual.

Marcon, L. ; Bleninger, T. ; Mannich, M. Seasonal and diurnal bubbling events in a brazilian subtropical reservoir. *ASLO 2018 Summer Meeting*. Victoria, British Columbia.

Marcon, L. ; Bleninger, T. ; Mannich, M. Monitoramento continuo de ebulição de gases em um reservatório subtropical. *XXII Símposio Brasileiro de Recursos Hídricos*, Nov. 2017, Florianópolis – SC.

Marcon, L.; Honorita, C O ; Bleninger, T. . Plume Analysis at the end of the Near Field Region. *International Symposium on Outfall Systems*, 2016. Ottawa - Ca.